INFORMATION TO USERS

This manuscript has been reproduced from the microfilm master. UMI films the text directly from the original or copy submitted. Thus, some thesis and dissertation copies are in typewriter face, while others may be from any type of computer printer.

The quality of this reproduction is dependent upon the quality of the copy submitted. Broken or indistinct print, colored or poor quality illustrations and photographs, print bleedthrough, substandard margins, and improper alignment can adversely affect reproduction.

In the unlikely event that the author did not send UMI a complete manuscript and there are missing pages, these will be noted. Also, if unauthorized copyright material had to be removed, a note will indicate the deletion.

Oversize materials (e.g., maps, drawings, charts) are reproduced by sectioning the original, beginning at the upper left-hand corner and continuing from left to right in equal sections with small overlaps.

ProQuest Information and Learning
300 North Zeeb Road, Ann Arbor, MI 48106-1346 USA
800-521-0600

Effect of ion beam irradiation on interfacial structure in bilayers

Randa Abdouche
Centre for the Physics of Materials
Department of Physics, McGill University
Montréal, Québec, Canada

August 2000

A Thesis submitted to the
Faculty of Graduate Studies and Research
in partial fulfillment of the requirements for the degree of
Doctor of Philosophy

To Cathy and Nick.

CONTENTS

FIGURES AND TABLES

FIGURES

TABLES

RÉSUMÉ

L'effet du bombardement ionique sur la structure des bicouches de Ni/Fe et de Co/Cu est étudié. Ces bicouches ont une magnéto-résistance géante et des propriétés de transport magnétique intéressantes.

Le profil des interfaces est examiné en utilisant quatre différentes représentations. Ces différentes représentations sont simulées à l'aide d'un modèle de N étapes linéaires. Il a été observé qu'une fonction d'erreur représente mieux la structure des interfaces. La différence entre les interfaces graduelles et les interfaces rugueuses est présentée, spécifiquement en ce qui concerne leurs effets sur la reflectivité spéculaire et non-spéculaire des rayons X.

Une méthode d'acquisition et de traitement de données permettant de séparer les composantes spéculaire et non-spéculaire de diffraction, ainsi que d'obtenir l'intensité intégrée absolue est élaborée. Un programme est développé en langage C pour permettre de calculer la réflexion rasante et l'intensité de la diffraction non-spéculaire des rayons X. La comparaison de ces calculs aux résultats expérimentaux permet d'obtenir les différents paramètres de structure.

Par l'étude de la réflexion rasante des rayons X, les profils de densité électronique des structures de six bicouches de Ni/Fe et de Co/Cu sont obtenus pour différentes doses de bombardement. Il a été observé que la diffusion entre les différentes couches augmente avec la dose.

Nous avons mené une étude plus détaillée de la structure des bicouches ayant la configuration Si/Ni(500Å)/Fe(500Å). Il a été observé qu'avec l'augmentation de la dose les interfaces deviennent plus rugueuses et la distance de corrélation entre les hauteurs diminue.

La structure crystallographique des échantillons a été déterminée en utilisant la diffraction de rayons X à grand-angle. Il a été observé que les bicouches de Si/Ni/Fe sont polycristalline avec des fortes textures de fcc Ni(111) et de bcc Fe(101) parallèles au substrat. Les études par microscopie électronique ont démontré que le volume des grains augmente avec la dose, ce qui est en accord avec ceux calculés à partir des pics de Bragg. Les résultats de la microscopie électronique sont en accord raisonnable avec les résultats de l'analyse par rayons X.

ABSTRACT

In the present thesis, we study the change in structural properties induced by ion beam irradiation of Ni/Fe and Co/Cu bilayers using various x-ray scattering techniques. These bilayers exhibit interesting GMR and magnetotransport properties.

We show that an N-step model is useful in simulating any given electron density profile. We test four different interface profile functions in fitting the reflectivity and conclude that the error-function profile best describes our samples. Different types of interfaces are introduced, namely graded and rough interfaces, together with a discussion of their representation and their effect on both specular reflectivity and non-specular x-ray intensity.

We develop a data acquisition and processing method in order to separate the specular and diffuse components of x-ray scattering and to obtain the normalized reflectivity. A computer program in C was developed to calculate the x-ray reflectivity (XRR) and diffuse scattering intensity and to fit the theoretical calculation to the experimental data using a non-linear least-squares fitting method.

By fitting the XRR data of six bilayers of Ni/Fe and Cu/Co of different thicknesses and deposition sequence, the electron density profiles are constructed for different irradiation doses, ϕ. The intermixing at interfaces is found to increase with increasing ϕ. No change in the bulk materials electron density is observed upon irradiation of four single layers of these materials.

A more detailed study is performed on Si/Ni(500Å)/Fe(500Å) bilayers. From diffuse-scan fits we find that as ϕ increases the interfaces become rougher, more jagged and the height-height correlation length of the roughness decreases. The intermixing can be approximated using the ballistic model of ion mixing.

Using high-angle x-ray diffraction (XRD) measurements, the samples are found to be polycrystalline with a strong texture of fcc Ni(111) and bcc Fe(101) parallel to the substrate surface. Both plane-view and cross-sectional transmission electron microscopy (TEM, XTEM) images show that in-plane and out-of-plane grain sizes increase with ϕ, in good agreement with out-of-plane grain sizes calculated from Bragg peaks. The high-angle x-ray Bragg peak positions agree well with selected-area electron diffraction (SAED) rings. The iron oxide parameters obtained from XTEM and SAED patterns agree well with XRR results.

ACKNOWLEDGMENTS

First, I wish to thank my thesis supervisor, Prof. Mark Sutton, for introducing me to this exciting field of research. I would also like to thank him for his continuous help and guidance throughout the accomplishment of this work. His financial help is mostly appreciated and I am grateful to him for permitting me to write this thesis from home while taking care of my newborn baby. I would also like to thank him for his careful reading and constructive criticism of this thesis.

I also benefitted from courses given by Profs. Martin Grant, Dominic Ryan and Cliff Burgess and from the Experimental Methods in Physics course given by Profs. Mark Sutton, Peter Grütter, Dominic Ryan, Zaven Altounian and Louis Taillefer.

I would like to express my special thanks to Maria Dikeakos for her enormous help during this research, especially for meeting strict deadlines. I would like also to thank Jean-François Pelletier for his help and encouragement throughout my studies, especially for reviewing the French abstract with Khalid Laaziri and for help in printing the TEM images with Juan Gallego.

Many special thanks to Mrs. E. Engelberg for her time, her advice and support which helped me a lot for the continuation of this thesis. Many thanks also to Rainer Ullmann for his much appreciated help.

During my stay at McGill I enjoyed the friendship and benefitted from many useful discussions with Eric Dufresne, Jacques Mainville, Tianqu Gu, Hao Biao, Ou Mao, Erol Girt, Li Cheng and Dok Won-Lee.

Many thanks to Paula Domingues, Joanne Longo, Diane Koziol, Lynda Corkum and Cynthia MacDonald for administrative support, to John Egyed for the workshop course, to Frank Van Gils, Steve Kecani and the workshop group for technical help, especially in fabricating the sample holder, and to Juan Gallego and Mikko Karttunen for computer help.

Many special thanks to my undergraduate Professor Nabil K. Gobran, to my aunt Gilberte Bailouni and to my talented friend Marie Saheb for their continuous encouragement, advice and moral support.

The research was financially supported by Dow Hickson fellowship and David Stewart Memorial McGill Major fellowship and by the Physics department and the Center for the Physics of Materials.

Finally, I would like to thank all my family members for their understanding,

support and encouragement throughout these long years, especially my parents who came on several occasions from Egypt to help take care of my children, my husband who took care of everything while I was writing the thesis, and my lovely children. Merci beaucoup ma belle Catherine pour ton aide et ta patience. Merci Nicolas.

1

INTRODUCTION

Thin films composed of artificially grown multilayer structures constitute an interesting class of materials having new mechanical, optical, electrical, magnetic and superconducting properties useful for a large number of important applications. These unique properties are a result of the periodicity of the layered materials [1]. By changing the material in each layer and the layer thicknesses, it is often possible to optimize the desired properties of the system [2].

Many applications for multilayers are being pursued, including mirrors for soft x-rays [3] and neutrons [4], high-critical-current superconductors [5], magnetoresistive heads [6] and magneto-optical recording materials [7].

In particular, multilayers consisting of alternating layers of magnetic and non-magnetic materials show interesting giant magnetoresistance (GMR) [6, 8] and perpendicular magnetic anisotropy [9] characteristics, both of which demonstrate their potential for applications [10].

In order to explain the motivation for the present work we will briefly discuss the GMR effect and outline some of the previous research work done in this field.

Magnetoresistance (MR) is defined as the change in electrical resistance of a material in response to a magnetic field. When a magnetic field is applied to a normal (i.e. not ferromagnetic) metal, the resistance is seen to *increase* with the intensity of the field, regardless of the relative orientation of the field with respect to the current and to the crystallographic axes. This phenomenon is called ordinary or *positive* magnetoresistance [11]. This can be explained by the fact that in the presence of a magnetic field, electron trajectories become convoluted (e.g. helical), and the mean

free path of the electrons decreases as the magnetic field increases.

On the other hand, in ferromagnetic systems, which in the absence of an applied field consist of several magnetic domains, the phenomenon of *negative* magnetoresistance is observed [12]. The application of an external magnetic field *decreases* the resistance by up to an order of magnitude in fields as small as 100 Oe. This is explained by the fact that the external field changes the domain structure and produces a single-domain crystal. Two effects then take place. First, the electron trajectories become less convoluted because of the presence of a uniform internal field, and second the removal of the domain walls eliminates a source of electron scattering [13]. Both effects result in longer mean free paths and thus lower resistance. This is why permalloy (a mixture of nickel and iron) is used as a magnetoresistive sensor in reading heads for magnetic hard disk drives in computers.

An even more dramatic effect, called giant magnetoresistance (GMR), was discovered in 1988 by Baibich *et al.* [6]. They have studied the magnetoresistance of Fe/Cr superlattices prepared by molecular-beam epitaxy, with different thicknesses of the Cr spacer layers. At zero magnetic field there exists an antiferromagnetic (AF) coupling of the neighbouring Fe layers via the Cr layers. By applying a magnetic field, they discovered a huge MR in superlattices with thin Cr layers. This GMR was ascribed to spin-dependent transmission of the conduction electrons between Fe layers through Cr layers. This GMR was found to oscillate as a function of the spacer thickness, with maxima at specific values of the Cr layers thickness.

The antiparallel coupling between Fe layers was observed earlier in Fe/Cr/Fe trilayer structures by spin-polarized low-energy electron diffraction experiments [14] and by the light-scattering and magneto-optical measurements [15]. The discovery of GMR in Fe/Cr superlattices is promising for applications to magnetoresistance sensors and caused a very large amount of research to be dedicated to understanding the GMR effect (see for example [16, 17]) and to finding other possible combinations of transition metals which show this effect, possibly with weaker AF couplings. Examples of investigated superlattices include, to mention but a few, Co/Ru, Co/Cr

and Fe/Cr [18], Co/Cu [8], Fe/Nb [19], Fe/Cr, Co/Cu and Fe/Cu [20] and permalloy/Au [21].

In a study by S.S.P. Parkin [22], the oscillatory indirect magnetic exchange coupling between ferromagnetic layers of Fe, Co, Ni or Ni alloys separated by transition metals spacers was investigated. It was found that the oscillatory indirect magnetic exchange coupling effect is a general phenomenon and the period was determined in all the transition metals in which the coupling was observed.

Many of the physical properties depend sensitively on the structural properties, such as interdiffusion and roughness, to the extent that physical properties can often be predicted if structure and composition are known with sufficient precision. It is not always true that structural and compositional *perfection* are the most desirable traits for magnetic films. Interfacial roughness may, for example, enhance magnetic coupling [23]. Coupling across nonmagnetic layers also relies on structural aspects of the spacer layers. Interdiffusion and roughness may modify the details of the interactions, but the distinction between roughness and interdiffusion is very difficult to do experimentally [11].

For example, giant magnetoresistance with low saturation field was found for $Ni_{80}Co_{20}$/Cu multilayers (MLs) [24]. We have participated in a study concerning the effect of cumulative interface roughness on the magnetization in these AF-coupled MLs [25]. Cumulative interface roughness is the accumulation of small intrinsic interface roughness in each layer, which becomes more pronounced as the number of bilayers (N) increases. By preparing samples with N varying from 8 to 100 and studying their structure using low-angle x-ray reflectivity (XRR) measurements it was found that as N increases, the interface roughness increases as is clearly shown by the damping of the second-order superlattice Bragg peaks, and by the deviation from linearity in M-H curves, which can be attributed to a roughness-related extrinsic anisotropy.

In order to study the effect of structure on the magnetic properties of thin films, bilayers and multilayers, well-established techniques able to modify the structural

properties and a variety of methods for structural probing and analysis are needed.

To modify the structural properties, preparation of samples with artificially induced, controlled defects is needed. There are both *in situ* and *ex situ* techniques used to modify the structure of samples. Examples of in situ techniques include roughening interfaces with codeposition [26] and changing deposition conditions, e.g. growth temperature [27].

We have participated in a study with the Thin Films Group of University of Montreal[1] concerning the effect of deposition temperature (T_s) on the texture and magnetic properties of sputtered Ni/Fe multilayers [28]. In this study, multilayers with the configuration $[Ni(86Å)/Fe(29Å)]_{11}$ were deposited by magnetron sputtering onto glass substrates. By changing the deposition temperature from room temperature to 300°C a systematic change in texture from (111) to (200) and an increase in grain size were found. The superlattice modulations were clearly visible in low-angle XRR measurements for all the multilayers deposited up to 250°C, however, the peaks intensities decrease with increasing T_s indicating enhanced mixing of Ni and Fe across interfaces.

The saturation resistivity (ρ_s) of the multilayers (with the applied field parallel to the current) decreases initially as T_s increases up to 200°C, which is associated with an increase in grain size hence a reduction of electron scattering at grain boundaries. At higher T_s, alloying across the layers leads to an increase in ρ_s. Also, the total anisotropic magnetoresistance as well as its field sensitivity were found to increase with T_s.

These in situ techniques have the disadvantage of affecting the crystallography of the sample. Moreover, the study is performed on different samples, hence the comparison between the results is often inconclusive. On the other hand, ex situ techniques, such as post-growth annealing [29] and ion beam irradiation, offer the possibility of systematically modifying the structure of a *single* sample, thus providing conclusive information about structural and magnetic properties.

[1]Groupe de recherche en physique et technologie des couches minces, Université de Montréal.

In recent years the technique of ion beam irradiation (IBI) of multilayered samples has been used extensively for the formation of a mixed layer at the interfaces [30]. Examples of these studies include Ni-implanted iron [31, 32], Ar^{2+} irradiation of Au/Ni superlattices [33], Kr irradiation of Fe/Ni MLs [34], Ar^{+}-irradiated Co/Pd MLs [35], Xe^{+}-irradiated Fe/Cr MLs [36], Ne^{+} irradiation of Ag/Fe superlattices [37], Kr irradiation of Au/Ni MLs [38] and noble gas irradiation of Fe/Ni MLs [39].

In particular, we have studied, in collaboration with the Thin Films Group of University of Montreal[1], the effect of ion irradiation and subsequent annealing on Co/Cu MLs [40, 41].

First, multilayers with the configuration Cu(50Å)/[Co(16Å)/Cu(20Å)]$_{30}$/Cu(30Å) deposited by magnetron sputtering were irradiated with 1 MeV Si^{+} ions with doses ranging from 10^{12} to 10^{15} ions/cm^2. For ion-beam doses up to 10^{13} cm^{-2}, no changes in resistivity, MR or magnetization were observed [40]. The saturation resistivity (ρ_s) of the multilayer was found to increase noticeably as a function of total ion dose from 10^{13} up to 10^{15} ions/cm^2, whereas the resistivities of 1000Å Cu and Co pure films were nearly unchanged upon irradiation with the same doses. This suggests that the large increase in ρ_s in the Co/Cu MLs is connected with *interface* disorder induced by IBI, and is not due to any bulk defects produced in the Cu or Co layers by the beam.

Low-angle XRR measurements have confirmed the ion-beam-induced interface disorder in our samples whereas high-angle x-ray diffraction revealed little change in crystallographic texture. It was also found that the saturation magnetic field decreases as ion dose increases, while the remanence ratio (M_r/M_s) increases (where M_r and M_s are the remanence and the saturation magnetization, respectively). This indicates that the AF coupling strength between the magnetic layers and the AF-coupled fraction are systematically reduced by irradiation. The GMR was found to fall rapidly with ion dose in contrast to the results found for Fe/Cr MLs [36].

The increase in GMR with irradiation dose in Fe/Cr MLs was explained in terms

[1]Groupe de recherche en physique et technologie des couches minces, Université de Montréal.

of the enhanced spin-dependent electron scattering at the interfaces. In contrast, the decrease in MR by irradiation of our Co/Cu MLs can be understood to a large extent by a reduced fraction of AF-coupled domains rather than by enhanced interface scattering.

In a later study [41], multilayers with the configuration $[Co(17Å)/Cu(tÅ)]_{30}$ with t=22 and 34 Å were deposited by sputtering techniques. With these Cu thicknesses, the multilayers are situated at the 2^{nd} and 3^{rd} peaks of the GMR oscillation. These multilayers were irradiated by 1 MeV Si^+ ions to doses ranging from 10^{12} to 5×10^{14} ions/cm^2. Some of the irradiated samples were subsequently annealed in vacuum to temperatures up to 325°C.

Low-angle XRR measurement of the as-deposited multilayer (t(Cu)=34Å) reveals clear first- and second-order superlattice peaks, which confirms that the Co/Cu interfaces are well-defined. After irradiation at 2×10^{14} cm^{-2}, the intensities of the two superlattice peaks are reduced, indicating increased interface roughness. A fit to the as-deposited multilayer reflectivity data gave an interface roughness value of 5.7 ± 0.5 Å, whereas after irradiation at 2×10^{14} cm^{-2}, an intermixing region between the Co and Cu layers with a width of $\approx$11Å was deduced from the fit.

After annealing at moderate temperatures, the superlattice peaks in the low-angle XRR curves fully recovered their original intensities and linewidths. This shows that annealing causes a back-diffusion from the metastably mixed regions and causes the reformation of relatively abrupt interfaces. The fit to this spectrum shows no interdiffusion between the Co and Cu layers. This reversible behaviour is attributed to the equilibrium immiscibility of Cu and Co.

Examining the resistivity and the MR behaviour it was found that the saturation resistivity (ρ_s) of the multilayer increases progressively with ion doses above 10^{13} ions/cm^2 [40], as previously mentioned. Since in these multilayers the electron mean free path is comparable to the layer thickness, this increase in ρ_s can be directly connected with enhanced electron scattering as a result of ion-beam mixing across interfaces.

Upon subsequent annealing it was found that the resistivities of the irradiated multilayers decrease dramatically, and get very close to that of the non-irradiated sample which suggests that significant demixing at the interfaces occurs on heating.

The GMR was found to decrease monotonically with ion dose for these Co/Cu multilayers [40] but increases sharply upon annealing at different temperatures up to 300°C. This increase is mostly due to the interfacial demixing process and is accompanied by an improvement in the AF coupling between the Co layers. When annealing temperatures are increased above 300°C, the MR starts to decrease for all the multilayers as the multilayer structure begins to break down.

Therefore, ion irradiation of Co/Cu multilayers was found to cause a monotonic decrease in the GMR while subsequent annealing increases it. Hence, the AF interlayer coupling and the GMR can be reversibly altered *ex situ* over a wide range in a *single* Co/Cu multilayer with little effect on the crystallographic texture of the sample.

From our Ni/Fe [28] and Co/Cu [40, 41] studies, we have tested in situ and ex situ techniques able to modify the interfacial structure and hence to affect the GMR and the magnetotransport properties of these multilayers. The ion beam irradiation, as an ex situ technique, proved to be well suited for systematically modifying the structure of a single sample by successive irradiation to different doses. These results have motivated us to further study in more details the effect of IBI on the interfacial structure of Ni/Fe and Co/Cu samples.

A variety of techniques for structural analysis is now available which permits the determination of atomic scale structure using diffraction techniques and macroscopic morphology using electron microscopy techniques.

Different electron microscopy techniques include conventional electron microscopy, Lorentz electron microscopy, scanning electron microscopy with polarization analysis (SEMPA), scanning tunneling microscopy (STM), atomic force microscopy (AFM) and magnetic force microscopy (MFM).

Conventional diffraction techniques have been used extensively to determine the

structure of bulk materials. These techniques, including neutron, electron and x-ray diffraction, are well established and can be used reliably.

Neutron scattering can give, in principle, the same structural information as x-rays, but it offers lower intensity and resolution and is limited to major facilities. However, it can be used to determine the magnetic structure because of a neutron's magnetic cross section.

X-ray analysis is the best established and probably the most powerful probe of overall structural characterization. Well-established techniques exist to deal with structures of great complexity, with defects and with structural rearrangements. Furthermore, synchrotron x-ray sources provide enormous intensity, thereby opening new avenues to the x-ray study of chemical, and even magnetic, structure [11].

X-ray diffraction (XRD) also offers high spatial sensitivity, high penetration for studying buried interfaces and a nondestructive capability for studying real-time processes. It is therefore well suited for studying the structure of multilayers.

Several diffraction geometries exist in order to probe different properties of the samples. Low-angle x-ray diffraction profile gives the Fourier transform of the electron density profile. By fitting the low-angle reflectivity data it is possible to obtain the electron density profile of the sample perpendicular to the interfaces, the thickness and the root-mean-square (rms) roughness of the different layers. High-angle x-ray diffraction, on the other hand, gives information about the crystallographic structure of the bulk materials, whereas x-ray diffuse scattering measurements are essential in order to probe the in-plane structure and the roughness structure at the interfaces.

These x-ray scattering techniques have been used extensively in a very large number of studies. Examples include the use of XRD to study multilayers [10, 42, 43], thin films [44], surfaces [45], liquid surfaces [46] and liquid crystals [47]. In situ high-angle XRD during annealing was also used to study $Ni_{81}Fe_{19}$/Ag multilayers [48].

Kortright *et al.* [49] summarize the use of soft x-ray synchrotron radiation facilities in research in magnetism and magnetic materials, including the use of time-resolved measurements and examples of present and future opportunities in this field.

In particular, x-ray diffuse scattering (XDS) has received much attention in recent years since the derivation of the scattering cross section from a single surface [50, 51], and later a description of the diffuse scattering from multilayer interfaces [52, 53, 54]. It has been used to study the structure of roughness at surfaces and interfaces, and to investigate the interfacial roughness correlations in multilayers. Examples include the study of roughness structure and self- and cross-correlations in thin films [55], bilayers [56], metallic multilayers [57, 58, 59, 60, 61], amorphous multilayers [62], multilayers with stepped interfaces [63, 64], multilayer waveguides [65], grating surfaces [66] and organic multilayers [67, 68]. It has also been used to follow the evolution of the interfacial roughness of Fe/Au multilayers as a function of time [69].

In order to obtain structure information, modeling of the multilayer structure is required in order to compare the calculated intensity of the modeled multilayer with the measured intensity. Since many types of disorder can be present in a multilayer, including layer thickness fluctuations, interface disorder, crystalline disorder and interdiffusion, a large number of model parameters has to be included. Several scattering models have included discrete layer-thickness fluctuations and continuous fluctuations on the interface distance in their calculations (see for example [70, 71, 72]). Furthermore, the values of the parameters obtained from this kind of fits represent the averaged value over all the layers in the multilayer stack.

Since we are mainly interested in the interfacial changes which occur upon IBI, these effects could be better studied using bilayer samples. In this way the number of interfaces will be limited leading to a small number of fit parameters and therefore a more detailed study of the interface structure could be performed.

In the present thesis we will study the effect of IBI on the structure of Ni/Fe and Co/Cu bilayers. Recent studies on Ni-Fe samples include the study of the magnetic anisotropy of thin Fe films grown on Ni films of 140Å thickness on Si substrates [73]. The magnetic anisotropy was measured using SQUID magnetometry. The change in the magnetic anisotropy with the Fe layer thickness was correlated to a structural phase transition of Fe from fcc to bcc with increasing Fe thickness. In a more recent

study [74]. Parkin *et al.* have investigated the structure and magnetic properties of Fe/Ni and Fe/$Ni_{81}Fe_{19}$ MLs using XRD and SQUID magnetometry. They found that the Fe layers undergo a transition from a distorted fcc(001) phase to a nearly relaxed fcc(001) phase to a bcc(011) phase with increasing Fe layer thickness. The phase change is accompanied by changes in the magnetic properties.

This change in Fe thin film phase was also found by Heinz *et al.* [75]. They have investigated the crystallography of ultrathin Fe, Ni and Co films grown epitaxially on Cu for various film thicknesses using quantitative low-energy electron diffraction (LEED). For thicknesses of Fe up to 4 monolayers, the film has an fcc structure on average. This is consistent with the ferromagnetism in the film. For thicker films (5-10 monolayers) an isotropic fcc structure is formed. The subsurface region becomes non-magnetic or antiferromagnetic. At higher thicknesses a transition to bcc-iron occurs. It was found that both structural and magnetic properties of Fe/Cu(111) depend considerably on the details of the film growth.

Co, however, has the freedom to stack either in an fcc sequence or in its native hcp sequence. It turned out that the growth of Co on Cu(111) depends sensitively on whether or not the cobalt is capped by copper layer. For the first 2 monolayers of cobalt, the Co film largely copies the fcc stacking of the Cu substrate. Above this thickness, the Co is increasingly dominated by hcp stacking. Around and above 5 monolayers of Co, the hcp structure dominates. But if the Co layer is capped by a Cu layer (as in Cu/Co/Cu sandwiches or Co/Cu MLs), the Co domains show fcc stacking. The Co/Cu(111) MLs with Co layers stacked in an fcc sequence exhibit strong magnetic anisotropy with oscillatory magnetic coupling across the Cu layers and an associated GMR ([75] and references therein).

The magnetic anisotropy and the orbital magnetic moment of Fe, Ni and Co thin films were also calculated theoretically [76]. Fe/Ni MLs were also investigated using XRR and magnetization measurements [77] and using magnetic force microscopy [78].

DC magnetron-sputtered $Ni_{81}Fe_{19}$/Cu MLs were found to have high field sensitivity and thermally stable GMR properties [79]. These properties are very promising

for magnetic head application. XRD and transmission electron microscopy (TEM) were used to characterize the structure of these MLs. XRD was also used to study the thermal expansion behaviour of $Fe_{1-x}Ni_x$/Cu MLs in the temperature range of 10-300 K [80]. Low thermal expansion coefficient was found at the Invar composition (x=0.35), whereas larger coefficients were found for either lower or higher Ni concentrations.

Nitrogen diffusion into Ni/Fe bilayers was investigated [81]. Nitrogen was implanted into the top Ni layer. It was found that subsequently part of the N diffused into the Fe layer. Depth profiles of N in the bilayers were recorded as a function of implantation dose and temperature using nuclear reaction analysis technique. Using XRD and cross-sectional transmission electron microscopy (XTEM) techniques it was found that nitrides are formed in iron below the Ni/Fe interface in the absence of radiation damage [82].

The mixing parameters in Ni and Fe crystals covered with a thin Zr layer were determined using in situ Rutherford backscattering spectroscopy (RBS) during irradiation with ions of various masses (from N to Xe) [83]. The distribution function of mixed atoms and the mixing rate were studied as a function of ion fluence.

Finally, the effect of IBI of Cr/Fe/Ni MLs with 100 keV Xe ions was studied [84]. XRD and Mossbauer spectroscopy were used for structural characterization. It was found that both irradiation with Xe to a dose of 2×10^{16} ions/cm^2 and pulsed laser irradiation produce a complete mixing of the layers and form a disordered solid state solution. Later, Cr/Fe/Ni MLs were irradiated successively by 80 MeV Si ions and 150 and 200 MeV Ag ions [85]. Significant modifications at the interfaces took place. XRR measurements showed increased interfacial roughness after irradiation and Mossbauer measurements provided evidence of intermixing after irradiation by 200 MeV Ag ions. Heavy ion irradiated ML was compared with annealed and low-energy ion irradiated samples. Phases formed at the interfaces of iron are similar in all three cases.

Co/Cu MLs were also largely studied recently. Different sample preparation tech-

niques were used to deposit the samples, such as magnetron sputtering [86, 87, 88, 89], unbalanced magnetron sputtering with and without an applied d.c. substrate bias [90], electrodeposition [91, 92, 93, 94, 95], pulsed laser deposition [96] and molecular beam epitaxy [97, 98].

The effect of annealing on the magnetism and magnetic structure of Co/Cu MLs was studied (see for example [86, 87, 88]). The magnetization and MR ratio of these MLs were investigated [95, 92]. It was found that the GMR of Co/Cu MLs depends on the volume fraction of ferromagnetic regions [40, 86, 87]. The value of the GMR was found to be altered irreversibly when an applied magnetic field is increased to the saturation and back to zero at room temperature [99].

The effect of hydrogen implantation on the structural, magnetic and electrical properties of Co/Cu MLs was investigated [100]. A particularly attractive combination of high sensitivity and low hysteresis was obtained at the second AF peak by alternating very thin Co layers $\approx$3Å with 15Å thick Cu layers [101]. Theoretical calculations of the conductivity and GMR in Co/Cu MLs were also given [102].

In particular, we are more interested in studies concerning the structure of Co/Cu MLs and its effect on the magnetic properties. Several methods were used to investigate the structure, such as in situ helium atom scattering to measure the interlayer spacing during growth [103], field-ion microscopy and three-dimensional atom-probe analysis [104], transmission electron microscopy (TEM) and energy dispersive x-ray spectroscopy [96], x-ray absorption spectroscopy [105], polarization-dependent x-ray absorption fine structure (XAFS) [106], in situ scanning tunneling microscopy [107], XRR and high-angle x-ray diffraction [89] and specular and diffuse x-ray diffraction [97, 98, 108, 109].

As previously observed [75], Co has the freedom to stack either in an fcc or an hcp sequence. It was found to stack in an fcc sequence with hcp parts in it in the MLs prepared by pulsed laser deposition [96], whereas the hcp structure was observed in magnetron sputtered MLs [89] together with a mixed amorphous CoCu layer at the interface due to the diffusion between Co and Cu. This might be the cause of the

relatively small MR value found for these MLs while electrodeposited Co/Cu MLs on indium-tin oxide glass substrate exhibit a large MR ratio [95]. The growth mode of Co on Cu was found to be quite different from that of Cu on Co [107]. The Co tends to nucleate in small islands (<50Å) [107, 105, 75].

The interfaces in a set of Co/Cu MLs were studied by low-angle anomalous x-ray diffraction [109]. The MLs were deposited by magnetron sputtering on oxidized Si substrate. The Co/Cu thickness ratio was equal to unity and the total sample thickness was around 700Å. An accurate and unambiguous determination of the mesoscopic structure of these MLs has been achieved using XRR measurements and diffuse scattering scans. By fitting both specular and off-specular scans, a unique set of fit parameters was obtained. The thickness, rms roughness of each layer together with the horizontal and vertical correlation lengths and the Hurst parameter of the surface were obtained.

The main objective of the present thesis is to investigate the effect of IBI on the structure of Co/Cu and Ni/Fe bilayers. These combinations of materials were chosen because of interesting GMR or magnetotransport properties [28, 40, 41]. Furthermore, as previously mentioned, we choose to limit ourselves to the study of bilayers in order to reduce the number of fit parameters, hence simplify the interpretation and obtain a more detailed analysis of the interface structure. The detailed change in the roughness structure of the interfaces in Ni/Fe bilayers as a result of IBI to various ion doses will be determined using x-ray specular and off-specular scans. High-angle XRD scans will also be performed in order to determine the crystallographic structure of the bilayers. Our results will be compared to TEM and XTEM images obtained for some of the bilayers at different ion doses. Single layers of Ni, Fe, Co and Cu will also be studied in order to determine the effect of irradiation on their bulk electron densities.

The structure of the thesis will be as follows. Chapter 2 includes the theoretical calculations of the x-ray reflectivity. We also present the different methods used to calculate the x-ray diffuse scattering cross-section and explain briefly the ion-solid interaction mechanism.

Chapter 3 presents the experimental techniques used to prepare, irradiate and measure our samples. It also includes a description of the different types of interfaces and the simulation method used in order to calculate the reflectivity from these interfaces. Examples of a typical reflectivity curve and a diffuse scan curve are also included.

Chapter 4 presents the results of a survey performed on the single layers and the bilayers. The fits to the reflectivity data from these samples are shown together with the parameters obtained and the electron density profiles calculated from the fit parameters.

A more detailed study of the Fe/Ni bilayers is presented in chapter 5. Other x-ray scattering techniques are also used to characterize these bilayers, namely, x-ray diffuse scattering and high-angle x-ray diffraction. Some TEM and XTEM images are also presented for comparison with the x-ray results. Finally, a conclusion is given in chapter 6.

2

THEORETICAL BACKGROUND

As mentioned in the introduction, we will irradiate bilayers of Ni/Fe and Co/Cu by 1 MeV Si^+ ions and characterize their structure at each stage of irradiation using x-ray reflectivity (XRR) and x-ray diffuse scattering (XDS) measurements. In order to extract information about the structure, we will model our samples and calculate the theoretical XRR and XDS intensity for these models. The theoretical calculations will then be fit to the experimental data using least-squares fitting program.

Several methods have been developed for the calculation of XRR and XDS intensities. In this chapter we will briefly introduce these theories, which gives a lengthy set of equations that can be skipped rather quickly to the method which we use to calculate the reflectivity in sec. 2.1.3 and the diffuse scattering intensity calculations in sec. 2.2.2.

We assume that the structure of our interfaces obeys the scaling hypothesis, and hence the interfaces are treated as self-affine surfaces. The height-height correlation function used in our calculations is also introduced.

Finally, we present a summary of the different models treating the ion beam effects, namely, the ballistic model and the thermodynamic model.

2.1 X-ray specular scattering

X-ray scattering measurements consist of monitoring the intensity of a reflected x-ray beam from a sample surface relative to the intensity of the incident beam as a function of the wave vector transfer, $\mathbf{q}$, defined as $\mathbf{q} = \mathbf{k_2} - \mathbf{k_1}$, where $\mathbf{k_1}$ and $\mathbf{k_2}$ are the incident and reflected wave vectors, respectively. The direction of $\mathbf{q}$ with respect

to the sample surface determines the direction in which the structure is probed [110].

In conventional optics, the incidence and reflection angles (γ_i and γ_o) are defined as the angles which the direction of the incident or the reflected wave vector, respectively, makes with the normal to the surface. In x-ray scattering formalism, however, the incident and reflected angles (θ_i and θ_o) are defined between the beam direction and the surface of the material, i.e., $\theta_i = \pi/2 - \gamma_i$ and $\theta_o = \pi/2 - \gamma_o$.

For specular reflectivity, the angles θ_i and θ_o are equal, so that **q** is oriented normal to the sample surface and is given by the relation $q=4\pi \sin\theta/\lambda$ (where $\theta = \theta_i = \theta_o$ and λ is the wavelength of the incident x-ray radiation). In the region of small **q**, large length scales are probed, hence the material can be considered homogeneous and atomic structure may be ignored. Reflectivity can be treated either in an optical formalism using Fresnel's law and considering the material as continuous media with dielectric boundaries or in the diffraction formalism considering the material as a collection of scatterers.

2.1.1 *X-ray reflection from ideal interfaces*

Consider first the reflection of x-rays from a perfectly smooth interface separating two homogeneous media having refractive indices n_1 and n_2. Let θ_i denote the angle of incidence in medium 1 and θ_t the angle of refraction (or transmission) in medium 2, both measured between the direction of the beam and the plane of the interface. Snell's law states that:

$$\frac{cos\ \theta_i}{cos\ \theta_t} = \frac{n_2}{n_1}. \tag{2.1}$$

If the second medium is optically more dense ($n_2 > n_1$), the refracted angle is real for all incident angles. If, however, $n_2 < n_1$, θ_t will only be real for values of θ_i satisfying the condition $cos\ \theta_i \leq n_2/n_1$. The angle θ_c is called the critical angle and is given by:

$$cos\ \theta_c = \frac{n_2}{n_1}. \qquad n_2 < n_1. \tag{2.2}$$

For values of $\theta_i \leq \theta_c$, total external reflection of the incident wave in medium 1 occurs.

By applying boundary conditions to the electric and magnetic fields at the interface, the following Fresnel equations for the reflection and transmission coefficients are obtained:

$$r_s = \frac{n_1 sin\theta_i - n_2 sin\theta_t}{n_1 sin\theta_i + n_2 sin\theta_t}, \tag{2.3}$$

$$t_s = \frac{2n_1 sin\theta_i}{n_1 sin\theta_i + n_2 sin\theta_t}, \tag{2.4}$$

$$r_p = \frac{n_2 sin\theta_i - n_1 sin\theta_t}{n_2 sin\theta_i + n_1 sin\theta_t}, \tag{2.5}$$

$$t_p = \frac{2n_1 sin\theta_i}{n_2 sin\theta_i + n_1 sin\theta_t}, \tag{2.6}$$

where s and p denote the two different polarization components [111].

The refractive index of materials in the x-ray wavelength range is given by:

$$n = 1 - r_e \frac{\lambda^2 N_o}{2\pi} F, \tag{2.7}$$

where $r_e = e^2/mc^2$ is the classical electron radius, λ is the x-ray wavelength, N_o is the number density of atoms and F is the structure factor given by:

$$F = f_o + (\Delta f') + i(\Delta f''). \tag{2.8}$$

where f_o=Z is the atomic scattering factor at zero-momentum transfer and $\Delta f'$ and $\Delta f''$ are the real and imaginary parts of the dispersion corrections to f_o, respectively, and are tabulated for most materials as a function of x-ray wavelength [112]. Using equation 2.8, the refractive index could be written as:

$$n = 1 - \delta - i\beta, \tag{2.9}$$

where δ and β are given by:

$$\delta = r_e \frac{\lambda^2 N_o}{2\pi} (f_o + \Delta f'), \tag{2.10}$$

$$\beta = r_e \frac{\lambda^2 N_o}{2\pi} (\Delta f''). \tag{2.11}$$

β is also related to the linear absorption coefficient of the material, μ, by the relation:

$$\beta = \frac{\lambda}{4\pi} \mu. \tag{2.12}$$

From equation 2.9 we can see that n<1 for x-rays, therefore total external reflection will take place whenever x-rays are incident from vacuum (or air) onto the surface of a material with an angle $\theta_i < \theta_c$. Since θ_c is small, by expanding the cosine function in equation 2.2 to second order in θ we obtain the relation:

$$\theta_c = (2\delta)^{1/2}. \tag{2.13}$$

Typical values of θ_c are in the range of 0.1° to 0.6° for most materials and depend on the electron density. For small values of θ_i, the Fresnel reflectivity is shown in figure 2.1 as a function of wave vector transfer, q, and is given approximately by the relation:

$$R_f \approx \left(\frac{\theta_c}{2\theta_i}\right)^4 \approx \left(\frac{q_c}{2q}\right)^4. \tag{2.14}$$

i.e. the reflectivity falls very fast with increasing θ or the scattering wave vector q.

2.1.2 X-ray reflection from a stratified medium

A stratified medium is a medium whose properties are constant throughout each plane perpendicular to a fixed direction, e.g. a multilayer consisting of a succession of thin plane parallel films.

Consider a plane, time-harmonic electromagnetic wave propagating through a stratified medium. Taking the plane of incidence to be the yz-plane, and z the direction of stratification, by solving Maxwell's equations for a TE wave we obtain [111]:

$$E_x(z) = U(z)e^{i(k_o\alpha y-\omega t)}, \tag{2.15}$$

$$H_y(z) = V(z)e^{i(k_o\alpha y-\omega t)}, \tag{2.16}$$

where $k_o = 2\pi/\lambda$ is the magnitude of the wave vector of the incident radiation, $\alpha = ncos\theta$ where n is the refractive index of the medium and θ is the angle between the incident wave vector and the surface of the film. It turns out that the x and y components of the electric (or magnetic) vectors in the plane z=0 are related to the corresponding components in an arbitrary plane z=constant through a 2×2 matrix,

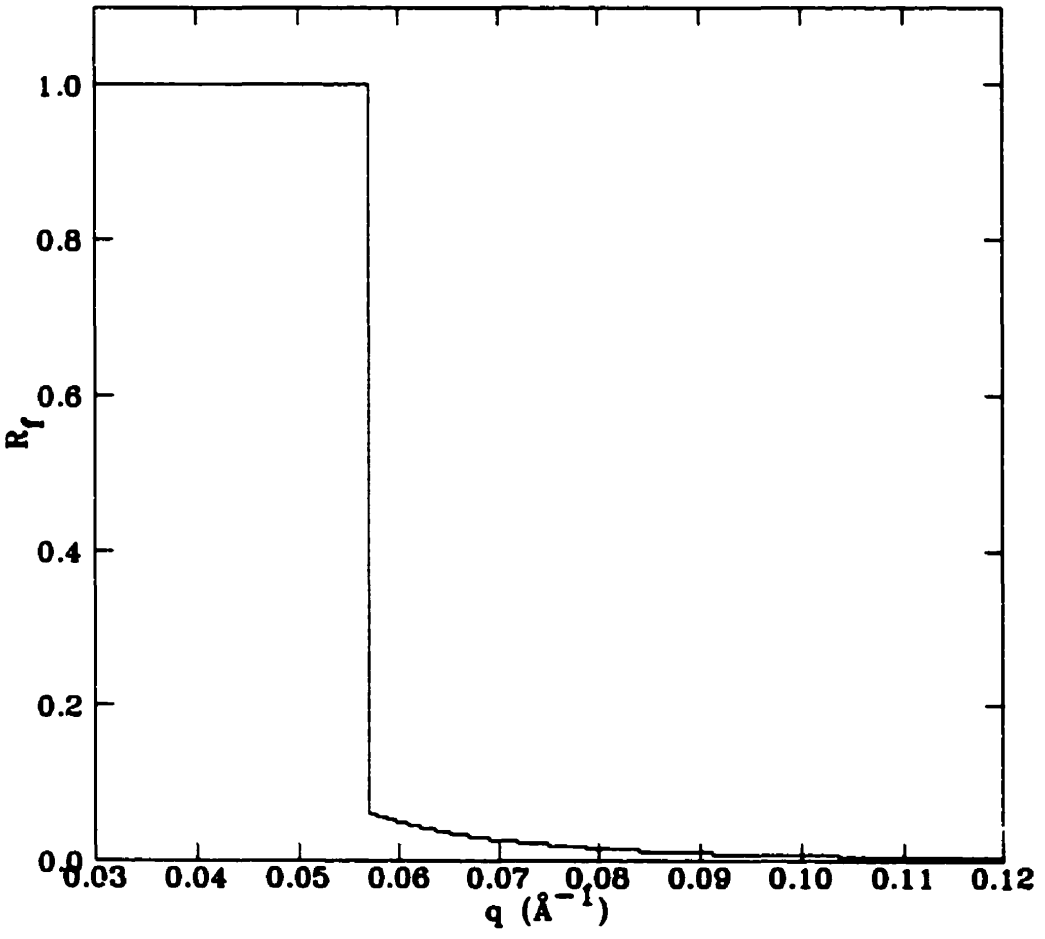

Figure 2.1: Fresnel reflectivity falls very fast with increasing wave vector transfer q, as given by equation 2.14.

M, called the characteristic matrix of the medium.

$$\begin{pmatrix} U_o \\ V_o \end{pmatrix} = M \begin{pmatrix} U(z) \\ V(z) \end{pmatrix}. \tag{2.17}$$

For a homogeneous dielectric film, the characteristic matrix M is given by [111]:

$$M(z) = \begin{pmatrix} cos(k_o n z sin\theta) & -\frac{i}{p} sin(k_o n z sin\theta) \\ -ipsin(k_o n z sin\theta) & cos(k_o n z sin\theta) \end{pmatrix}. \tag{2.18}$$

where $p = nsin\theta$. For a stratified medium consisting of a pile of thin homogeneous films extending from $0 \leq z \leq z_1$, $z_1 \leq z \leq z_2$, ..., $z_{N-1} \leq z \leq z_N$ with characteristic matrices M_1, M_2, ..., M_N, the characteristic matrix of the whole structure, M, is given by the product of the matrices of the individual layers:

$$M(z_N) = M_1(z_1)M_2(z_2 - z_1)...M_N(z_N - z_{N-1}). \tag{2.19}$$

The reflection and transmission coefficients are given by:

$$r = \frac{(m_{11} + m_{12}p_l)p_1 - (m_{21} + m_{22}p_l)}{(m_{11} + m_{12}p_l)p_1 + (m_{21} + m_{22}p_l)}. \tag{2.20}$$

$$t = \frac{2p_1}{(m_{11} + m_{12}p_l)p_1 + (m_{21} + m_{22}p_l)}. \tag{2.21}$$

where m_{ij} are the elements of the characteristic matrix of the medium, p_1 and p_l are the p parameter for the first and last layers, respectively. The reflectivity and transmissivity are then given by:

$$R = |r|^2. \tag{2.22}$$

$$T = \frac{p_l}{p_1} |t|^2. \tag{2.23}$$

Another approach to solve the problem of x-ray reflection from a stratified medium consists in decomposing the field into two plane waves that must satisfy Snell-Descartes law [113] given by:

$$q_{\parallel}^2 + q_{\perp}^2 = n^2 k_o^2. \tag{2.24}$$

where $q_{\|}$ and $q_{\perp}$ are the tangential and perpendicular components of the wave vector $\mathbf{q}$, respectively. One of the plane waves, T, propagates in the transmission direction while the other, R, propagates in the reflection direction:

$$T = A^{+} e^{iq_{\perp}z}. \tag{2.25}$$

$$R = A^{-} e^{-iq_{\perp}z}. \tag{2.26}$$

This method leads to the Fresnel matrix, F, which gives the transformation of the (T, R) fields at the crossing between two media, instead of the (U, V) representation:

$$\begin{pmatrix} T \\ R \end{pmatrix}_2 = F \begin{pmatrix} T \\ R \end{pmatrix}_1. \tag{2.27}$$

where F is given by:

$$F = \frac{1}{2} \begin{pmatrix} 1 + \frac{\xi_1}{\xi_2} & 1 - \frac{\xi_1}{\xi_2} \\ 1 - \frac{\xi_1}{\xi_2} & 1 + \frac{\xi_1}{\xi_2} \end{pmatrix}, \tag{2.28}$$

where:

$$\xi^2 = n^2 - cos^2\theta, \qquad for\ TE\ waves. \tag{2.29}$$

$$\xi^2 = \frac{n^2 - cos^2\theta}{n^4}. \qquad for\ TM\ waves. \tag{2.30}$$

This leads to the following expressions for the reflection and transmission coefficients:

$$r = \frac{\xi_2 - \xi_1}{\xi_2 + \xi_1}. \tag{2.31}$$

$$t = \frac{2\xi_2}{\xi_1 + \xi_2}. \tag{2.32}$$

2.1.3 X-ray reflection from rough surfaces

Vidal & Vincent [114] have included the effect of surface and interface roughness on the matrix coefficients and in the calculation of the reflection and transmission coefficients. The matrix relating the components of the electric field below and above an interface separating media 1 and 2 is given by:

$$P = \begin{pmatrix} p_{11} exp[-(\beta_1 - \beta_2)^2 \frac{\sigma^2}{2}] & p_{12} exp[-(\beta_1 + \beta_2)^2 \frac{\sigma^2}{2}] \\ p_{21} exp[-(\beta_1 + \beta_2)^2 \frac{\sigma^2}{2}] & p_{22} exp[-(\beta_1 - \beta_2)^2 \frac{\sigma^2}{2}] \end{pmatrix}, \tag{2.33}$$

where,

$$p_{11} = (1 + \frac{\beta_1}{\beta_2})exp[-i(\beta_1 - \beta_2)y], \quad (2.34)$$

$$p_{12} = (1 - \frac{\beta_1}{\beta_2})exp[+i(\beta_1 + \beta_2)y], \quad (2.35)$$

$$p_{21} = (1 - \frac{\beta_1}{\beta_2})exp[-i(\beta_1 + \beta_2)y], \quad (2.36)$$

$$p_{22} = (1 + \frac{\beta_1}{\beta_2})exp[+i(\beta_1 - \beta_2)y], \quad (2.37)$$

and,

$$\beta_i = k_o\sqrt{n_i^2 - cos^2\theta}. \quad (2.38)$$

y is the direction normal to the interface and σ is the rms roughness of the interface. The reflectivity and transmissivity will then be given in terms of the elements P_{ij} of matrix P by the relations:

$$R = |\frac{P_{21}}{P_{11}}|^2. \quad (2.39)$$

$$T = \frac{\beta_1}{\beta_2}|\frac{2}{P_{11}}|^2. \quad (2.40)$$

We follow this method of calculation in our program in order to calculate the reflectivity of our samples and fit its value to the experimental data.

2.2 X-ray diffuse scattering

In specular scattering, the wave vector **q** has no component parallel to the surface and hence no information is obtained about the in-plane structure of interfaces. Only information about the variation in the electron density perpendicular to the interfaces is obtained. In order to obtain lateral information about the roughness structure at interfaces, off-specular or diffuse x-ray scattering, in which $\theta_i \neq \theta_o$, has to be measured and the appropriate parameters should be obtained by fitting the experimental data to the theoretical calculations.

In this section we will briefly present the results of several methods which have been used to derive the x-ray diffuse scattering cross section from rough interfaces.

2.2.1 Diffuse scattering from a single rough surface

a) Using the Born approximation

Sinha *et al.* [51] have calculated the specular and diffuse x-ray scattering cross sections from rough surfaces using the Born approximation (BA). They obtained the following results:

$$S_{spec}(\mathbf{q}) = \frac{4\pi^2}{q_z^2} e^{-q_z^2\sigma^2} \delta(q_x)\delta(q_y), \tag{2.41}$$

where the delta functions represent the condition for specular reflection and.

$$S_{diff}(\mathbf{q}) = \frac{1}{q_z^2} e^{-q_z^2\sigma^2} \int\int_{S_o} dXdY[e^{q_z^2 C(X,Y)} - 1]e^{-i(q_x X + q_y Y)}, \tag{2.42}$$

where $C(X,Y)$ is the height-height correlation function of the interface, which will be further discussed in sec. 2.3. $S(\mathbf{q})$ is defined as the cross section per unit area surface/$(N^2 r_e^2)$. N is the number density of the scattering particles and $r_e = e^2/mc^2$ for x-ray scattering.

The specular part is equal to the scattering cross section from a smooth surface multiplied by a pseudo-Debye-Waller factor, $exp(-q_z^2\sigma^2)$, to account for the effect of roughness. The diffuse component depends on the in-plane roughness structure through the height-height correlation function.

The Born approximation uses the kinematical approach where the x-ray reflection is described by scattering processes from separate electrons and the multiple scattering is neglected. It is therefore a valid approximation at incident and reflected angles larger than the critical angle of total external reflection, θ_c. Near θ_c, dynamical methods have to be used in order to account for multiple x-ray scattering and to include the effect of total external reflection. This can be done by using the distorted-wave Born approximation (DWBA).

b) Using the distorted-wave Born approximation

In the DWBA, the roughness is considered as a perturbation on the exact solution of the wave equation for an ideal smooth interface. The specular scattering cross

section is given by [51]:

$$\left[\frac{d\sigma}{d\Omega}(k_1,k_2)\right]_{spec} = L_xL_y\delta(q_x)\delta(q_y)k_o^2 sin^2\theta_i|\tilde{R}(\mathbf{k_1})|^2, \quad (2.43)$$

where $\mathbf{k_1}$ and $-\mathbf{k_2}$ are the normal and time-reversed incident wave vectors, respectively. L_xL_y is the area of the surface and $|\tilde{R}(\mathbf{k_1})|$ is given by:

$$|\tilde{R}(\mathbf{k_1})|^2 = |R(\mathbf{k_1})|^2 e^{-q_z q_z^t \sigma^2}, \qquad q_z \geq q_c, \quad (2.44)$$

where q_z and q_z^t are the z-components of the wave vector transfer in vacuum and in the medium, respectively, and $R(\mathbf{k_1})$ is the reflectivity from a smooth surface. Therefore, the effect of roughness is again to multiply the reflectivity by a Debye-Waller-type factor. The diffuse scattering cross section is given by:

$$\left[\frac{d\sigma}{d\Omega}\right]_{diff} = L_xL_y\frac{|k_o^2(1-n^2)|^2}{16\pi^2}|T(\mathbf{k_1})|^2|T(\mathbf{k_2})|^2 S(\mathbf{q_t}), \quad (2.45)$$

where:

$$S(\mathbf{q_t}) = \frac{exp\{-[(q_z^t)^2+(q_z^{t*})^2]\sigma^2/2\}}{|q_z^t|^2}\int\int_{S_o} dXdY(e^{|q_z^t|^2C(X,Y)}-1)e^{-i(q_xX+q_yY)}, \quad (2.46)$$

where $T(\mathbf{k_1})$ and $T(\mathbf{k_2})$ are the transmission coefficients calculated for the incident and exit angles, respectively.

The factor $|T(\mathbf{k_1})|^2|T(\mathbf{k_2})|^2$ in equation 2.45 is not obtained using the Born approximation. For large q_z, $|T|^2 \simeq 1$ and $q_z^t \simeq q_z$ and eq. 2.45 reduces to the BA. The diffuse scattering cross section for a 10 mm-thick Pyrex glass [51] calculated using eq. 2.45 is shown in fig. 2.2. As seen from the figure, when the incident or exit angle is equal to θ_c (θ_i=0.2° or 0.8°), $|T(\mathbf{k_1})|^2$ or $|T(\mathbf{k_2})|^2$ has a maximum and peaks appear in the diffuse scattering. These maxima are called Yoneda wings or anomalous reflections and their origin lies in the fact that the electric field at the surface reaches a maximum of twice the incident field resulting in greater diffuse scattering. The central peak appears because the surface is very jagged, as explained in sec. 2.3.

2.2.2 *Diffuse scattering from rough multilayers*

a) Using the distorted-wave Born approximation

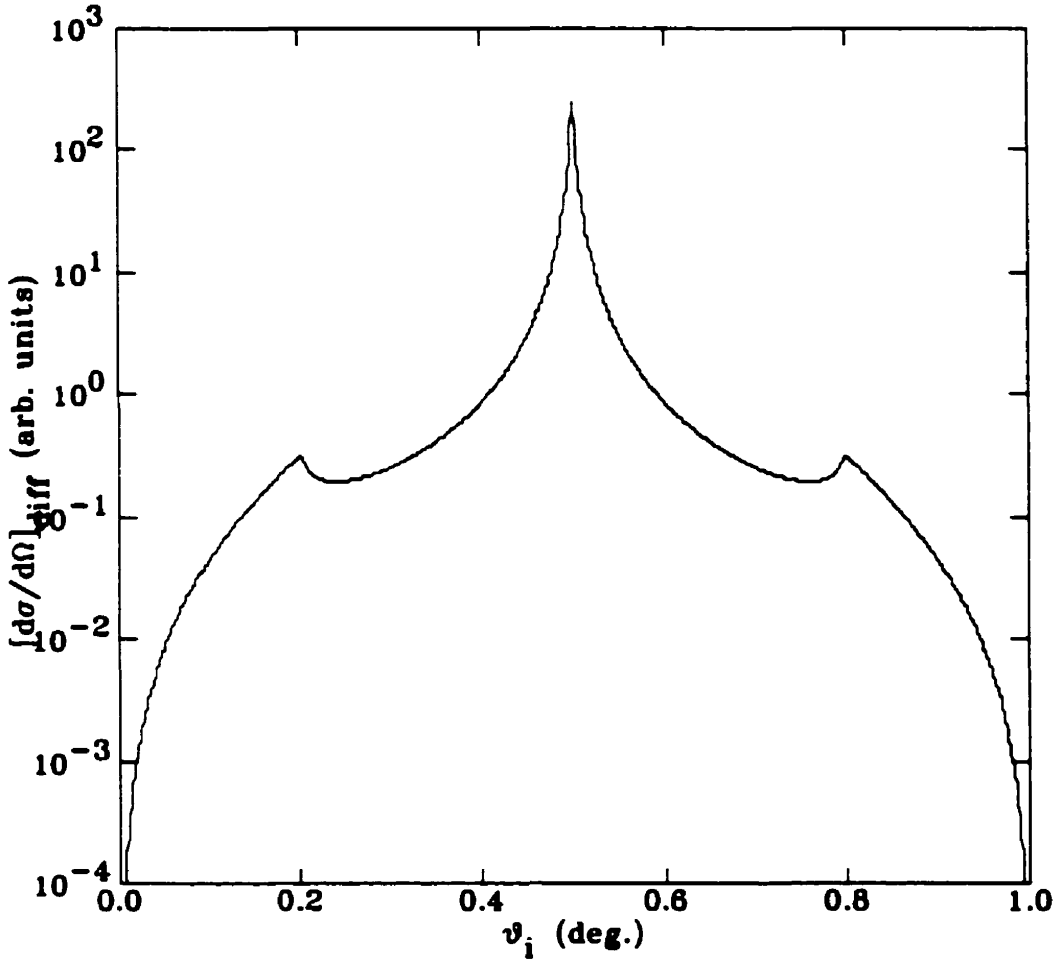

Figure 2.2: Calculation of diffuse scattering cross section in the distorted-wave Born approximation using eq. 2.45 for a 10 mm-thick Pyrex glass at constant $2\theta = 1.0°$ [51]. The central peak appears because the surface is very jagged, as explained in sec. 2.3. The Yoneda wings are clearly visible at θ_i=0.2° and 0.8°, respectively.

The work of Holý *et al.* [53] in the area of x-ray diffuse scattering should be mentioned. They have extended the derivation of Sinha *et al.* using the DWBA to the case of diffuse scattering from rough multilayers. The following expression was obtained for the diffuse scattering cross section:

$$\begin{aligned}\left[\frac{d\sigma}{d\Omega}\right]_{diff} = \frac{k_o^4}{16\pi^2}\sum_{j=1}^{N} & |n_j^2 - n_{j-1}^2|^2 \left[S_{00}^j(|T_1^{j+1}T_2^{j+1}|^2 + |R_1^{j+1}R_2^{j+1}|^2)\right. \\ & + S_{11}^j(|T_2^{j+1}R_1^{j+1}|^2 + |T_1^{j+1}R_2^{j+1}|^2) \\ & + 2Re[S_{02}^j T_1^{j+1}T_2^{j+1}(R_1^{j+1}T_2^{j+1})^* + (S_{02}^j R_1^{j+1}R_2^{j+1})^* T_1^{j+1}R_2^{j+1} \\ & + S_{01}^j T_1^{j+1}T_2^{j-1}(T_1^{j-1}R_2^{j+1})^* + (S_{01}^j R_1^{j+1}R_2^{j+1})^* R_1^{j+1}T_2^{j+1} \\ & \left. + S_{03}^j T_1^{j+1}T_2^{j-1}(R_1^{j+1}R_2^{j-1})^* + S_{21}^j T_2^{j+1}R_1^{j+1}(T_1^{j+1}R_2^{j-1})^*\right]. \end{aligned} \tag{2.47}$$

where j denotes the layer number with $j = 1$ being the vacuum and $j = N + 1$ is the substrate. n_j is the refractive index of the j^{th} layer. $R_{1,2}$ and $T_{1,2}$ are the complex amplitudes of the reflected and transmitted beams, respectively, for the state 1 and the time-inverted state 2, and S_{mn}^j is the structure factor defined by:

$$\begin{aligned} S_{mn}^j = & \frac{1}{q_{mz}^{j-1}(q_{nz}^{j-1})^*} exp\left[-\sigma_j^2((q_{mz}^{j-1})^2 + (q_{nz}^{j-1})^{*2})/2\right] \\ & \times exp\left[-i(q_{mz}^{j-1} - q_{nz}^{j-1^*})z_j\right] \int\int_S dXdY exp\left[-i(q_x X + q_y Y)\right] \\ & \times \left\{exp\left[q_{mz}^{j-1}(q_{nz}^{j-1})^* C_j(X,Y)\right] - 1\right\}. \end{aligned} \tag{2.48}$$

where $m, n = 0, \ldots, 3$. σ_j is the rms roughness of the j^{th} layer. $C(X,Y)$ is the height-height correlation function and $\mathbf{q_m^{j-1}}$ are the momentum transfer in layer $j+1$ defined as:

$$\mathbf{q_0^{j-1}} = \mathbf{k_2^{j+1}} - \mathbf{k_1^{j-1}}, \mathbf{q_1^{j-1}} = \mathbf{k'^{j+1}_2} - \mathbf{k_1^{j+1}}, \mathbf{q_2^{j-1}} = \mathbf{k_2^{j+1}} - \mathbf{k'^{j+1}_1}, \mathbf{q_3^{j+1}} = \mathbf{k'^{j-1}_2} - \mathbf{k'^{j+1}_1}, \tag{2.49}$$

where $\mathbf{k_1}$ and $\mathbf{k'_1}$ are the incident and reflected wave vectors for state 1, respectively, and $\mathbf{k_2}$ and $\mathbf{k'_2}$ are the corresponding wave vectors for the time-inverted state 2.

We can see the dependence of the diffuse scattering cross section on the different transmission coefficients and on the correlation function. Holý *et al.* have further

extended their derivation to include both horizontal and vertical correlations of roughness profiles [54].

b) Using the reciprocity theorem

In our fitting program, we follow the method of Daillant *et al.* [52] in order to calculate the x-ray diffuse scattering cross section using the reciprocity theorem. The use of the reciprocity theorem of electrodynamics [115] is analogous to the use of Green functions, but it explicitly shows the symmetry in the source and detector positions in scattering problems. It has been used to solve different problems in electric circuits [116] and its relevance to the problem of scattering by rough surfaces has been widely developed by Croce [117].

Consider a multilayer consisting of $(N-1)$ layers denoted as $1,2,.....N-1$, between the vacuum denoted as 0 and the substrate denoted as N, as shown in fig. 2.3. The expression for the diffuse scattering cross section from this multilayer is given by [52]:

$$\begin{aligned}\left[\frac{d\sigma}{d\Omega}\right]_{diff} &= \sum_{\mp}\sum_{j=1}^{N}\sum_{k=1}^{N}(n_j^2-n_{j-1}^2)(n_k^2-n_{k-1}^2)\\ &\times\Big[(u_j^{+s}u_j^{+d}u_k^{\mp s*}u_k^{\mp d*}+u_j^{-s}u_j^{-d}u_k^{\pm s*}u_k^{\pm d*})S_{\mp}(q_j,q_k,z_j,z_k)\\ &+(u_j^{+s}u_j^{+d}u_k^{\mp s*}u_k^{\pm d*}+u_j^{-s}u_j^{-d}u_k^{\pm s*}u_k^{\mp d*})S_{\mp}(q_j,q_k',z_j,z_k)\\ &+(u_j^{+s}u_j^{-d}u_k^{\mp s*}u_k^{\mp d*}+u_j^{-s}u_j^{+d}u_k^{\pm s*}u_k^{\pm d*})S_{\mp}(q_j',q_k,z_j,z_k)\\ &+(u_j^{+s}u_j^{-d}u_k^{\mp s*}u_k^{\pm d*}+u_j^{-s}u_j^{+d}u_k^{\pm s*}u_k^{\mp d*})S_{\mp}(q_j',q_k',z_j,z_k)\Big], \qquad (2.50)\end{aligned}$$

where n_j is the refractive index of layer j, $u_j^{+(s,d)}$ and $u_j^{-(s,d)}$ are the amplitudes of the electric field in layer j in the downward (+) and upward (-) directions, respectively, s denoting the incident wave (source) and d the reflected wave (detector), and $S_{\mp}(q_j,q_k,z_j,z_k)$ is the structure factor given by:

$$\begin{aligned}S_{\mp}(q_j,q_k,z_j,z_k) &= A\frac{k_o^4}{16\pi^2}\frac{exp(-\frac{1}{2}q_{jz}^2<z_j^2>-\frac{1}{2}q_{kz}^{*2}<z_k^2>)}{q_{jz}q_{kz}^*}\\ &\times\int\int dXdY(e^{\mp q_{jz}q_{kz}^*C_{jk}(X,Y)}-1)e^{i(q_x'X+q_y'Y)}, \qquad (2.51)\end{aligned}$$

where $A = L_xL_y/\sin\theta_o$ is the illuminated area, θ_o being the angle of incidence,

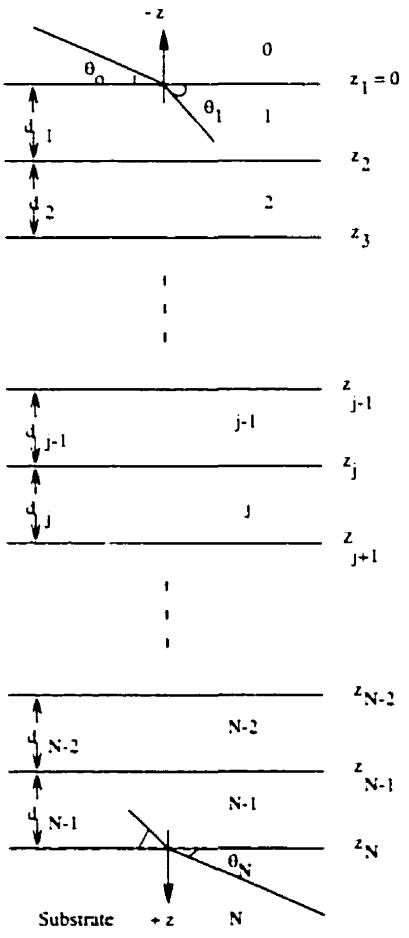

Figure 2.3: Schematic representation of a multilayer with N-1 layers denoted as 1,2.....N-1 between the vacuum, denoted as 0, and the substrate, denoted as N. The angle of incidence on the multilayer surface is θ_o and the angle of refraction in layer j is denoted by θ_j. d_j is the thickness of layer j and z_j is the height of the interface between layers $j-1$ and j.

$<z_j^2> = \sigma_j^2$ is the mean-square roughness of layer j, $C_{jk}(X,Y) = <z_j(X,Y)z_k(0,0)>$ is the height-height correlation function, $\mathbf{q_j} = \mathbf{k_j^s} + \mathbf{k_j^d}$ and $\mathbf{q'_j} = \mathbf{k_j^s} - \mathbf{k_j^d}$.

The expression given by eq. 2.50 for the x-rays diffuse scattering cross section from rough multilayers obtained using the reciprocity theorem proved to be equivalent to the results obtained using the DWBA. We can see the symmetry in the source and detector positions in eq. 2.50. In order to evaluate this differential cross section we need to calculate the electric field in each layer and to evaluate the structure factor.

In our program, the electric field within each layer is calculated recursively using the matrix method explained in section 2.1.2 [111]. The electric and magnetic fields

within the j^{th} layer (in the s polarization, but the polarization doesn't matter for x-rays at grazing incidence) may be written as:

$$E_{jx}(z) = U_j(z)e^{i(k_o n_j cos\theta_y - \omega t)}. \quad (2.52)$$

$$H_{jy}(z) = V_j(z)e^{i(k_o cos\theta_y - \omega t)}. \quad (2.53)$$

The amplitudes of the electric and magnetic fields are decomposed into a downward and an upward propagating plane waves, i.e.:

$$U_j(z) = u_j^+ e^{ik_{jz}z} + u_j^- e^{-ik_{jz}z}, \quad (2.54)$$

$$V_j(z) = p_j u_j^+ e^{ik_{jz}z} - p_j u_j^- e^{-ik_{jz}z}. \quad (2.55)$$

where $p_j = n_j sin\theta_j$ and $k_{jz} = k_o p_j$.

Then, following the procedure of Bloch *et al.* [118], by starting at the substrate and assuming that its thickness is semi-infinite such that no wave is reflected back from it, we can apply the conditions $u_N^+ = t$ and $u_N^- = 0$ where t is the transmission coefficient of the multilayer, and obtain the values of the electric field amplitude within each layer recursively.

Now we have to evaluate the structure factor $S_{\mp}(q_j, q_k, z_j, z_k)$ given by eq. 2.51 in order to calculate the differential cross section. This structure factor depends on the specific form of the height-height correlation function of the interfaces. The next section will be devoted to a discussion of self-affine surfaces and to obtain an expression for the height-height correlation function, $C_{jk}(X, Y)$.

2.3 Height-height correlation function

In order to characterize the roughness structure of interfaces, let us consider a growing surface where some roughening occurs during preparation. The rough surface can be described by a single-valued, continuous height function, $H(\mathbf{r}, t)$, above a reference surface as shown in fig. 2.4. The growth of the rough surface could be represented by several models. A widely-used model to represent the growth of a surface is the

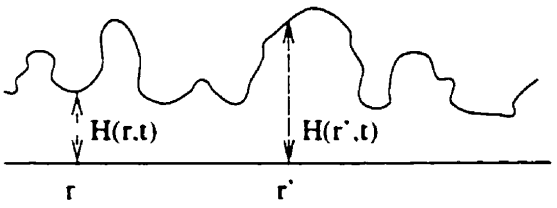

Figure 2.4: Schematic representation of a rough surface. The surface height is described by a single-valued, continuous function, $H(\mathbf{r}, t)$, above a reference surface.

Kardar, Parisi and Zhang (KPZ) model, in which the evolution of $H(\mathbf{r}, t)$ follows the following Langevin equation [119]:

$$\frac{\partial H(\mathbf{r}, t)}{\partial t} = \nu \nabla^2 H(\mathbf{r}, t) + \lambda [\nabla H(\mathbf{r}, t)]^2 + \eta, \tag{2.56}$$

where ν is an effective surface stiffness, λ is the non-linear coefficient and η is random white noise.

At time $t = 0$ the substrate is assumed to be perfectly flat then fluctuations will build up of both lateral ($\zeta_{||}(t)$) and normal ($\zeta_{\perp}(t)$) extensions during growth. The scaling hypothesis states that for lateral and normal length scales smaller than $\zeta_{||}$ and $\zeta_{\perp}$, respectively, the statistical properties of the growing surface are not expected to change after scaling the system. The lateral and normal dimensions are not equivalent and cannot be scaled by the same factor. Hence, the surface cannot be considered as self-similar, but should be treated as self-affine taking into account the difference between the parallel and normal dimensions [120].

If the lateral position vector $\mathbf{r}$ is scaled by a factor b, $H(\mathbf{r}, t)$ by b^{-h} and t by b^z then the rescaled surface $\tilde{H}(\mathbf{r}, t)$ should possess the same statistical properties as $H(\mathbf{r}, t)$, where $\tilde{H}$ is given by:

$$\tilde{H}(\mathbf{r}, t) = b^{-h} H(b\mathbf{r}, b^z t), \qquad z > 0, \ 0 < h < 1. \tag{2.57}$$

By assuming that $[H(\mathbf{r}, t) - H(\mathbf{r}', t)]$ is a Gaussian random variable whose distribution depends on the absolute difference $r = |\mathbf{r} - \mathbf{r}'|$, we may define the height difference correlation function of the interface, $g(r, t)$, by the following expression:

$$g(r, t) \equiv <[H(\mathbf{r}, t) - H(\mathbf{r}', t)]^2>, \tag{2.58}$$

where the average is taken over all pairs of points on the surface which are separated by the distance r. Using eq. 2.57 and setting $b = 1/r$, the height difference correlation function of the interface, $g(r,t)$, will be given by:

$$\begin{aligned} g(r,t) &= b^{-2h} g(br, b^z t) \\ &= r^{2h} g(t/r^z). \end{aligned} \tag{2.59}$$

The asymptotic behaviour of $g(r,t)$ is given by:

$$g(r,t) \simeq \begin{cases} (t/r^z)^{2\beta}, & t/r^z << 1, \\ const., & t/r^z >> 1, \end{cases} \tag{2.60}$$

where $\beta = h/z$. Now consider a self-affine surface, as defined by Mandelbrot [121], which has evolved in a growth process and is assumed now to be in a metastable state. The scaling hypothesis does not justify the choice of any functional form for $g(r)$ as long as it satisfies the asymptotic behaviour given by eq. 2.60. Also, in practice, there will be an upper cutoff limit for the lateral correlation length, $\zeta_{||}$ (which will be denoted simply as ζ from now on), because of the finite sample size or as a result of a macroscopic surface treatment, among many possible reasons. Therefore, a simple form for the height difference correlation function might be given by:

$$g(r) = 2\sigma^2[1 - e^{-(r/\zeta)^{2h}}], \tag{2.61}$$

which saturates at a value of $2\sigma^2$, where σ is the rms roughness of the surface. From the definition of $g(r)$ and by translational invariance we can write:

$$\begin{aligned} g(r) &= <[H(\mathbf{r}) - H(\mathbf{r}')]^2> \\ &= <H(\mathbf{r})^2> + <H(\mathbf{r}')^2> - 2<H(\mathbf{r})H(\mathbf{r}')> \\ &= 2<H(\mathbf{r})^2> - 2<H(\mathbf{r})H(\mathbf{r}')>. \end{aligned} \tag{2.62}$$

Writing $< H(\mathbf{r})^2 >= \sigma^2$ as the mean-square roughness and using equation 2.61 for $g(r)$, the height-height correlation function, $C(r)$, will be given by:

$$C(r) \equiv <H(\mathbf{r})H(\mathbf{r}')> = \sigma^2 e^{-(r/\zeta)^{2h}}, \qquad 0 < h \leq 1. \tag{2.63}$$

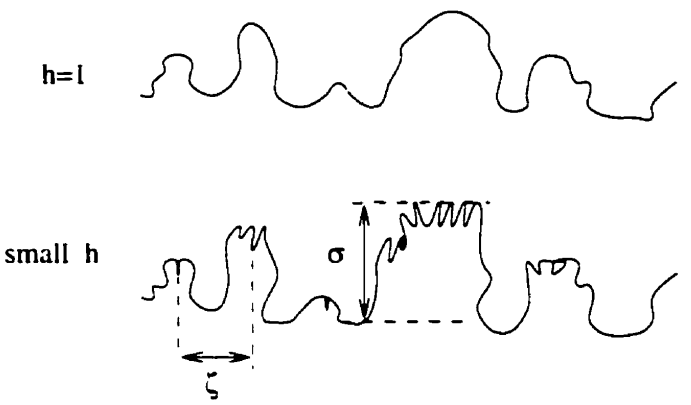

Figure 2.5: Effect of roughness exponent on the surface roughness structure for two surfaces having the same values of σ and ζ. $h = 1$ produces smooth hills and valleys whereas small values of h represent extremely jagged surfaces.

The exponent h, called the roughness exponent or the Hurst parameter, determines the smoothness of the surface and its fractal dimension. As shown in fig. 2.5, for two surfaces having the same values of σ and ζ, small values of h represent extremely jagged surfaces, whereas values of h approaching 1 produce smooth hills and valleys. The surface fractal dimension is given by $D = 3 - h$. The effect of the roughness exponent on the x-ray diffuse scattering cross section is shown in fig. 2.6. For $h = 1$ there is no maximum of the diffuse intensity near the specular peak position ($\theta_i = \frac{1}{2}(2\theta)$), whereas for values of $h < 0.5$ a broad maximum appears in that region, as also shown in fig. 2.2.

Other functions representing the height-height correlation $C(r)$ have been used to study the x-ray diffuse scattering (see for example ref. [122]), but the function defined in eq. 2.63 is the most widely used because of its simple mathematical form. Therefore we use it in our program in order to calculate the diffuse scattering cross section from rough multilayers.

The double integral in eq. 2.51 can be solved analytically for certain values of h only (h=0.5 or 1). However, in order to obtain better fits, the integral is evaluated numerically in our fitting program such that h can take up any value between 0 and 1, in spite of the fact that the numerical calculation is very time consuming.

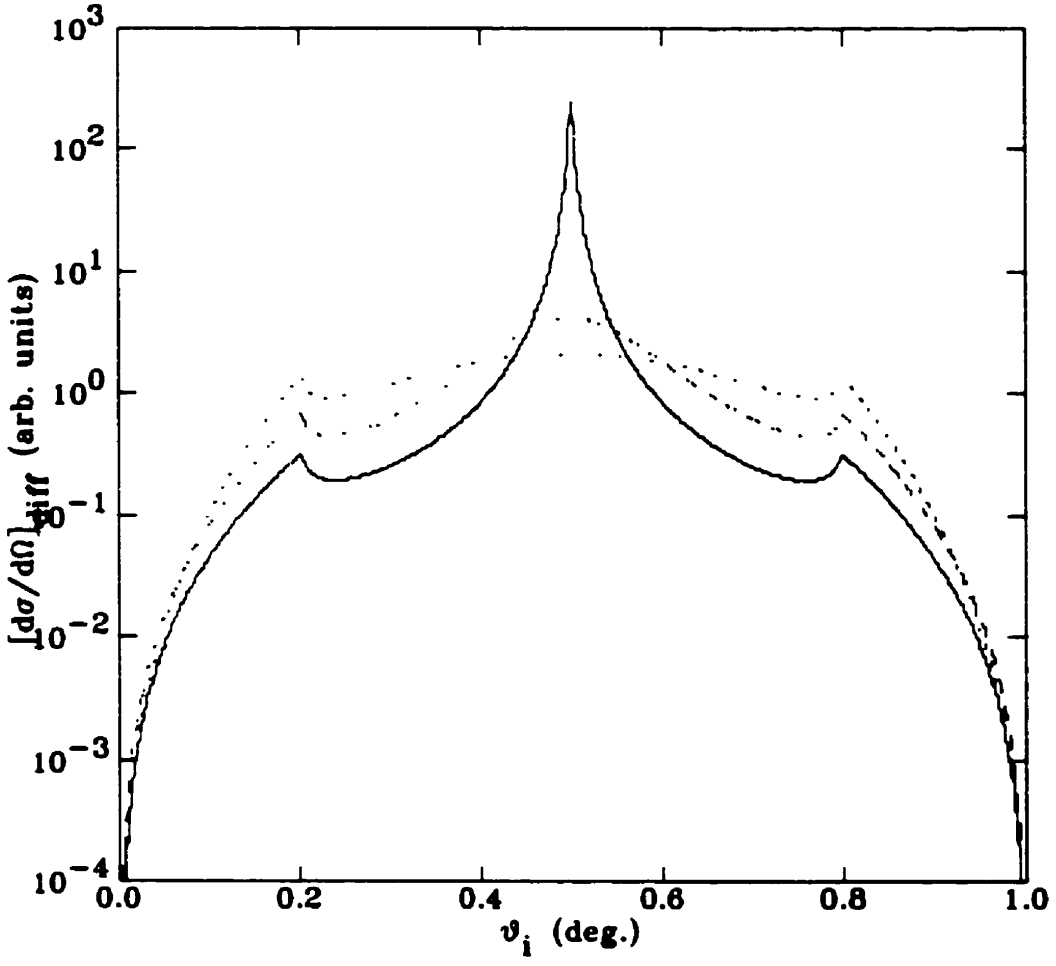

Figure 2.6: Effect of roughness exponent on the diffuse scattering cross section measured at constant $2\theta = 1.0°$: solid line: $h = 0.2$: dashed line: $h = 0.5$: dotted line: $h = 1$.

2.4 Ion beam irradiation

Since we use ion beam irradiation in order to induce intermixing in our samples, we will briefly introduce the models used to calculate the effect of ion bombardment on the amount of mixing.

Ion beam processing of materials results from the introduction of atoms into the surface layer of a solid by bombardment of the solid with ions in the eV to MeV energy range. Several types of processing have been studied, namely, ion implantation, ion beam mixing, ion-induced phase transformations and ion beam deposition.

Ion dose or fluence is defined as the number of ions per centimeter square implanted into the sample (ions/cm^2). The dose rate or flux is given in units of ions per second per centimeter square (ions$\cdot$s$^{-1}\cdot$cm^{-2}).

As an implanted ion slows down in the solid it makes many violent collisions with the lattice atoms, displacing them from their lattice sites. These displaced atoms, in turn, displace others, with the result of the production of a highly-disordered, isolated region around the path of the ion. At sufficiently high doses the individual localized disordered regions may overlap forming an amorphous or metastable crystalline layer [123]. *Ion beam mixing* is defined as the atomic intermixing and alloying which can occur at the interface between two different materials during ion irradiation.

The ion mixing effect is affected by the ballistics or kinematics of the ion-target interaction, the formation of collision cascades and the ion dose, ϕ. Both ballistic and cascade effects can be altered by changing the mass of the irradiating ion. It was found that ion mixing has similar characteristics to thermal interatomic diffusion in that both the amount of mixing at the interface and the width of thermally-diffused layer are proportional to $t^{1/2}$, where t denotes the time of mixing or diffusion.

Two types of models are used to describe the ion beam mixing processes, the ballistic models and the thermodynamic models. The ballistic models are temperature-independent and depend only on the ballistic aspects of atomic collisions, such as atomic mass and density, whereas the thermodynamic models take into account the

thermodynamic properties of solids.

2.4.1 Ballistic models of ion mixing

The ballistic model of Sigmund and Gras-Marti [124] includes two main contributions to ion mixing, namely, recoil mixing and cascade mixing.

a) Recoil mixing

Recoil mixing is the transport of atoms through repeated single collision events between the incident ions and the target atoms. For high-energy collisions, the target atoms recoil far from their initial location. The number of atoms that undergo recoil mixing varies linearly with ion dose and with the damage energy deposited per unit length, F_D, and is temperature-independent.

Theoretical calculations predict that the concentration of recoil atoms decays as an inverse power of the total relocation depth. This relation has been observed experimentally in ion mixing of bilayers ([125] and references therein).

b) Cascade mixing

Collision cascade is the multiple displacement sequence of collision events, in which an initially displaced target atom produces secondary recoil atom displacements, which in turn displace additional atoms. These displaced atoms have a much smaller kinetic energy than the incident ion energy, and after many generations of collision cascades they move in nearly random directions, which can therefore be approximately described by random walks. The sum of these atomic displacements across the interface between two materials gives rise to cascade mixing.

The random walk nature of cascade mixing yields a Gaussian spread of the impurity profile for an initially sharp distribution. The depth distribution of implanted ions is shown in fig. 2.7 for the cases in which the ion mass is less than or greater than the target mass. The standard deviation of this Gaussian distribution, Ω, is called the cascade mixing width. The following relation was derived for the cascade mixing

width of the beam [124]:

$$\Omega^2 = \frac{1}{3}\Gamma_o \frac{F_D}{N}\xi_{21}\frac{R_c^2}{E_c}\phi, \tag{2.64}$$

where $\Gamma_o = 0.608$. F_D is the energy deposited per unit length due to nuclear collisions, N is the atomic density, $\xi_{21} = [4M_1M_2/(M_1 + M_2)^2]^{1/2}$, where M_1 and M_2 are the masses of the atoms involved in the collisions, E_c is a threshold displacement energy, R_c^2 is the mean-square range associated with E_c and ϕ is the ion dose.

By using 1 MeV Si^+ ions to irradiate our samples, we are mainly in a linear mixing regime of the top few layers, as represented by the leftmost segment of the curve in fig. 2.7(a). The highest concentration of Si^+ ions in our samples occurs deep into the substrate.

From eq. 2.64 we notice that $\Omega \propto \phi^{1/2}$ which is similar to a thermal random walk where $\Omega \propto t^{1/2}$. By setting $\Omega^2 = 4D_{eff}t$, the effective diffusion coefficient is found to scale with the dose ($D_{eff} \propto \phi$) and with the damage energy ($D_{eff} \propto F_D$). As seen from eq. 2.64, the cascade mixing width and, subsequently, the effective diffusion coefficient depend only on the atomic number, mass and density, hence only on the ballistic properties of the materials involved. It is also independent of temperature, because the kinetic energy of the displaced atoms from either recoil mixing or cascade mixing is much greater than the thermal energy of lattice vibration.

2.4.2 *Thermal spikes and radiation-enhanced diffusion*

At the end of a collision cascade, which lasts approximately 10^{-13} to 10^{-11} s, thermal spikes are formed. A thermal spike is a limited volume inside a solid with the majority of atoms temporarily in motion in a state of quasi-equilibrium. A local temperature may be defined within the spike, which is estimated to be very high. At these high temperatures the materials parameters, such as the heat capacity and the thermal diffusivity, are taken from bulk liquid state values. This process lasts about 10^{-11} to 10^{-10} s.

Following the thermal-spike stage a uniform temperature throughout the solid is achieved. Thermally-activated migration of vacancy and interstitial defects generated

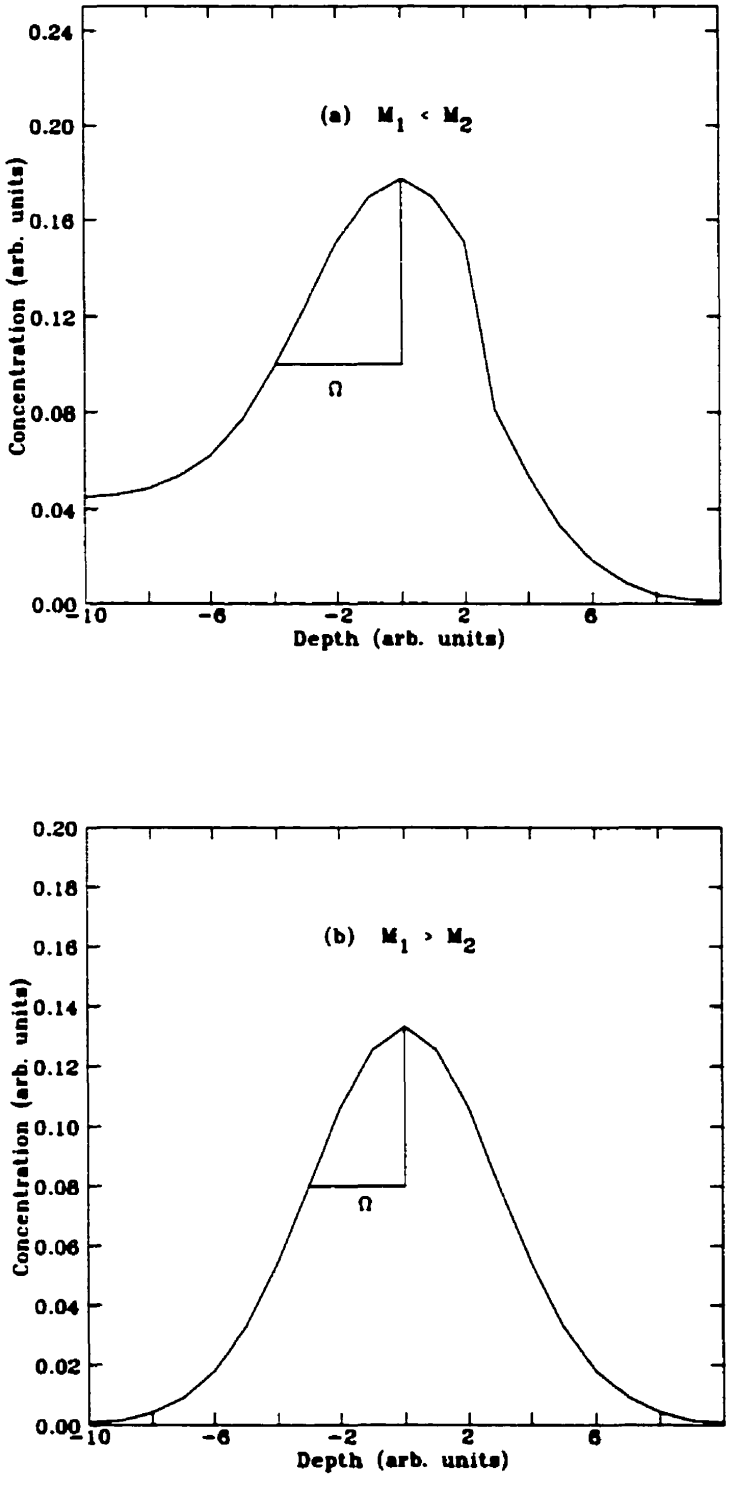

Figure 2.7: Gaussian depth distribution of implanted ions for the cases in which: a) the ion mass is less than the target mass; b) the ion mass is greater than the target mass. The standard deviation, Ω, is called the cascade mixing width.

during the collision cascade can occur at high enough temperatures and contributes to mixing during a delayed stage. This is known as *radiation-enhanced diffusion* and occurs in the relaxation stage which can last for a period exceeding 10^{-9} s.

2.4.3 Thermodynamic aspects of ion mixing

Ballistic models of ion mixing alone could not properly describe the mixing process since they do not consider the importance of the chemical driving forces which play an important role when concentrated alloys are formed. Two important contributions to the thermodynamic aspects of ion mixing come from the heat of mixing and the cohesive energy.

a) Heat of mixing effects

Two materials which are completely miscible will be well intermixed by ion irradiation in contrast to immiscible systems which can remain unchanged after irradiation. As an example let us compare the Au/Cu and the W/Cu systems. Both systems have nearly identical ballistic parameters, atomic density and atomic mass, such that their ballistic response to ion mixing should be the same. However, experimental data showed that the Au is well intermixed with the Cu while the W is relatively unchanged after irradiation. This is attributed to the miscibility differences in the two systems.

It was observed that systems having a negative heat of mixing show large mixing rates whereas systems possessing zero or positive heat of mixing undergo little or no mixing upon irradiation. The more negative the enthalpy difference between the two materials, the greater the tendency to form an alloy.

Binary systems with a sufficiently large and positive heat of mixing will have a phase separation under ion bombardment. If the sample temperature is sufficiently low, ion irradiation can cause intermixing, however, when the sample temperature is increased, the mixed layer will back-segregate into its components. This process is called demixing.

We have observed the demixing phenomenon in Co/Cu multilayers [41] as discussed in chapter 1. The heat of formation of intermetallic compound CoCu is +13 kJ/g.at [126]. Therefore, Co and Cu are immiscible and it is hard to form an intermixing region between them. By irradiating Co/Cu multilayers by Si^+ ions at liquid-nitrogen temperature (77K) a small intermixing width was established. However, annealing the samples caused a back-diffusion and the formation of sharper interfaces.

b) Cohesive energy effects

Cohesive energy is the energy that holds a material together, it is defined as the difference between the energy of the solid and the energy of the same number of free neutral atoms at infinite separation. Since the higher the cohesive energy the stronger the atoms in a solid are bonded together, we should expect more atomic displacement created in a low ΔH_{coh} solid than in a high ΔH_{coh} solid under identical ion bombardment conditions. It was found that the mixing rate is directly proportional to $(\Delta H_{coh})^2$, therefore systems with a lower cohesive energy have a higher mixing rate.

Finally, we would like to mention that Johnson *et al.* [127] have developed a phenomenological expression for the ion mixing rate which explicitly includes the heat of mixing, ΔH_{mix}, and the cohesive energy, ΔH_{coh}, effects:

$$\frac{d(4\tilde{D}t)}{d\phi} = \frac{K_1 F_D^2}{\tilde{N}^{5/3}(\Delta H_{coh})^2}\left(1 + K_2\frac{\Delta H_{mix}}{\Delta H_{coh}}\right), \tag{2.65}$$

where K_1 and K_2 are fitting parameters, F_D is the damage energy per unit length and $\tilde{N}$ is the average atomic density. It was experimentally verified that this equation provides a reasonable prediction of the ion beam mixing rate in metal/metal bilayer systems irradiated with heavy ions at low temperatures.

3

EXPERIMENTAL METHOD

In the present chapter we will explain the experimental techniques used in order to prepare our samples, irradiate them with high-energy ions and characterize their structure using different x-ray and transmission electron microscopy (TEM) techniques.

Section 3.1 deals with the choice of our samples and their preparation using rf magnetron sputtering. Next we discuss the ion beam irradiation (IBI) techniques in section 3.2.

In order to characterize the structure of our bilayers at each irradiation stage we perform x-ray reflectivity (XRR), x-ray diffuse scattering (XDS) and high-angle x-ray diffraction (XRD) measurements. One of the samples is further studied using TEM techniques.

The XRR and XDS measurements are performed using a high-resolution triple-crystal x-ray diffractometer. The diffractometer setup, alignment, filtering of the Cu K_{α_2} line and sample alignment are discussed in section 3.3.1.

Section 3.3.2 explains the process of data acquisition. We show examples of a typical XRR curve and of an ω-scan and point out their most common features. We then explain in detail how our data is processed in order to separate the diffuse-scattering component from the specularly-reflected component and to normalize our reflectivity curves.

In order to fit the XRR and XDS data a model has to be chosen for our samples, as discussed in section 3.4. Section 3.4.1 presents the different types of interfaces and explains the origin of diffuse scattering. In order to test different interface profile

functions we use a simulation method described in sec. 3.4.2. Then, the footprint correction applied at very small incident angles is explained in section 3.4.3. Section 3.4.4 presents the non-linear least-squares fitting procedure used to fit the experimental data to the theoretical calculations in order to obtain the different structural parameters.

Finally, sections 3.5 and 3.6 describe, respectively, the high-angle x-ray diffractometer and the transmission electron microscope which are used in order to further characterize the structure of our samples.

3.1 Sample preparation

As mentioned in chapter (1), Ni/Fe and Co/Cu multilayers exhibit some interesting magnetic properties which are affected by ion beam irradiation (IBI). This effect is attributed to structural changes occurring at the interfaces of these multilayers upon irradiation. The purpose of the present thesis is to investigate the effect of IBI on the structural properties of Ni/Fe and Co/Cu.

These changes are mainly occurring at the interfaces, including the change in the roughness structure of interfaces and the interdiffusion between neighbouring layers. As mentioned earlier, in order to facilitate the interpretation of XRR and XDS data we will limit ourselves to the study of single layers and bilayers of these materials.

Two groups of samples were deposited using rf magnetron sputtering onto thermally oxidized Si(100) wafers having a 3000 Å SiO_2 layer on top. First, we started with a set of bilayers of Ni/Fe and Co/Cu with different deposition sequence. These bilayers have the configuration Ni(2000Å)/Fe(100Å), Fe(2000Å)/Ni(100Å), Co(2000Å)/Cu(100Å) and Cu(2000Å)/Co(100Å) with the 100 Å layers being deposited on the surface. Three samples of each of these four configurations were deposited on a single piece of Si substrate of dimensions 20×6 mm^2 using a contact mask to create the three distinct samples as shown in fig. 3.1. The base pressure before each deposition was less than 2×10^{-7} torr. Deposition rates were 1.2 Å/s for Fe, 1.7 Å/s for Ni [28], 2 Å/s for Cu and 1 Å/s for Co [40]. These deposition rates were calibrated using a

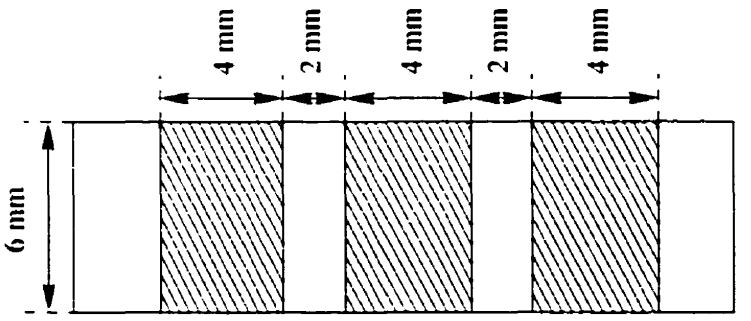

Figure 3.1: Three samples having the same configuration (shaded areas) are deposited simultaneously on the same piece of substrate (non-shaded) of dimensions 20 × 6 mm^2.

quartz-crystal monitor. The Ar(99.999%) pressure was 3 mtorr and the rf power was 200 W.

Using the same contact mask, three distinct single layers of each of the following elements: Fe, Ni, Co and Cu of a thickness of 500 Å each were also deposited on the same kind of substrate. The purpose of studying the single layers is to verify the effect of ion beam irradiation on the electron density of each single material, and hence to distinguish between the effect of irradiation on the bulk materials and on the interfaces of the bilayers.

By depositing three samples of each configuration simultaneously we wanted to obtain three identical samples, then by irradiating each of them to a different ion dose we can realize a fast survey of the effect of different ion doses on several sample configurations. However, XRR measurements of the three as-deposited samples of each configuration revealed differences in the thicknesses of the corresponding layers. This measurable thickness gradient along the sample length is caused by the slight difference in the distance between the source and the different points on the target during the sputtering process, causing different deposition rates at different points along the substrate. Moreover, the roughness of the corresponding interfaces of the different as-deposited samples were not exactly identical.

These small differences caused inconveniences when trying to compare the results after irradiation. Also the small size of these samples caused the loss of a part of

the incident beam intensity because the slit size had to be reduced, as will be further discussed in chapter 4. Therefore, for a subsequent more detailed study, the samples were deposited with a rectangular geometry of 15mm high × 4mm wide.

Since Co/Cu samples were widely covered in literature, as we have seen in chapter (1), we will focus our attention on Ni/Fe bilayers. Two sets of bilayers were prepared with the configuration Fe(500Å)/Ni(500Å) and Ni(500Å)/Fe(500Å) onto Si(100)/SiO_2 substrate wafers by rf magnetron sputtering techniques [128]. The substrate temperature was maintained at 40 ± 3°C during deposition and the same Ar pressure and power settings were maintained as for the previous samples. Layer thicknesses were computer-controlled during deposition and subsequently verified by low-angle x-ray reflectivity measurements.

The thicknesses of the latter samples were chosen to be of 500Å/500Å because of the difficulties that we faced while fitting the data from the earlier bilayers with thicknesses of 2000Å/100Å. The 100Å layer was too thin, and in the case of the Fe(100Å) layer on top its oxidation caused the data to be difficult to interpret. Also the 2000Å layer was too thick to measure its modulations by our diffractometer resolution.

3.2 Ion beam irradiation

Normal incidence ion beam irradiation experiments were performed in a vacuum of 10^{-7} torr with 1 MeV Si^+ ions. To limit heating effects during irradiation the samples were placed in thermal contact with a copper block kept at the liquid-nitrogen temperature (77 K) and the beam current was maintained below 50 nA/cm^2. For the first set of bilayers and single layers which were deposited as three distinct samples on the same piece of substrate, one sample was kept without irradiation while the other two were irradiated at 2×10^{14} and 1×10^{15} ions/cm^2, respectively.

For the second set of samples, two samples were chosen with the configuration Si/SiO_2/Fe(500Å)/Ni(500Å) and Si/SiO_2/Ni(500Å)/Fe(500Å) and a series of successive irradiation by 1 MeV Si^+ ions was carried out on each of them with ion doses

ranging from 1×10^{15} to 1.9×10^{17} ions/cm^2. This ion energy was selected because in these 1000Å-thick samples the energy loss of the 1 MeV ions is roughly 200 keV, such that only a very small fraction (<0.1%) of the implanted ions comes to rest in the bilayer, the rest being transmitted or backscattered. Consequently, a uniform mixing profile throughout the bilayer is expected. X-ray reflectivity (XRR), x-ray diffuse scattering (XDS) and high-angle x-ray diffraction measurements were carried out for each stage of irradiation.

3.3 X-ray reflectivity and diffuse-scattering measurements

3.3.1 The diffractometer

Setup

The x-ray reflectivity and diffuse scattering experiments reported in this thesis are performed using a high-resolution triple-crystal x-ray diffractometer. Fig. 3.2 shows the layout of the instrument [129, 130].

The x-ray source is powered by a Philips generator (type 1793) with a water cooling system. A copper x-ray tube is used for the measurements, operated under power settings of 40kV x 40mA. An area of the anode of 0.4mm x 12mm is illuminated by accelerated electrons from its tungsten filament. The take-off angle of the x-rays is 6°. The x-ray tube has four beryllium windows along its sides to allow the x-rays to pass through. The two windows along the long sides of the tube allow a long spot of x-rays to pass through. From the other two windows along the short sides of the tube, a point source can be obtained. We use a point source with a beam cross-section of 0.4x1.2 mm^2.

For high resolution, the monochromator and the analyzer are both high quality single crystals such as germanium or silicon having Darwin width of 3.5×10^{-5} rad for their (111) diffraction peak [129, 131]. In a lower resolution setup, the priority is given to the intensity requirement. The monochromator and analyzer are replaced by a crystal with a mosaic structure such as graphite, with width typically $\approx 0.1°$ which gives higher intensity at the expense of lower resolution.

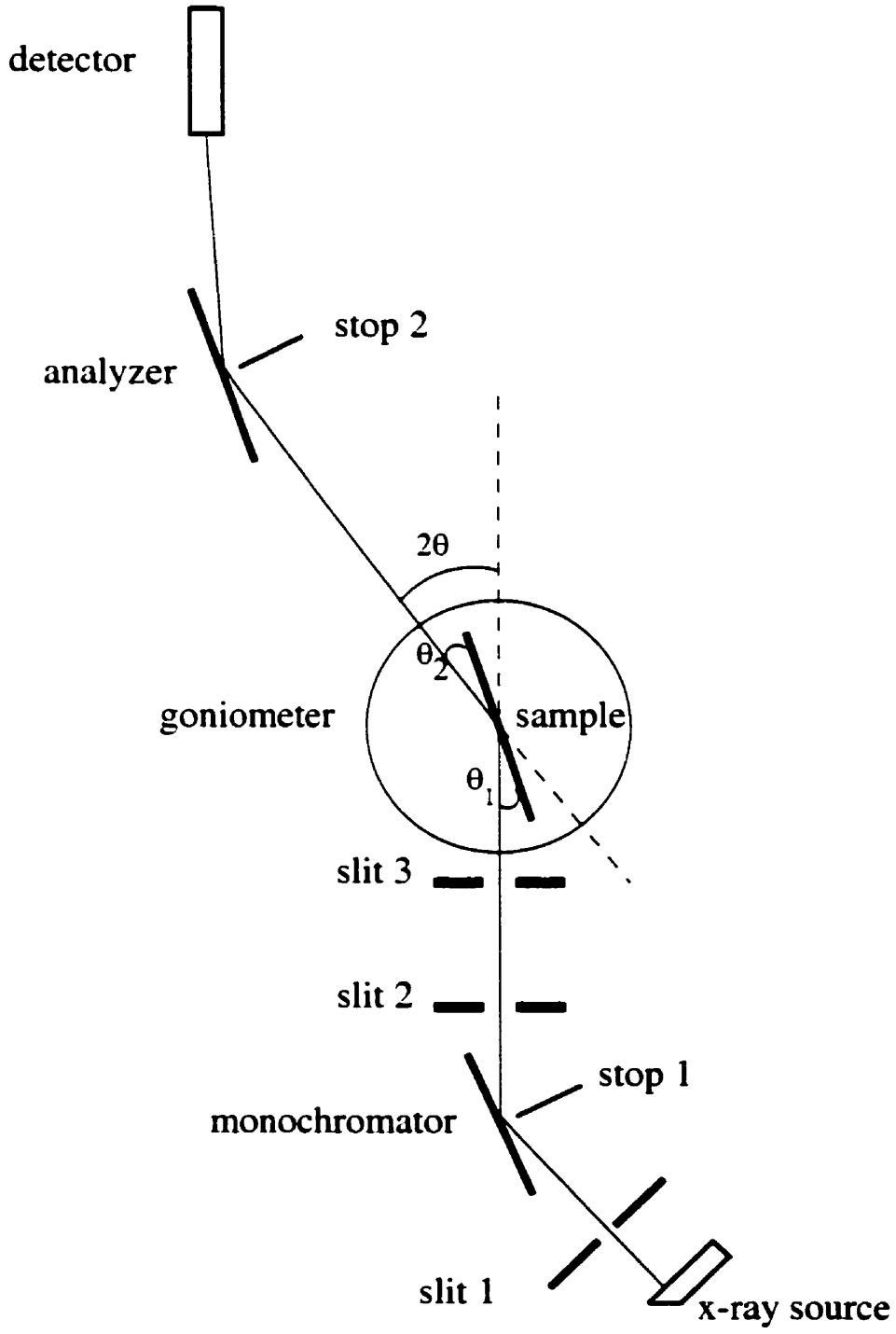

Figure 3.2: The diffractometer.

For our measurements we use the (111) diffraction peak of high-quality Ge single crystals for the monochromator and the analyzer. They are both mounted on manually adjustable goniometers. The monochromator is fixed once aligned, while the analyzer is mounted on the 2θ-arm of the sample goniometer and can rotate around the central axis of the goniometer.

The sample crystal is mounted on a four-axis goniometer and it has three degrees of freedom for rotational movement and two degrees of freedom for lateral movement. The goniometer is assembled with Huber goniometer components (Huber 5023: 2-circle goniometer, Huber 421) and a lateral moving x-y stage (Huber 5102) with a slide range of ± 15 mm and a positioning accuracy of 0.005 mm. It is driven by stepping motor controller PC58 from Oregon Micro Systems. The stepping motor controller can move with the minimum step size of 0.00025° for 2θ, ϕ and χ, and of 0.00005° for θ.

A Canberra scintillation detector is used with pre-amplifier (Canberra 1702) with a high voltage supply (Canberra 3102) to generate electrons by absorbing photons, a pulse amplifier and pulse height analyzer (model 1718) with a power supply (model 2000) to select the right energy of the photons. Photons are reflected by the crystal according to Bragg's law in more general form:

$$2d\ sin\theta\ =\ n\lambda_o, \qquad n\ =\ integer. \tag{3.1}$$

Usually n=1, the radiation of wavelength $\lambda = \lambda_o/2$ cannot go through because Ge(222) is a forbidden reflection. But the radiation $\lambda = \lambda_o/3$ can pass if n=3 by third order diffraction. The pulse height analyzer makes sure that the window is centered at the energy corresponding to λ_o and has a width narrower than the energy difference between λ_o and $\lambda_o/3$. This energy discriminator is necessary to reduce the miscount of photons by suppressing the higher harmonics and the low voltage noise of the preamplifier. By tightening the energy window of the pulse height analyzer, less photons contribute to our signal. This reduces the dark counts at the expense of slightly reducing the overall intensity. This trade-off is worthwhile at higher angles when our signal gets weak, because lowering the dark current allows us to detect

weaker signals (lowering the noise such that the signal-to-noise ratio becomes higher).

The energy of x-ray photons generated from Cu target is 8.04 keV [132]. By using a window of $\Delta V/V = 4/3.8$ for the pulse height analyzer to accept pulse amplitudes between V and $V + \Delta V$, we were able to lower the dark counts from 0.147 cps to 0.032 cps at the expense of reducing the arm-zero intensity from 1.02×10^5 cps to 0.55×10^5 cps at maximum power (40kVx40mA). Most of this dark current comes from the electronic circuits and from random scattering.

The slits are used to reduce the background. Slits 1 and 2 are used to better define the beam spatially. Slit 3 is the most effective slit in the system because it controls the size of the beam incident on the sample. It is driven by computer-controlled stepping motors and the opening can be narrowed or opened with an accuracy of 0.001 mm in size.

Copper has two close and strong characteristic emission lines (K_{α_1} and K_{α_2}) at wavelengths of 1.54051 Å and 1.54433 Å, respectively [133]. The K_{α_1} line has twice the intensity of the K_{α_2} line, so in the setup, K_{α_1} radiation is the central wavelength and everything is supposed to line up with respect to it. Ideally, the rotation center of the goniometer should be on this line, but in practice it will deviate by a small amount due to the limited precision of adjustment. This deviation is in the order of 10^{-2} mm. The K_{α_2} line also goes through the instrument but can be filtered out by special alignment. It does not, however, pass over the center of rotation.

Filtering of the K_{α_2} line

For the purpose of our measurements, the K_{α_2} line was filtered out and only the K_{α_1} line is incident on the sample. This is achieved by making the distance between the monochromator and the sample longer and narrowing the slits before the sample just enough to filter the K_{α_2} line and let K_{α_1} line pass.

The wavelength of Cu K_{α_1} is smaller than the wavelength of Cu K_{α_2} by 0.00382 Å, hence the two lines will be angularly separated after the Ge monochromator by 0.068° in 2θ, as shown in fig. 3.3. For a beam width of 0.5 mm, the distance between the monochromator and the sample must be at least about 830 mm to make the K_{α_2} line

completely spatially separated from the K_{α_1} line. Thus, by properly adjusting slit 3, the K_{α_2} line can be removed. Fig. 3.4 shows the distances between the crystals that we use for our setup.

From fig. 3.3 we can see the incident x-ray beam intensity at minimum power settings (15kV x5mA) with Ge(111) monochromator and analyzer crystals at the (+,+) setting. In part (a) of the figure the original incident beam intensity is shown before evacuating the flight path or removing the K_{α_2} line. Both K_{α_1} and K_{α_2} lines are seen with a separation of 0.068°. The intensity of the K_{α_1} line is almost twice that of the K_{α_2} line. By filtering out the K_{α_2} line the beam intensity will decrease mainly due to the divergence of the beam, but also due to the absence of the K_{α_2} intensity and the air attenuation of the longer optical path undergone by the x-rays. This latter effect is decreased by adding an evacuated flight path between the monochromator and the sample position, which increases the intensity by more than 1.6 times, as shown in part (b) of the figure.

Part (c) of figure 3.3 shows the incident beam after removing the K_{α_2} line by narrowing down slits 3 just before the sample. The resolution function of the diffractometer was studied in detail in reference [129]. It was found that at small angles the HWHM of the resolution function is around 0.007° for 2θ direction, and around 0.003° for ω direction. The removal of K_{α_2} improves the resolving power of the instrument at lower angles. As we can see from fig. 3.3, the spread due to the separation of the K_{α_1} and K_{α_2} lines is 0.068°. Thus, the removal of the K_{α_2} line increases the resolving power by an order of magnitude. Another advantage is that the centering of the sample becomes more accurate. To center a sample we usually adjust its position to be parallel to the x-ray beam and cut the beam intensity by half. Because K_{α_2} line has a slightly different incident angle than the K_{α_1} line, if the K_{α_2} is not removed, when the sample cuts half the intensity of the beam it may still not be well centered. By filtering out the K_{α_2} line, we are sure to center the position of the sample on the K_{α_1} line and on the center of rotation of the goniometer to an accuracy of 10^{-2} mm.

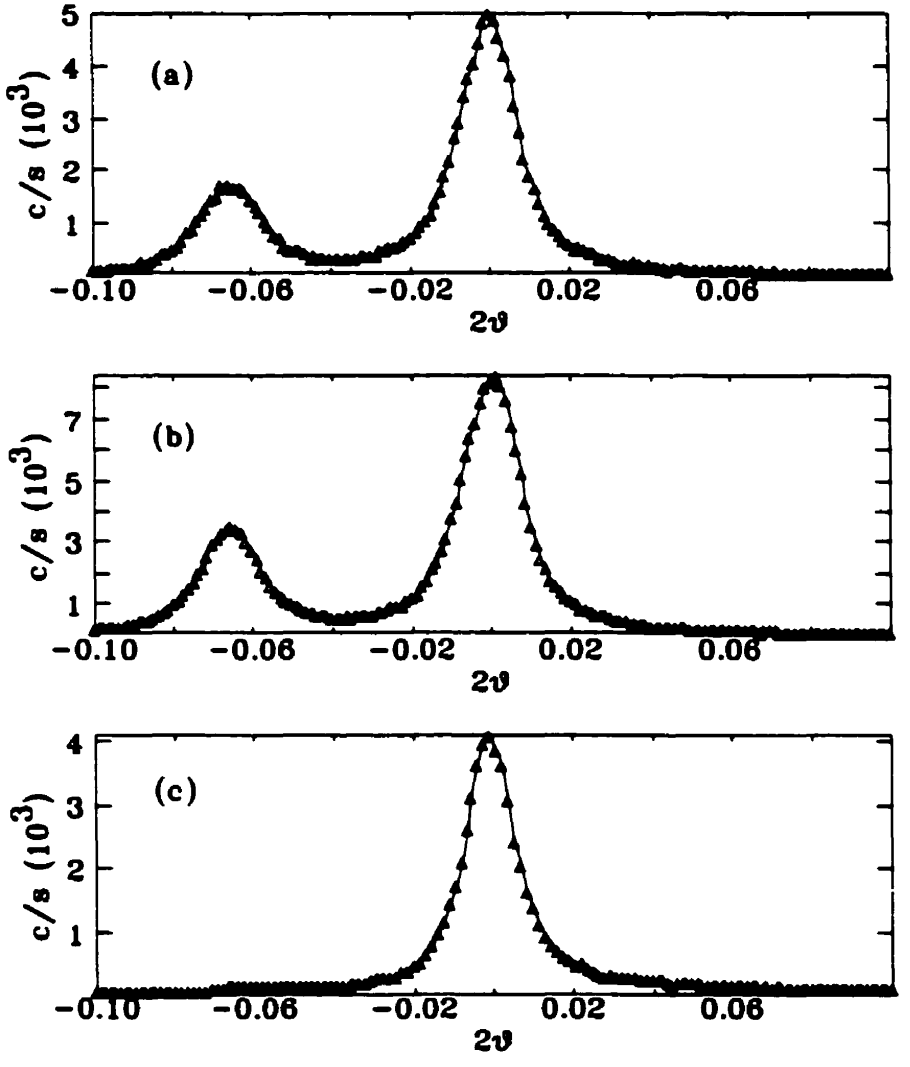

Figure 3.3: Incident x-ray beam intensity at minimum power settings (15kV x 5mA) with Ge(111) monochromator and analyzer crystals at the (+,+) setting. Slits 1 are 1.75mm wide x 2.0mm high and slits 2 after the monochromator are 1.5mm wide x 11.0mm high. no filters are used: a) original intensity with slits 3 wide open and no flight path; b) after evacuating the flight path; c) after filtering out the K_{α_2} line by narrowing slits 3 just before the sample to 0.7mm wide x 10.0mm high.

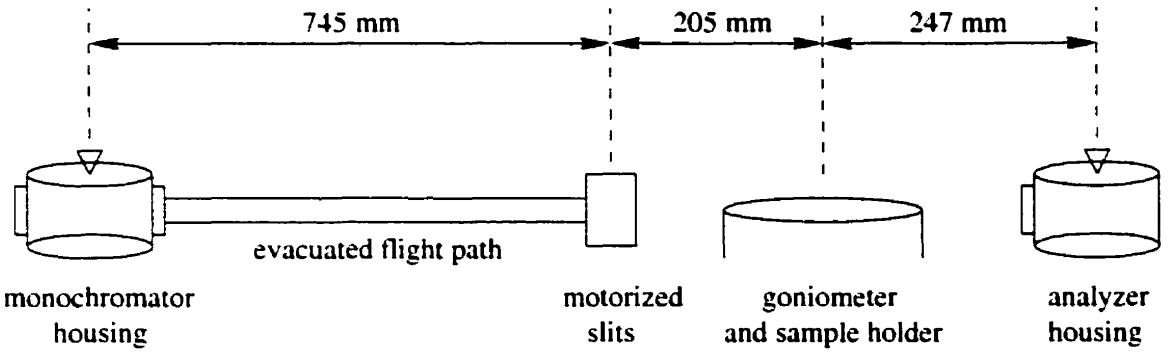

Figure 3.4: Distances used for our diffractometer setup.

Sample holder

As mentioned earlier, the sample crystal is mounted on a four-axis goniometer on a lateral moving x-y stage. It has two degrees of freedom for lateral movement. Our first set of samples are deposited as three distinct samples on a single piece of substrate of dimensions 20×6 mm^2, with the area of each sample about 4×6 mm^2, as shown in fig. 3.1.

As a consequence of these small sample dimensions, the x-y stage on the goniometer is not enough to align each of the samples. A z-stage had to be designed and fabricated using an adjustable height rack and pinion post from Edmund Scientific Company which allows the movement of the sample in the vertical direction within a range of 20 mm. By narrowing the slits, the vertical height of the beam can be decreased, then using the new xyz-stage, the desired sample can be well aligned in the x-ray beam.

3.3.2 Data acquisition and processing

In our reflectivity measurements the 2θ range is typically $0.3° < 2\theta < 4°$. This is a large range compared to a normal Bragg peak measurement and the angular error introduced by the goniometer may cause detectable shift of ω which leads to the inaccuracy of the measurement. One way to solve this problem is to make a small mesh around the $\omega = 0$ region for each fixed 2θ, spanning 2 or 3 times the HWHM of the resolution function. Then the maximum data for each 2θ value is chosen, which should represent the intensity at effective zero ω. This is not good in the region

where the signal is weak because we are mostly measuring the background. Another more feasible method is to average the data around a narrow region of the specular ridge. This reduces the error caused by the goniometer positioning inaccuracy but the average, which is equivalent to an integration over ω, may take into account some intensity from the diffuse part.

Figure 3.5 shows a typical $\theta - 2\theta$ scan for a 500Å-thick Ni layer deposited on Si substrate, obtained by performing an ω-scan at each 2θ-value then calculating the integrated intensity under each peak, as will be discussed later. We can clearly see the region of total external reflection extending until the critical angle around $2\theta = 0.74°$. Following the critical angle, the intensity falls off rapidly as $(2\theta)^{-4}$ as given by Fresnel's equation 2.14 for the reflection from a perfect surface. This fall-off will even be faster for the reflection from rough surfaces because the Fresnel reflectivity will be multiplied by a Debye-Waller-type correction factor to account for the effect of roughness. The top surface roughness will mainly dominate this effect because of the relatively large change in density upon going from vacuum to solid matter. The effect of buried interface roughness usually results in damping of the interference maxima at large angles.

The periodicity of the oscillation peaks determines the thickness of the Ni layer. By transforming from real space into reciprocal space, the spacing between maxima, Δq, will be given by $\Delta q = 2\pi n/d$, where n is the refractive index of the layer and d its thickness. The amplitude of the oscillations depends on the electron density contrast between the film and the substrate whereas their relative phase depends on the sign of the density change at the buried interface.

An example of a typical ω-scan, also referred to as diffuse scan, transverse scan, ω-rock or rocking curve, is shown in fig. 3.6. In this kind of measurement the detector is fixed at a certain 2θ value and the scattered intensity is measured as a function of the angle of incidence, θ, by rocking the sample around the specular peak. At $\theta=\frac{1}{2}(2\theta)$ we can clearly see the specular peak. Yoneda wings appear when the incident or the reflected wave vectors makes an angle with the surface equal to the critical angle of

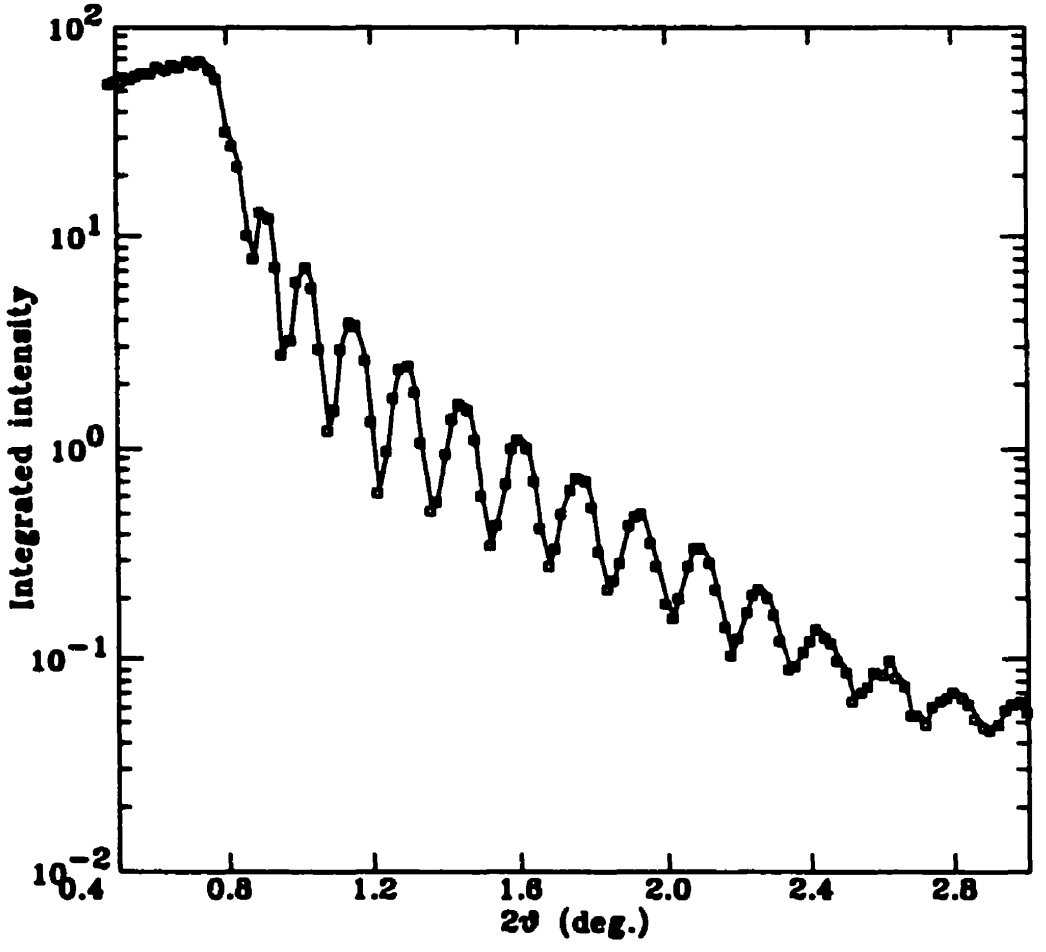

Figure 3.5: Typical $\theta-2\theta$ scan for a 500Å-thick Ni film deposited on Si substrate. The critical angle position is clearly visible at $2\theta = 0.74°$. Following the critical angle, the intensity falls off rapidly over three orders of magnitude. The distance between adjacent oscillation peaks varies inversely with the thickness of the Ni layer whereas the amplitude of the oscillations is proportional to the electron density contrast between the Ni and the Si layers. Solid line is a guide to the eye.

total external reflection, θ_c. This happens in our example at $\theta = 0.36°$ and $\theta = 0.64°$, respectively, as seen from fig. 3.6. The origin of these peaks was explained using the distorted-wave Born approximation (DWBA), as stated in sec. 2.2.1. According to eq. 2.45, at these angles the transmission coefficient of the incident or the reflected waves has a maximum and causes the appearance of these wings.

The integrated intensity under this curve is composed of three parts: a constant dark counts level which can be easily subtracted out, the specular intensity and the diffuse background. The area under the specular peak determines the reflectivity whereas the diffuse background comes from the incoherent scattering of x-rays from the roughness structure in our sample. As seen from eq. 2.46, the structure factor depends on the in-plane height-height correlation function of the interfaces, $C(X, Y)$. Thus, by fitting the diffuse intensity, the parameters of the correlation function can be obtained.

Therefore, in our measurements we need to separate the specular reflectivity from the diffuse background. This is achieved by performing an ω-rock at each fixed 2θ-value. Each of these ω-rocks is then fit using non-linear least-squares program to a lineshape which is the sum of a Gaussian and a Lorentzian of equal widths and unit areas. We write the approximation function for the lineshape in the form [134, 135]:

$$f(\Gamma, \eta, x, x_o) = \frac{(1-\eta)}{\pi}\frac{\Gamma^2}{\Gamma^2 + (x - x_\circ)^2} + \eta\sqrt{\frac{ln2}{\pi}} * exp[-(\frac{x - x_\circ}{\Gamma})^2 ln2] \quad (3.2)$$

where η is the Gaussian fraction, $x_\circ$ is the peak position and Γ is the HWHM of both the Gaussian and the Lorentzian lineshapes. The fitting curve may be written as:

$$f_{fit}(\Gamma, \eta, x, x_o, I, bg) = bg + I * f(\Gamma, \eta, x, x_o) \quad (3.3)$$

where bg is the diffuse background, I is the integrated intensity under the peak and f is the lineshape function defined in eq. 3.2. Fig. 3.7 shows some examples of these fits.

From each fit we obtain the integrated intensity, I, the background which is a measure of the diffuse scattering, the HWHM, Γ, of the peak, the Gaussian fraction, η, and the deviation of the peak position from the $\omega = 0$ position, $x - x_\circ$.

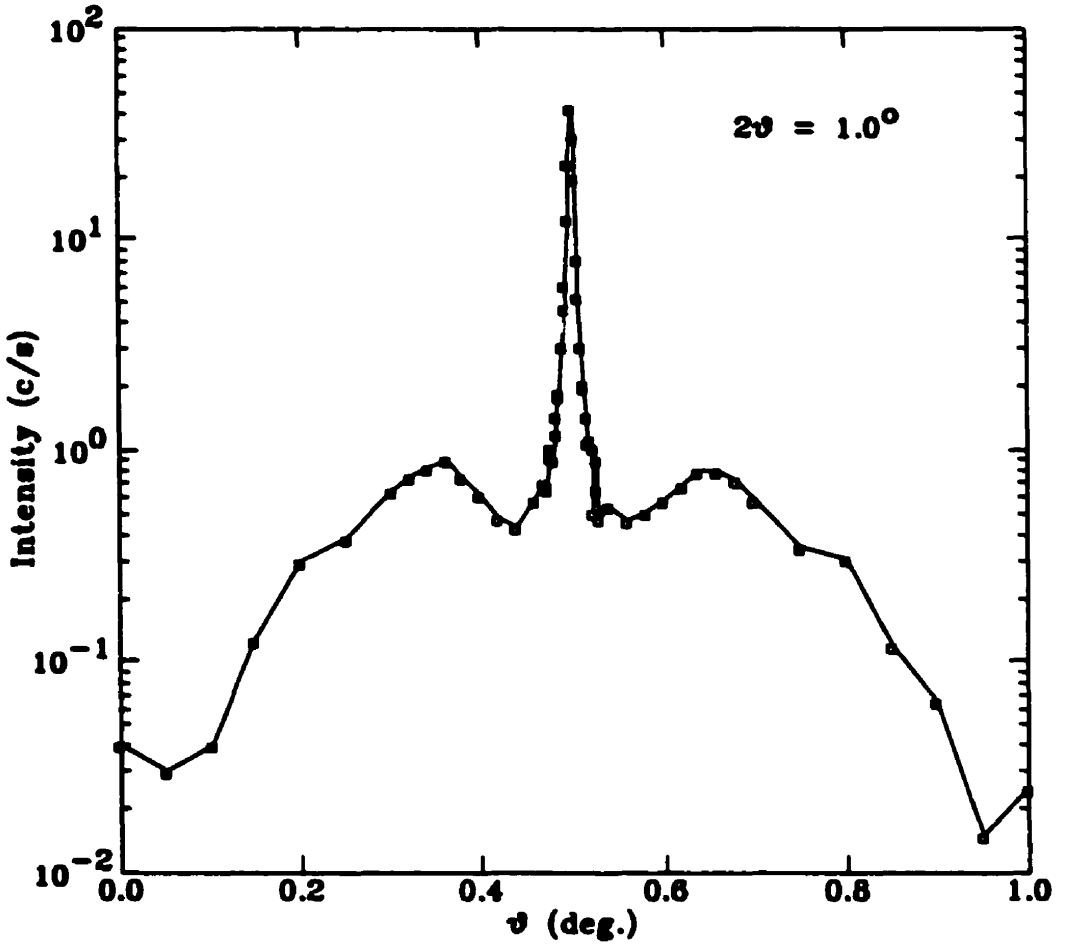

Figure 3.6: Typical ω-scan at $2\theta = 1.0°$ for the bilayer $Si/SiO_2/Ni(500Å)/Fe(500Å)$. The specular peak is clearly visible at the position $\theta = \frac{1}{2}(2\theta)$. Two Yoneda wings appear at $\theta = 0.36°, 0.64°$ where the incident or the reflected angle, respectively, is equal to the critical angle for total external reflection, θ_c. Solid line is a guide to the eye.

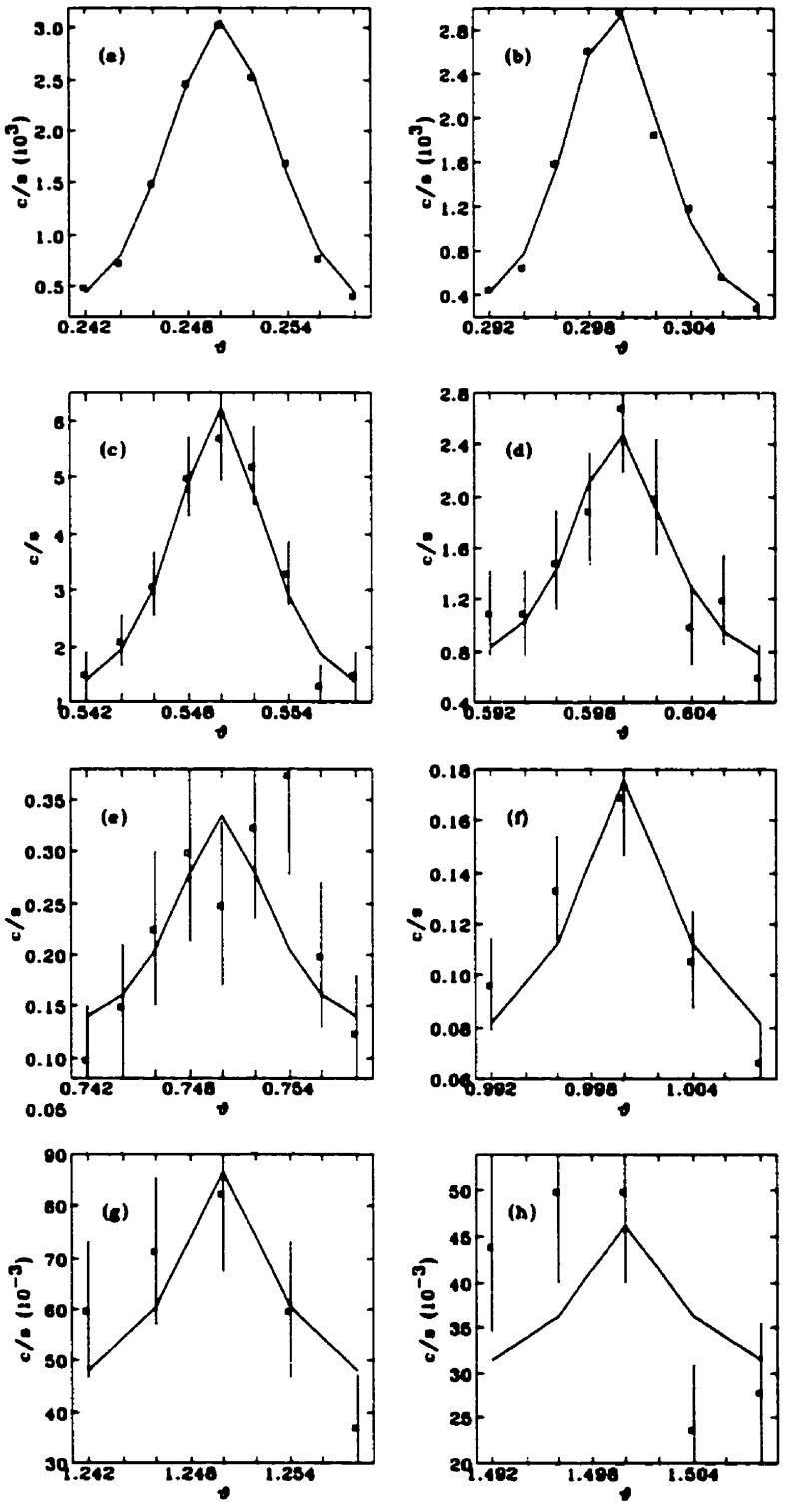

Figure 3.7: Example of lineshape fits to the ω-rocks using eq. 3.3 at different 2θ values: a) $2\theta = 0.5°$; b) $2\theta = 0.6°$; c) $2\theta = 1.1°$; d) $2\theta = 1.2°$; e) $2\theta = 1.5°$; f) $2\theta = 2.0°$; g) $2\theta = 2.5°$; h) $2\theta = 3.0°$. The function is calculated only at the data points.

As seen from the examples in fig. 3.7, the counting rate drops over several orders of magnitude in the range $0.5° < 2\theta < 3.0°$. In order to measure the reflectivity over this wide signal range with the same accuracy, the counting time is increased as we go to higher 2θ values, going from 5 seconds per data point at low 2θ values to 500 seconds per point at $2\theta > 2.5°$. This takes very long scanning time and in order to limit this time we increase the step size in 2θ from 0.01° to 0.02° as we go to higher 2θ values and decrease the number of data points taken at each ω-scan. After taking these measures into account each sample takes around 50 hours to scan as compared to 20 hours for a direct θ-2θ scan.

Fig. 3.8 shows the parameters that we obtain from fitting a series of ω-rocks using the previously-defined lineshape function. The χ^2 is shown in part (a) and is given by eq. 3.8. The non-linear least-squares fitting aims at minimizing χ^2. At small 2θ-values, the measured intensity is high and the statistical error is small, such that any small deviation of the calculated fit from the experimental data would result in large χ^2 values. At large 2θ-values, on the other hand, our signal is very weak and the statistical error is large, therefore the calculated fit will most likely go through all the data points and the χ^2 value will be smaller.

The fraction η of the Gaussian content is shown in part (b). We can see that η varies between 0 and 0.5, for an average of about 0.2, which shows that our lineshape content is mostly Lorentzian. In parts (c) and (d) of the figure, it is shown that the HWHM and the peak position vary a little during our fit. As seen from the data in fig. 3.7, at higher values of 2θ we have fewer data points and weaker signal-to-noise ratio such that it is harder to determine the HWHM and the peak position accurately. Since the HWHM depends on the resolution of the diffractometer setup, these two parameters are not expected to vary with 2θ. Therefore, they are fit at small 2θ values to obtain an estimate of the HWHM value and of the accuracy of the goniometer movement, then they are kept fixed at higher angles in order to determine the diffuse background and the integrated intensity more accurately. Part (d) shows the deviation of the peak position from the $\omega = 0$ value in order to obtain a clear

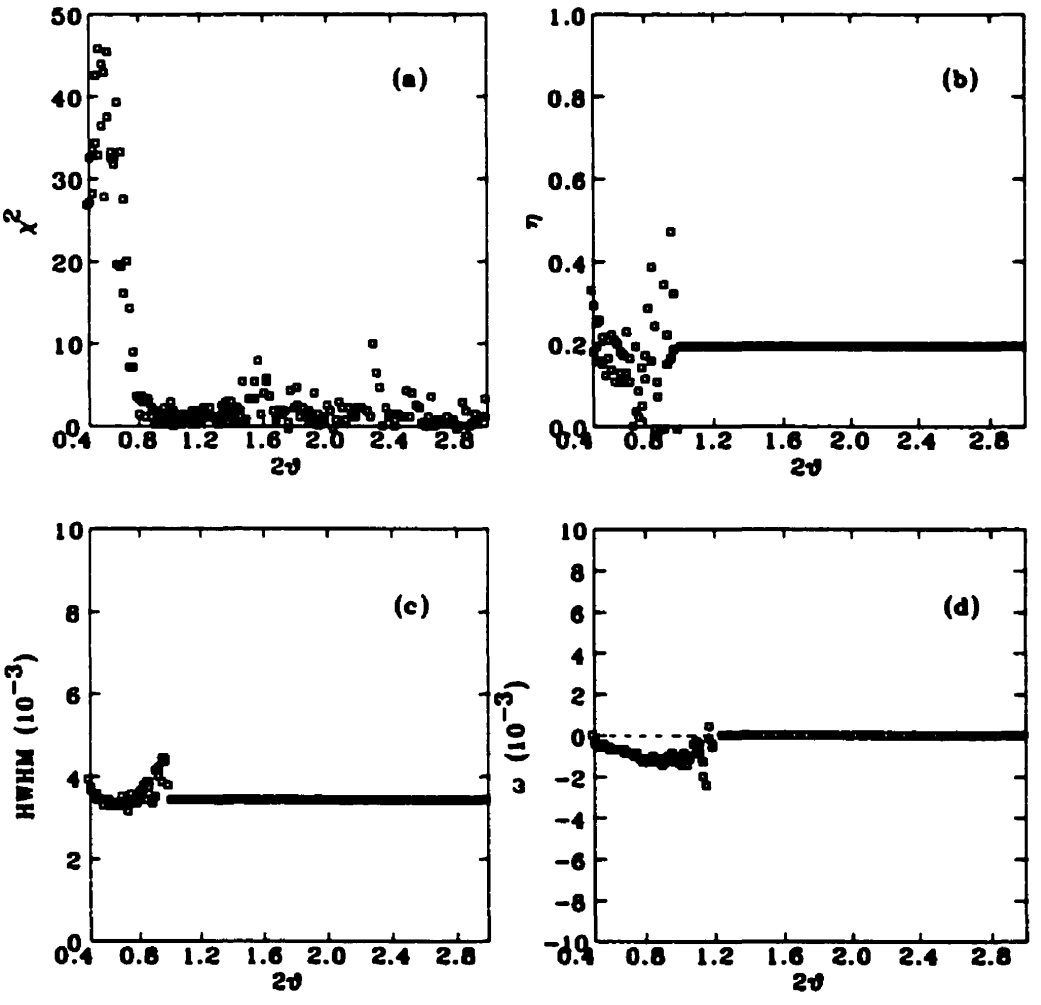

Figure 3.8: The parameters obtained from the lineshape fits: a) the χ^2 value: b) the Gaussian content of the lineshape, η; c) the HWHM of the peak; and d) the accuracy of the goniometer movement. These parameters are further explained in the text.

estimation of the goniometer accuracy.

In this way, we have separated the specular integrated intensity from the diffuse background. The diffuse background level is then multiplied by the θ-scan range in order to obtain the integrated diffuse intensity. The two separated components for this particular sample are shown in fig. 3.9.

By calculating the integrated intensity under the arm-zero peak, I_o, shown in part (c) of fig. 3.3, we can obtain the absolute reflectivity, R, by normalizing the specular integrated intensity, I, shown in fig. 3.9 by the integrated intensity of the incident x-ray beam, $R = I/I_o$. Finally, the footprint correction, explained in sec. 3.4.3, must be applied in order to account for the fact that at small incident angles the sample does not subtend the whole incident beam. This correction will further reduce the intensity of the reflected beam.

3.4 Modeling method

In order to fit our x-ray reflectivity and diffuse scattering data a model has to be chosen for our samples. We have to keep the number of variables in the least-squares fitting to a minimum such as to obtain the most reliable results. Thus, we try to keep our model as simple as possible.

Our model consists of a stack of individual layers each having a constant electron density value. The first layer is the substrate, which in our case is silicon coated with a layer of silicon oxide on top. The substrate is measured first and fit in order to obtain the SiO_2 thickness, and both the Si and SiO_2 roughness and electron densities. This allows us to fix some of those parameters during subsequent fits and hence reduce the number of fit variables. Another measure to reduce the number of variables in reflectivity fits is to obtain the normalized reflectivity as explained in section 3.3.2 and so the intensity parameter could be kept constant. Following the SiO_2 layer we have one layer of material (in case of our single layer samples) or two layers (in case of bilayers). We try first to fit our data without adding any oxide layers on the surface, if the fits are not satisfactory we add a surface oxide layer to the model.

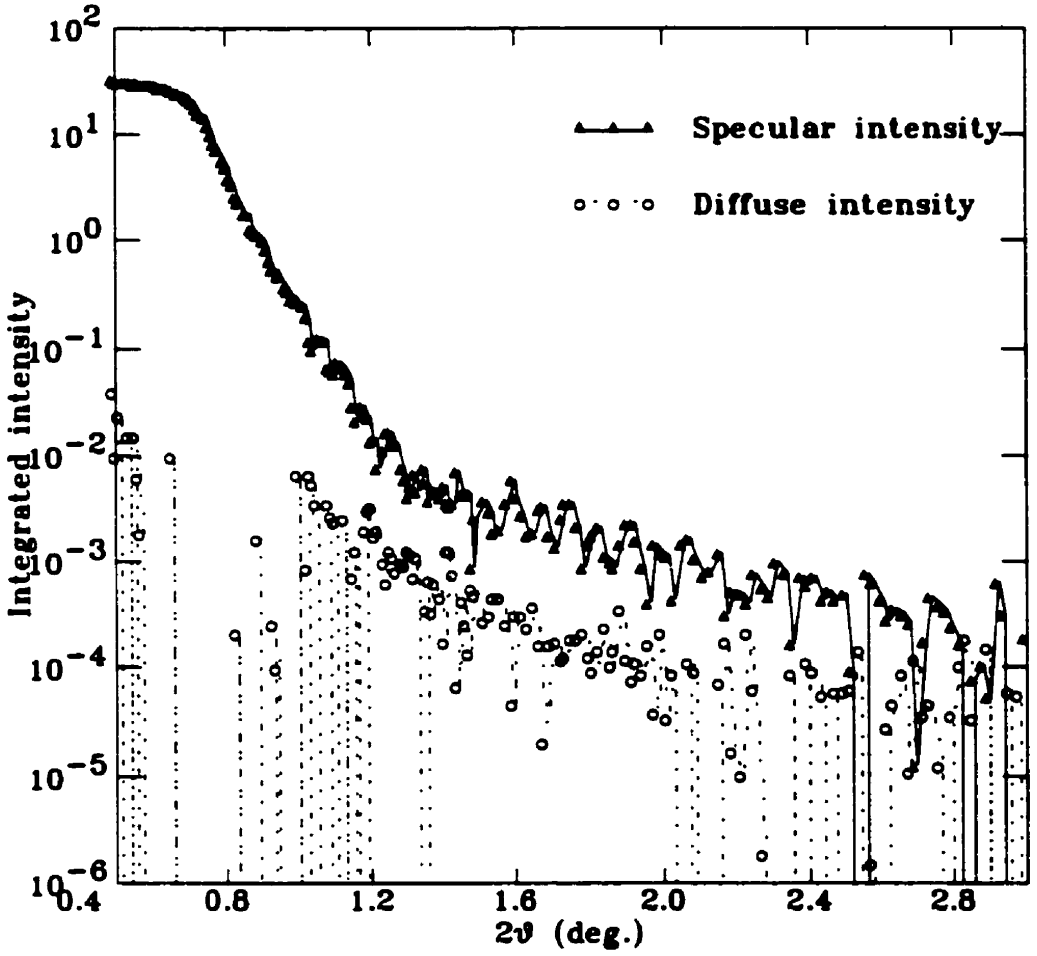

Figure 3.9: Specular (solid triangles) and diffuse (open circles) integrated intensities for the bilayer $Si/SiO_2/Ni(500Å)/Fe(500Å)$ irradiated at 1×10^{15} ions/cm^2.

Each layer in our model is characterized by four parameters, the thickness, the roughness, the refractive index given by eq. 2.9 and the absorption coefficient given by eq. 2.12.

A program was written in C language in order to calculate the theoretical x-ray reflectivity and x-ray diffuse scattering intensity. The XRR calculation follows the matrix method [114] explained in section 2.1.3 and the diffuse scattering calculation follows the derivation of Daillant *et al.* [52] given in section 2.2.2. The calculated intensities are then fit to the experimental data using a non-linear least-squares fitting program in order to extract the values of the different fit parameters.

However, many representations can be used in order to model the interfaces. In the next sections we will present the different types of interfaces and explain the simulation method which we use in order to test the effect of the different electron density profiles on the calculated reflectivity.

3.4.1 Interface types

Interfaces can be divided into two categories, rough interfaces and diffuse or graded interfaces, as shown in fig. 3.10. In an ideal structure, the interface would be smooth and sharp as shown in part (a) of the figure. But normally an interface can be rough or graded (as shown in parts (b) and (c) of fig. 3.10, respectively). The interface roughness originates partly from replication of the roughness of the substrate and additional roughness is induced during the crystal growth. The diffuseness is most likely the result of mixing of the layers during deposition or subsequent treatment such as annealing or irradiation. This diffuseness causes a smooth and continuous decrease of scattering density normal to the interface. Real, non-ideal interfaces exhibit a combination of both rough and graded structures as shown in part (d) of the figure.

These two kinds of interfaces, rough and graded, are not completely equivalent. Although in both cases, the deviation from an ideal smooth interface causes the loss of part of the specular reflectivity, in the case of a rough interface that part of the energy flux goes into diffuse scattering and may or may not go into the transmitted

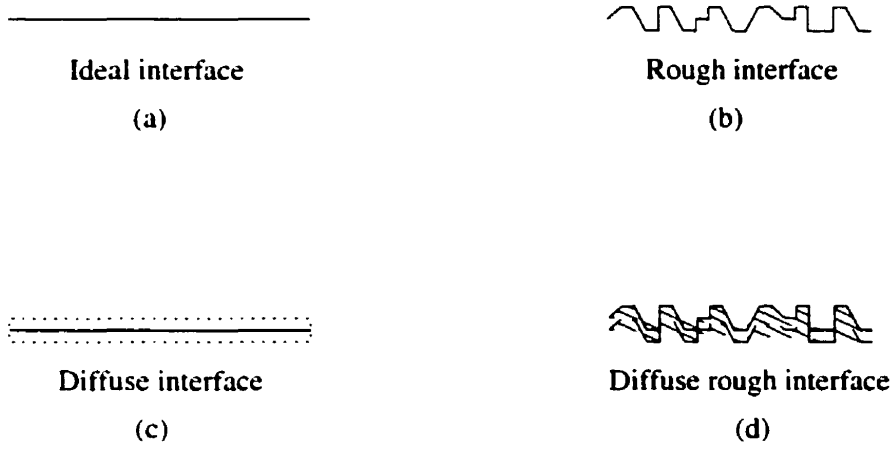

Figure 3.10: Different kinds of interfaces.

beam, while in the case of a graded but smooth interface all the energy flux goes either into specular reflection or transmitted beam, no diffuse scattering component can be measured.

The reason for this difference is that the diffuse scattering originates from the incoherent scattering of x-rays by the roughness structure of *rough* interfaces. Graded interfaces, on the other hand, can be represented by many thin uniform slabs, each of which has a *smooth* surface but a different electron density value. These smooth surfaces do not cause any incoherent x-ray scattering, and therefore no diffuse scattering component can be measured from them. A graded interface causes a less abrupt change in the refractive index and so enhances the transmission coefficient.

Therefore, we cannot tell the difference between rough and graded interfaces just by measuring the specular reflectivity since both types reduce the specularly-reflected intensity. A measure of the diffuse scattering intensity is essential in order to distinguish between them.

Moreover, rough interfaces can be further divided into four categories [63]: a) perfectly conformal rough interfaces, where the roughness of all interfaces are perfectly identical; b) uncorrelated roughness, where each interface has an independent roughness profile; c) partially correlated roughness with constant total roughness

per interface, where the roughness of an interface is partially duplicated in a subsequent interface along with a superposition of random fluctuations; and d) cumulative partially correlated roughness, where each interface duplicates the roughness of the previous one and adds on it its own roughness such that the roughness increases from the bottom to the top of the stack. These effects are very important in a multilayer structure.

In order to fit our diffuse scattering data we assume Gaussian roughness fluctuations at the interfaces, as given by eq. 2.63. For simplicity, we assume that in our samples there are no cross-correlations between the roughness of the different interfaces, i.e. we consider the case of uncorrelated roughness. We rewrite the expression for the correlation function as:

$$C_{jk}(X,Y) = \begin{cases} \sigma_j^2 e^{-(R/\zeta)^{2h}} & for\ j = k, \\ 0 & for\ j \neq k, \end{cases} \tag{3.4}$$

in order to explicitly express the absence of any cross-correlations, where $R \equiv (X^2 + Y^2)^{1/2}$.

3.4.2 *Interface modeling*

The evaluation of specular scattering from a non-ideal interface requires the determination of the interface profile function. Ideally, if the exact three-dimensional structure of the interface were known, then the actual profile could be calculated numerically. In general, however, such detailed knowledge of the structure of the interface is not available and the interface profile is usually modeled using a simple analytical function. Stearns [136] lists several useful models of the interface profile, their derivatives and their Fourier transforms. He states that the classical diffusion of two materials produces a variation in composition at the interface which is best described by an error function, in which case the derivative is a Gaussian. Bai et al. [44] studied the composition profile of a Ni/Fe alloy thin film using resonant x-ray reflectivity measurements. They used a series of straight line segments to approach the in-depth electron density profile at the interfaces. They found that the linear

segment approximation is a better choice than using step functions for the electron density profile. They had to use up to three linear segments to approach the real electron density at the top interface, which in our case would give too many parameters for the fit, but they obtained good fits and consistent parameters at five different x-ray energies.

In order to choose an electron density profile suitable to describe the structure of our samples we would like to test several possible representations. Figure 3.11(a) shows three different interface profiles for a 100 Å layer using an error function, a hyperbolic tangent function and an arc-tangent function. As seen from the figure, the error function and the hyperbolic tan profiles almost coincide while the arc-tan profile is a little smoother. The x-ray reflectivity calculated for this layer of material using the different interface profile functions is shown in fig. 3.11(b). Again, we can see that the calculated reflectivity using the arc-tan function profile differs a little from the reflectivity calculated using the error function and the tanh electron density profiles. This is due to the fact that the scattering factor is proportional to the Fourier transform of the electron density gradient across the interface:

$$f(q) = \int_{-\infty}^{\infty} \left[\frac{d\rho(z)}{dz}\right] e^{-iqz} dz. \tag{3.5}$$

While the derivative of the error function is a Gaussian whose Fourier transform is also a Gaussian and that of the tanh function is an exponential, the Fourier transform of the derivative of the arc-tan function is a Lorentzian and hence is smoother than the Gaussian and exponential functions giving a slightly different reflectivity.

For a graded interface, the variation in composition at the interface follows an error function, whose derivative is a Gaussian. Whereas for a rough interface, as represented schematically in fig. 2.4, the interface position varies at different depths with respect to an average interface. The probability distribution of the interface height deviation from an ideal surface is assumed to follow a Gaussian distribution.

If the interface can be represented by an error function, as in the case of graded interfaces, we can calculate the reflectivity from such a structure exactly. However, we would like to be able to calculate the reflectivity from any given electron density

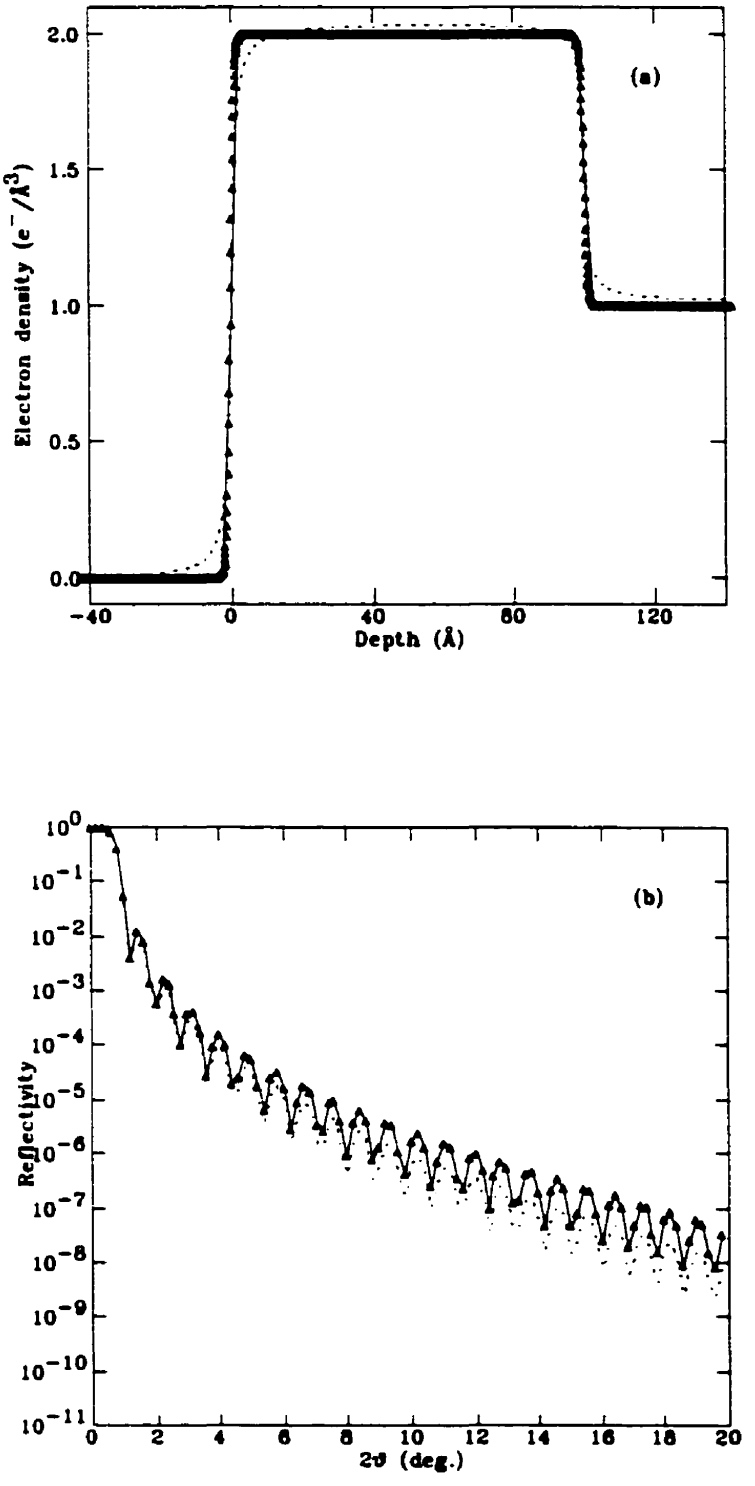

Figure 3.11: a) Different function representations of the electron density profile. b) Calculated reflectivity using different interface function representations. Dotted line, arc-tan; triangles, tanh; solid line, erfc.

profile. In order to simulate any given electron density profile we divide the interface into N linear steps as shown in fig. 3.12(a), and calculate the reflectivity from this structure.

First, we test the accuracy of this simulation method using an error function profile for which the reflectivity can be exactly calculated. Fig. 3.12(b) shows the effect of increasing the number of linear steps N of an error function profile on the calculated reflectivity. The exact reflectivity for this layer is given by the solid line. As expected, by increasing N the calculated reflectivity using the step model becomes accurate to larger values of 2θ. However, the calculation saturates at a certain point due to round-off errors from multiplying a very large number of matrices (a matrix for each linear step). Hence, increasing the number of linear steps beyond N=100 is not useful and we get approximately the same reflectivity result. But the calculation is accurate beyond $2\theta = 10°$ which is large enough in our case since our measurements extend only to 4°.

Therefore, by dividing any given interface profile function into N linear steps, with N a sufficiently large number, and calculating the reflectivity from this structure by considering each of these steps as a separate layer with a certain thickness and electron density value, we obtain a very good approximation to the exact reflectivity from that interface profile.

In fitting our experimental data we tried four different interface profile functions using the N-step simulation method, as discussed in section 4.2. We found that the error function profile best represents the structure of our samples and used it to model the roughness and the interdiffusion at the interfaces. In some cases of our fits, the roughness turned out to be comparable to the layer thickness. In order to understand the density profiles implied by our model at these large values of roughness, we use the N-step model to simulate the interface profile and calculate the reflectivity as shown earlier.

Figure 3.13 shows the effect of increasing roughness on the calculated reflectivity. The roughness values range from very small (5 Å) to a roughness equal to the layer

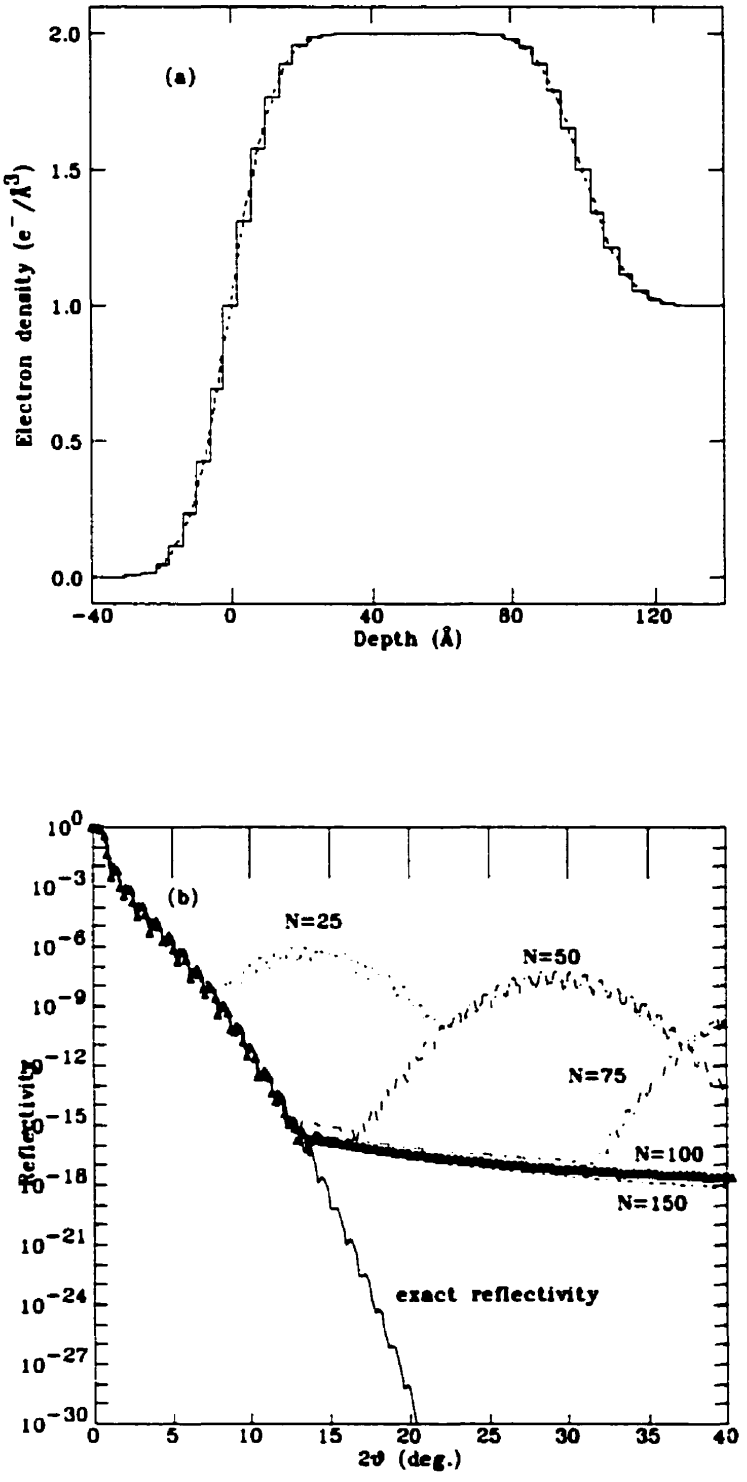

Figure 3.12: a) Linear steps electron density profile (solid line, N=50) used to simulate an error function profile (dashed line). b) Calculated reflectivity using the step interfaces shown in part (a) for different values of N compared to the exact reflectivity calculated using error function interface profile (solid line).

thickness (100 Å). As seen from the figure, the reflectivity falls off very steeply as the roughness increases. The electron density profiles for this material are shown in fig. 3.14. For roughness values less than 25% of the layer thickness the effect of roughness is to smooth out the transition at the interface, but as the roughness becomes comparable to the layer thickness it affects the effective electron density of the layer. As the roughness increases to 50% and even to 100% of the layer thickness the effective electron density of the layer is reduced. The interface extends into the center of the layer, representing an interdiffusion of the layers across this interface. Hence, in our model when we obtain a large value for the roughness of a layer compared to its thickness, it implies lower effective electron density for the layer in question and more interdiffusion across the interface.

3.4.3 Footprint correction

There is an instrumental correction for collecting data with small q_z scans called the footprint correction [135]. This correction arises because when the x-rays are incident with a glancing angle at the sample surface, only part of the x-ray photons hits the sample. Therefore the reflected photon counts are reduced. As the sample rotates to higher θ, more radiation is intercepted and thus reflected by its surface. If the intensity of the incident x-rays is uniformly distributed across the horizontal width of slit 3 of the diffractometer, the factor of footprint correction P_{f_1} for K_{α_1} line of the x-rays is given by:

$$P_{f_1} = \frac{L}{w} sin\theta, \qquad if \quad \theta <= sin^{-1}\frac{w}{L}, \tag{3.6}$$

$$P_{f_1} = 1, \qquad otherwise, \tag{3.7}$$

where L is the lateral length of the sample parallel to the x-ray beam and w is the horizontal width of the incident x-ray beam as defined by slit 3. We assume that our sample has no surface miscut angle. Also since we block out the K_{α_2} line from hitting the sample, we do not need to consider the footprint correction due to this line.

Figure 3.15(a) shows the footprint correction for K_{α_1} line for a sample 4 mm wide and a beam width of 0.75 mm. We can see that at $\theta = 0$ no photons hit the sample

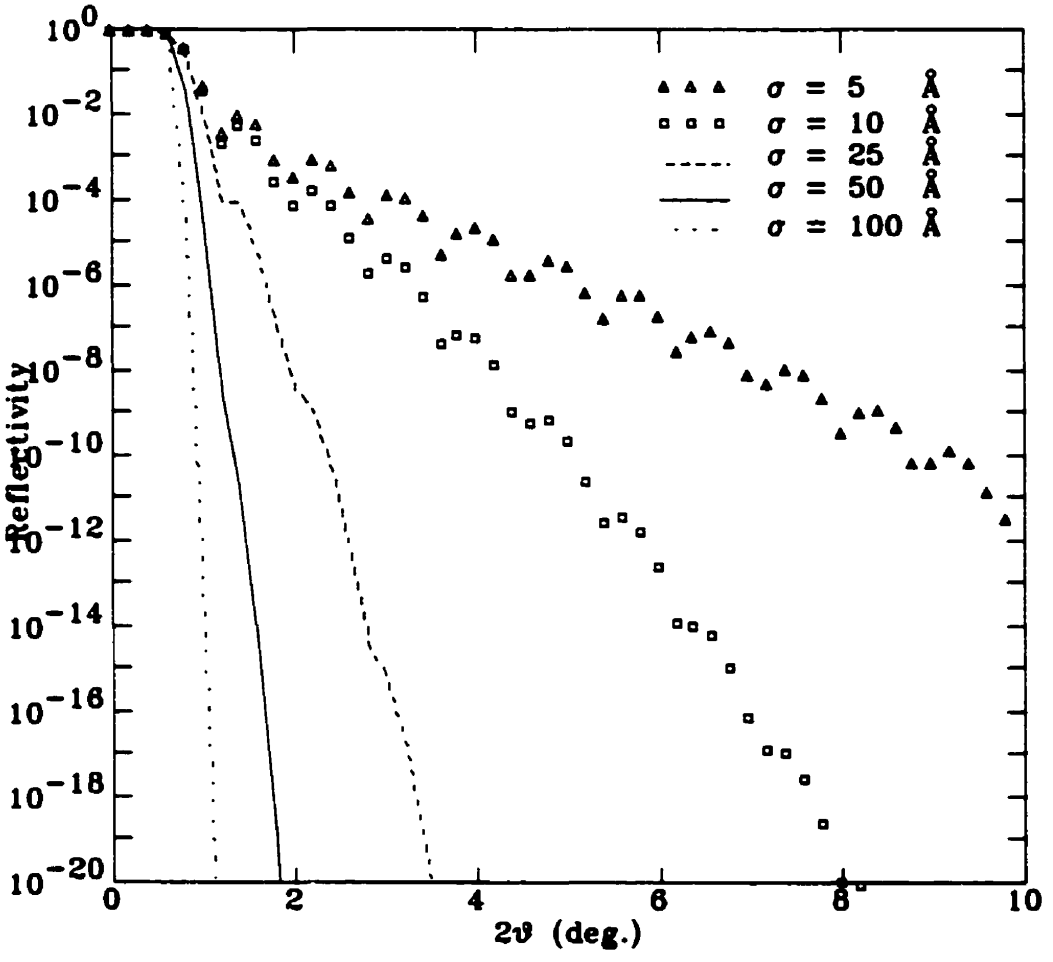

Figure 3.13: Effect of roughness on the calculated reflectivity of a 100 Å-thick layer having an electron density of 2.0 $e^-/Å^3$ deposited on a substrate with an electron density of 1.0 $e^-/Å^3$.

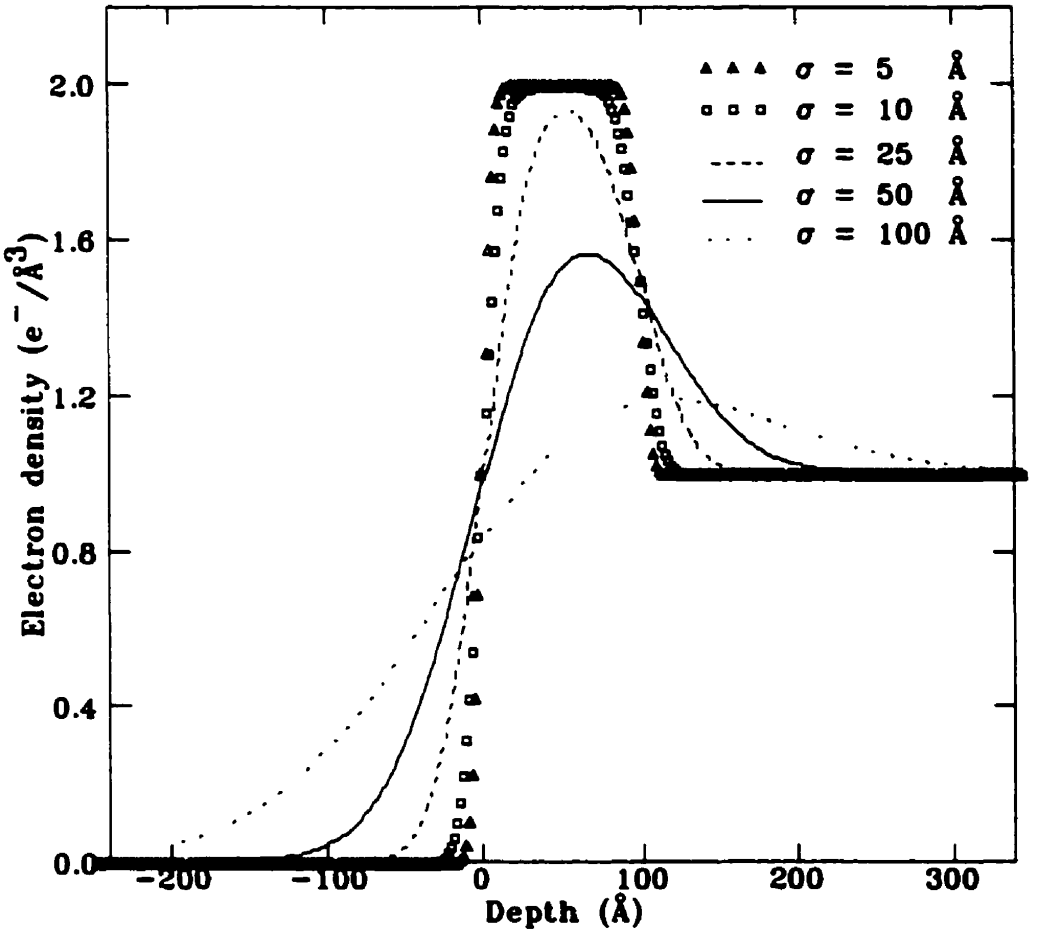

Figure 3.14: Effect of roughness on the electron density profile of a 100 Å-thick layer. As the roughness increases to 50% and even to 100% of the layer thickness, the effective electron density of the layer decreases and more interdiffusion appears across the interface.

because the sample should be perfectly parallel to the incident beam due to our alignment, and the K_{α_2} line is removed. As θ increases, more photons start hitting the sample. It is only at $\theta = 10.8°$ (q_z=1.53Å^{-1}) that all of K_{α_1} is intercepted by our sample. Since our measurements extend only to $\theta = 2.0°$ it is very important to include the footprint correction into our model. Figure 3.15(b) shows the effect of the footprint correction on the reflectivity from a Si/SiO_2/Ni(500Å)/Fe(500Å) bilayer. The solid line represents the calculated reflectivity without taking the footprint correction into account, while the dashed line shows the effect of including this correction. The measurement in this example extends only to $\theta = 1.5°$ hence the footprint correction reduces the reflected beam intensity over the entire range.

3.4.4 Fitting procedure

Our model calculations are fit to the experimental data using a non-linear least-squares fitting program in order to determine the appropriate physical parameters for our samples. The fitting procedure minimizes:

$$\chi^2 = \sum_{i=1}^{N} (R_i^e - R_i^c)^2/\sigma_i^2, \tag{3.8}$$

where R_i^e and R_i^c are the experimental and calculated x-ray reflectivity, respectively, N is the total number of data points and σ_i^2 is the weighting function. The choice of the weighting function is very important since our data varies over more than four orders of magnitude in reflectivity. At high reflected intensities, two factors will introduce more error on the counts: variation in the beam intensity and sample alignment. This will produce an error significantly larger than the one introduced on the basis of counting statistics, so it is more appropriate to treat it as a percentage error rather than as counting statistics. At low reflected intensities, a weighting function determined by the counting statistics and proportional to the number of counts is the appropriate form [137]. The overall weighting factor is calculated as the sum of two terms arising from a percentage uncertainty at high intensities and counting statistics at low intensities, given by:

$$\sigma_i{}^2 = R_i{}^e + (\alpha R_i{}^e)^2, \tag{3.9}$$

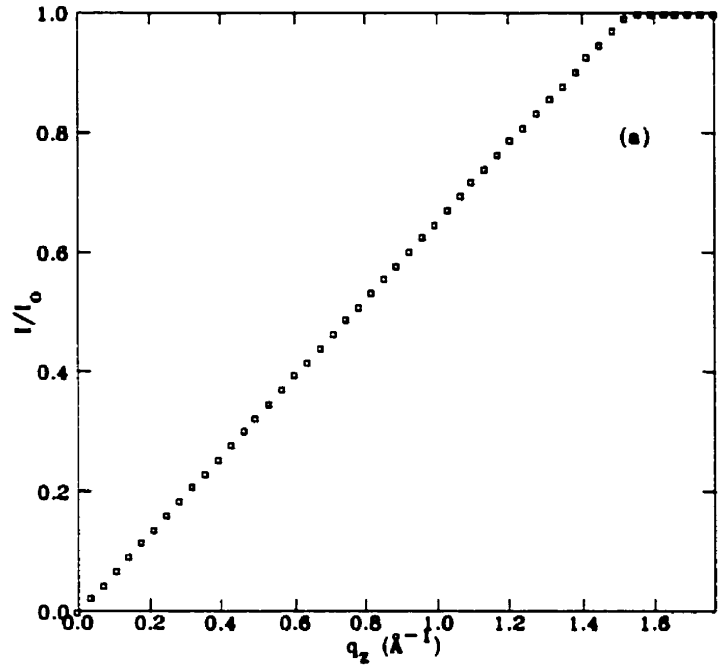

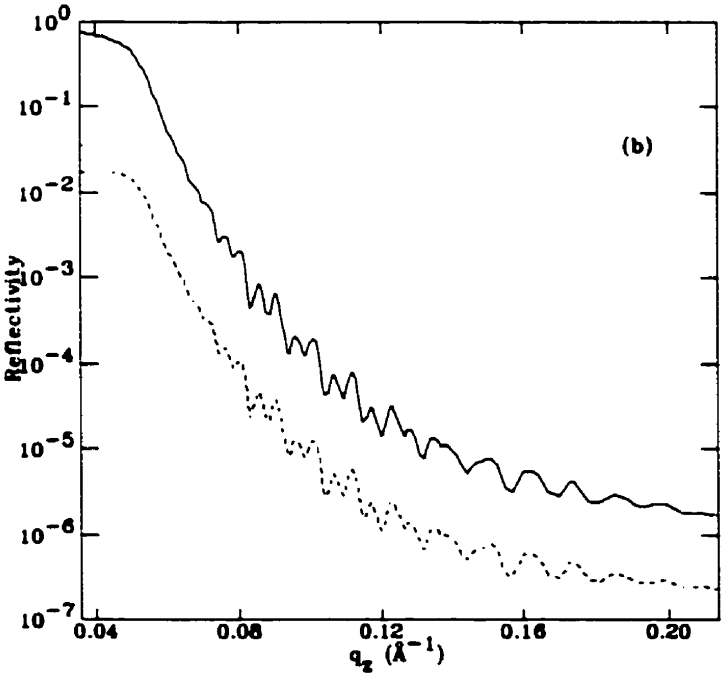

Figure 3.15: (a) Footprint correction calculated for a sample 4 mm wide and a beam width of 0.75 mm. (b) Calculated reflectivity from a $Si/SiO_2/Ni(500Å)/Fe(500Å)$ bilayer without footprint correction (solid line) and with the footprint correction (dashed line).

where α is the fractional uncertainty. The variation in the beam intensity at low angles is estimated to be of the order of 10-15%. In our fits we typically use $\alpha = 0.05$ since we found that this value is large enough to cover the systematic errors.

3.5 High-angle x-ray diffraction

The crystallographic structure of the samples is investigated using high-angle x-ray diffraction measurements. A Nicolet-Stoë double-crystal powder diffractometer is used with Cu K_α radiation at low-resolution setup using a graphite analyzer and operated at 45 kV x 25 mA power settings.

3.6 TEM and XTEM measurements

Several samples with the configuration $Si/SiO_2/Ni(500Å)/Fe(500Å)$ were deposited at the same time. Each of these samples was irradiated to a different ion dose and characterized by low-angle x-ray reflectivity and high-angle x-ray diffraction measurements both before and after irradiation. The as-deposited samples were found to be almost identical.

Plane-view and cross-sectional transmission electron microscopy (TEM and XTEM) analyses were carried out on these samples by P. Desjardins[1] in order to verify their structure especially at the interfaces. These TEM measurements were performed using a Philips CM12 microscope with a LaB_6 filament operated at 120 kV [128]. Specimens were prepared using mechanical grinding to a thickness of $\approx 30\mu$m followed by Ar^+ ion milling in a liquid-N_2-cooled stage. The incident beam angle and energy were progressively reduced from 15° to 11° and from 5 keV to 3.5 keV in order to minimize radiation damage artifacts and to obtain samples with relatively even thickness distributions.

[1] Materials Science and Engineering Department, the Coordinated Science Laboratory, and the Materials Research Laboratory, University of Illinois at Urbana-Champaign.

4

RESULTS OF THE SURVEY

In the present chapter we will present the results of a survey performed on eight samples, four of which are single layers of Ni, Fe, Cu and Co and the other four are bilayers of Fe/Ni and Co/Cu with different deposition sequences. Our purpose is to identify the structural changes that occur in these samples upon ion irradiation. We want to study the behaviour of several materials in a relatively fast survey and then to perform a more detailed study based on the information obtained from this survey.

In order to accomplish this study the samples were deposited by rf triode sputtering techniques and irradiated by 1 MeV Si^+ ions to doses of 2×10^{14} and 1×10^{15} ions/cm^2. X-ray reflectivity measurements and x-ray diffuse scattering scans were performed on each of these samples at each stage of irradiation.

We would like to answer some questions such as what is the best method for data acquisition? How should we process this data? What is the optimal setting for our diffractometer? How reliable are the results of the fit? How good is the estimation of the errors in the various parameters? Is there a change in the electron density of the different layers upon irradiation? Is our measurement sensitive enough to tell? What is the best configuration for our sample in order to obtain good data, best thicknesses to be well resolved by our setup? Do we see any roughening or intermixing at the interfaces upon ion irradiation? Can we tell the difference by measuring the diffuse scattering? At what range of ion doses do we see changes in the structural properties? What model should we use to represent our samples? and so on.

In an attempt to make a fast survey we deposited three distinct samples of each configuration on the same piece of substrate using a contact mask. The dimensions

of the obtained samples are shown in fig. 3.1. The purpose of this deposition method is to obtain three identical samples, deposited at the same deposition conditions and then to irradiate two of them to two different irradiation doses and keep the third one as deposited. Then by characterizing those three samples we can obtain the structural changes after irradiation.

In our study, all of the samples are deposited on the same type of thermally-oxidized silicon substrate. In order to reduce the number of fit parameters when fitting the reflectivity data of our samples we start by measuring and fitting the reflectivity of the Si/SiO_2 substrate. The obtained substrate parameters are then used in subsequent fits to the other samples. Section 4.1 presents the data and fit to the substrate reflectivity.

An important question arises on how to model the interfaces of our samples? Generally speaking there are two types of interfaces, rough interfaces and graded interfaces as discussed in sec. 3.4.1. Rough interfaces have a random distribution of surface heights in x,y while graded interfaces have a smooth and continuous change in the refractive index normal to their surface. The roughness in an interface comes from the replication of the roughness of the substrate and more roughness could be introduced during deposition or irradiation. The graded interfaces are produced by intermixing of the different layers. Real interfaces however are usually a mixture of both types.

A rough interface could be well represented by an error function profile whereas a purely graded interface might be better represented by a linear profile. In order to test these representations we fit the reflectivity data of the Ni sample using four different interface profile functions. These functions are the error function interface, the linear interface, the hyperbolic tangent interface and the arc-tangent interface. The results are presented in sec. 4.2.

Once we have decided which model to use, we fit the reflectivity data for the other samples at the different irradiation doses. From the fit parameters we construct and plot the evolution of the electron density profile with irradiation dose. The fits, fit

parameters and electron density profiles for the single layers are presented in sec. 4.3.2 while those for the bilayers are presented in sec. 4.4.2.

Finally, sec. 4.5 presents the x-ray diffuse scattering measurements performed on the bilayers together with a qualitative description of the results and a discussion of how to differentiate between the different types of interfaces. A conclusion to this survey is presented in sec. 4.6.

4.1 Substrate measurement

As mentioned earlier, our samples are deposited on thermally oxidized Si(100) wafers. SiO_2 is chosen as the substrate instead of Si because Si is more reactive with Ni or Fe than SiO_2 upon deposition or irradiation. Details of sample preparation and irradiation are given in sections 3.1 and 3.2, respectively.

In order to minimize the number of fitting parameters, we start by measuring the x-ray reflectivity of the substrate. The data is fit to a standard optical model [111] based on the recursive method of Vidal and Vincent [114]. As explained in sec. 3.4, the model consists of a semi-infinite layer of silicon followed by a layer of silicon oxide. Each layer is represented by four parameters, the thickness, the roughness, the electron density and the absorption coefficient. The roughness of the interface and the surface roughness are represented by error functions. The calculated curves are fit to the experimental data using a non-linear least-squares fitting program.

Fig. 4.1 shows the experimental data (dotted line) and calculated fit (solid line) for the reflectivity of the substrate. We can see from the data that the region of total external reflection extends up to the critical angle of 2θ=0.42° ($q_z = 0.03$ Å^{-1}). The reflectivity in this region is less than unity due to the footprint correction, as explained in sec. 3.4.3. Above the critical angle there is a rapid fall-off in the reflectivity which for ideal surfaces follows $\approx q_z^{-4}$ according to Fresnel's equation 2.14, and drops even faster for rough surfaces. This means that the reflectivity measurement must be made very near and above the critical angle and that the measurement must have a very large dynamic range, spanning many orders of magnitude of reflectivity.

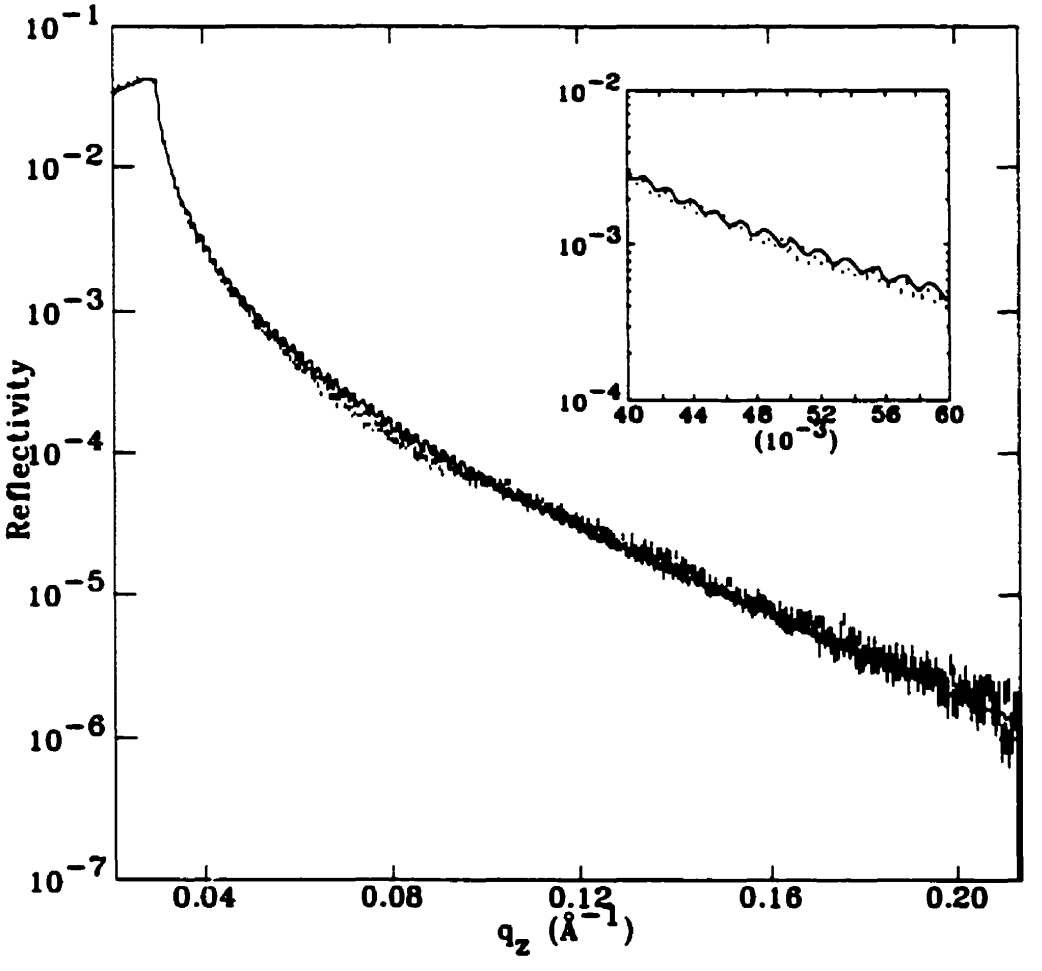

Figure 4.1: Si/SiO_2 substrate reflectivity data (dotted line) and fit (solid line).

As we can see from the inset, the wiggles in the experimental data are very weak because the 3000 Å SiO_2 layer is too thick to be well resolved by our setup. In fact, any thickness between 3000 Å and 5000 Å gives almost the same fit. The error of 6.43 Å in the thickness obtained from the fit is an artifact of the fitting process. In fact the error should be much larger than that. We have chosen the 3000 Å value for the thickness because it is the approximate value known from the thermal oxidation process. This choice of SiO_2 thickness does not affect the subsequent fits for the samples which are deposited on this type of substrate.

There is a small discrepancy between the experimental data and the calculated fit which shows that more work could be done to refine our model. In fact a large number of studies concerning the structure and reactivity of the Si/SiO_2 interface have been performed. First, concerning the structure of the oxide film in the interfacial region where the chemical bonding transition from crystalline Si to amorphous SiO_2 occurs, these studies suggest the existence of an interfacial layer approximately 10 Å thick, and perhaps a thicker layer up to 50 Å of suboxide formation and compressed SiO_2. The thickness and density of this suboxide region depends sensitively on the preparation conditions of the oxide and subsequent annealing procedures [138, 139].

Second, the roughness of the Si/SiO_2 and SiO_2/vacuum interfaces have been examined by x-ray reflectivity as well as by other techniques. It was found that interfacial roughness is mostly a function of substrate preparation and that thermal oxidation of Si leads to an abrupt Si/SiO_2 interface [140, 141]. For thermally oxidized Si samples, Woronick et al. [142] measured surface roughnesses of 1.0 to 10 Å for films ranging from 120 to 1200 Å thick. Herald et al. [143] and Chason et al. [144] measured a surface roughness of about 4.0 Å for 300 to 500 Å thick thermally grown films. SiO_2 surfaces smoother than about 3.0 Å have not been observed.

This shows that we might need to include an intermediate layer in our model in order to obtain a better fit, but nevertheless we obtained an abrupt Si/SiO_2 interface, and our surface roughness of 6.67 Å agrees well with the results of other studies. Since the study of Si/SiO_2 structure in itself is not the purpose of the present thesis and

Layer	Thickness (Å)	Roughness (Å)	ρ_e^f ($e^-/Å^3$)	ρ_e^c ($e^-/Å^3$)	μ (cm^{-1})
SiO_2	3006±6	6.67±0.09	0.664±0.001	0.648	113.54
Si	–	10±3	0.709±0.006	0.710	173.75

Table 4.1: Parameters of the substrate obtained from fitting the reflectivity data.

our fit results agree generally well with other studies, we will consider the present model to be suitable enough to represent our substrate.

The parameters obtained from the fit and the calculated electron densities are given in table 4.1 where ρ_e^f is the electron density of the layer obtained from the fit, ρ_e^c is the calculated electron density and μ is the calculated absorption coefficient. The experimental and theoretical electron densities of Si agree within the experimental error while those of SiO_2 differ by 0.016 $e^-/Å^3$ which is beyond our experimental error. The parameters obtained from the fit are used in subsequent fits for samples which are deposited on the same type of substrate. From these parameters we can construct the electron density profile for the substrate, which is shown in fig. 4.2.

4.2 *Interface profile functions*

In this section we attempt to answer the question of how to model the interfaces of our samples? For this purpose we test four possible representations for the interface profile by using them to fit the reflectivity data of the Ni single layer. These representations are the error-function interface, the linear interface, the tanh interface and the arc-tan interface. From each fit we obtain the parameters of the different layers then plot the electron density profile for the sample. The results are shown for each interface profile function. From the fits we determine the type of interface function that gives us the best agreement with the experimental data.

The Ni sample is deposited on Si/SiO_2 substrate as discussed in sec. 3.1, then irradiated with 1 MeV Si^+ ions to doses of 2×10^{14} and 1×10^{15} ions/cm^2, as discussed in sec. 3.2. The data presented below was collected by measuring a mesh and fitting the ω-scan at each 2θ value to an equal-width Gaussian-Lorentzian lineshape

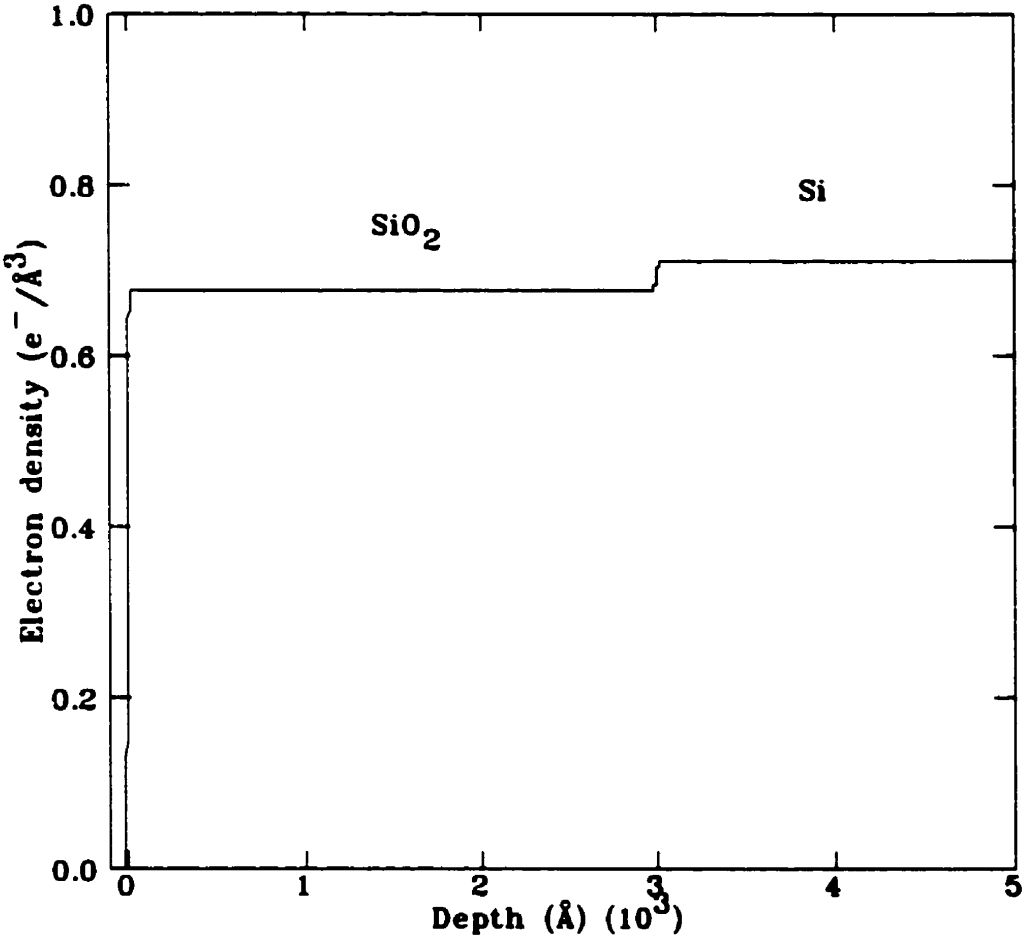

Figure 4.2: Electron density profile for the Si/SiO_2 substrate constructed from the fit parameters given in table 4.1.

Layer	ρ_e^f ($e^-/Å^3$)	ρ_e^c ($e^-/Å^3$)	μ (cm^{-1})
NiO	1.76±0.04	1.81	282.24
Ni	2.22±0.02	2.27	475.65

Table 4.2: The electron densities and absorption coefficients of Ni and NiO.

as discussed in sec. 3.3.2 in order to obtain the absolute reflectivity and to separate the diffuse scattering component.

The model used to fit the Ni reflectivity data consists of four layers, the substrate Si, followed by the SiO_2 layer, then the single layer of Ni and finally an oxide layer on the top. The main fitting parameters are the thickness, the roughness, the electron density and the absorption coefficient of the different layers. We use the substrate parameters given in table 4.1. The NiO and Ni electron densities are first calculated then fit for the as-deposited sample and kept constant for the irradiated ones. For the absorption coefficients we use the calculated values since we have found that the fit is not very sensitive to the change in these values.

4.2.1 Error-function interface

The first function tested for the interface region is the error-function representation. Figure 4.3 shows the experimental data and the calculated fits for the Ni as-deposited sample and the two irradiated samples using an error-function interface profile. We can see that the fits agree reasonably well with the experimental data.

The calculated values for the Ni and NiO electron densities and absorption coefficients (ρ_e^c and μ) together with the electron density values obtained from the fit (ρ_e^f) are given in table 4.2. The NiO electron densities almost agree within the experimental error, while the Ni electron densities differ by only 0.05 $e^-/Å^3$ but do not agree within the estimated error of ±0.02 $e^-/Å^3$. The thickness and roughness of the different layers obtained from these fits are listed in table 4.3. For this type of interface function, the SiO_2 roughness is allowed to vary during the fit to represent the interdiffusion at the SiO_2/Ni interface.

As mentioned earlier, three Ni samples are deposited on the same piece of substrate

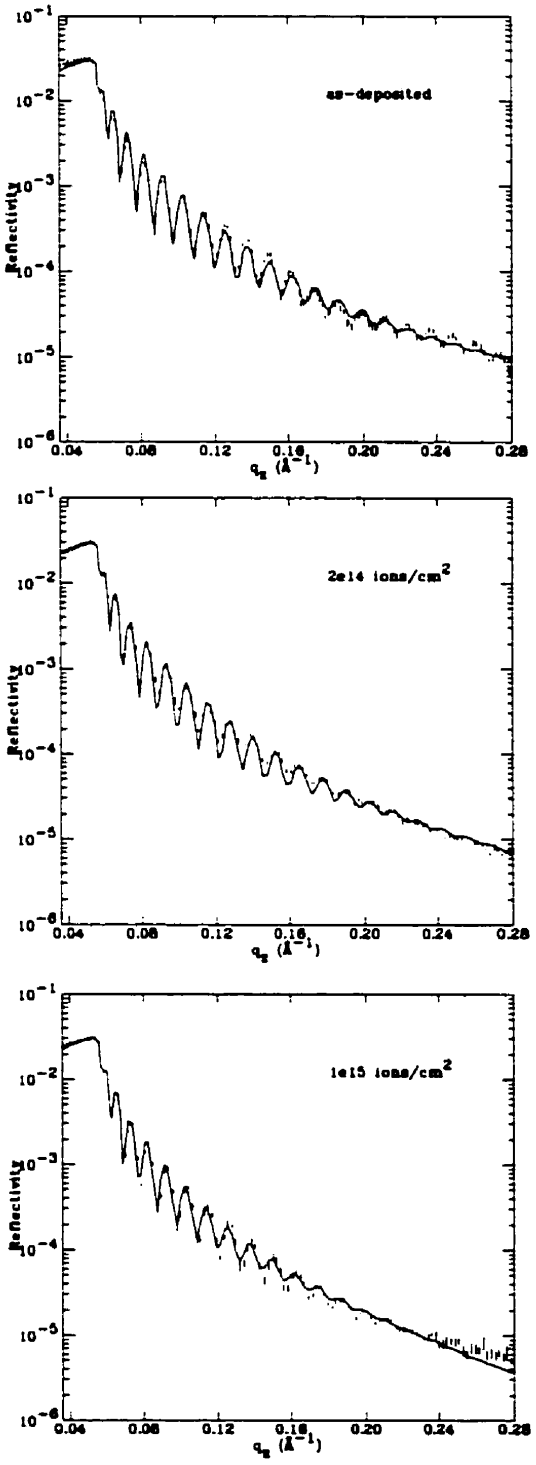

Figure 4.3: Fits (solid line) to $Si/SiO_2/Ni(500Å)$ reflectivity data (dotted line) before and after irradiation to two different irradiation doses using error-function interface profile.

Parameter	as-deposited	2×10^{14} ions/cm^2	1×10^{15} ions/cm^2
NiO thickness (Å)	7±3	8±3	8±2
NiO roughness (Å)	1.7±0.4	2.6±0.8	3.9±0.1
Ni roughness (Å)	9±3	12±5	16±2
SiO_2 roughness (Å)	11.5±0.3	11.5±0.8	14.4±0.8

Table 4.3: Parameters of the Si/SiO_2/Ni(500Å) sample before and after irradiation obtained from fitting the reflectivity data using an error-function interface profile.

and two of them are irradiated to the different ion doses. These two samples are found to have a slightly different thickness for the Ni layer. The thicknesses obtained from the fits are 468±1Å and 458±3Å. The centers of these samples are 12 mm apart, giving a thickness gradient of 0.847Å/mm.

From the parameters given in table 4.3 it is found that the roughness of the different layers increases with increasing the irradiation dose. The electron density profile is calculated using these parameters and is plotted in fig. 4.4. Figure 4.4(a) shows the electron density profile for the SiO_2/Ni interface and the Ni/NiO interface. It is seen that there is a slight change in the electron density profile upon irradiation. In figure 4.4(b) it is shown that there is some intermixing between the Ni and NiO layers at the interface, this intermixing increases with the irradiation dose. For the SiO_2/Ni interface, no change is obvious at the low irradiation dose of 2×10^{14} ions/cm^2 but the intermixing increases at the higher dose of 1×10^{15} ions/cm^2 as shown in fig. 4.4(c).

4.2.2 Linear interface

There are three interfaces in our model, the Si/SiO_2, the SiO_2/Ni and the Ni/NiO interfaces. Since we suspect and want to verify the interdiffusion between the bulk material and the substrate at the SiO_2/Ni interface upon irradiation, this interface representation is changed to the different function shapes to test their effect on the fit.

The material/oxide interface is always represented in our fits by an error function because it is most probably a rough interface with a random distribution of heights in

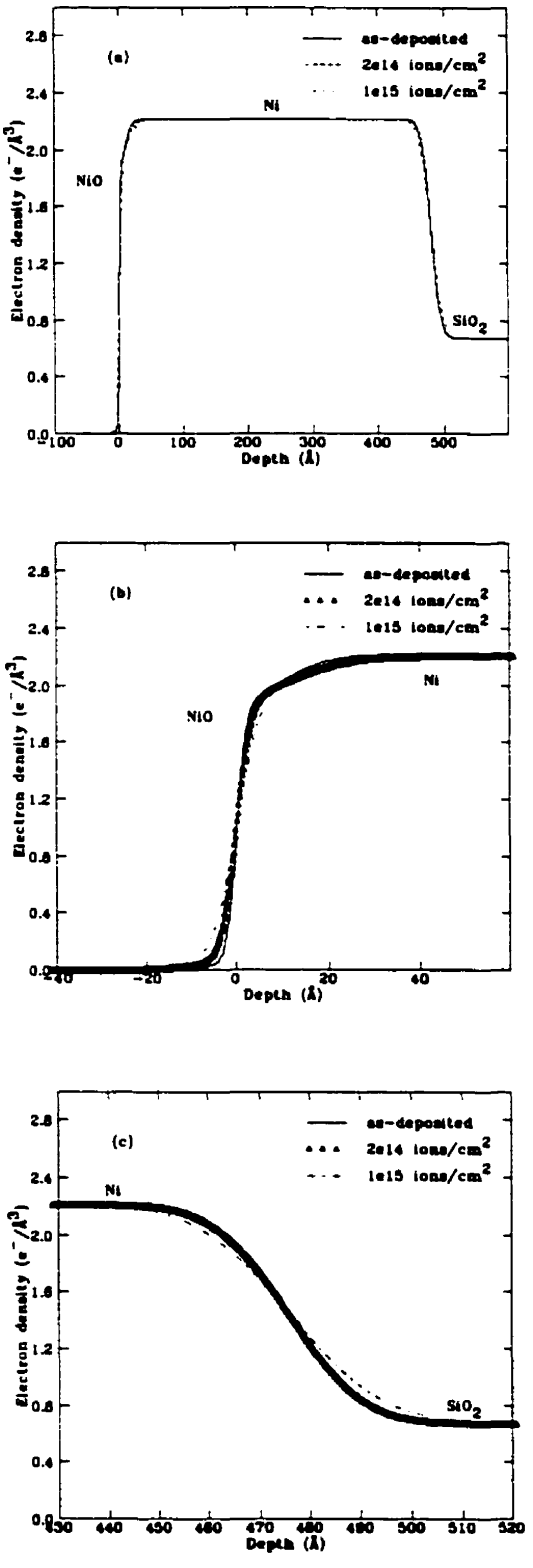

Figure 4.4: Electron density profile of $Si/SiO_2/Ni(500Å)$ using error function interface: a) $SiO_2/Ni/NiO$ interfaces; b) Ni/NiO interface; c) SiO_2/Ni interface.

x and y and is best represented by this type of function. Also we always represent the Si/SiO_2 interface by an error function and use the parameters obtained from fitting the substrate reflectivity data. Effectively, the fit is not sensitive to the roughness of the Si layer, as will be discussed shortly.

Therefore, in the following fits we change the representation of the SiO_2/Ni interface only. In the present section, this interface is represented by a linear function profile. This linear function is simulated in our model by dividing the interface into 10 sections of equal thickness and using an average electron density at each step, as discussed in sec. 3.4.2 and shown in fig. 3.12(a). We chose to limit the number of steps to 10 because when this number was increased no noticeable change in the fit was observed. Hence, we keep the number of steps at the smallest possible number which produces no significant change in the calculated fit in order to limit the number of simulated layers in our model thus minimizing the fitting time. (Note that here only the interface is divided into N steps whereas in fig. 3.12(a) the whole sample thickness was divided into linear steps, therefore the present number of steps N is much smaller).

Fig. 4.5 shows the fit to the same experimental data of the Ni sample using the SiO_2/Ni linear interface profile. We can see that we do not obtain excellent fits as we did using the error-function interface profile. The fit using a linear interface shows large dips in the calculated reflectivity which are not seen in the experimental data. Knowing that our resolution is high enough so that we could see such dips in the experimental data if they really existed, we conclude that those dips originate from our model because of the discontinuity in the linear interface profile.

The obtained parameters are listed in table 4.4, the SiO_2/Ni interface parameter represents the thickness of the linear interface between the SiO_2 and the Ni layers. Comparing the parameters given in tables 4.3 and 4.4 we find that the NiO thickness and roughness have much higher values using the linear interface profile than using the error-function profile. We should however obtain almost the same parameters since the Ni/NiO interface is represented by an error function in both cases. This is

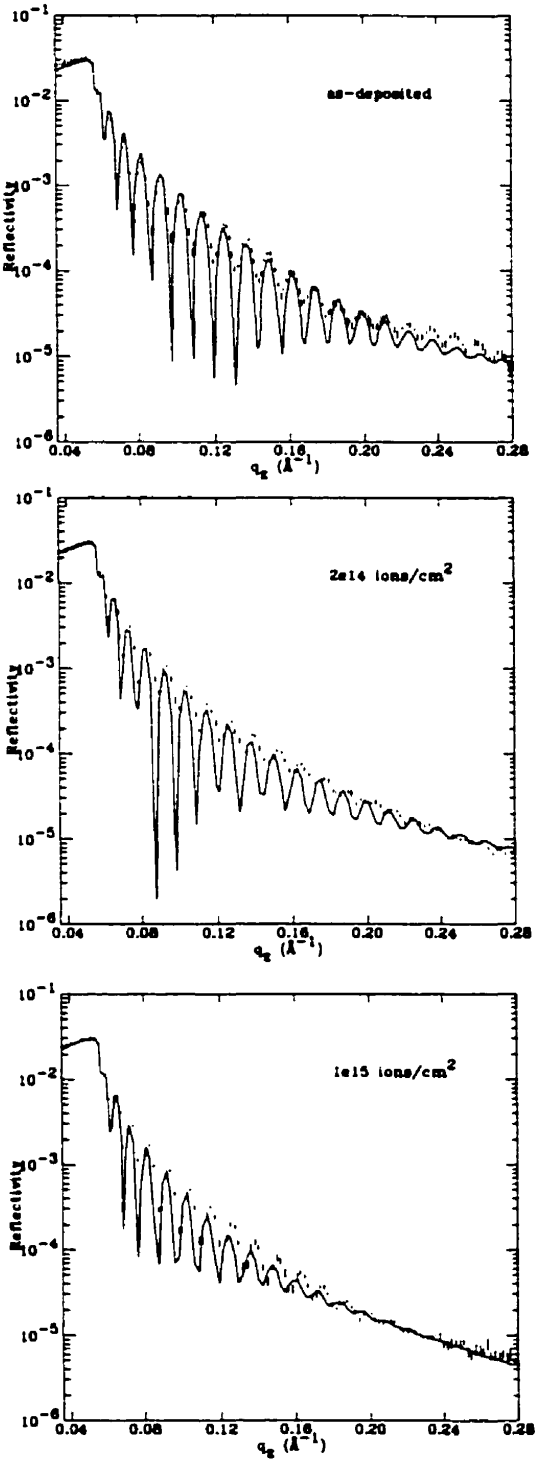

Figure 4.5: Fits (solid line) to Si/SiO_2/Ni(500Å) reflectivity data (dotted line) using linear interface profile.

Parameter	as-deposited	2×10^{14} ions/cm^2	1×10^{15} ions/cm^2
NiO thickness (Å)	10±2	18±2	18±4
NiO roughness (Å)	9.2±0.4	10.4±0.6	13.8±0.9
Ni roughness (Å)	8±2	14±5	14±5
SiO_2/Ni interface (Å)	0.0	3.86±0.0002	9.5±0.5

Table 4.4: Parameters of the Si/SiO_2/Ni(500Å) sample before and after irradiation obtained from fitting the reflectivity data using a linear function interface profile.

an artifact of the fit, the least-squares fitting procedure attempts to improve the dips and minimize the χ^2 parameter by increasing the NiO thickness and roughness.

The electron density profile is calculated using these parameters and is plotted in fig. 4.6. Again, we have increased intermixing at the Ni/NiO interface upon increasing the irradiation dose as shown in fig. 4.6(b). By comparing figures 4.4(c) and 4.6(c) we see that the obtained electron density profile depends on the chosen interface model.

4.2.3 *Hyperbolic-tangent and arc-tangent interfaces*

Two more interface profiles were tested for this sample. The fits to the Si/SiO_2/Ni(500Å) reflectivity data using a hyperbolic-tangent function and an arc-tangent function to represent the SiO_2/Ni interface profile are shown in figures 4.7 and 4.8, respectively. Again, the Si/SiO_2 and the Ni/NiO interfaces are represented by an error function. The tanh and the arc-tan interfaces are simulated by dividing the interface into 10 steps and using an average electron density at each step. The substrate parameters are taken from table 4.1 and the Ni and NiO electron densities and absorption coefficients are taken from table 4.2.

From these figures we can see large discrepancies between the experimental data and the calculated fits. The parameters obtained from the fits are given in tables 4.5 and 4.6, respectively. Once again, the least-squares fitting program attempts to improve the fit and reduce its χ^2 parameter by increasing the thickness and roughness of the NiO layer.

The electron density profiles are calculated using these parameters and are plotted

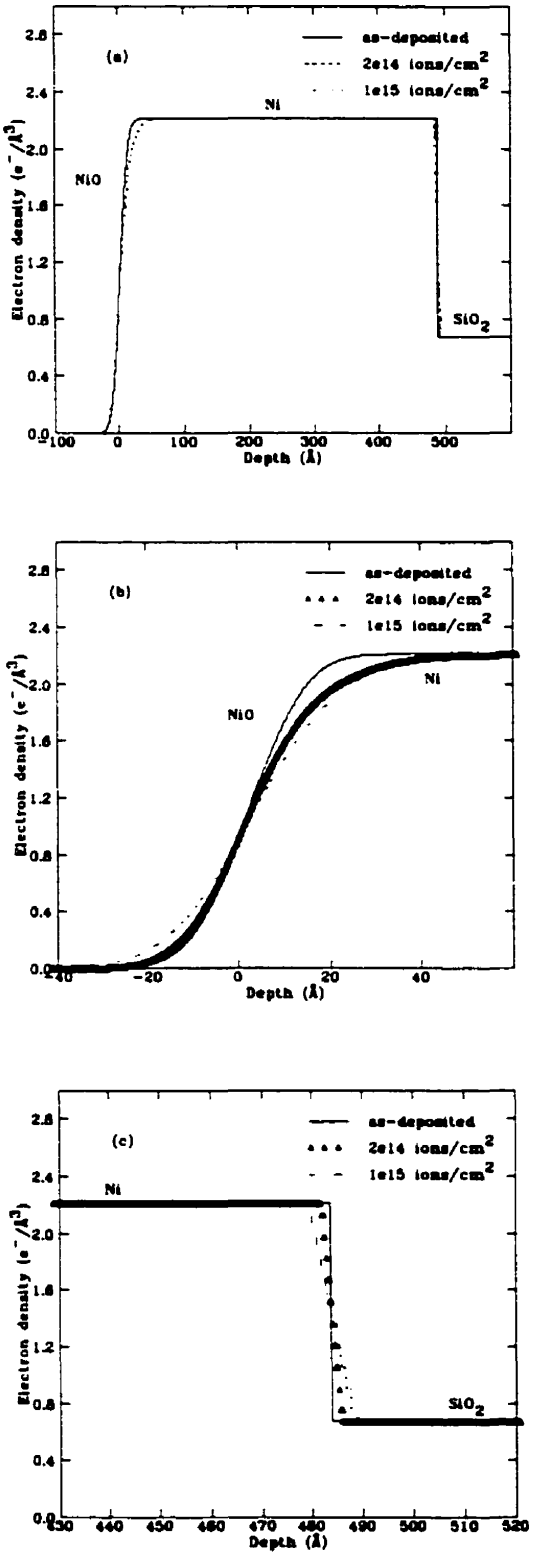

Figure 4.6: Electron density profile of $Si/SiO_2/Ni(500Å)$ using linear function interface: a) $SiO_2/Ni/NiO$ interfaces; b) Ni/NiO interface; c) SiO_2/Ni interface.

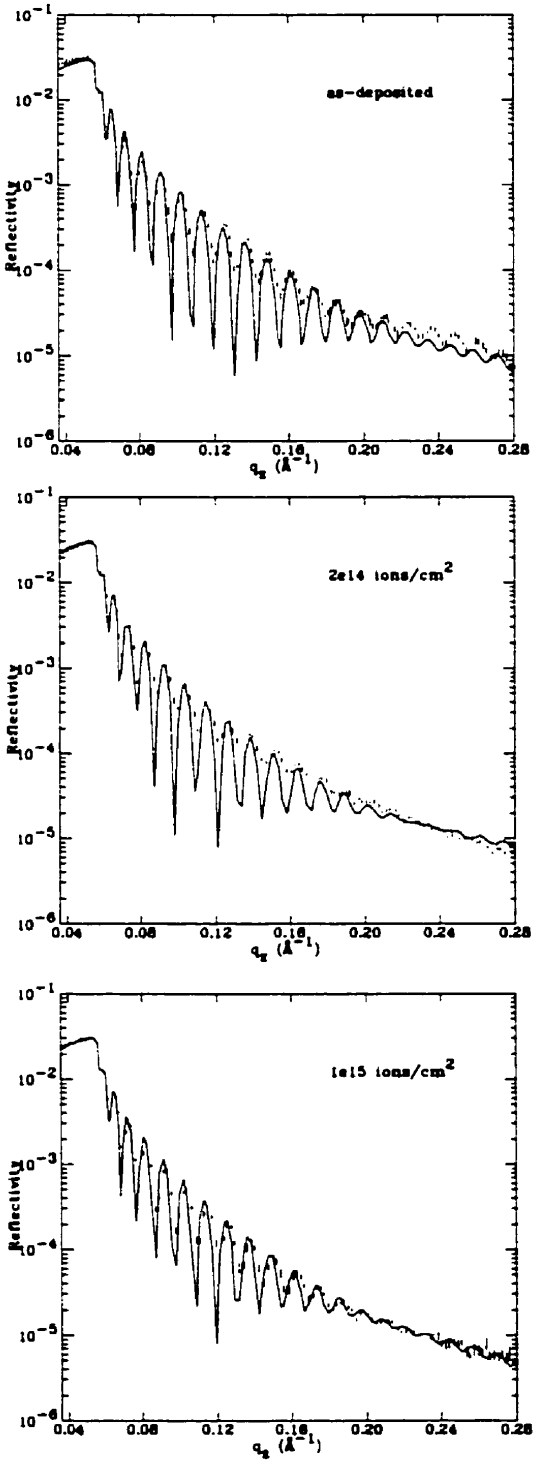

Figure 4.7: Fits (solid line) to $Si/SiO_2/Ni(500Å)$ reflectivity data (dotted line) using tanh interface.

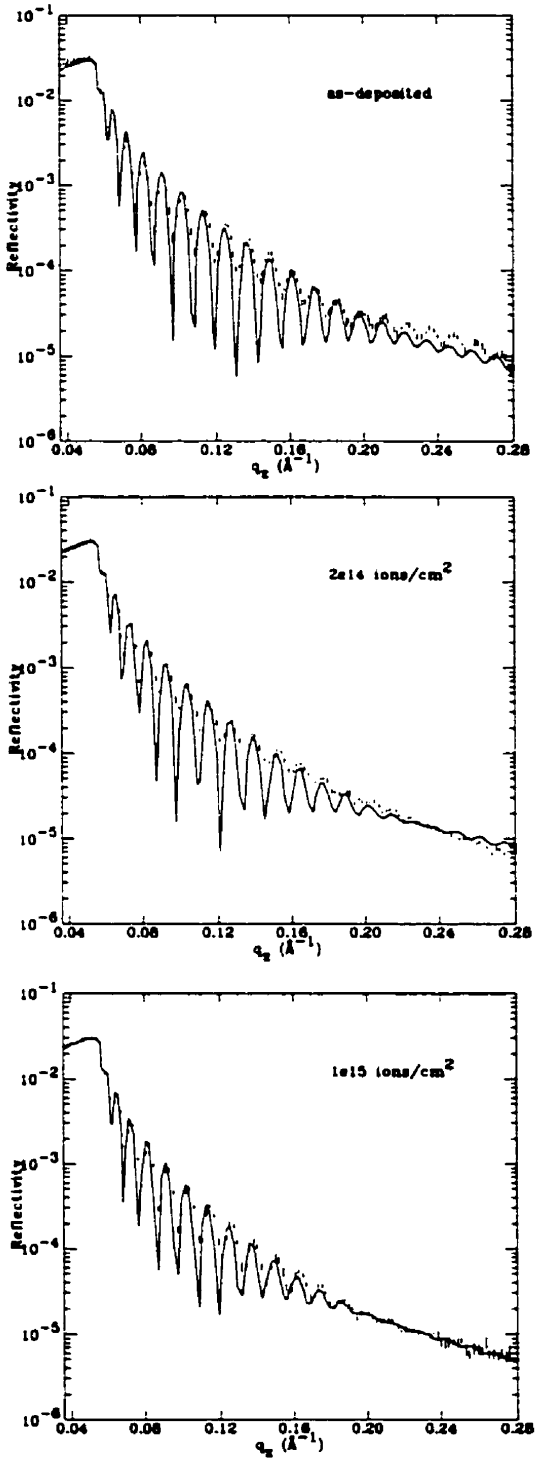

Figure 4.8: Fits (solid line) to $Si/SiO_2/Ni(500Å)$ reflectivity data (dotted line) using arc-tan interface.

Parameter	as-deposited	2×10^{14} ions/cm^2	1×10^{15} ions/cm^2
NiO thickness (Å)	14±1	14±1	16±1
NiO roughness (Å)	8.1±0.4	9.7±0.6	10.2±0.4
Ni roughness (Å)	5±1	7±1	7.3±0.4
SiO_2/Ni interface (Å)	3±1	3.7±0.8	29±2

Table 4.5: Parameters of the Si/SiO_2/Ni(500Å) sample before and after irradiation obtained from fitting the reflectivity data using a tanh function interface profile.

Parameter	as-deposited	2×10^{14} ions/cm^2	1×10^{15} ions/cm^2
NiO thickness (Å)	14±1	14±1	15±1
NiO roughness (Å)	8.1±0.5	9.7±0.6	11.9±0.7
Ni roughness (Å)	5±1	7±1	8.9±0.8
SiO_2/Ni interface (Å)	3±1	3.6±0.8	30±2

Table 4.6: Parameters of the Si/SiO_2/Ni(500Å) sample before and after irradiation obtained from fitting the reflectivity data using an arc-tan function interface profile.

in figures 4.9 and 4.10, respectively. Comparing parts (b) of these figures we can see the dependence of the Ni/NiO interface evolution on the specific functional form used to represent the interface profile.

From this survey of the four different interface profile functions we conclude that the calculated fit depends sensitively on the functional form used to represent the interface. The structure of our samples is best described using the error-function interface profile, therefore in all subsequent fits the interfaces will be represented by an error-function representation.

4.3 Single layers of Fe, Cu and Co

4.3.1 Single layers model

Following the method described in sec. 3.4 we use a model consisting of four layers in order to fit the Fe, Co and Cu reflectivity data. The layers represent the substrate Si followed by the SiO_2 layer, then the bulk material and finally an oxide layer at the

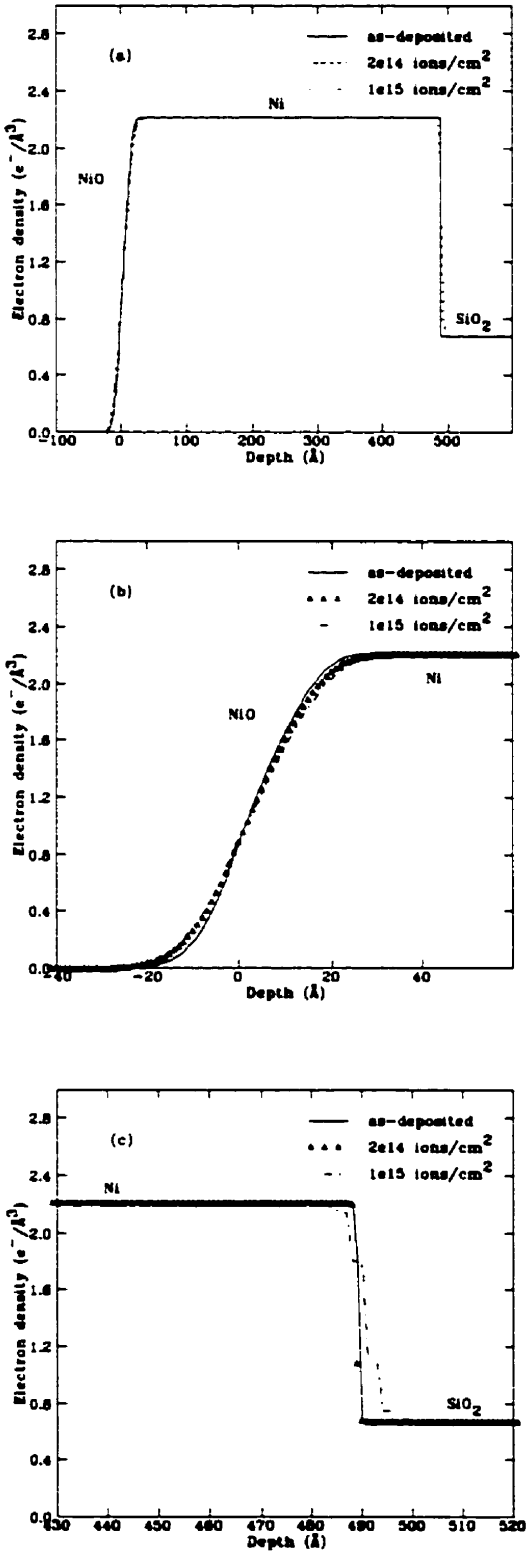

Figure 4.9: Electron density profile of $Si/SiO_2/Ni(500Å)$ using tanh interface: a) $SiO_2/Ni/NiO$ interfaces; b) Ni/NiO interface; c) SiO_2/Ni interface.

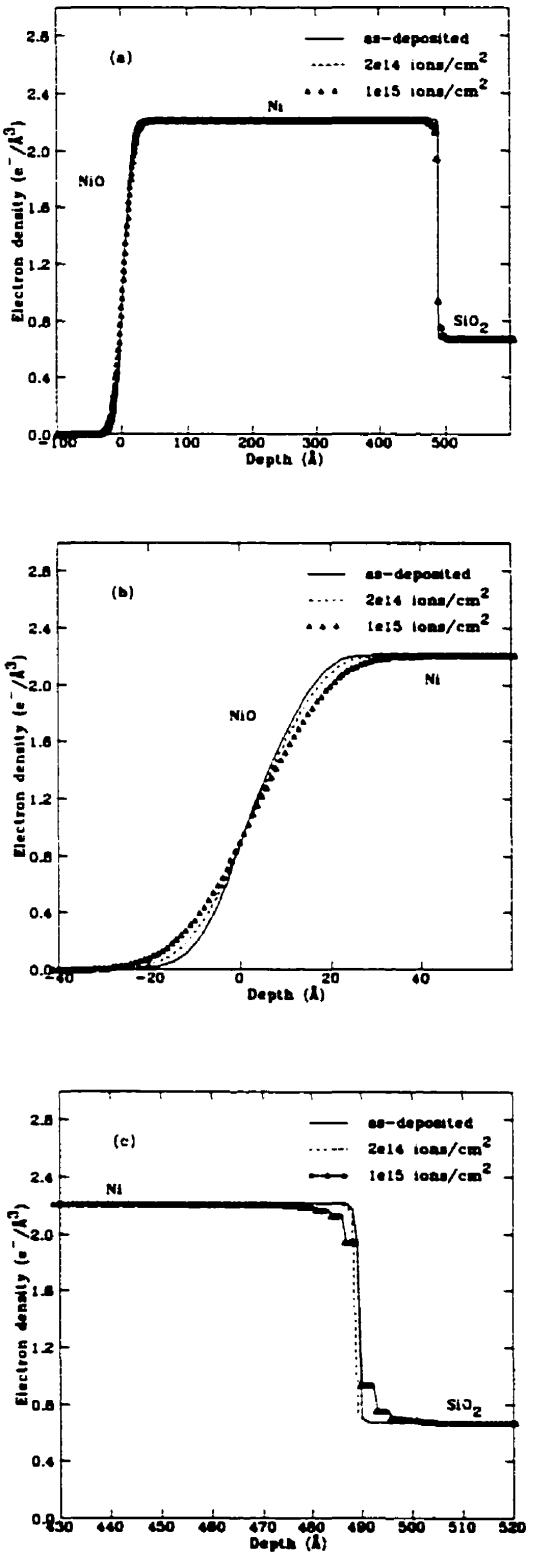

Figure 4.10: Electron density profile of $Si/SiO_2/Ni(500Å)$ using arc-tan interface: a) $SiO_2/Ni/NiO$ interfaces: b) Ni/NiO interface: c) SiO_2/Ni interface.

top.

The substrate parameters are fixed to their values given in table 4.1, except for the SiO_2 roughness whose variation represents its intermixing with the bulk material. The electron density values for the different layers are first calculated then fit for the as-deposited samples and kept constant, as much as possible, for the irradiated ones. We use the calculated values for the absorption coefficient of the different materials since it was found that the fits are not very sensitive to the change in these values.

As done previously for the Ni single layer, the reflectivity of each sample is measured by performing a mesh and fitting the ω-scan at each 2θ value to an equal-width Gaussian-Lorentzian lineshape as discussed in sec. 3.3.2 in order to obtain the absolute reflectivity and to separate the diffuse scattering component.

4.3.2 Discussion of the single layers results

The experimental data and calculated fits for the reflectivity of the Fe, Cu and Co samples at the different irradiation doses as well as the electron density profiles constructed from the fit parameters are shown in figures 4.11 to 4.16. The calculated values of the absorption coefficient (μ) and of the electron density (ρ_e^c) are tabulated together with the electron density values obtained from the fits (ρ_e^f), and the thickness and roughness parameters of the different layers are given in tables 4.7 to 4.12.

From the experimental data we can see that we obtain very good oscillations in our reflectivity curves over a range that covers four orders of magnitude, down to reflectivity values in the order of 10^{-6}. This is due to several factors. First, by tightening the energy window of the pulse height analyzer we were able to reduce the dark counts so that we can detect weaker signals, as explained in section 3.3. Second, by using the data acquisition method explained in section 3.3.2 we were able to separate the diffuse scattering component from the specular component. We obtained the normalized reflectivity data which also helped in reducing the fitting parameters by one, because the intensity now remains fixed during the fits.

In general, the calculated fits agree reasonably well with the experimental data. From fig. 4.11 we can see that the shape of the reflectivity curves for Fe is different from

the other samples. There is a long wavelength fringe superimposed on the reflectivity curve. This is due to the presence of the surface iron oxide layer. It causes an obvious kink in the data which starts at around $q_z \approx 0.16$ Å^{-1} for the as-deposited sample and moves to smaller q_z values as the irradiation dose increases.

Also, from fig. 4.12(b) we can see that for the as-deposited sample and the sample irradiated at 2×10^{14} ions/cm^2 the oxide layer electron density is close to the calculated FeO electron density, while at the higher irradiation level of 1×10^{15} ions/cm^2 the oxide layer electron density decreases to approach the calculated electron density of Fe_3O_4, as given in table 4.7.

For the Cu sample we note that the Cu layer roughness decreases as the irradiation dose increases, as given in table 4.10, contrary to the behaviour of the other samples. Also, the oxide layer thickness increases noticeably at the higher irradiation dose of 1×10^{15} ions/cm^2. As seen from fig. 4.13, at the higher irradiation dose the fit to the reflectivity data is not very good from the 3rd to the 6th peak. We obtain some large dips which were accounted for by the fitting routine by abruptly decreasing the Cu layer roughness and increasing the oxide layer thickness significantly. These changes are only artifacts of the fitting process and do not represent the real changes occurring in the sample.

Another artifact of the fitting process is seen in the Co sample results. As seen from table 4.12 and figures 4.16(b) and 4.16(c) both the Co roughness and the SiO_2 roughness decrease dramatically at the higher irradiation dose. We can notice the bad fit at the 4th peak in fig. 4.15 at the high-irradiation dose which is responsible for these sudden drops in the roughness values.

But in general the common trend observed from the fits is that the roughness of the different layers increases with increasing the irradiation dose, which represents more intermixing at the interfaces. No change in the bulk materials electron density was observed upon irradiation at the present doses.

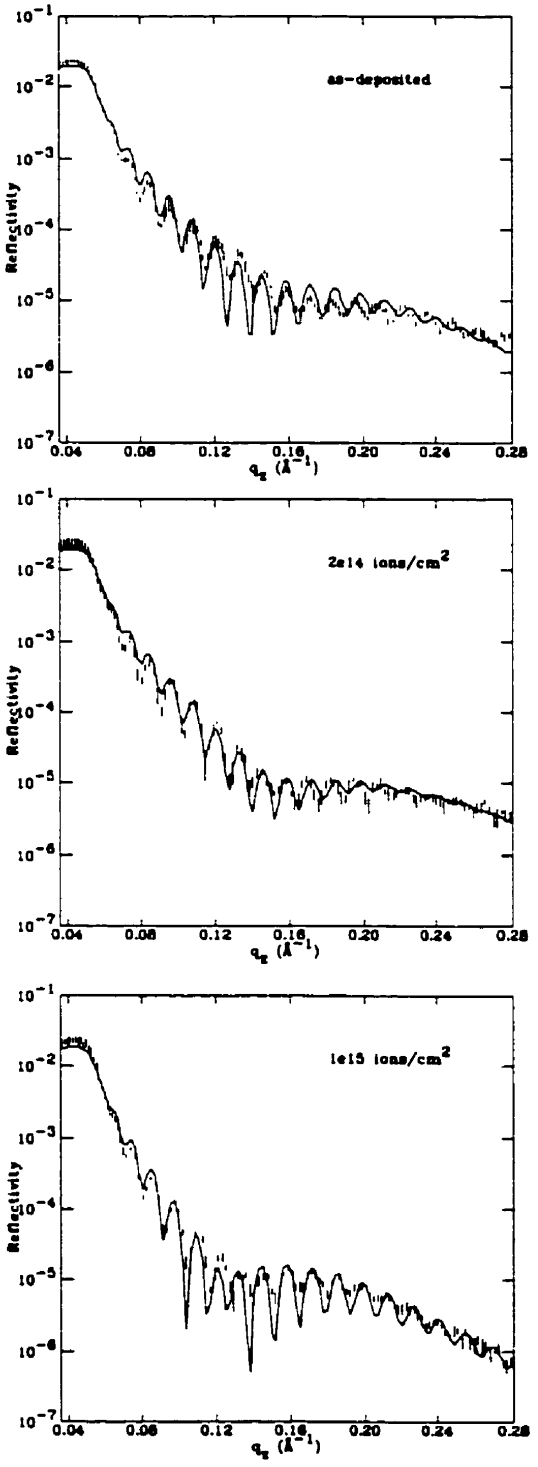

Figure 4.11: Fits (solid line) to $Si/SiO_2/Fe(500Å)$ reflectivity data (dotted line) at the different irradiation doses.

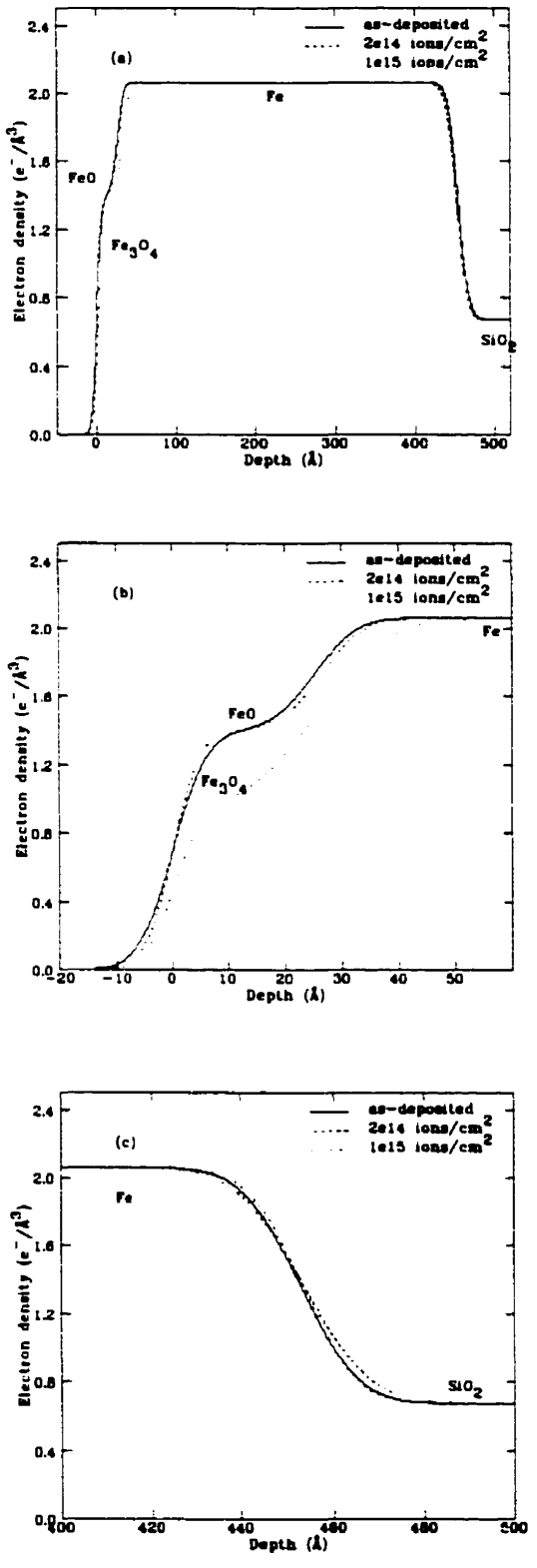

Figure 4.12: Electron density profile of $Si/SiO_2/Fe(500Å)$ single layer: a) $SiO_2/Fe/Fe$-oxide interfaces; b) Fe/Fe-oxide interface; c) SiO_2/Fe interface.

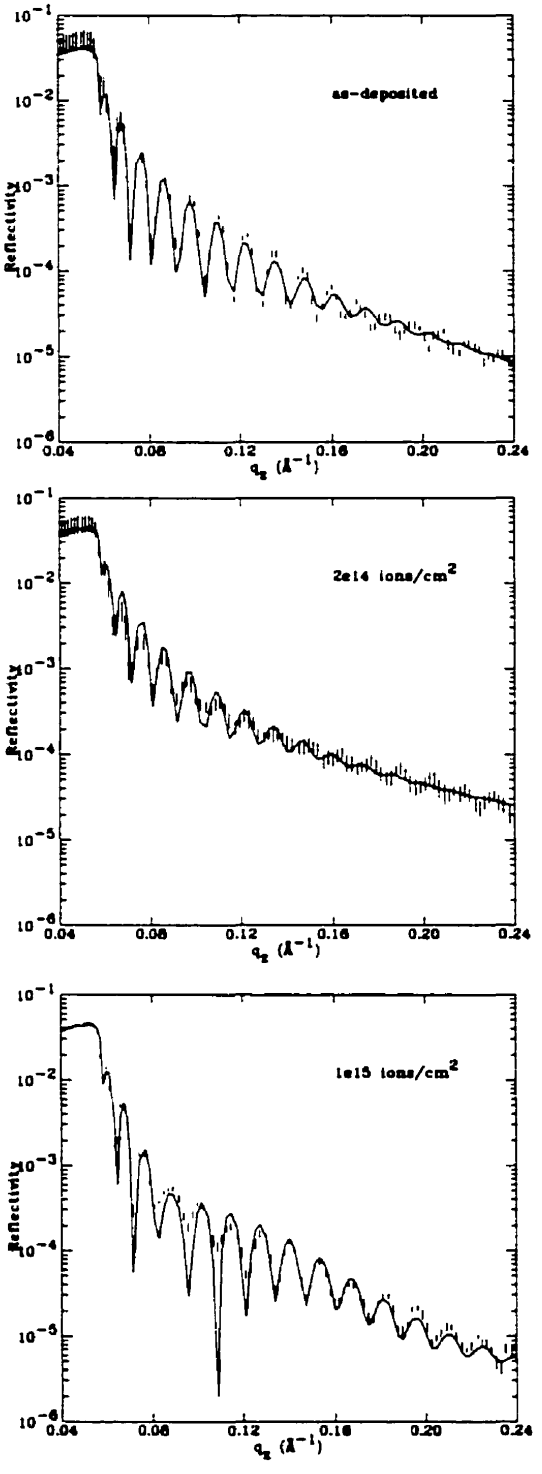

Figure 4.13: Fits (solid line) to $Si/SiO_2/Cu(500Å)$ reflectivity data (dotted line) at the different irradiation doses.

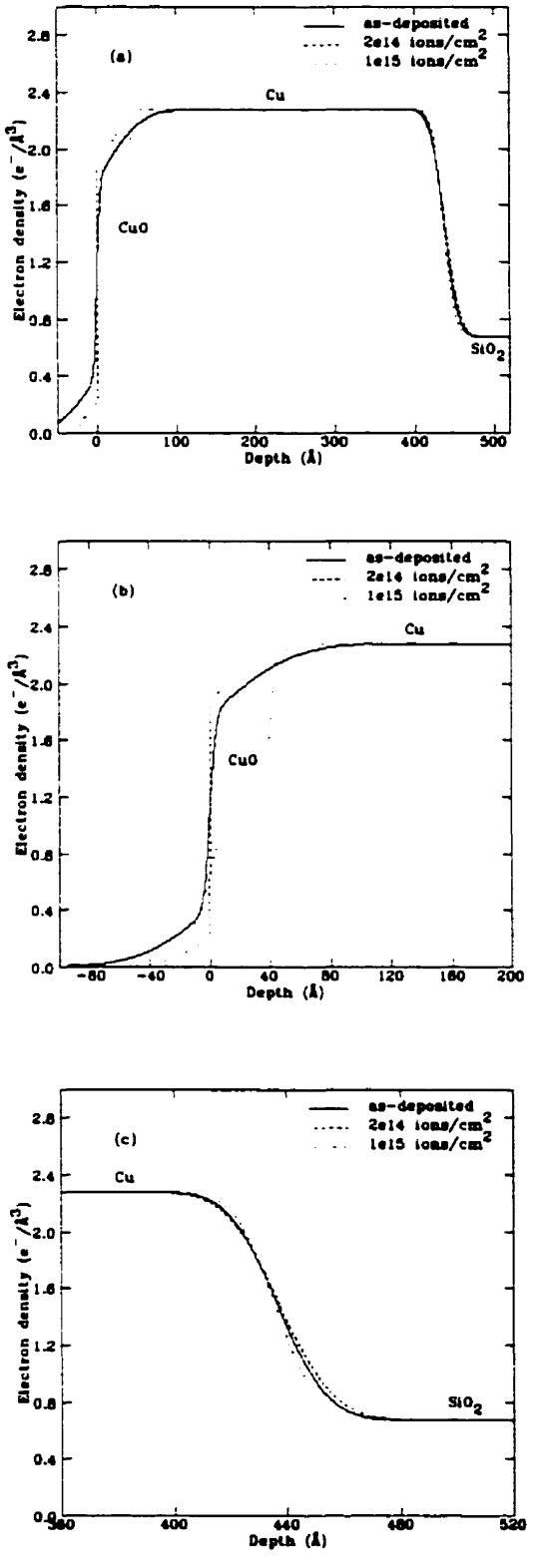

Figure 4.14: Electron density profile of $Si/SiO_2/Cu(500Å)$ single layer: a) $SiO_2/Cu/CuO$ interfaces; b) Cu/CuO interface; c) SiO_2/Cu interface.

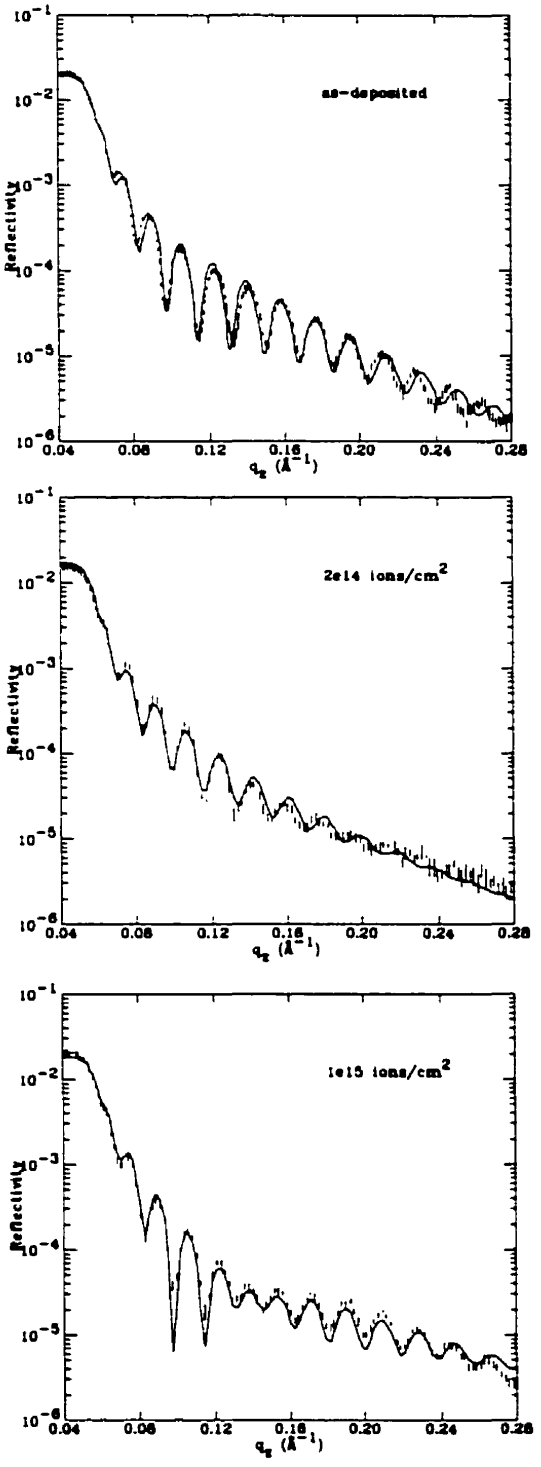

Figure 4.15: Fits (solid line) to $Si/SiO_2/Co(500Å)$ reflectivity data (dotted line) at the different irradiation doses.

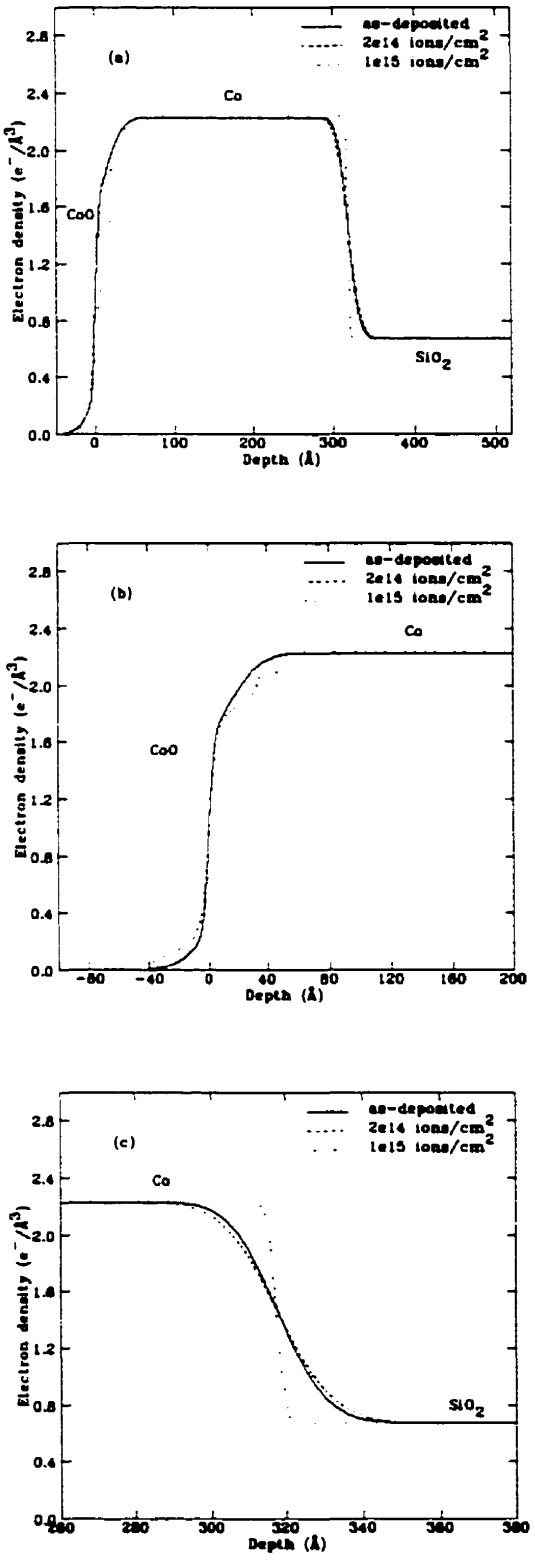

Figure 4.16: Electron density profile of $Si/SiO_2/Co(500Å)$ single layer: a) $SiO_2/Co/CoO$ interfaces: b) Co/CoO interface: c) SiO_2/Co interface.

Layer	ρ_e^f ($e^-/Å^3$)	ρ_e^c ($e^-/Å^3$)	μ (cm^{-1})
FeO	1.4±0.1	1.23	1500.80
Fe_3O_4	0.9±0.2	0.72	600.20
Fe	2.06±0.04	2.11	2501.91

Table 4.7: The electron densities and absorption coefficients of Fe and iron oxides.

Parameter	as-deposited	2×10^{14} ions/cm^2	1×10^{15} ions/cm^2
FeO thickness (Å)	25±1	26±1	–
FeO roughness (Å)	5±1	4±1	–
Fe_3O_4 thickness (Å)	–	–	25.4±0.4
Fe_3O_4 roughness (Å)	–	–	4.1±0.3
Fe roughness (Å)	6±2	6±2	9.9±0.6
SiO_2 roughness (Å)	10±1	12±1	9.4±0.4

Table 4.8: Parameters of the Si/SiO_2/Fe(500Å) sample before and after irradiation obtained from fitting the reflectivity data.

Layer	ρ_e^f ($e^-/Å^3$)	ρ_e^c ($e^-/Å^3$)	μ (cm^{-1})
CuO	1.35±0.03	1.31	174.80
Cu	2.29±0.02	2.28	515.96

Table 4.9: The electron densities and absorption coefficients of Cu and CuO.

Parameter	as-deposited	2×10^{14} ions/cm^2	1×10^{15} ions/cm^2
CuO thickness (Å)	5±1	10±3	41.8±0.7
CuO roughness (Å)	3.4±0.1	4.1±0.2	12.6±0.5
Cu roughness (Å)	39±4	27±6	2.9±0.2
SiO_2 roughness (Å)	13.7±0.4	15.1±0.7	11.4±0.5

Table 4.10: Parameters of the Si/SiO_2/Cu(500Å) sample before and after irradiation obtained from fitting the reflectivity data.

Layer	ρ_e^f (e$^-$/Å^3)	ρ_e^c (e$^-$/Å^3)	μ (cm^{-1})
CoO	1.26±0.05	1.30	1539.69
Co	2.23±0.02	2.25	3079.37

Table 4.11: The electron densities and absorption coefficients of Co and CoO.

Parameter	as-deposited	2×10^{14} ions/cm^2	1×10^{15} ions/cm^2
CoO thickness (Å)	8±2	14.3±0.9	23.7±0.4
CoO roughness (Å)	3.9±0.2	4.1±0.1	9.6±0.3
Co roughness (Å)	18.6±0.8	29.8±0.9	9.9±0.3
SiO_2 roughness (Å)	9.1±0.3	12.1±0.3	2.1±0.2

Table 4.12: Parameters of the Si/SiO_2/Co(500Å) sample before and after irradiation obtained from fitting the reflectivity data.

4.4 Bilayers of Ni/Fe and Co/Cu

4.4.1 Bilayers model

Our main objective is to study the effect of MeV ion irradiation on the structure of magnetic multilayers of Ni/Fe and Cu/Co, and hence understand the changes in the giant magnetoresistance (GMR) and in the magnetotransport properties of these multilayers which occur upon ion irradiation. Most of these changes occur at the interfaces between the different layers, hence our model has to include each layer represented individually in order to study in detail the structural changes occurring at the interfaces. Since a multilayer consists of a bilayer repeated N times, where N=11 for our Ni/Fe samples [28] and N=30 for our Co/Cu samples [40, 41], and since each layer is represented in our model by four parameters, this will produce a very large number of parameters in our model and the fit will not be reliable at all. Normally to study a multilayer one assumes that it consists of identical bilayers and models only one bilayer repeated N times with the same parameters. In order to obtain more detailed interface structure information we will study only individual bilayers of these materials. This will allow us to minimize the number of parameters while obtaining a clearer picture of the interface profiles.

For this purpose bilayers were prepared with the configurations Si/SiO_2/ Fe(2000Å)/ Ni(100Å), Si/SiO_2/Ni(2000Å)/Fe(100Å), Si/SiO_2/Co(2000Å)/Cu(100Å) and Si/SiO_2/ Cu(2000Å)/Co(100Å). The bilayers were deposited on the same type of thermally-oxidized Si substrate as three distinct samples of each configuration on the same piece of substrate, one of which was kept as-deposited and the other two were irradiated by 1 MeV Si^+ ions to doses of 2×10^{14} and 1×10^{15} ions/cm^2. The samples were characterized by low-angle x-ray reflectivity measurements and x-ray diffuse scans at each stage of irradiation.

In order to fit the x-ray reflectivity data our model is essentially the same as for the single layers, with the addition of one extra layer. The substrate parameters are again taken from table 4.1 and the calculated values for the absorption coefficients (μ) and the electron density values (ρ_e^f) obtained from the previous fits for the different

materials are taken from tables 4.2, 4.7, 4.9 and 4.11. These values are kept fixed and only the thickness and roughness of the different layers are varied during the fit. These measures are taken in order to minimize the number of fit parameters and to obtain more reliable fits.

4.4.2 Discussion of the bilayers results

The reflectivity data and fits for the four Ni/Fe and Co/Cu bilayers together with the electron density profiles constructed from them are shown in figures 4.17 to 4.24. Tables 4.13 to 4.16 list the various thickness and roughness parameters obtained from the fits.

From our bilayers survey we can see that changing the deposition sequence gives different results. For the Fe/Ni bilayers, having the Fe layer on the top causes the appearance of some peaks which don't exist for the opposite deposition sequence. These peaks are difficult to fit which suggests that they might originate from some iron oxides which are not taken into account in our model. We modeled the oxide by only one layer of a particular thickness and electron density while there could be more than one iron oxide layer formed. Adding another layer of oxide with different electron density might help the fit at the expense of increasing the number of fit parameters. The obtained fits are reasonable enough and so no change in the model will be introduced.

For the $Si/SiO_2/Fe(2000Å)/Ni(100Å)$ bilayer very small changes occur upon irradiation. The oxide layer electron density was found to be 1.84 ± 0.07 $e^-/Å^3$ which agrees well with the calculated value for the NiO electron density of 1.81 $e^-/Å^3$ within the experimental error. As we can see from table 4.13 the Ni layer roughness is very high compared to its thickness, namely a roughness of 30 Å for a thickness of 77.45 Å. The effect of this very high roughness is seen in the electron density profile of fig. 4.18(c) where the effective Ni electron density is reduced from 2.22 to around 2.18 $e^-/Å^3$ for the as-deposited sample and even to less than 2.16 $e^-/Å^3$ for the irradiated samples. This effect of high roughness was discussed in sec. 3.4.2 and was shown in fig. 3.14.

For the oppositely-deposited sample, the oxide layer electron density was found to

be 1.21±0.02 $e^-/Å^3$ which is close to the calculated value of the FeO electron density of 1.23 $e^-/Å^3$ and agrees with it within the experimental error. Another artifact of the fit occurs at the higher irradiation dose as we notice a decrease in the FeO layer roughness and a sudden increase in the Fe layer roughness as given in table 4.14.

For the Co/Cu bilayers more changes are observed for the sample with the Cu layer on top than for the oppositely-deposited sample. We found that having the Cu layer on the top causes the Co/Cu interface to become sharper upon irradiation whereas when changing the deposition sequence we do not observe this behaviour. As seen from table 4.15, the roughness of the Co layer decreases dramatically from 35 Å in the as-deposited sample to only 9 Å at the higher irradiation dose. This is seen in fig. 4.22(c) where the interface between the Co and Cu layers becomes sharper upon irradiation. This is due to the fact that Co and Cu are immiscible and there is only a metastable liquid miscibility between them at high temperatures (1495°C) [145, 146].

In an attempt to confirm the obtained results and to make certain that this is not another artifact of the fit we added an extra layer in our model between the Co and the SiO_2 to represent a possible formation of a Co_2Si or CoSi or $CoSi_2$ layer, but the fits did not improve. In fact, we can see from fig. 4.21 that we obtain better-defined wiggles in the experimental data as the irradiation dose increases, indicating the formation of better-defined layers and sharper interfaces.

For the oppositely-deposited sample no obvious change is noticed in the reflectivity curves upon irradiation, as can be seen from fig. 4.23. The oxide layer electron density was found to be 1.10±0.05 $e^-/Å^3$ which is close to the Co_3O_4 electron density of 1.16 $e^-/Å^3$.

In general, the overall trend observed is that the roughness of the different layers increases with increasing irradiation dose, representing more intermixing at the interfaces. No obvious change in the electron density of the bulk materials was detected as can be seen from our reflectivity curves, since the critical angle for total external reflection does not change with irradiation dose. In the next section we present the results of diffuse-scattering scans performed on these bilayers at different 2θ values.

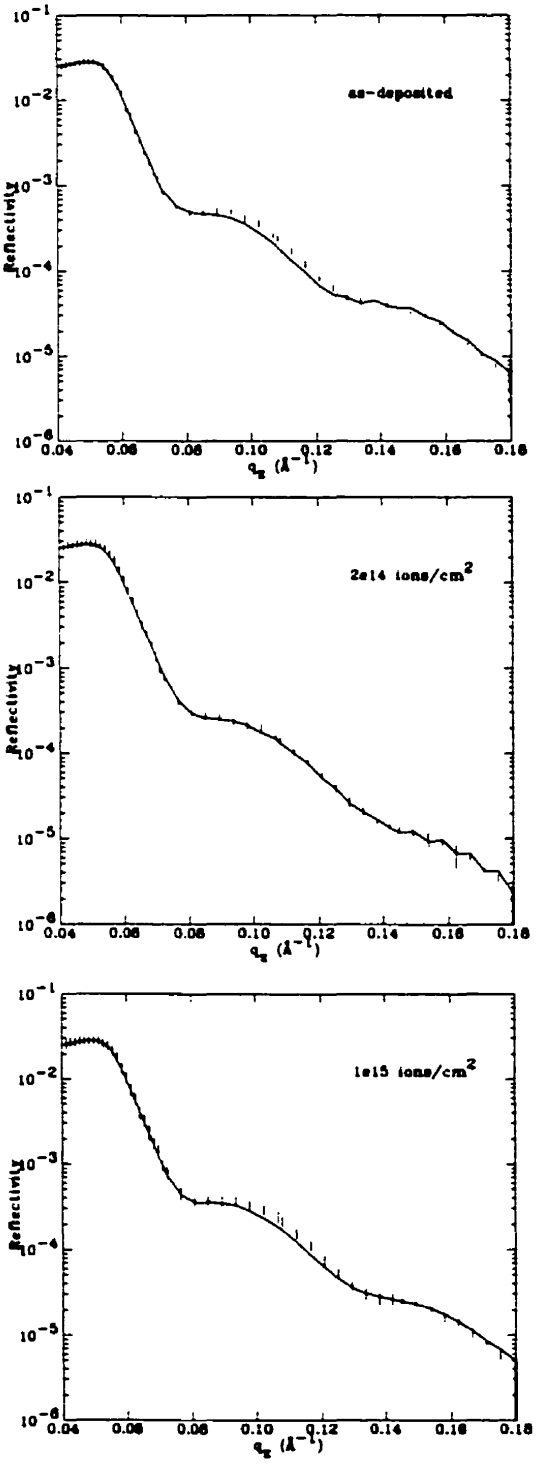

Figure 4.17: Fits (solid line) to $Si/SiO_2/Fe(2000Å)/Ni(100Å)$ reflectivity data (dotted line) at the different irradiation doses.

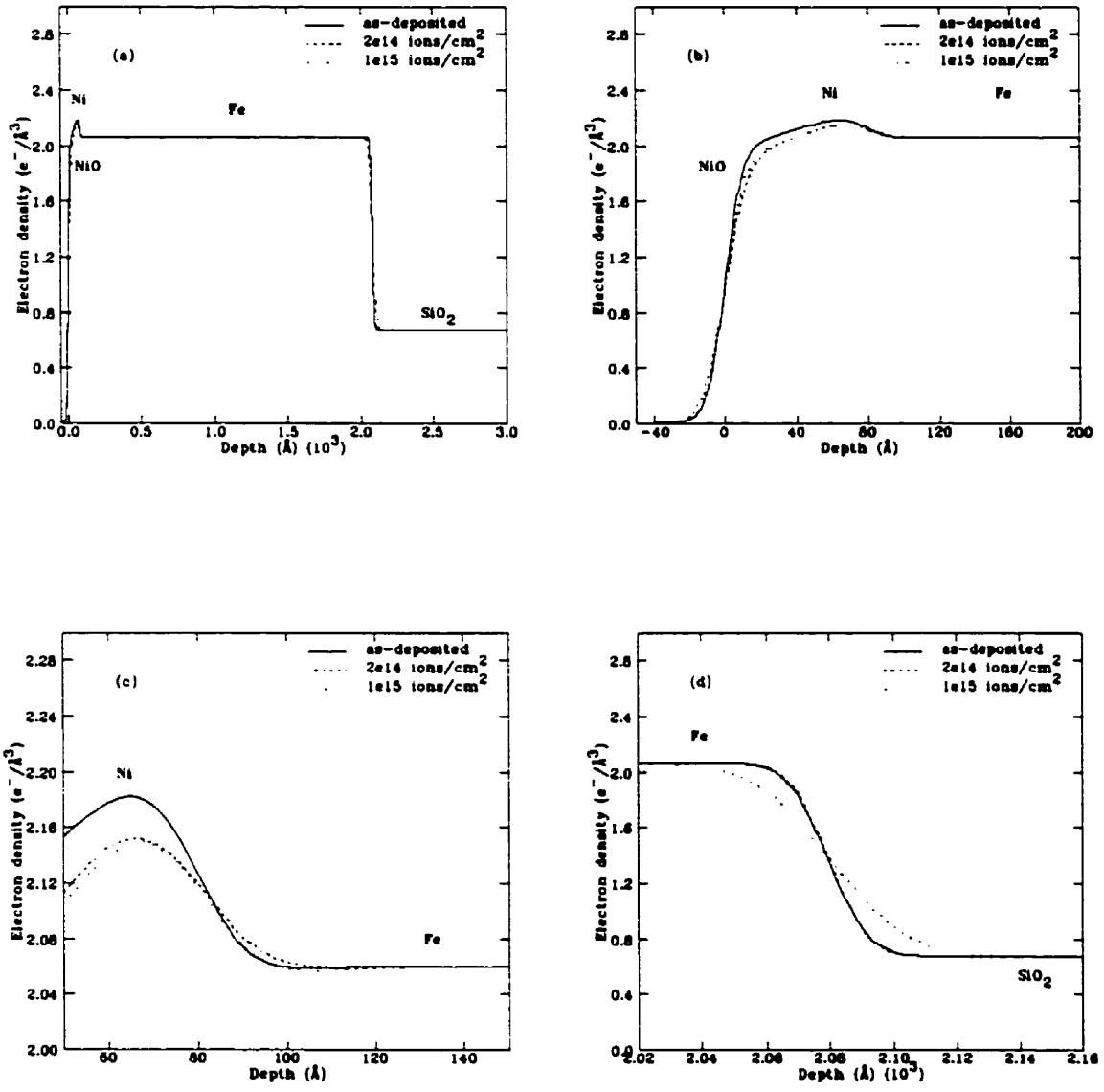

Figure 4.18: Electron density profile of $Si/SiO_2/Fe(2000Å)/Ni(100Å)$ bilayer: a) $SiO_2/Fe/Ni/NiO$ interfaces; b) Ni/NiO interface; c) Fe/Ni interface; d) SiO_2/Fe interface.

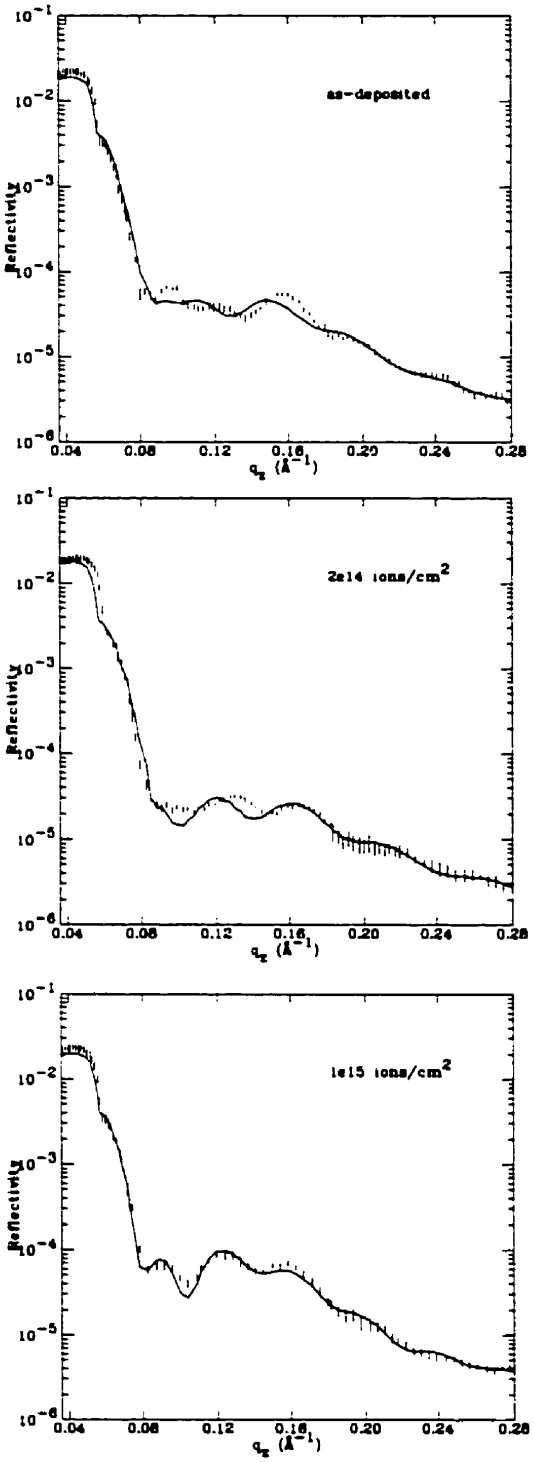

Figure 4.19: Fits (solid line) to $Si/SiO_2/Ni(2000Å)/Fe(100Å)$ reflectivity data (dotted line) at the different irradiation doses.

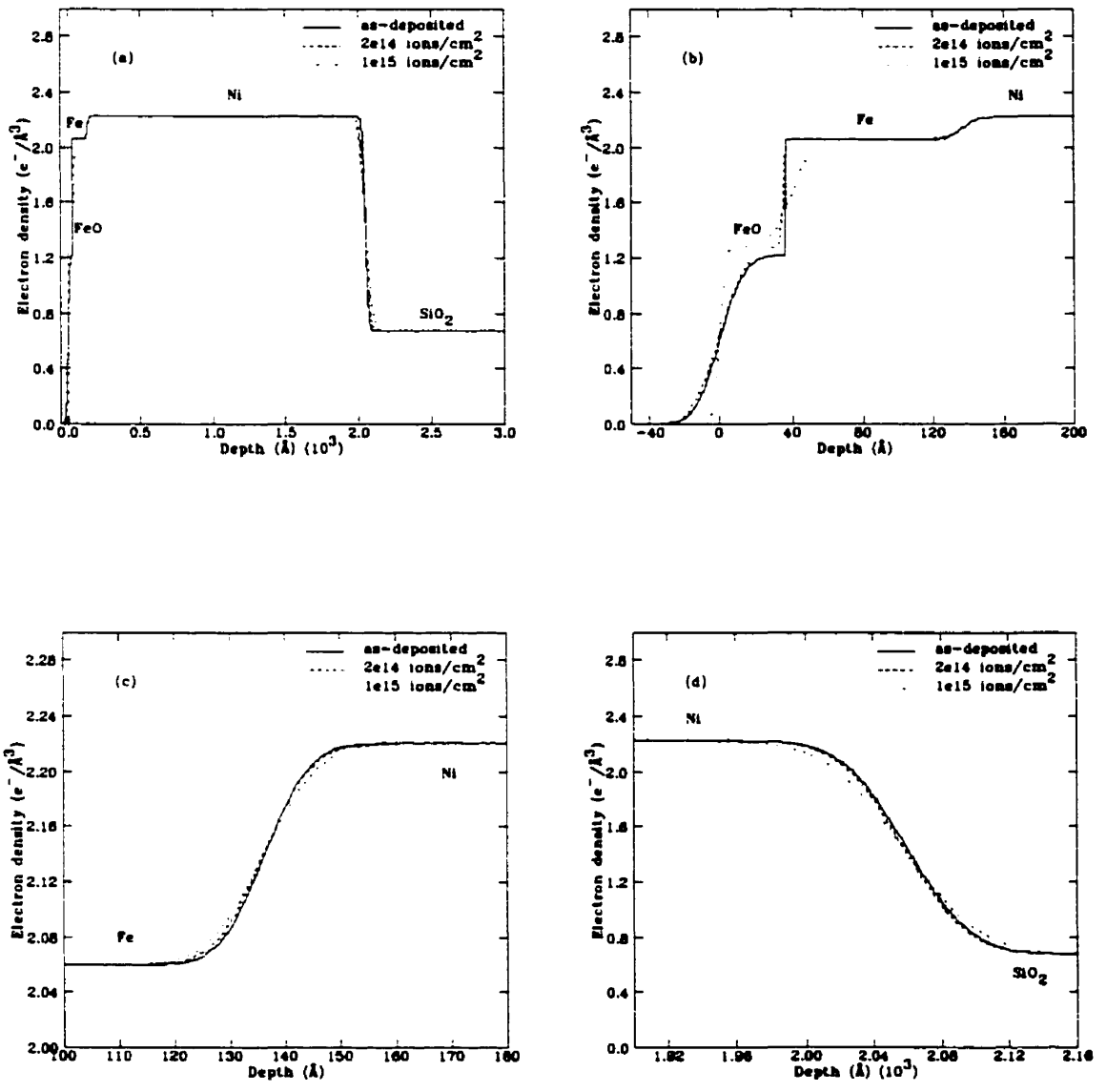

Figure 4.20: Electron density profile of $Si/SiO_2/Ni(2000Å)/Fe(100Å)$ bilayer: a) $SiO_2/Ni/Fe/FeO$ interfaces; b) Fe/FeO interface; c) Ni/Fe interface; d) SiO_2/Ni interface.

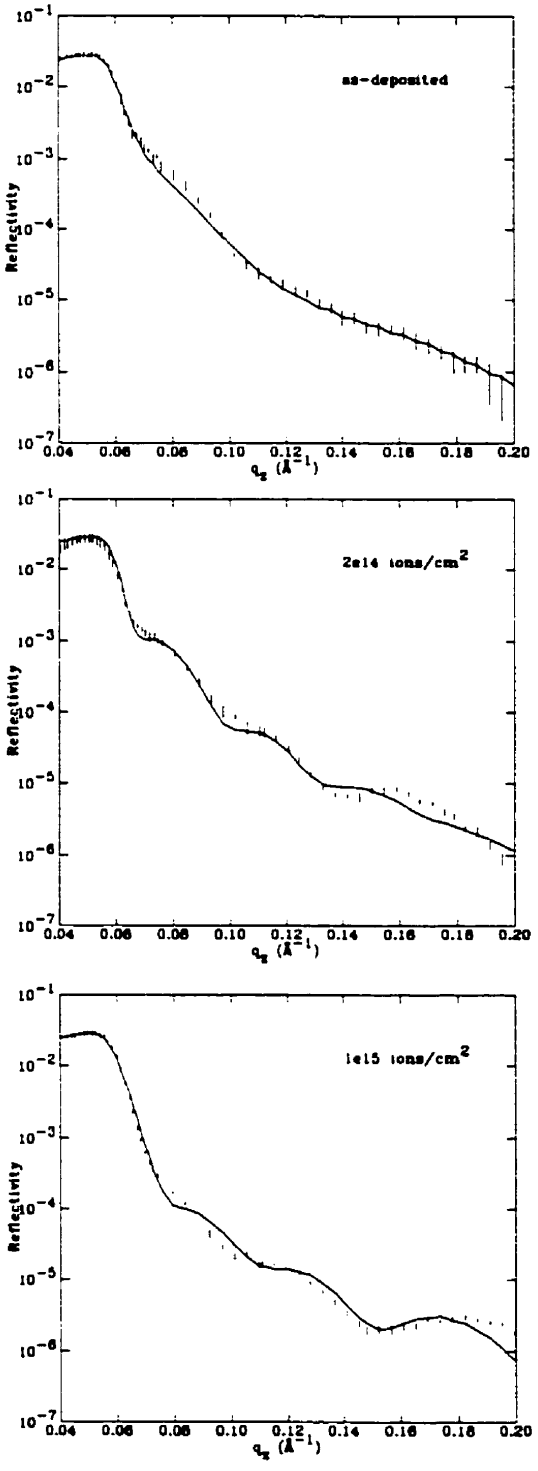

Figure 4.21: Fits (solid line) to Si/SiO_2/Co(2000Å)/Cu(100Å) reflectivity data (dotted line) at the different irradiation doses.

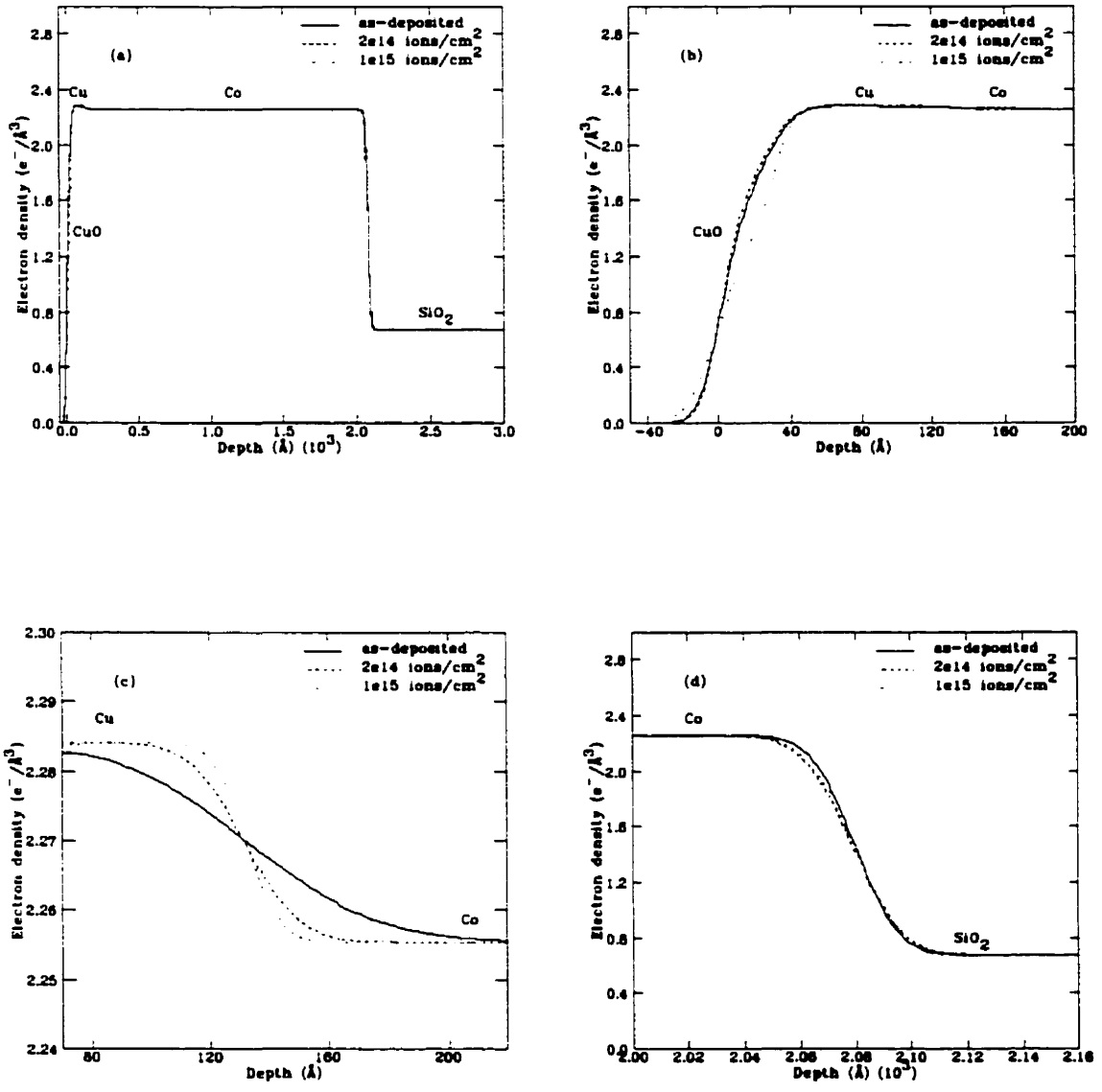

Figure 4.22: Electron density profile of $Si/SiO_2/Co(2000Å)/Cu(100Å)$ bilayer: a) $SiO_2/Co/Cu/CuO$ interfaces; b) Cu/CuO interface; c) Co/Cu interface; d) SiO_2/Co interface.

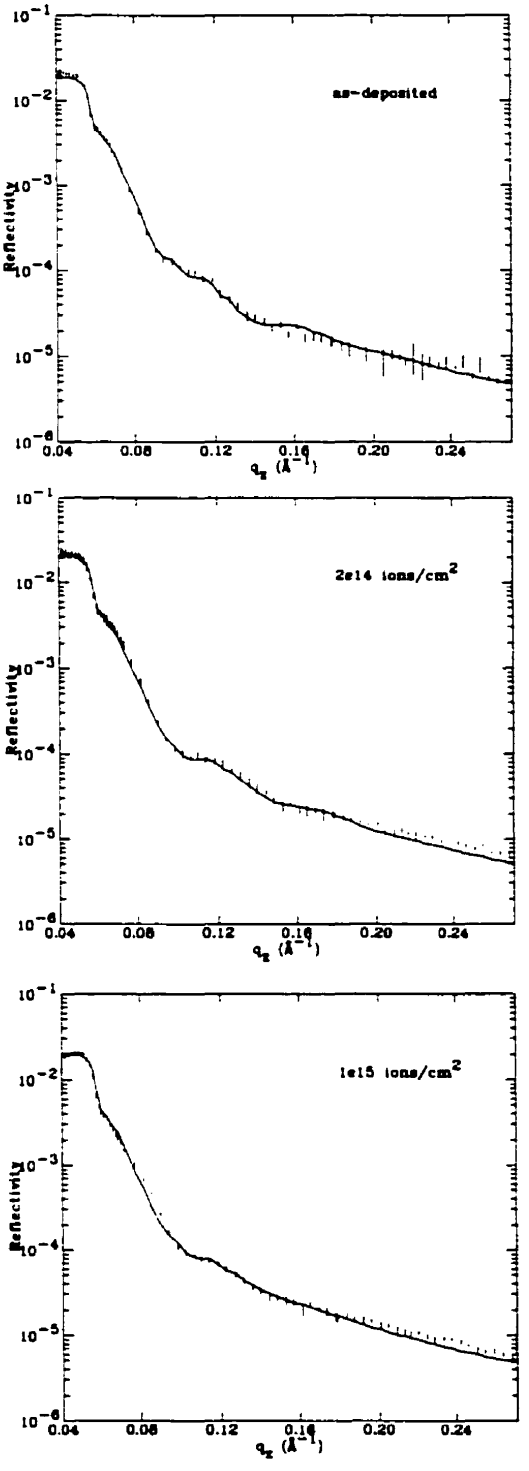

Figure 4.23: Fits (solid line) to Si/SiO_2/Cu(2000Å)/Co(100Å) reflectivity data (dotted line) at the different irradiation doses.

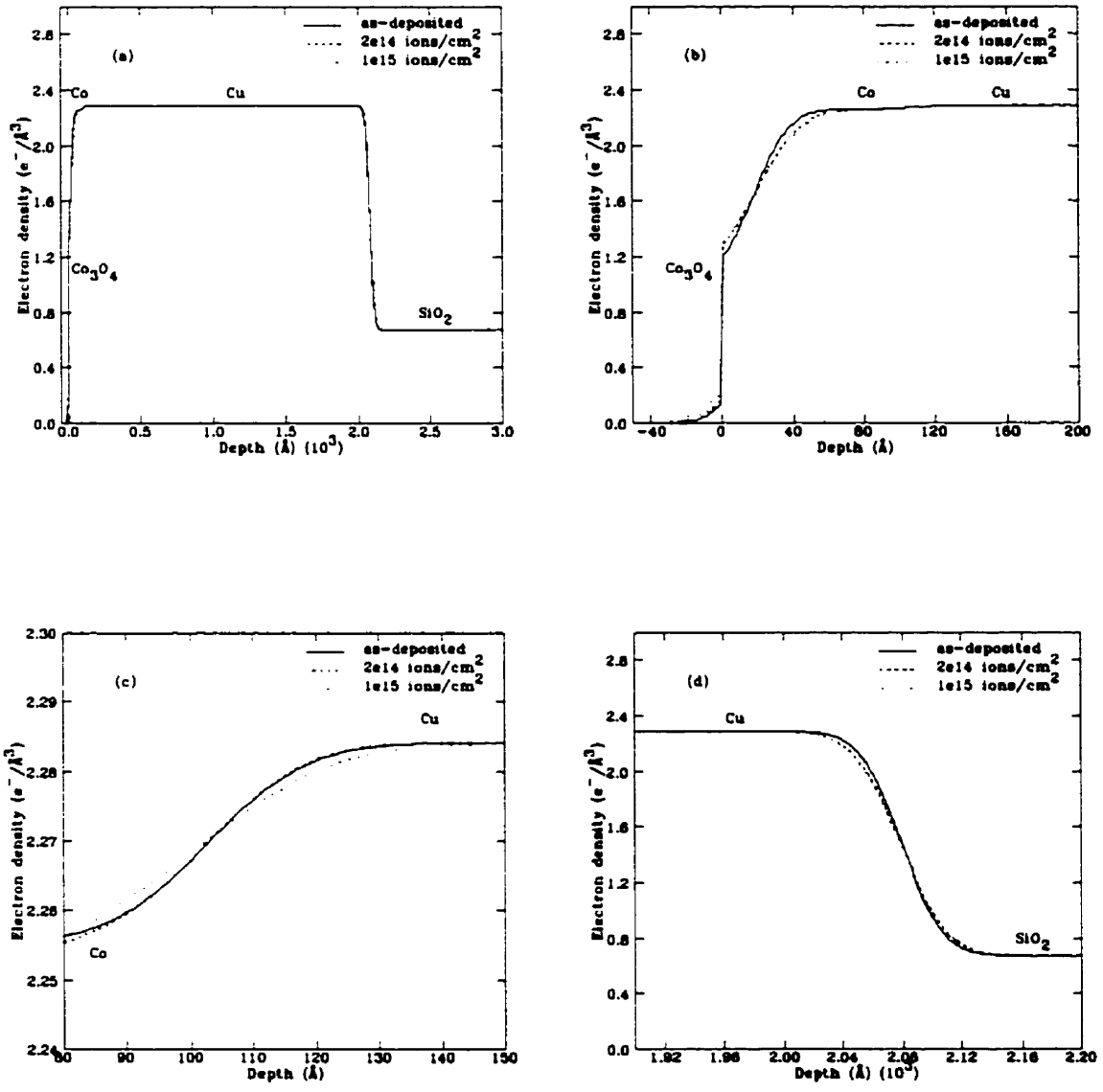

Figure 4.24: Electron density profile of $Si/SiO_2/Cu(2000Å)/Co(100Å)$ bilayer: a) $SiO_2/Cu/Co/Co_3O_4$ interfaces; b) Co/Co_3O_4 interface: c) Cu/Co interface: d) SiO_2/Cu interface.

Parameter	as-deposited	2×10^{14} ions/cm^2	1×10^{15} ions/cm^2
NiO thickness (Å)	25±5	33±2	34±3
NiO roughness (Å)	7.8±0.1	9.9±0.1	8.6±0.1
Ni roughness (Å)	30±5	29±5	32±3
Fe roughness (Å)	8±1	11.8±0.6	10.5±0.7
SiO_2 roughness (Å)	10±4	10±1	19±4

Table 4.13: Parameters of the Si/SiO_2/Fe(2000Å)/Ni(100Å) sample before and after irradiation obtained from fitting the reflectivity data.

Parameter	as-deposited	2×10^{14} ions/cm^2	1×10^{15} ions/cm^2
FeO thickness (Å)	35.5±0.4	33.2±0.3	40.1±0.7
FeO roughness (Å)	10.0±0.4	11.5±0.4	2.7±0.2
Fe roughness (Å)	1.7±0.3	1.6±0.3	9.1±0.5
Ni roughness (Å)	8.9±0.9	8.0±0.9	8.0±0.9
SiO_2 roughness (Å)	30±7	30±5	36±7

Table 4.14: Parameters of the Si/SiO_2/Ni(2000Å)/Fe(100Å) sample before and after irradiation obtained from fitting the reflectivity data.

Parameter	as-deposited	2×10^{14} ions/cm^2	1×10^{15} ions/cm^2
CuO thickness (Å)	25±4	23±9	32±2
CuO roughness (Å)	9±1	9±2	14±1
Cu roughness (Å)	14±2	15±3	9±1
Co roughness (Å)	35±5	15±2	9±1
SiO_2 roughness (Å)	13±4	14±3	14±3

Table 4.15: Parameters of the Si/SiO_2/Co(2000Å)/Cu(100Å) sample before and after irradiation obtained from fitting the reflectivity data.

Parameter	as-deposited	2×10^{14} ions/cm^2	1×10^{15} ions/cm^2
Co_3O_4 thickness (Å)	18±1	20±2	18±2
Co_3O_4 roughness (Å)	1.0±0.4	1.0±0.3	1.0±0.4
Co roughness (Å)	15.8±0.7	19.4±0.6	21.2±0.8
Cu roughness (Å)	12±1	13±2	17±2
SiO_2 roughness (Å)	22±3	25±6	25±4

Table 4.16: Parameters of the Si/SiO_2/Cu(2000Å)/Co(100Å) sample before and after irradiation obtained from fitting the reflectivity data.

4.5 X-ray diffuse scattering data

As mentioned earlier, there are two types of interfaces, rough interfaces and graded interfaces. We cannot distinguish between these two interface types by measuring the specular reflectivity alone since both of them cause a loss of part of the specular reflectivity. We have to measure the diffuse scattering in order to differentiate between them because a rough interface causes some diffuse scattering which increases with increasing roughness, whereas a graded interface does not cause any diffuse scattering and the loss in the specular reflectivity goes into the transmitted beam.

In order to qualitatively characterize our samples we measured the diffuse scattering by performing ω-scans on each bilayer at different 2θ values. The results are shown in figs. 4.25, 4.26, 4.27 and 4.28.

As seen from the figures, we obtain typical ω-scans as shown in fig. 3.6 and discussed in sec. 3.3.2. In most of these ω-scans we can see the Yoneda wings which appear at $\theta = \theta_c$ and $\theta = (2\theta) - \theta_c$, where θ_c is the critical angle for total external reflection of the material.

For example, $\theta_c = 0.399°$ for Ni, and we can see the first Yoneda wing at $\theta \approx 0.4°$ in all parts of fig. 4.25 and the second Yoneda wing at $\theta \approx 0.6°$, $0.8°$, $1.0°$, and $1.2°$ in figs. 4.25(a), 4.25(b), 4.25(c) and 4.25(d), respectively. Also the specular peak appears at $\theta = \frac{1}{2}(2\theta)$ and decreases in intensity as 2θ increases.

We can see the difference between the ω-scans for the Si/Fe/Ni bilayer in fig. 4.25 and those for the Si/Ni/Fe bilayer in fig. 4.26. For the earlier sample we have a lot

of diffuse scattering which changes with the irradiation dose whereas for the latter sample there is almost no diffuse scattering, what is measured is the dark counts which don't change with irradiation. From the specular reflectivity fits we found that the Ni layer in the Si/Fe/Ni bilayer was very rough. Its roughness was very high compared to its thickness. The ω-scans confirm this high roughness since it is the only sample where we can see a large diffuse scattering component, and the change in the diffuse scattering upon irradiation is obvious at all measured values of 2θ up to $2\theta = 1.6°$. For the other samples it is best to measure the diffuse scattering at values of $2\theta < 1.2°$.

We can thus conclude that the Ni/NiO interface in the Si/Fe/Ni sample is a rough interface whereas the interfaces in the Si/Ni/Fe sample are graded interfaces. This might also suggest that the linear interface profile would best represent the graded interfaces of the Si/Ni/Fe sample, in fact we were able to obtain a better fit using the linear interface profile only for the as-deposited sample.

The Si/Co/Cu and Si/Cu/Co samples both show some diffuse scattering at $2\theta = 1.0°$ but that scattering is more affected by the irradiation for the first sample than for the second one. At higher 2θ values the diffuse scattering decreases and at $2\theta > 1.2°$ we are merely measuring the dark counts.

From this survey, we cannot determine the effect of ion irradiation on the diffuse scattering. Although we notice some changes in the diffuse scattering curves upon irradiation, these changes are not consistent due to the fact that we are using three distinct samples of each bilayer configuration. In the next chapter we will use one sample of each bilayer configuration and irradiate it successively to the different irradiation doses in order to obtain more consistent and comparable results.

4.6 Conclusion of the survey

We see from this survey that x-ray reflectivity is a good tool for studying intermixing at the interfaces. We have established and tested a good setup for our diffractometer, by optimizing the slits settings, the pulse height analyzer settings and by including a

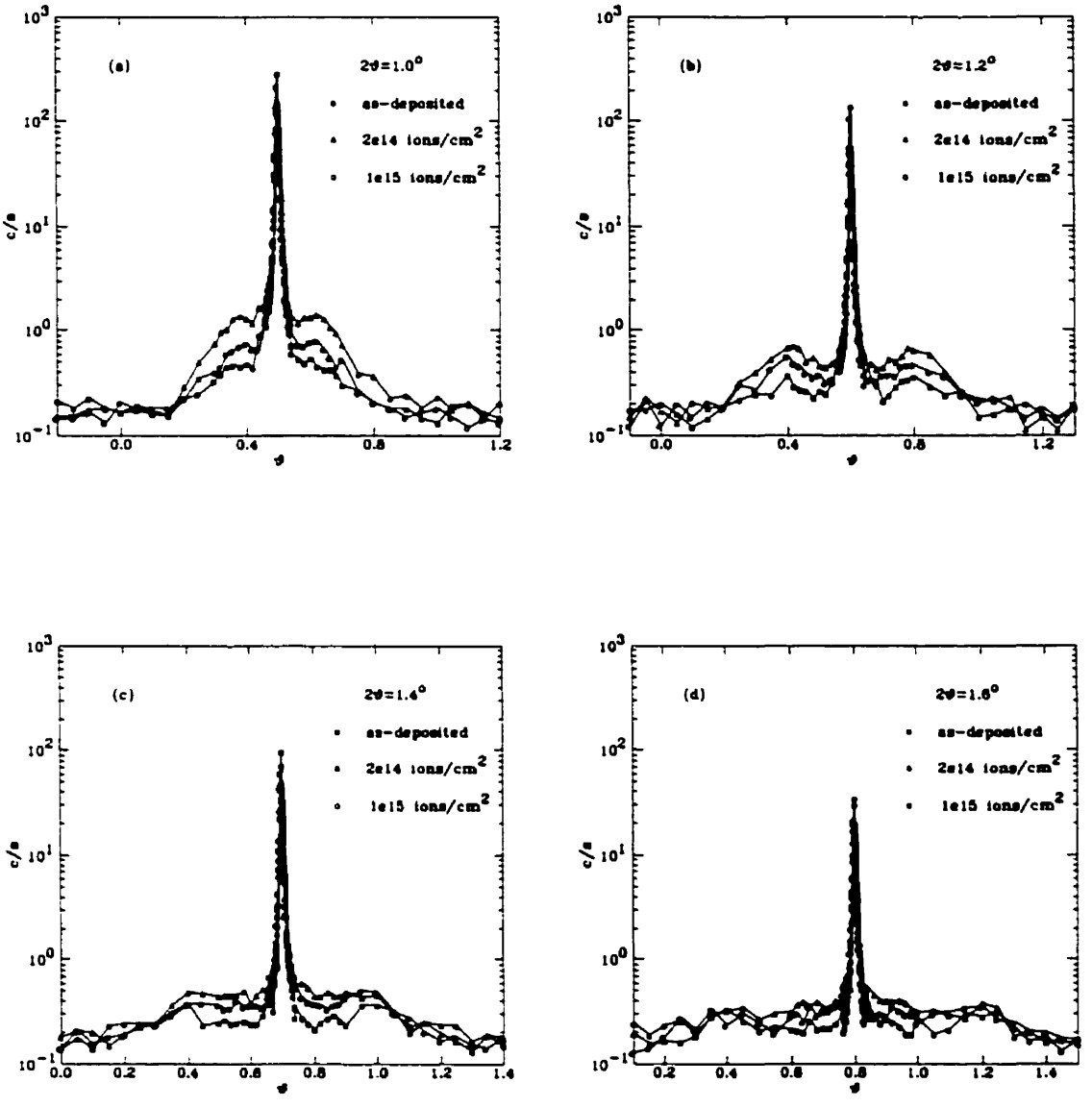

Figure 4.25: Omega scans of the bilayer $Si/SiO_2/Fe(2000Å)/Ni(100Å)$ at different 2θ values: a) $2\theta = 1.0°$; b) $2\theta = 1.2°$; c) $2\theta = 1.4°$; d) $2\theta = 1.6°$. The solid lines are guides to the eye.

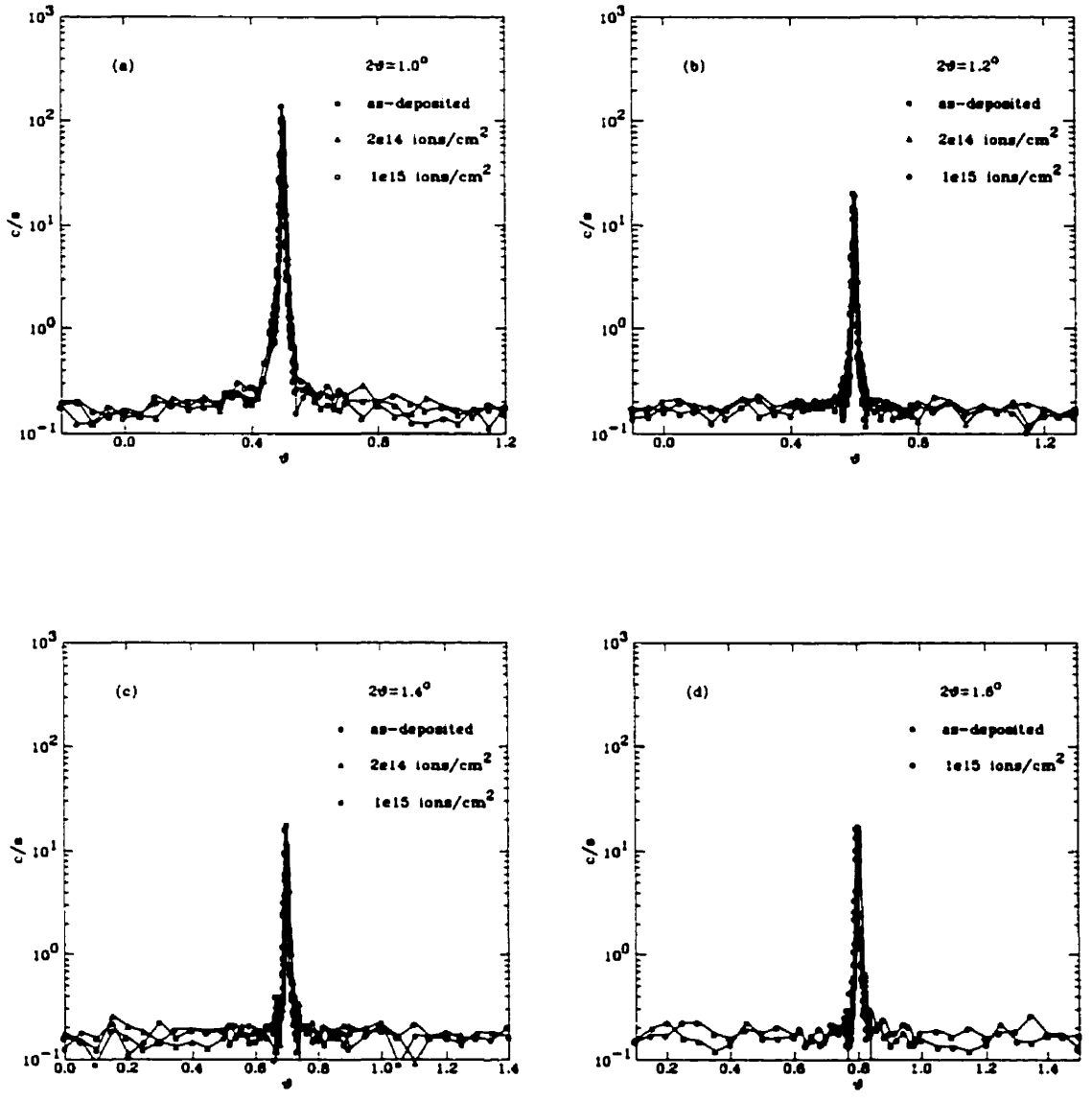

Figure 4.26: Omega scans of the bilayer $Si/SiO_2/Ni(2000Å)/Fe(100Å)$ at different 2θ values: a) $2\theta = 1.0°$: b) $2\theta = 1.2°$; c) $2\theta = 1.4°$: d) $2\theta = 1.6°$. The solid lines are guides to the eye.

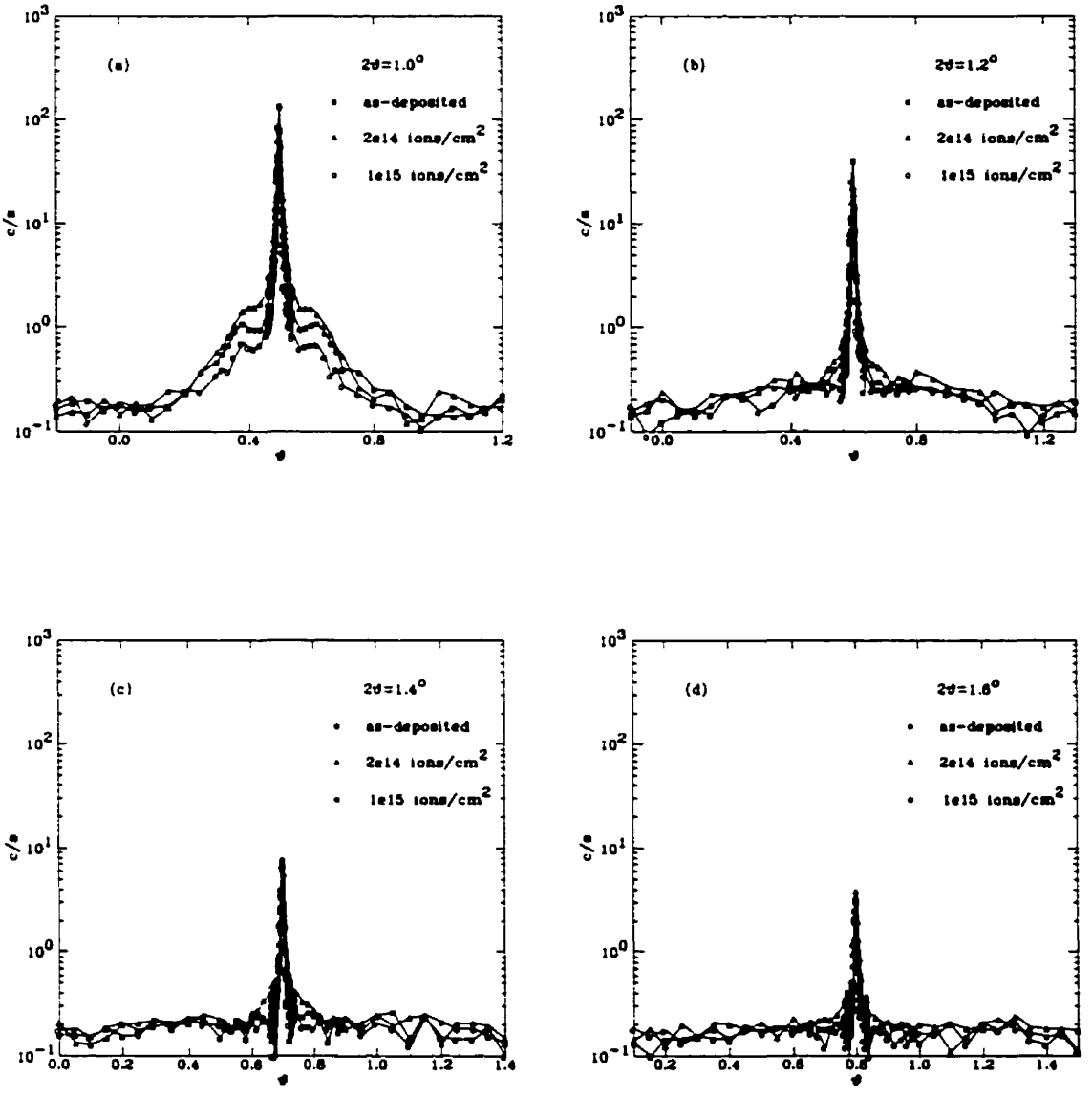

Figure 4.27: Omega scans of the bilayer $Si/SiO_2/Co(2000Å)/Cu(100Å)$ at different 2θ values: a) $2\theta = 1.0°$; b) $2\theta = 1.2°$; c) $2\theta = 1.4°$; d) $2\theta = 1.6°$. The solid lines are guides to the eye.

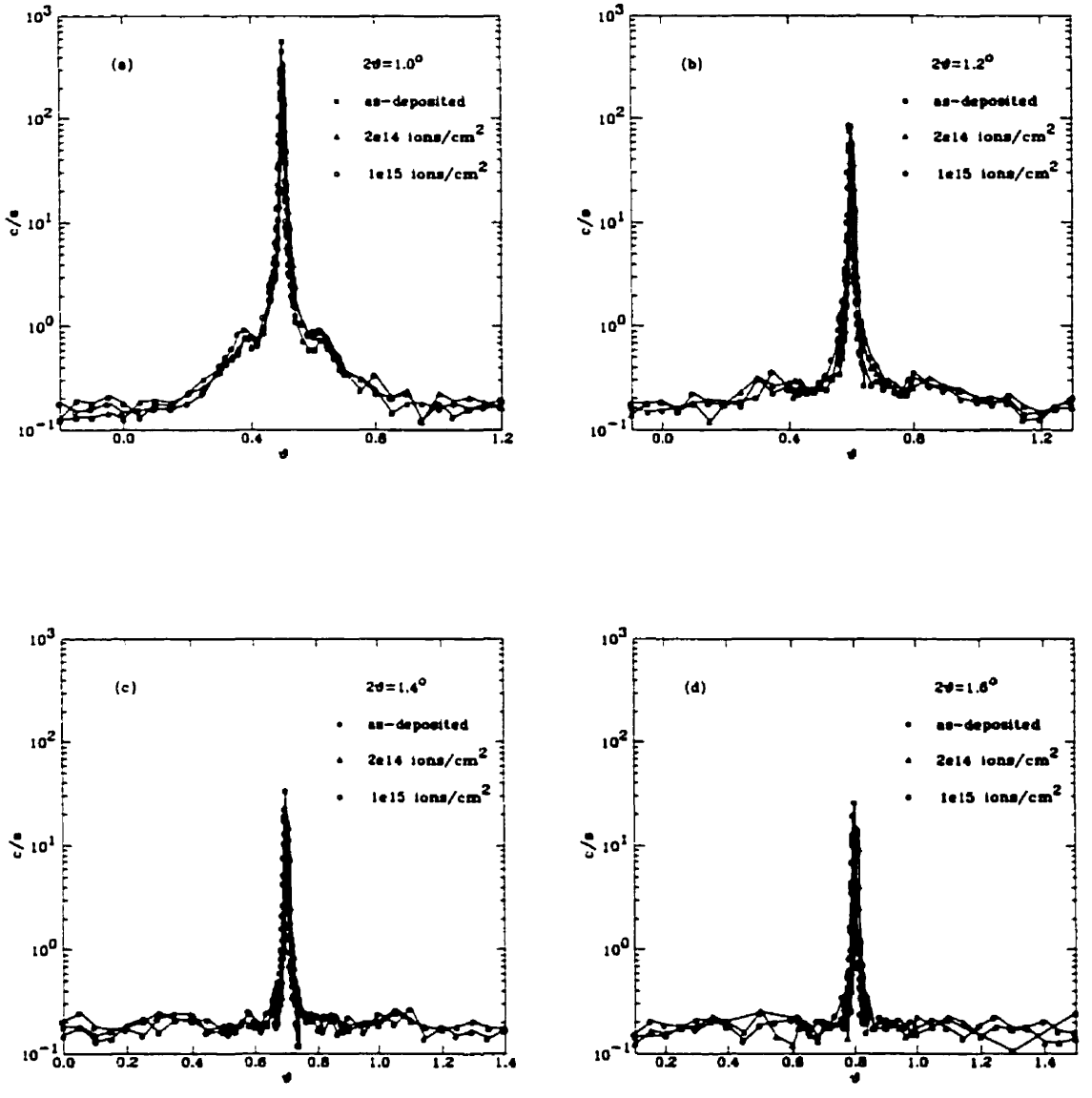

Figure 4.28: Omega scans of the bilayer $Si/SiO_2/Cu(2000Å)/Co(100Å)$ at different 2θ values: a) $2\theta = 1.0°$: b) $2\theta = 1.2°$; c) $2\theta = 1.4°$: d) $2\theta = 1.6°$. The solid lines are guides to the eye.

new sample holder and new stepping motor controllers.

Our method of data acquisition and processing enables us to obtain the normalized reflectivity data over several orders of magnitude and our modeling method gives us reasonable fits that agree well with the experimental data. We have also tested various representations for the interface profile and concluded that the error-function representation best describes our samples.

An important question arises on how accurate is the estimation of the thickness, roughness and electron density of the different layers in our reflectivity fits? As discussed in sec. 3.3.2, the thickness of the different layers determines the position of the peaks in the reflectivity curves, whereas the amplitude of the oscillations is proportional to the electron density contrast between the neighbouring layers. The roughness affects the overall decay of the reflectivity curve.

Hence in the fitting process, when the refractive indices and the thicknesses have reasonable values, a small change in the thickness will mainly displace the positions of the peaks which will cause a large change in the χ^2 value of the least-square fitting. This means that the thickness values obtained will be very reliable as long as those thicknesses are in a range that is well resolved by our setup and good oscillations have been obtained for them in the experimental data.

On the other hand, a small change in the electron densities will mainly affect the intensity and will not influence χ^2 as much, with the exception of the electron density value of the layer which determines the position of the critical angle. Any small change in this electron density value will cause a shift in the critical angle position and hence a large change in the χ^2 value. Therefore, this electron density value is more reliable, whereas the electron density contrast between the other layers is more reliable than their absolute values.

Concerning the roughness parameter, we know that the top surface usually displays the strongest scattering due to the relatively large change in electron density upon going from vacuum (or air) to solid matter. The scattering from the buried interfaces is usually weaker because of the smaller electron density contrast. Hence the overall

fall-off of the reflectivity curve with increasing q is dominated by the top surface roughness. The effect of buried interfaces roughness is usually the damping of the interference fringes at large q. Therefore the top layer roughness value is usually more reliable and the reliability of the roughness parameter of any interface decreases as the electron density contrast between the two layers sandwiching this interface decreases, because this particular interface will contribute less to the scattered intensity. If the change in an interface roughness parameter does not affect the fit at all, a smallest possible roughness value is chosen for this particular interface.

In general, the overall good fits obtained mean that the models are good approximation to the structure of our samples. The small discrepancies in the fits indicate that further improvements could still be added to our model. Although at some points the results of the fit were not convincing, the overall trend is clearly visible. We discussed the limits of reliability of our fits and obtained a good picture for the extent of our model.

Several other factors affected the accuracy of this data. First, the samples were very small in size (4 mm high×6 mm wide each) which forced us to reduce the height of the slit defining the beam just before the sample to 3 mm such that the total height of the incident x-ray beam would hit each individual sample without hitting the neighbouring ones. This caused the loss of an important part of the incident x-ray beam intensity which reduced our signal significantly and therefore reduced our measured signal-to-noise ratio. This reduction in incident intensity affects the data especially as we try to measure to higher 2θ values, since the reflectivity drops very fast over several orders of magnitude.

Second, although we try to obtain three identical samples for each configuration, some differences occur between those three as-deposited samples. The most obvious difference is in the thickness of the corresponding layers. There is a thickness gradient along the length of the samples which was measured to be 0.847Å/mm. Also, some differences in the roughness of the corresponding layers and in the thickness of the oxide layer exist, which affect the comparison of results at different irradiation doses.

Third, the 2000 Å layers are too thick to be resolved by our setup, hence we lose the information that could be obtained from these wiggles. Finally, the 2×10^{14} ions/cm^2 irradiation dose turned out to be very low, few changes are observed at this dose, if any. The 1×10^{15} ions/cm^2 dose causes some noticeable changes but is not high enough to produce a larger effect. Meanwhile, oxidation causes lots of changes (especially for iron) which sometimes are difficult to fit.

As a whole we obtained a good overview of the possibilities and accuracy of our measurements. We learned a lot about our model, its strengths and its weaknesses. We will try to overcome these difficulties by depositing bigger samples (15 mm high× 4 mm wide) of Fe/Ni bilayers with a more convenient thickness. In this case the vertical height of the slit defining the beam could be kept wide open (10 mm) in order to gain more signal for the incident x-ray beam and we are sure to have only one set of initial parameters to compare the structure evolution at each irradiation dose. Each of these samples will be irradiated successively to higher irradiation doses until more changes could be observed in the structure. The samples will be characterized at each irradiation stage by low-angle x-ray reflectivity and x-ray diffuse scattering measurements. Some of these samples will also be characterized by high-angle x-ray scattering and transmission electron microscopy techniques. The results are presented in chapter 5.

5

Detailed study of Fe/Ni bilayers

In this chapter we present the results of a detailed study performed on two Fe/Ni bilayers with opposite deposition sequences. In order to overcome the difficulties that we faced in our previous survey, the bilayers are deposited with the dimensions of 15 mm high×4 mm wide each, therefore the height of the slit defining the beam could be left wide open at 10 mm. This allows us to increase the incident x-ray beam intensity and hence to increase the measured signal-to-noise ratio, allowing us to obtain better scans at higher q values.

The individual Fe and Ni layers thicknesses are chosen to be 500Å each since we obtained very good oscillations in the reflectivity curves of the single layers at this thickness. Moreover, each bilayer is irradiated successively to higher doses and characterized at each irradiation stage, until all the specularly-reflected signal is lost and we obtain only the diffusely-scattered component. In this way we ensure two things: first, since we irradiate a single sample of each configuration our results will be comparable and our initial parameters will always be the same; second, the successive irradiation will make certain that we reach a high-enough irradiation dose in order to observe noticeable structural changes in our samples.

Identical $Si/SiO_2/Ni(500Å)/Fe(500Å)$ bilayers are also deposited and characterized by x-ray reflectivity (XRR) and high-angle x-ray diffraction (XRD) measurements. Each of these bilayers is then irradiated at a different irradiation dose, characterized again by XRR and XRD techniques, then studied by plane-view and cross-sectional transmission electron microscopy (TEM and XTEM) techniques. The obtained results are compared to the results of our x-ray structural study.

In section 5.1 we explain in detail how the diffusely-scattered component is separated from the specularly-reflected component. We also show that the specular reflectivity decreases with increasing irradiation dose until all of our signal represents the diffusely-scattered radiation. This is shown to occur at a different irradiation dose for the different samples.

Section 5.2 presents the x-ray reflectivity data and fits for the two bilayers while the x-ray diffuse scattering scans are presented in sec. 5.3. The high-angle x-ray diffraction measurements for the Si/Ni/Fe bilayer are presented in sec. 5.4 and the TEM and XTEM plots for this bilayer are given in sec. 5.5. Finally a discussion of these results follows in section 5.6.

5.1 Separating the diffuse scattering component from the specular reflectivity data

In this section we will explain in detail how our low-angle x-ray scattering data is processed in order to separate the diffuse scattering component and to obtain the specular reflectivity component only. This turns out to be very important at high irradiation doses (in the 10^{16} ions/cm^2 dose range) since the diffuse scattering component becomes very large relative to the specular component. Therefore, if the diffuse component is not subtracted out we cannot obtain meaningful fits since our model only calculates the specularly-reflected intensity.

There are several ways of measuring the low-angle reflectivity, as discussed in sec. 3.3.2. We can perform a direct $\theta - 2\theta$ scan, where the intensity is measured once at each 2θ value at the expected position of the peak ($\theta = \frac{1}{2}(2\theta)$). However, any angular error introduced by the goniometer movement will cause an inaccuracy of the measurement.

We can perform a small mesh around the $\omega = 0$ region for each fixed 2θ, then choose the maximum data point for each 2θ value, or average the data around the specular ridge. This will reduce the error caused by the goniometer positioning inaccuracy, but when the signal is weak we will be mainly measuring the background and the

average will take into account some intensity from the diffuse part.

The best method in order to separate the diffuse background is to perform an ω-rock at each fixed 2θ value, spanning several times the HWHM of the peak. Each of these ω-rocks will be composed of three parts: the dark counts, the diffuse background and the specular peak. The dark counts come mainly from the electronic circuits and from random scattering and represent a linear background which in our setup is measured to be 0.032 cps. This linear background is subtracted from the diffuse background.

In order to calculate the specular intensity and to separate the diffuse background, each of these ω-rocks is fit to an equal-widths Gaussian-Lorentzian lineshape (EWGL) given by equation 3.2. The fitting curve is given by eq. 3.3, where bg is the diffuse background. I is the integrated intensity under the specular peak and f is the lineshape function defined in eq. 3.2. From the fit parameters we obtain the diffuse background level (in counts-per-second) and the integrated intensity under the specular peak.

Examples of these fits are shown in fig. 5.1 where the diffuse background is represented by the shaded areas. We have chosen the data of the Si/Fe/Ni bilayer irradiated at 9×10^{16} ions/cm^2 as an example because the diffuse scattering background increases with irradiation dose, so by choosing a high irradiation dose we can better see the effect of the diffuse background on the specular peak. As can be seen from the figure and from fig. 3.7, as 2θ increases the peak intensity decreases and the diffuse background level increases with respect to the specular peak. The dark counts level is too low to appear on this scale.

By fitting the measured ω-rocks at each 2θ value we obtain the integrated specular intensity and the diffuse background for the samples at each irradiation stage. The obtained diffuse background level is in counts-per-second which should be transformed into an integrated intensity, by multiplying it by the width of our scan (0.016° in our case).

Figures 5.2 and 5.3 show the diffuse and the specular components of the scattering of the two bilayers at the different irradiation doses. The open squares represent

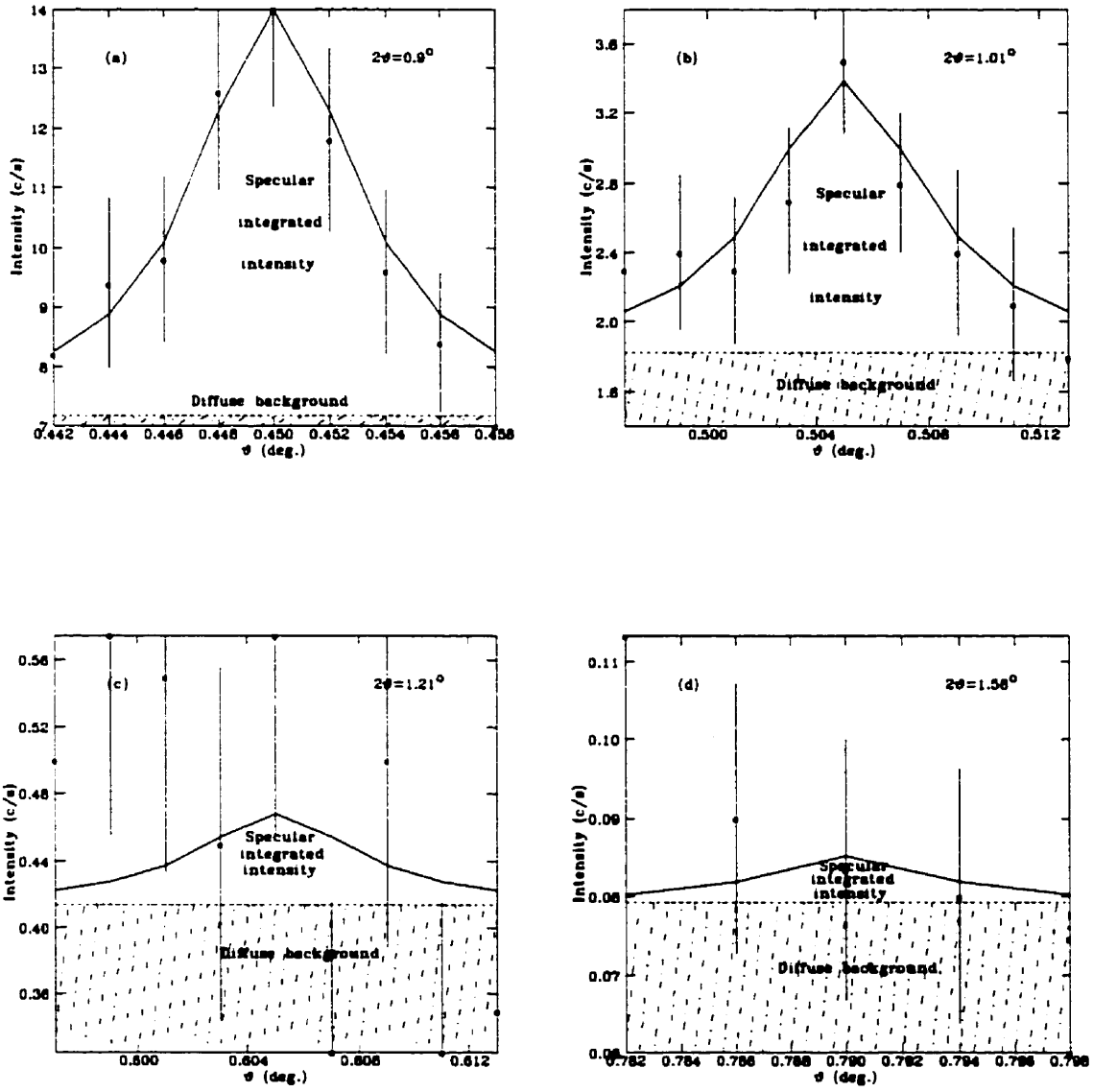

Figure 5.1: Fits (solid lines) to the ω-rocks experimental data (squares) of the $Si/SiO_2/Fe(500Å)/Ni(500Å)$ bilayer irradiated at 9×10^{16} cm^{-2} at different 2θ values. The fits are calculated at the experimental points only. The shaded areas represent the diffuse background. The dark counts are 0.032 cps which cannot be seen at this scale.

the total intensity (specular+diffuse) that we would obtain if we do not separate the diffuse part. The solid triangles represent the specular integrated intensity alone after separating the diffuse background, and the open circles represent the diffuse background after subtracting the dark counts and transforming it into an integrated intensity.

For the Si/Fe/Ni bilayer we can see from fig. 5.2(a) that for the as-deposited sample the specular integrated intensity (triangles) and the total integrated intensity (squares) almost coincide at all values of 2θ, showing that the diffuse scattering is weak and does not affect the measured specular intensity greatly. On the other hand, at the highest irradiation dose, fig. 5.2(d) shows that the specular intensity (triangles) is very weak, even weaker than the diffuse intensity (circles). At this dose, it is extremely important to separate the diffuse intensity before fitting the reflectivity. At intermediate irradiation doses, we can see from figures 5.2(b) and 5.2(c) that the diffuse part becomes more significant at lower angles as the irradiation dose increases.

For the oppositely-deposited bilayer, we see from fig. 5.3(c) that the specular scattering is affected at $2\theta > 1.5°$ whereas at the higher irradiation dose we have some specular scattering up to a 2θ value of around 0.8° as seen from fig. 5.3(d).

This shows us that the 10^{15} cm^{-2} irradiation dose is in fact high enough to see a few changes in the structure but the diffuse scattering is still weak at this level. As the dose is increased to 3×10^{16} cm^{-2} more diffuse scattering is measured and the specular intensity is more affected. At the 9×10^{16} cm^{-2} dose the Si/Fe/Ni bilayer loses most of its specular part and the signal is composed mainly of the diffuse scattering component, whereas the Si/Ni/Fe bilayer still has some specular scattering at this dose, and actually loses all the specular part when we further irradiate it at 1.9×10^{17} cm^{-2}. Therefore, the two bilayers lose their specular reflectivity part at different irradiation doses, showing different behaviour upon changing the deposition sequence.

In order now to obtain the reflectivity we have to normalize the specular integrated intensity by dividing it by the integrated intensity of the incident x-ray beam, as

explained in sec. 3.3.2. In the next section we present the fits to these reflectivity curves and the electron density profiles constructed from the fit parameters.

5.2 Low-angle x-ray reflectivity data

In this section we present the fits to the x-ray reflectivity data of the Si/Fe/Ni and the Si/Ni/Fe bilayers. The samples structure is approximated using the bilayers model described in sec. 4.4.1. The fit parameters are the thickness and roughness of the different layers. The electron densities and absorption coefficients are again taken from table 4.1 for the substrate, and from tables 4.2 and 4.7 for the Ni and Fe layers and oxides, respectively. All the interfaces are represented by error-function profiles.

Figures 5.4 and 5.5 show the experimental data and calculated fits for the Si/Fe/Ni and Si/Ni/Fe bilayers, respectively. Since we found in the last section that the Si/Fe/Ni sample lost most of its specular reflectivity at the 9×10^{16} cm^{-2} irradiation dose while the Si/Ni/Fe sample still had some measurable specular component at this dose, there are only 3 fits for the earlier sample and 4 fits for the latter one. We can see that by removing the diffuse scattering component from our data we are able to obtain good fits which agree reasonably well with the experimental data at all irradiation doses. Therefore, our model is a good approximation to the structure of our samples.

The values of the fit parameters are given in tables 5.1 and 5.2, respectively. As can be seen, the roughness values of the different layers increase with increasing irradiation dose, with the exception of the substrate roughness which fluctuates a little. However, as discussed in sec. 3.3.2, the fit is not very sensitive to the buried interfaces roughness and the obtained values for the surface and top interface roughness are more accurate.

The electron density profiles are constructed from the fit parameters and are shown in figures 5.6 and 5.7, respectively. As can be seen, there is an increased intermixing at the different interfaces as the irradiation dose increases. We can see here the advantage of having only one sample of each configuration irradiated successively to higher irradiation doses. The increase in intermixing region is systematic and we

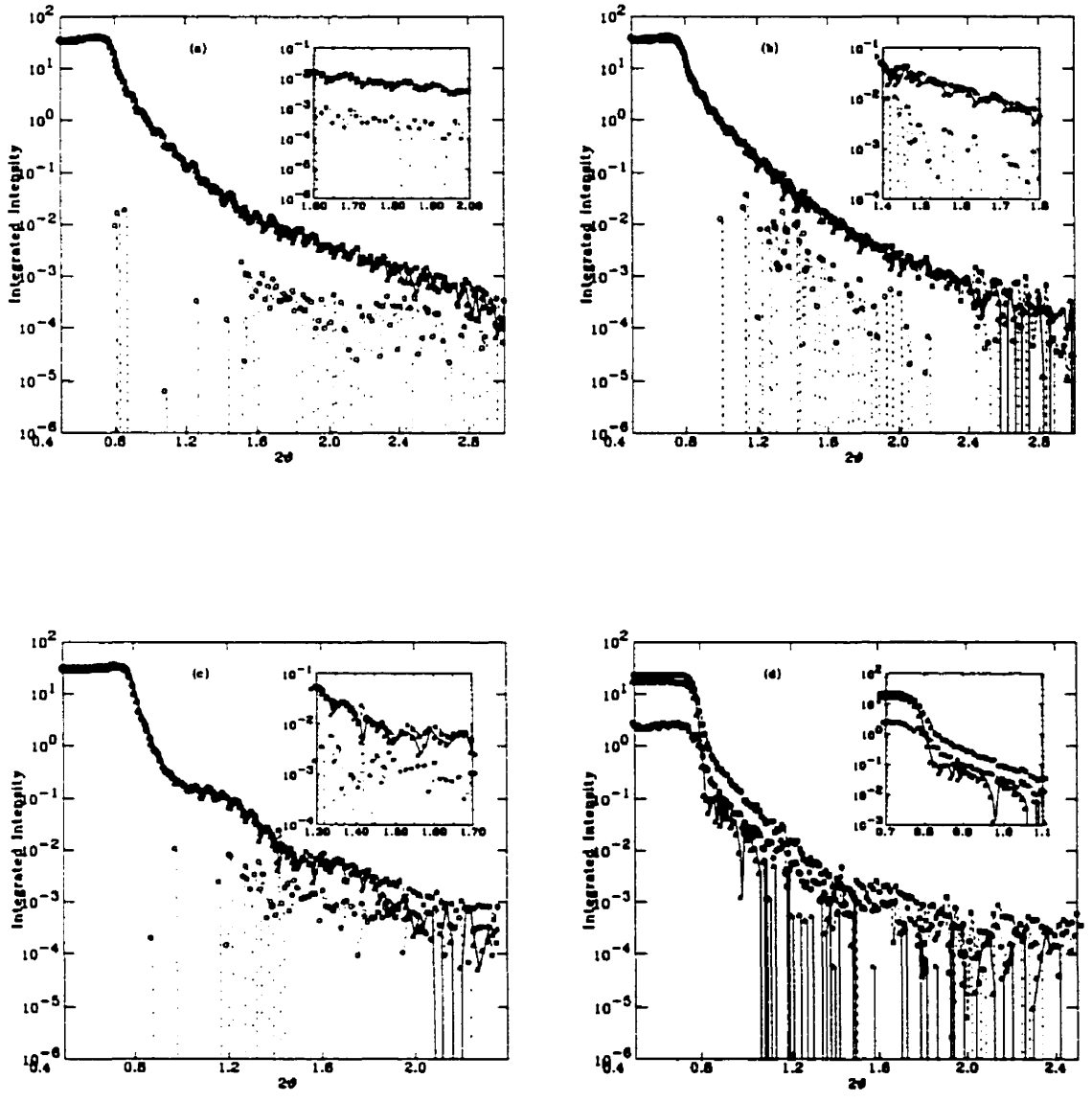

Figure 5.2: Separating the diffuse and specular components of the x-ray scattering of the bilayer $Si/SiO_2/Fe(500Å)/Ni(500Å)$; open squares: specular+diffuse; solid triangles: specular only; open circles: diffuse-dark; at the irradiation doses: a) as-deposited; b) 2×10^{15} cm^{-2}; c) 3×10^{16} cm^{-2}; d) 9×10^{16} cm^{-2}.

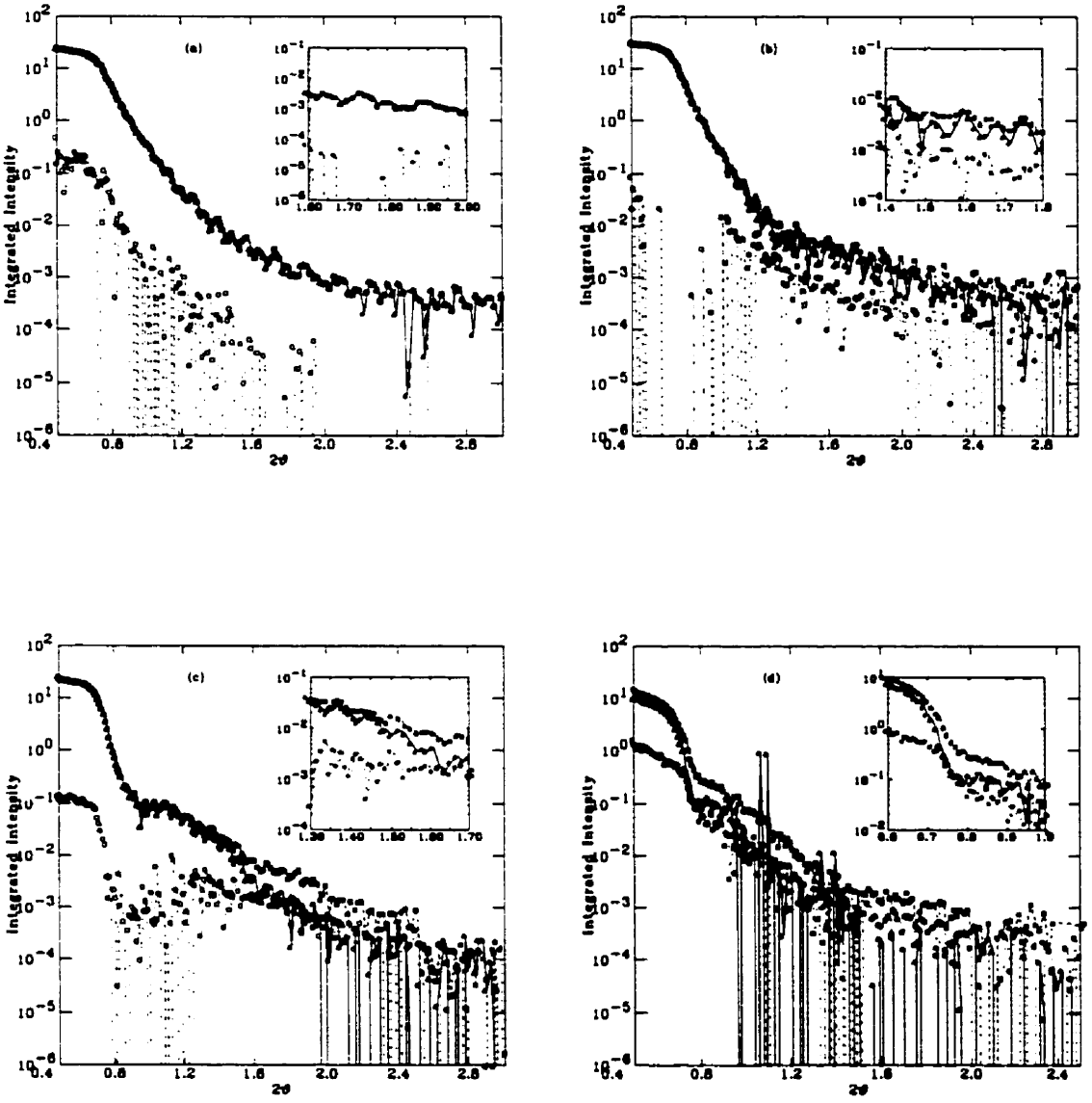

Figure 5.3: Separating the diffuse and specular components of the x-ray scattering of the bilayer $Si/SiO_2/Ni(500Å)/Fe(500Å)$; open squares: specular+diffuse: solid triangles: specular only: open circles: diffuse-dark; at the irradiation doses: a) as-deposited; b) 1×10^{15} cm^{-2}: c) 3×10^{16} cm^{-2}: d) 9×10^{16} cm^{-2}.

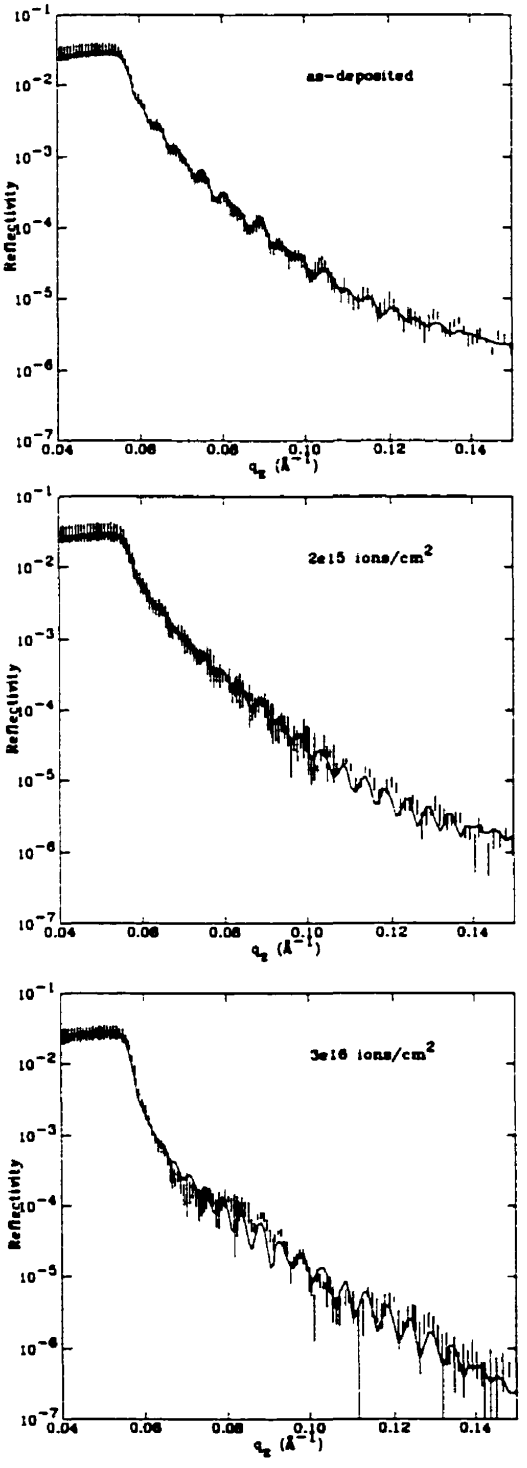

Figure 5.4: Fits (solid lines) to Si/SiO_2/Fe(500Å)/Ni(500Å) reflectivity data (dotted lines) at different irradiation doses.

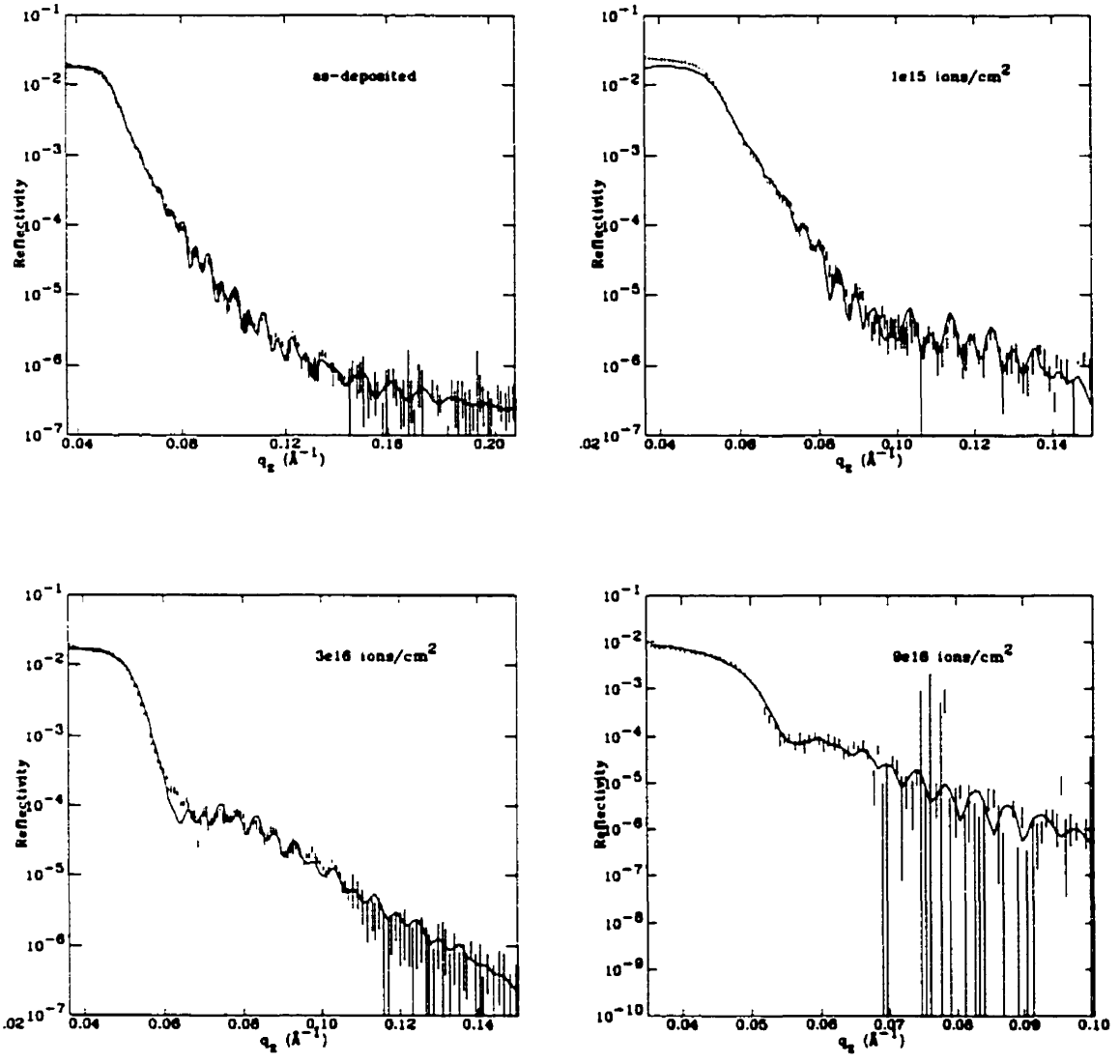

Figure 5.5: Fits (solid lines) to Si/SiO_2/Ni(500Å)/Fe(500Å) reflectivity data (dotted lines) at different irradiation doses.

Parameter	as-deposited	2×10^{15} ions/cm^2	3×10^{16} ions/cm^2
NiO thickness (Å)	23±1	28±1	30±2
NiO roughness (Å)	18.2±0.8	18.4±0.5	19.5±0.2
Ni roughness (Å)	8.9±0.4	12.9±0.9	45.8±0.7
Fe roughness (Å)	21±1	23±2	26±1
SiO_2 roughness (Å)	20±1	16±4	14±5

Table 5.1: Parameters of the Si/SiO_2/Fe(500Å)/Ni(500Å) sample at different irradiation doses obtained from fitting the reflectivity data.

Parameter	as-deposited	1×10^{15} ions/cm^2	3×10^{16} ions/cm^2	9×10^{16} ions/cm^2
Fe oxide thickness (Å)	35±1	36±1	72±1	101±1
Fe oxide roughness (Å)	12.2±0.9	13.1±0.7	13.8±0.6	26.6±0.7
Fe roughness (Å)	20.5±0.5	22.6±0.9	31.3±0.6	40.1±0.9
Ni roughness (Å)	2.2±0.2	15±2	20±3	30±5
SiO_2 roughness (Å)	16±1	16±1	21±2	20±1

Table 5.2: Parameters of the Si/SiO_2/Ni(500Å)/Fe(500Å) sample at different irradiation doses obtained from fitting the reflectivity data.

didn't have to correct for the thickness gradient as we had to in the results of our survey.

For the Si/Ni/Fe sample, the iron oxide thickness increased significantly at the two highest irradiation doses, to 72Å and 101Å, respectively. The iron oxide electron density value for the as-deposited sample is 0.6±0.2 $e^-/Å^3$ which is close to the Fe_2O_3 calculated electron density of 0.507 $e^-/Å^3$, and agrees with it within the experimental error. This value has changed systematically to become 0.9±0.2 $e^-/Å^3$ at the highest irradiation dose, which is closer to the electron density of Fe_3O_4, calculated to be 0.72 $e^-/Å^3$. These electron density values are found to be in good agreement with the position of the rings observed in the selected-area electron diffraction patterns (SAED), as will be discussed in sec. 5.5.

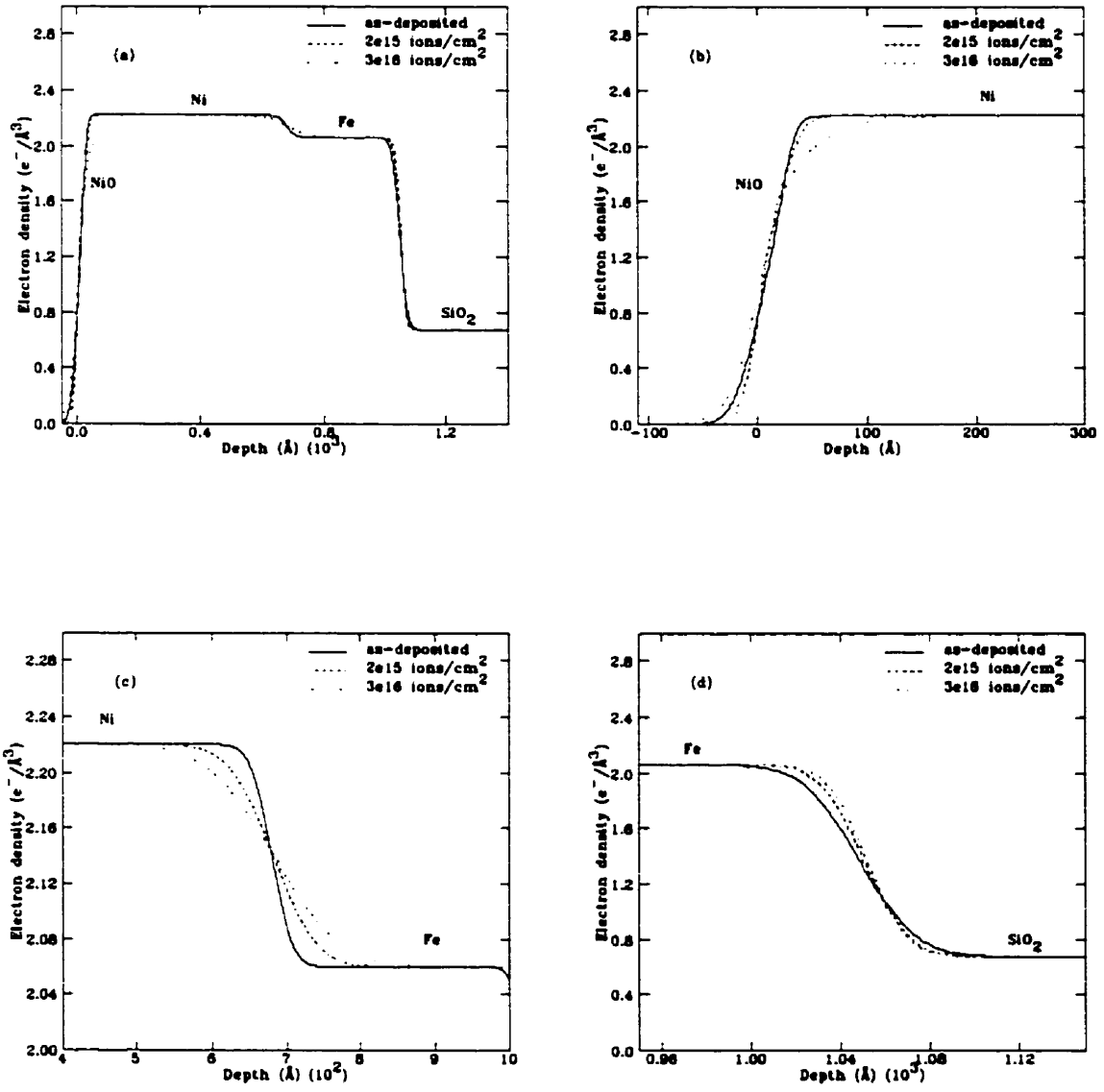

Figure 5.6: Electron density profile of $Si/SiO_2/Fe(500Å)/Ni(500Å)$ bilayer at different irradiation doses: a) $SiO_2/Fe/Ni/NiO$ interfaces: b) Ni/NiO interface: c) Fe/Ni interface: d) SiO_2/Fe interface.

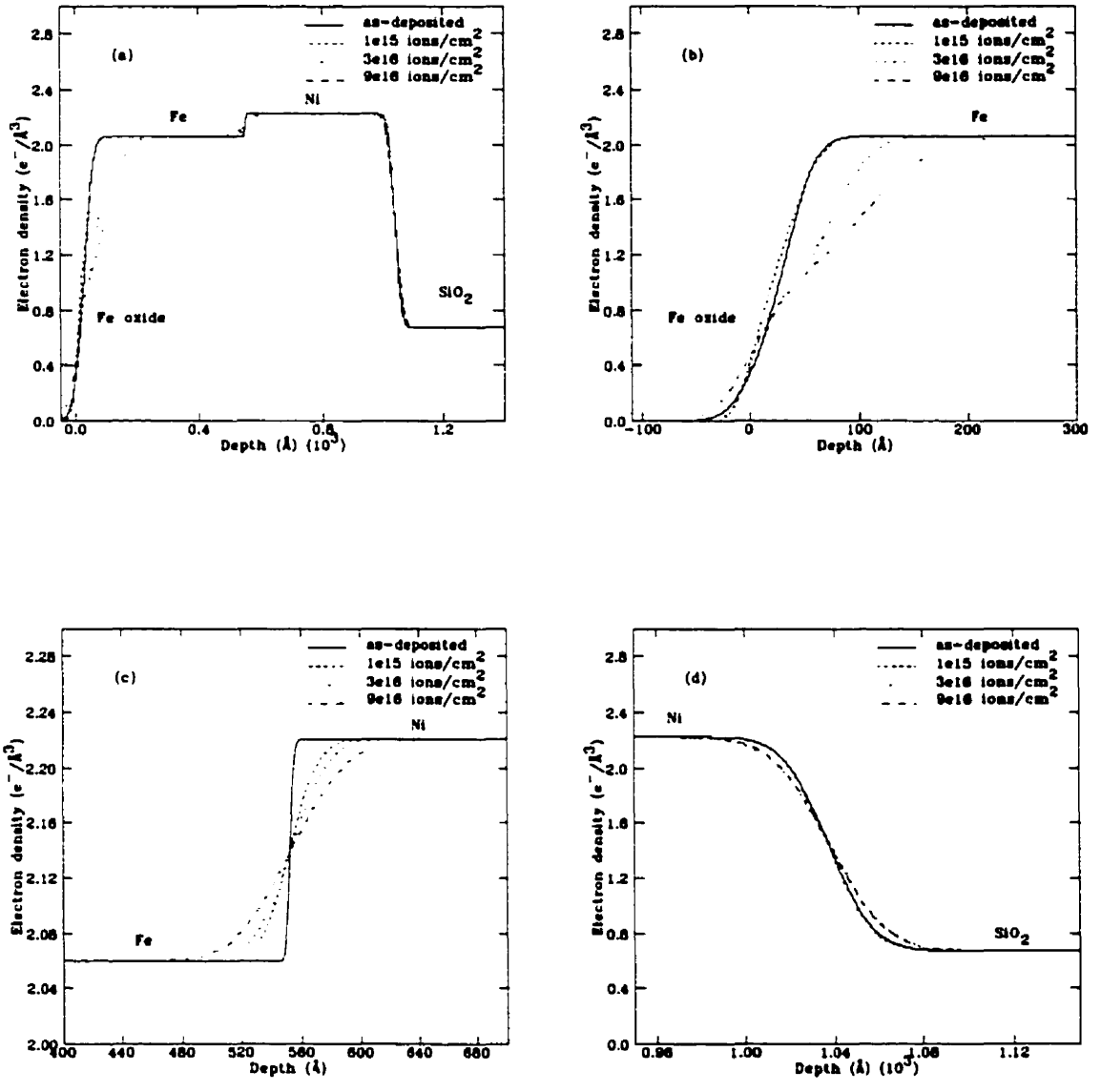

Figure 5.7: Electron density profile of $Si/SiO_2/Ni(500Å)/Fe(500Å)$ bilayer at different irradiation doses: a) SiO_2/Ni/Fe/Fe-oxide interfaces; b) Fe/Fe-oxide interface; c) Ni/Fe interface; d) SiO_2/Ni interface.

5.3 X-ray diffuse scattering data

As mentioned earlier, specular reflectivity measurements give us information about the structure normal to the interfaces, i.e. the thicknesses and electron densities of the different layers as well as their root-mean-square (rms) roughnesses. However, no explicit in-plane information can be obtained from the reflectivity scans. In order to obtain this kind of information we have to perform off-specular or diffuse scans, in which a component of the wave-vector transfer is parallel to the surface. These diffuse scans give us information about the in-plane structure, in particular the in-plane height-height correlation length of the roughness.

We have seen in sec. 5.1 that an estimate of the diffuse scattering is important even in estimating the specular reflectivity when the diffuse scattering becomes comparable to, or even greater than, the specular component. This might occur at large angles, and in our case at high irradiation doses.

In the present section we will show how to obtain information about the in-plane structure of the interfaces by analyzing the diffuse scattering data. Figures 5.8 and 5.9 show the diffuse scattering scans at different irradiation doses performed on the bilayers $Si/SiO_2/Fe(500Å)/Ni(500Å)$ and $Si/SiO_2/Ni(500Å)/Fe(500Å)$, respectively. We can clearly see the specular peak at the center of each of these scans. The intensity of this specular peak decreases as the irradiation dose increases, until it completely vanishes at the highest irradiation dose of 1.9×10^{17} ions/cm^2.

We can also see the two Yoneda wings in each of these scans at the position where the angle of incidence or the angle of reflection is equal to the critical angle of total external reflection, θ_c. The amount of diffuse scattering is represented by the area under these Yoneda wings. For the Si/Fe/Ni sample we can see that the diffuse scattering is almost the same at the first three irradiation doses, then it increases significantly at the fourth and fifth irradiation doses. For the oppositely-deposited sample, the intensity at the Yoneda wings decreases at the third irradiation dose but increases significantly at the fourth and fifth doses. This reduction in intensity however does not mean a decrease in the diffuse scattering, because if we take a closer look we can

see that the width at the bottom of the specular peak increases significantly at the third dose representing more diffuse scattering. This will be illustrated clearly in the fits to these scans.

As an example we will show the fits to the ω-scans for the Si/Ni/Fe bilayer. This bilayer is chosen because it will be further analyzed using high-angle x-ray diffraction measurements and transmission electron microscopy techniques, then all the obtained results will be compared. In order to fit the diffuse scattering scans we model the sample as a stack of five layers, as previously done for the specular reflectivity fits. The theoretical calculation of the diffuse scattering follows the method of Daillant *el al.* [52] explained in sec. 2.2.2. These calculations are fit to the experimental data using the non-linear least-squares fitting procedure explained in sec. 3.4.4.

In our calculations, the roughness structure at interfaces is described by the height-height correlation function given by eq. 3.4, where σ is the rms roughness of the interface determined from the specular fits, ζ is the in-plane correlation length and h is a measure of the fractal dimension of the interface given by $3 - h$. If $h = 1$ the fractal dimension of the interface is 2 (which equals its topological dimension) and the interface has a non-fractal (Gaussian) nature. This represents an interface with smooth hills and valleys whereas small values of h produce extremely jagged surfaces, as shown in fig. 2.5.

For the ω-scan fits, the specular and diffuse intensities are normalized and the values of the thickness, roughness, electron density and absorption coefficient of the different layers are kept constant, as much as possible, to their values obtained from the specular reflectivity fits in sec. 5.2. Therefore the only fit parameters are the correlation length, ζ, and the exponent, h.

The calculation of the diffuse scattering component is very time consuming because of the numerical integration, as discussed in sec. 2.3. In order to limit this time we have assumed that all the interfaces in our sample have the same correlation length and the same fractal dimension. Hence only one value for ζ and h is obtained from our fits.

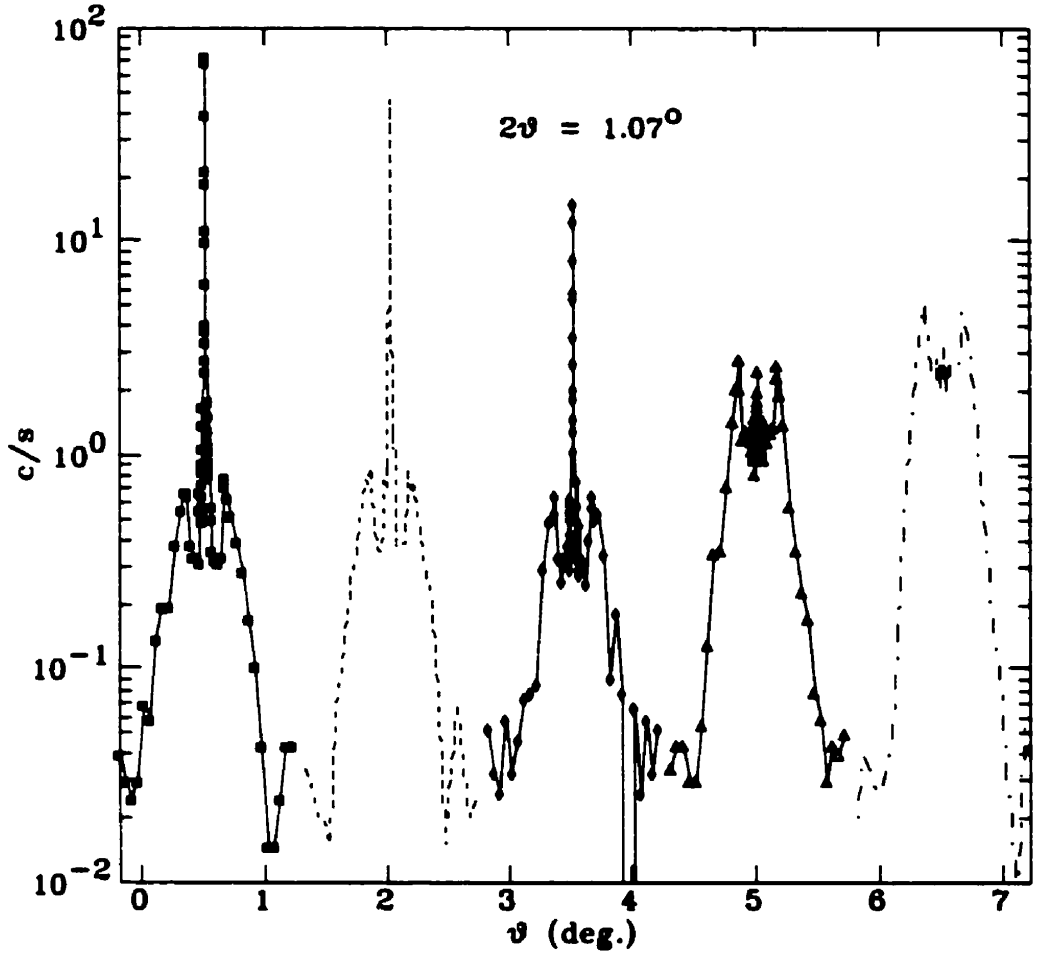

Figure 5.8: ω-scans performed on the bilayer $Si/SiO_2/Fe(500Å)/Ni(500Å)$ at $2\theta=1.07°$. The irradiation doses in ions/cm^2 from left to right are: 0, 2×10^{15}, 3×10^{16}, 9×10^{16} and 1.9×10^{17}, respectively. The plots are displaced horizontally for clarity without altering the scale. Lines are guides to the eye.

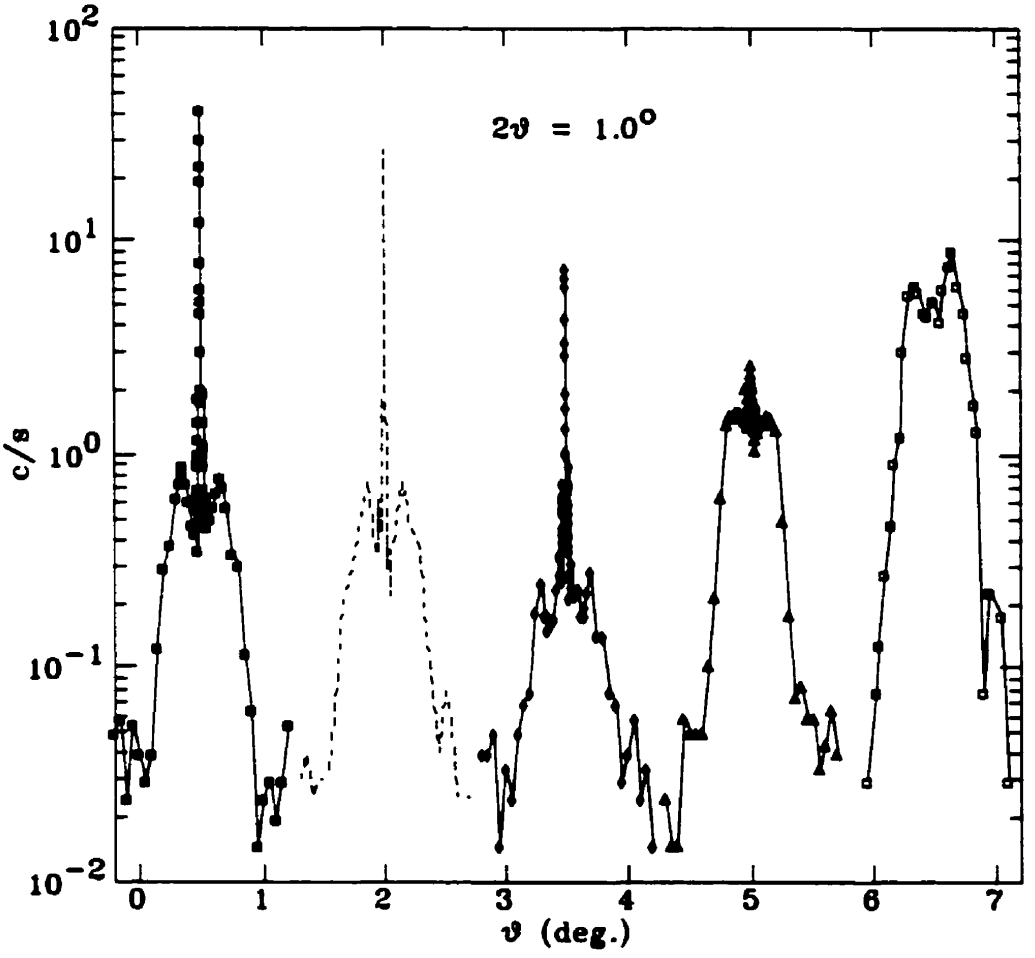

Figure 5.9: ω-scans performed on the bilayer $Si/SiO_2/Ni(500Å)/Fe(500Å)$ at 2θ=1.0°. The irradiation doses in ions/cm^2 from left to right are: 0, 1×10^{15}, 3×10^{16}, 9×10^{16} and 1.9×10^{17}, respectively. The plots are displaced horizontally for clarity without altering the scale. Lines are guides to the eye.

Figures 5.10 to 5.14 show the calculation and fits to the ω-scan data for the Si/Ni/Fe bilayer at different irradiation doses (o).

These ω-scans are the same as those shown in fig. 5.1 which are performed at each 2θ-value in order to obtain a mesh and to extract the specular reflectivity data, except that the mesh ω-scans include a few points only in a narrow range of θ (0.016°) around the specular peak and are approximated by an equal-widths Gaussian-Lorentzian lineshape in order to obtain the level of diffuse background and the integrated intensity under the specular peak. For the present ω-scans, in order to obtain information about the in-plane structure of our interfaces and to examine the roughness characteristics, we scan a much larger range in θ (0.9°) at constant 2θ-value, such that we can clearly see the Yoneda wings and our measurement extends far enough until the dark counts level. By fitting these scans to a model which describes the in-plane roughness structure at the interfaces we can obtain the height-height correlation length of the roughness and the fractal dimension of the interfaces.

As stated earlier, each of these ω-scans is composed of three components: the specular peak, the diffuse scattering and the dark counts. The dark counts form a constant linear background which is measured to be 0.032 cps.

The specular reflectivity and diffuse scattering components are calculated separately as explained in sections 2.1.3 and 2.2.2, respectively, and are added to the constant dark counts in order to obtain the total scattered intensity. This total intensity is then fit to the experimental data. The fits thus obtained are shown as solid lines in parts (a) of figures 5.10 to 5.14.

Parts (b) of these figures show a plot of each of these three components calculated separately at each irradiation dose (o). As can be seen, the specular component decreases as o increases until it completely vanishes at $o = 1.9 \times 10^{17}$ cm^{-2}. On the other hand, the diffuse component increases systematically with o.

At $o = 3 \times 10^{16}$ cm^{-2} we can see from fig. 5.12(a) that the experimental data at the bottom of the specular peak becomes broader. This is caused by a substantial increase in the diffuse component causing a hill in the nonspecular intensity near the

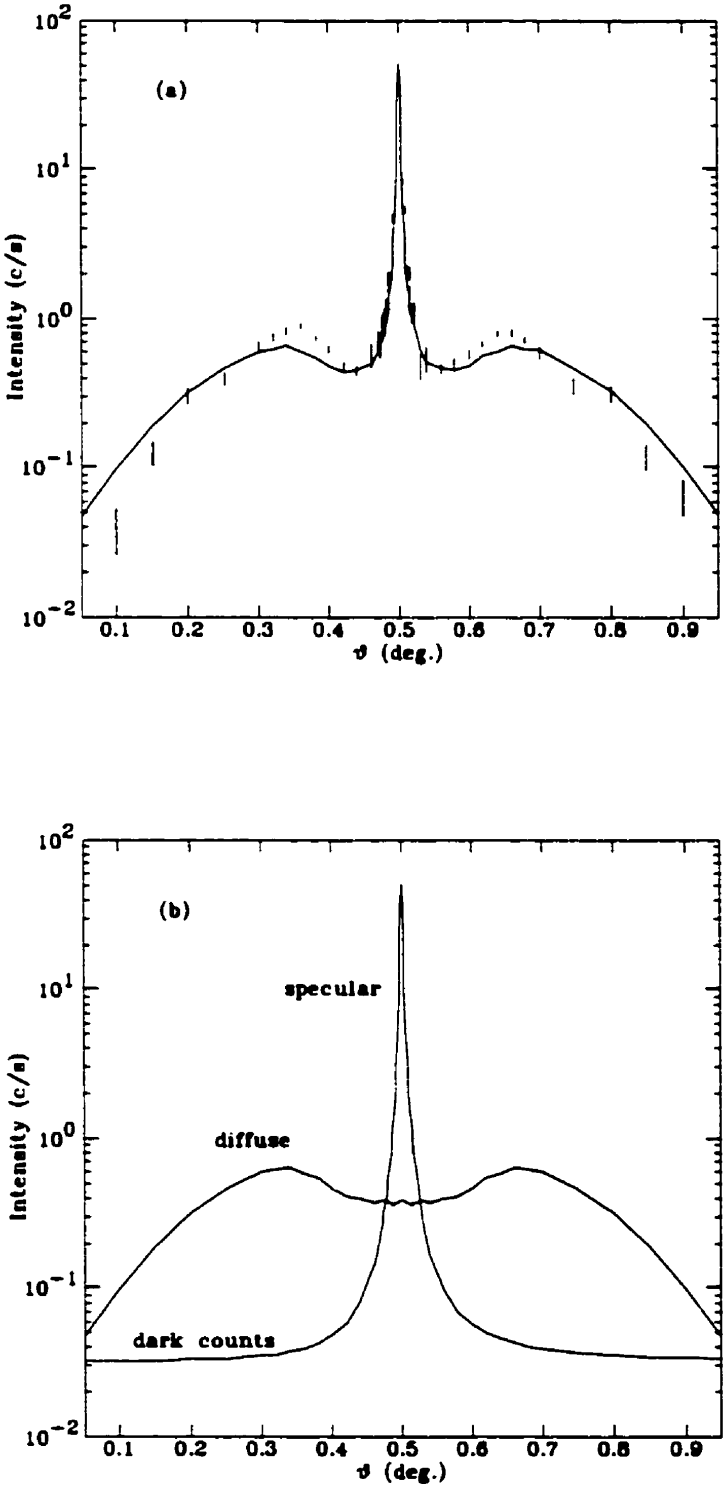

Figure 5.10: As-deposited $Si/SiO_2/Ni(500Å)/Fe(500Å)$ bilayer ω-scan at $2\theta = 1.0°$: a) fit (solid line) to the ω-scan data (dotted line): b) the specular and diffuse components of the calculated fit.

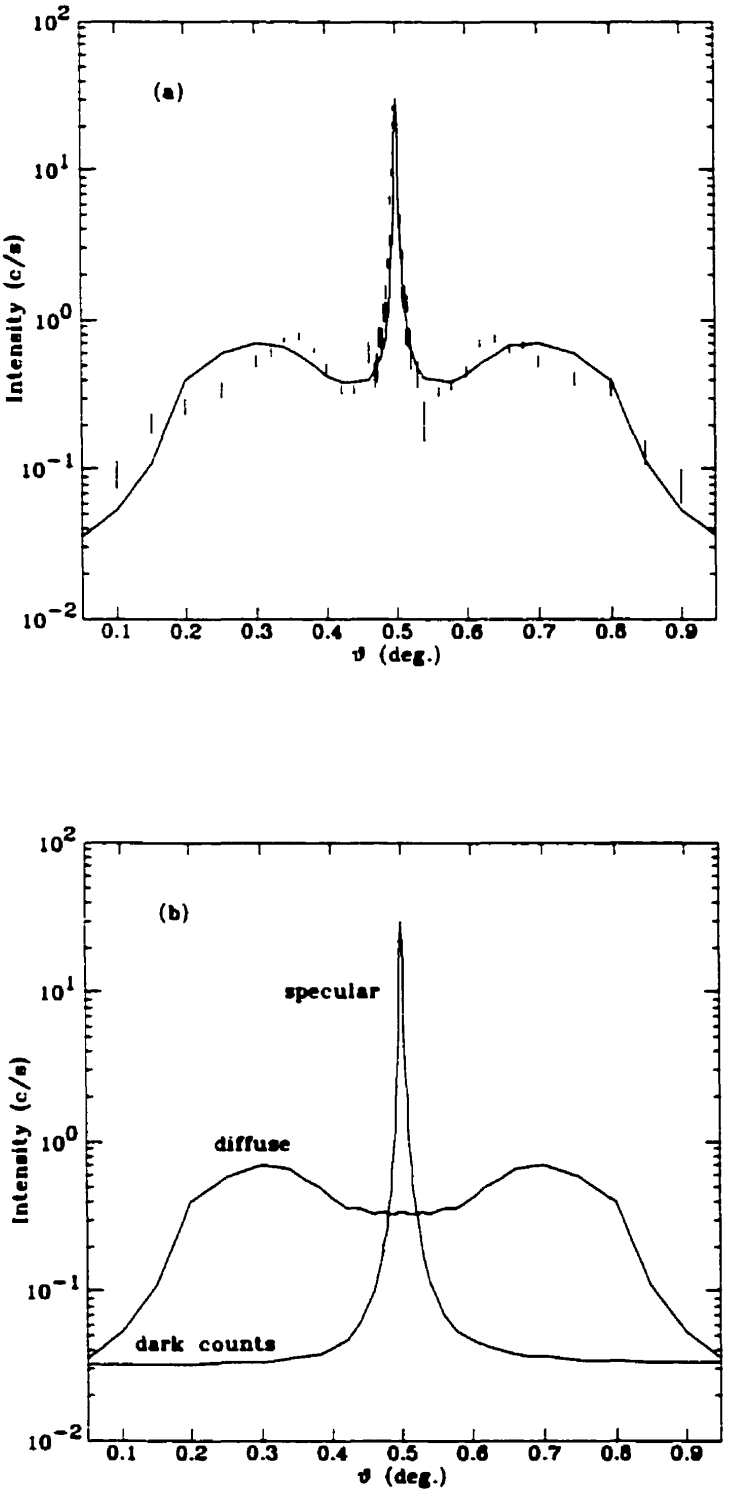

Figure 5.11: ω-scan performed at $2\theta = 1.0°$ for the $Si/SiO_2/Ni(500Å)/Fe(500Å)$ bilayer irradiated at 1×10^{15} ions/cm^2: a) fit (solid line) to the ω-scan data (dotted line); b) the specular and diffuse components of the calculated fit.

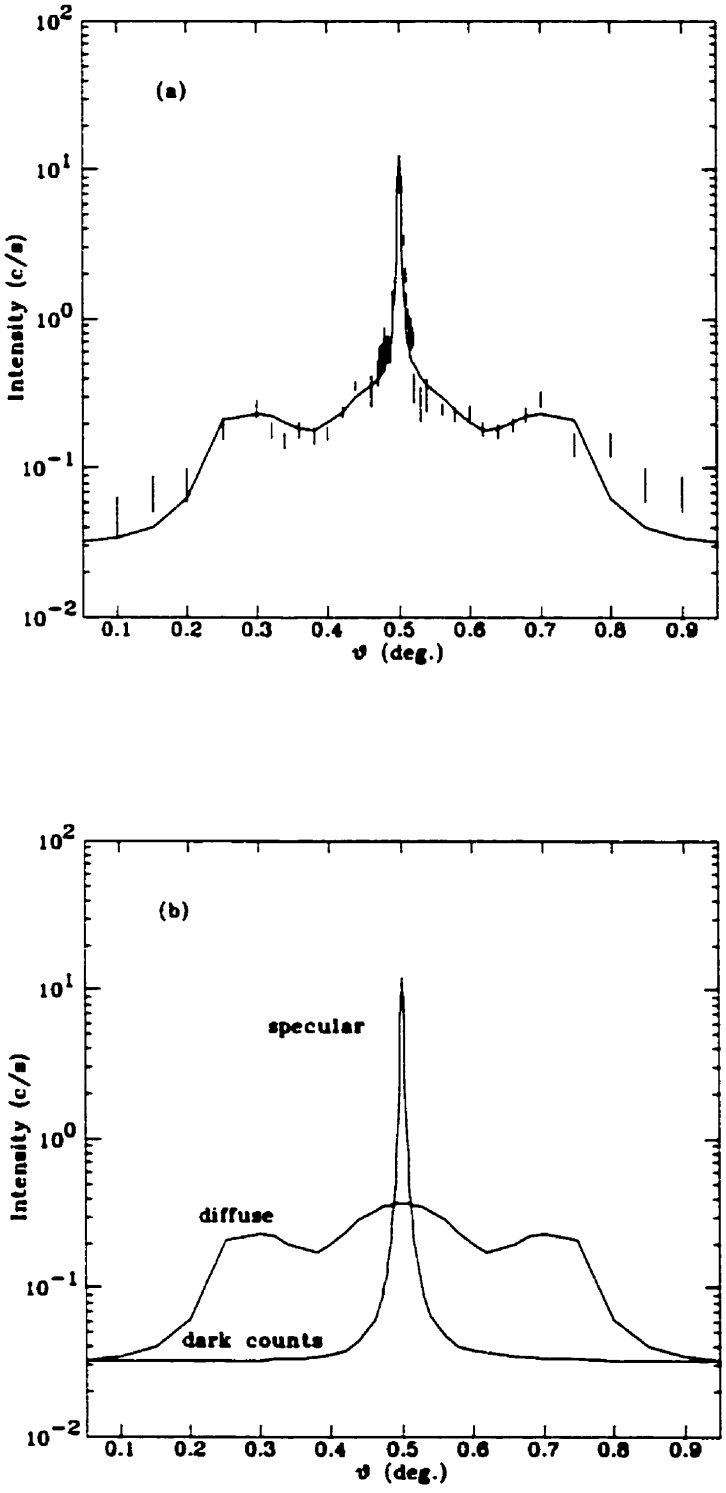

Figure 5.12: ω-scan performed at $2\theta = 1.0°$ for the $Si/SiO_2/Ni(500Å)/Fe(500Å)$ bilayer irradiated at 3×10^{16} ions/cm^2: a) fit (solid line) to the ω-scan data (dotted line): b) the specular and diffuse components of the calculated fit.

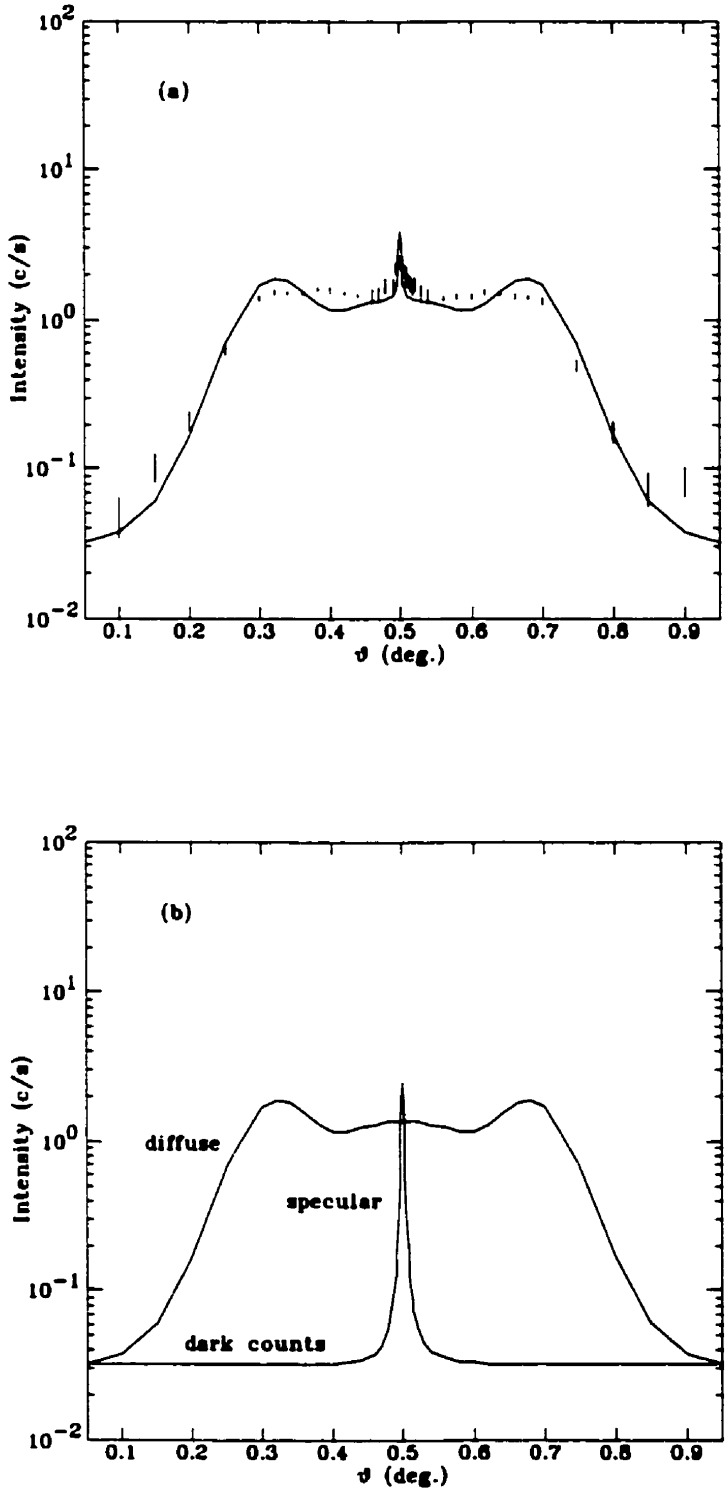

Figure 5.13: ω-scan performed at $2\theta = 1.0°$ for the $Si/SiO_2/Ni(500Å)/Fe(500Å)$ bilayer irradiated at 9×10^{16} ions/cm^2: a) fit (solid line) to the ω-scan data (dotted line); b) the specular and diffuse components of the calculated fit.

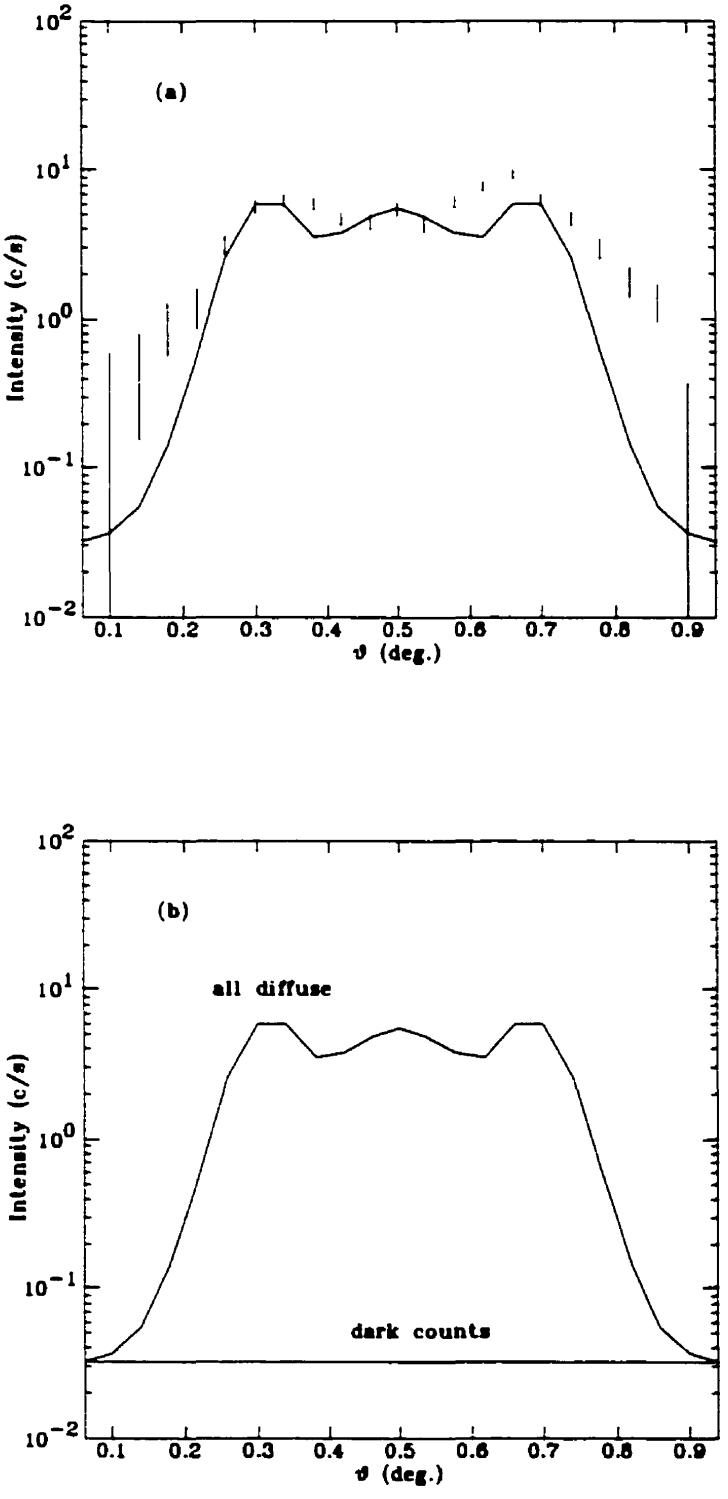

Figure 5.14: ω-scan performed at $2\theta = 1.0°$ for the $Si/SiO_2/Ni(500Å)/Fe(500Å)$ bilayer irradiated at 1.9×10^{17} ions/cm^2: a) fit (solid line) to the ω-scan data (dotted line); b) the dark counts and diffuse component of the calculated fit. no specular component is measured at this high irradiation dose.

specular peak as seen in fig. 5.12(b), which occurs because of a large increase in the Fe layer roughness. Another broad maximum in the diffuse scattering is observed at $\phi = 1.9 \times 10^{17}$ cm^{-2} near the specular peak, as seen in fig. 5.14(b), which is caused this time by the small value of h (h=0.17), since it was found that a maximum in the nonspecular scattering occurs at this position for $h < 0.5$ [53], as discussed in sec. 2.3.

The parameters obtained from these fits are the in-plane height-height correlation length of the roughness, ζ, and the exponent h. Figures 5.15(a) and 5.15(b) show the variation in the values of ζ and h with ϕ.

At low irradiation doses the interfaces are smooth as shown by the value of $h = 1$. As ϕ increases, the interfaces become more jagged and h decreases to 0.5 at $\phi = 3 \times 10^{16}$ cm^{-2} then decreases further to around 0.2 at higher doses. This represents an extremely jagged roughness structure at the interfaces, as seen from fig. 2.5. Furthermore, the height-height correlation length is large in the as-deposited sample, $\zeta = 220 \pm 7$ Å, but decreases systematically as ϕ increases until it reaches a small value of 16 ± 9 Å at the highest irradiation dose. This reduction in ζ also shows that the roughness texture becomes more jagged as the hills become closer to each other in the plane of the interfaces.

Figure 5.16(a) shows the effect of irradiation on the rms roughness of the different layers in our sample. Except for the SiO_2 roughness which almost doesn't change, the roughness of the Ni, Fe and iron oxide layers increases systematically with irradiation dose, ϕ. The obtained values agree very well with those obtained from the reflectivity fits. We note that any discrepancy between the roughness values obtained from the reflectivity fits, σ_{spec}, and those obtained from the diffuse scattering fits, σ_{diff}, arises from the difference between graded and rough interfaces. Whereas both kinds of imperfection reduce the specular intensity, only σ_{diff} contributes to the measured non-specular intensity. The fact that σ_{spec} and σ_{diff} values agree well with each other implies that our interfaces are mostly of the rough, not the graded, type.

We note that we can also obtain the values of the rms roughness of the different layers at $\phi = 1.9 \times 10^{17}$ cm^{-2} for which no specular reflectivity is measured. Hence

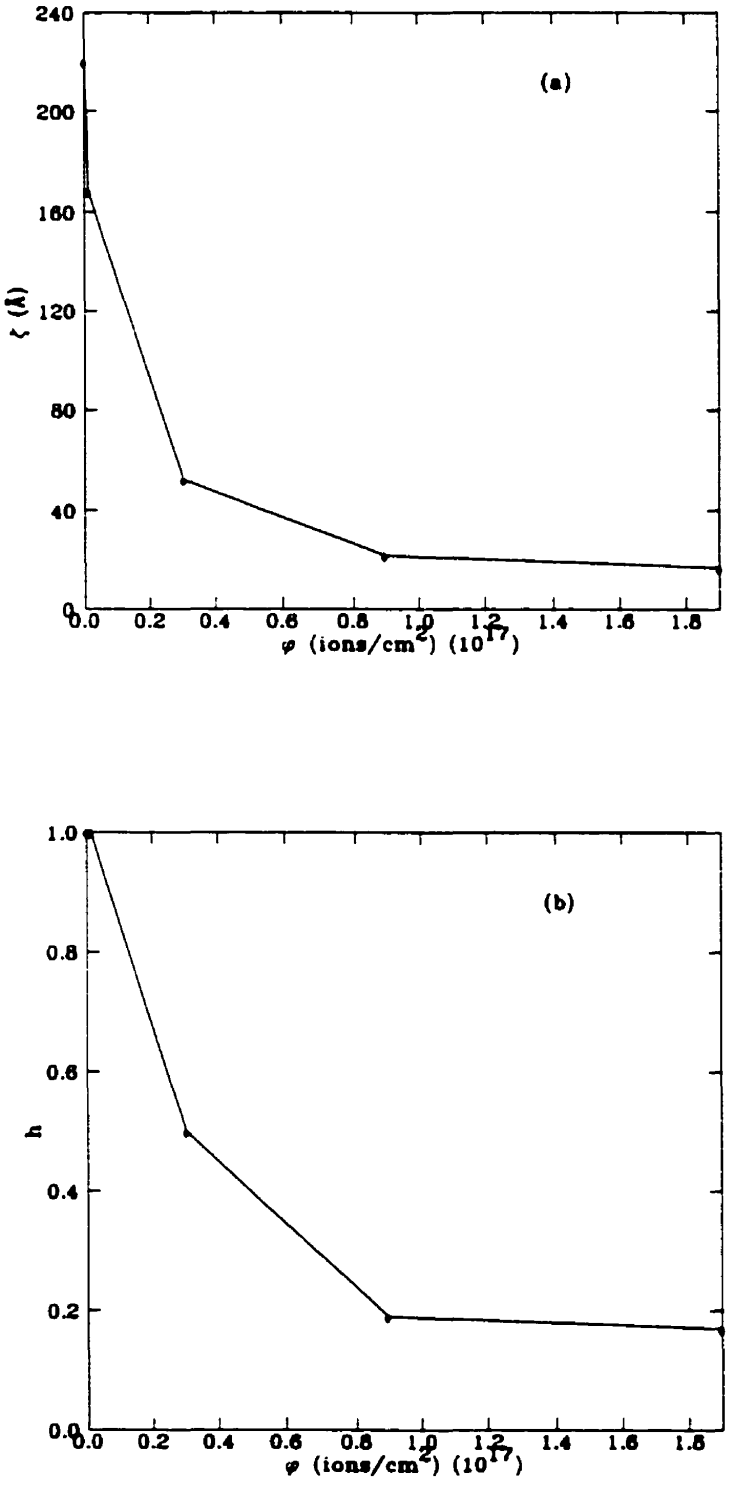

Figure 5.15: The effect of ion beam irradiation on: a) the height-height correlation length, ζ: and b) the exponent h. The solid lines are guides to the eye.

the diffuse scattering fits give us a way to analyze the sample structure when the specular reflectivity component is very weak.

In order to test the cascade mixing width dependence on the ion dose, given by eq. 2.64, a plot of the roughness of the Fe layer as a function of the square root of the dose is given in fig. 5.16(b). The data fits remarkably well to a straight line having a slope of 6.35±0.09 Å^2. In order to estimate the slope from eq. 2.64, typical values of F_D=35 eV/Å, R_c=10Å and E_c=25 eV are taken [41, 147]. The atomic masses of Si and Fe are used to calculate ξ_{21} and N is given by the atomic density of Fe. We obtain a slope of 18 Å^2, which is close to our experimental value giving the accuracy of the typical values we used. The calculation also yields a cascade mixing width of 77.5 Å at the highest irradiation dose of 1.9×10^{17} ions/cm^2 whereas experimentally, we obtain a roughness of 48.6 Å at this ion dose. Hence, the intermixing between the Fe and iron oxide layers can be approximated using the ballistic model of ion mixing.

Thus we can conclude that the interfaces in our sample are initially smooth with large height-height correlation length and small values of the rms roughness. As ϕ increases the correlation length decreases, the rms roughness at the different interfaces increases and the surface becomes more jagged, even extremely jagged at the two highest irradiation doses with $h \approx 0.2$ and $\zeta \approx 20$ Å. The ion beam mixing can be approximated using the ballistic model.

It was found that the ω-scans fits are more sensitive to the oxide layer electron density value and to the roughness values of the oxide and the top layers than the specular reflectivity fits. We were able to obtain the diffuse scans fits using the same values for the oxide electron density and roughness values as those obtained from the reflectivity fits, which confirms the accuracy of these values.

In general, the fits are reasonably good which shows that the present model approximates well the roughness structure of our interfaces. The discrepancies between the fits and the data show that the roughness of the interfaces is not exactly given by the simple expression used in our model. For example, we have assumed that all the interfaces in our sample have the same value of ζ and h which is an oversimplification

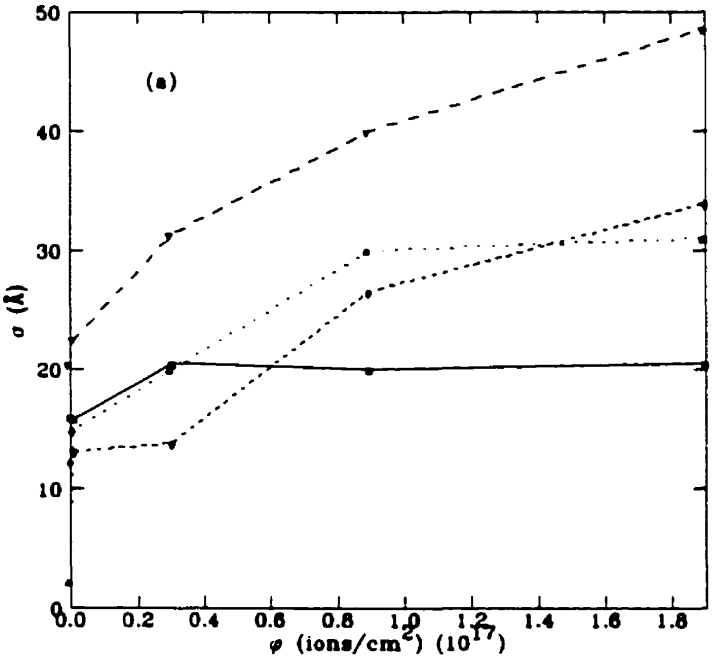

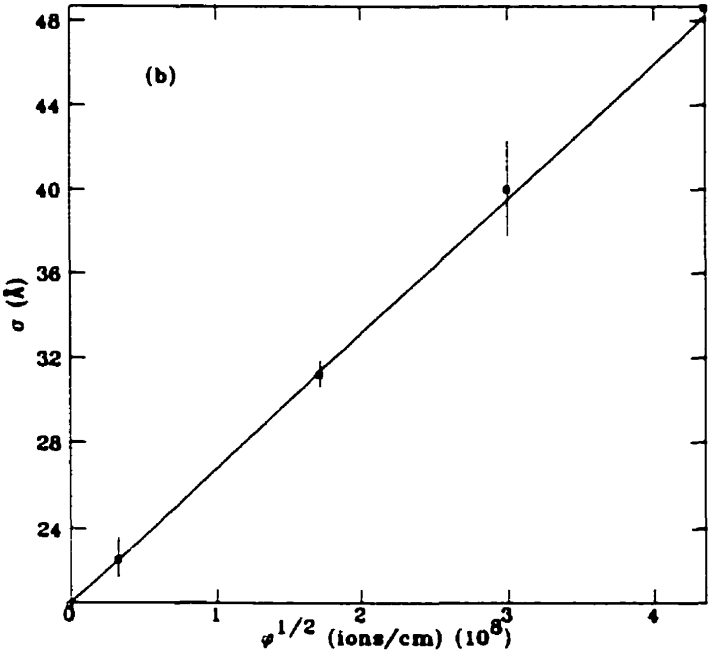

Figure 5.16: a) The effect of irradiation dose, ϕ, on the roughness of the different layers: short-dashed line: iron oxide, long-dashed line: Fe, dotted line: Ni, solid line: SiO_2. Lines are only guides to the eye; b) the roughness of the Fe layer, representing the cascade mixing width, is proportional to $\phi^{1/2}$. The solid line is a linear fit to the experimental points.

to the model. Furthermore, we consider the interfaces to be totally uncorrelated, whereas they might be partially or totally correlated which is not taken into account in our model.

5.4 High-angle x-ray diffraction data

We have seen that small-angle x-ray scattering gives us information about the average electron density in the layers of the sample as well as the rms roughness of the interfaces. However, it doesn't contain any information about the crystallographic structure of the bulk material. In order to probe this crystal structure, high-angle x-ray diffraction (XRD) measurements were performed on the $Si/SiO_2/Ni(500Å)/Fe(500Å)$ bilayer at the different irradiation doses. The results of these $\theta - 2\theta$ XRD scans in the range of 2θ from 40° to 100° are shown in fig. 5.17.

Several Bragg peaks were indexed as shown in the caption of the figure. Peak (2) located at $2\theta = 44.62°$ is very close to the bulk positions for fcc Ni(111)($2\theta = 44.53°$) and bcc Fe(101)($2\theta = 44.72°$). Much weaker Ni(002), Fe(112), Ni(113) and Ni(222)/Fe(202) Bragg peaks were also found indicating a polycrystalline structure for the bilayer. At all ion doses the integrated intensity of the main peak (2) is approximately 50 times larger than that for the other crystalline orientations indicating a strong texture with fcc Ni(111) and bcc Fe(101) planes parallel to the substrate surface [128]. Peak (1) located at $2\theta = 42.8°$ is close to the $Fe_3O_4(004)$ peak ($2\theta = 43.09°$). Figure 5.18 shows a narrower region of these high-angle scans.

We can see that the intensity of peak (1) increases with irradiation dose (ϕ) thus representing more surface iron oxide in agreement with the previous XRR analysis and with the TEM results presented in the next section. It is also seen that as ϕ increases the Ni(111)/Fe(101) Bragg peak shifts towards larger 2θ values and becomes sharper and more intense. This is caused by an overall reduction of structural disorder by the formation of larger grains. The average grain size in the growth direction, L, is

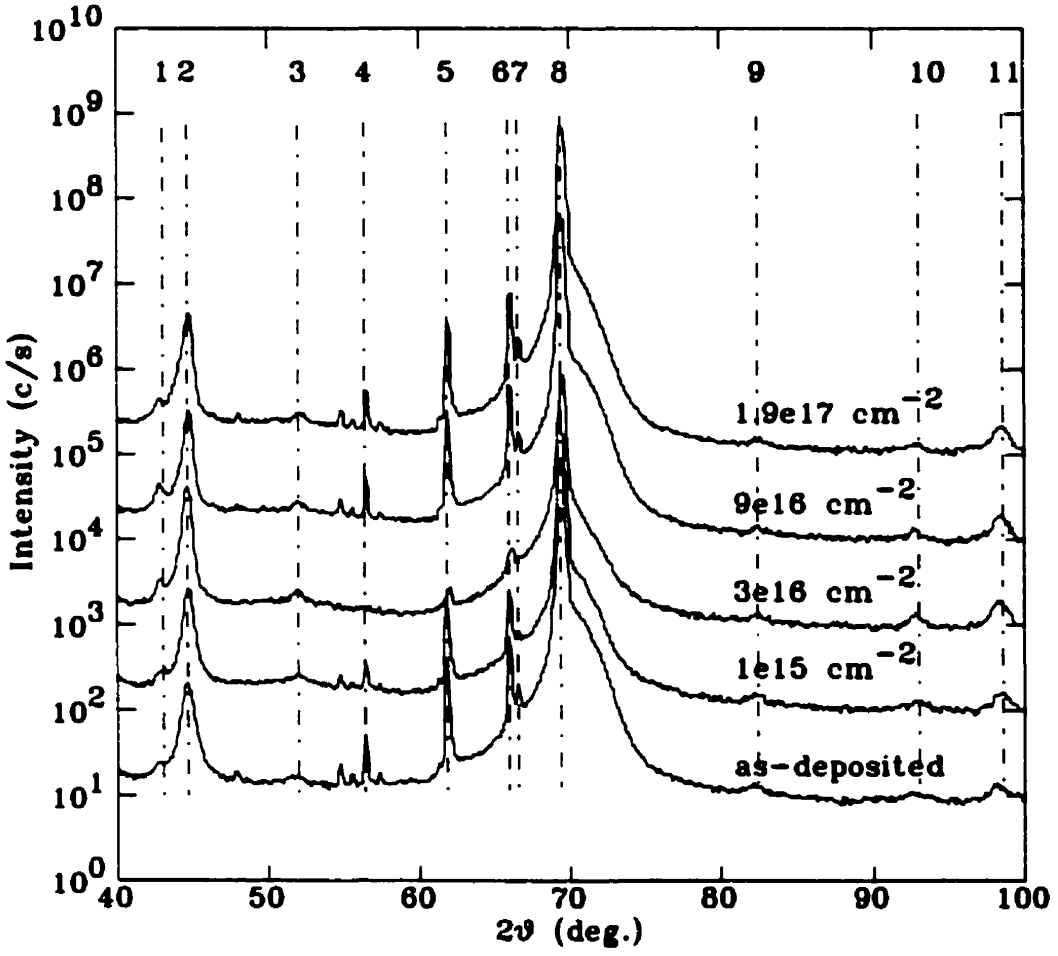

Figure 5.17: High-angle x-ray diffraction data for the $Si/SiO_2/Ni(500Å)/Fe(500Å)$ bilayer at different irradiation doses. The experimental data is displaced vertically for clarity without altering the scale. The different Bragg peaks correspond to: 1) $Fe_3O_4(004)$; 2) Ni(111)/Fe(101); 3) Ni(002); 4-8) SiO_2; 9) Fe(112); 10) Ni(113); 11) Ni(222)/Fe(202).

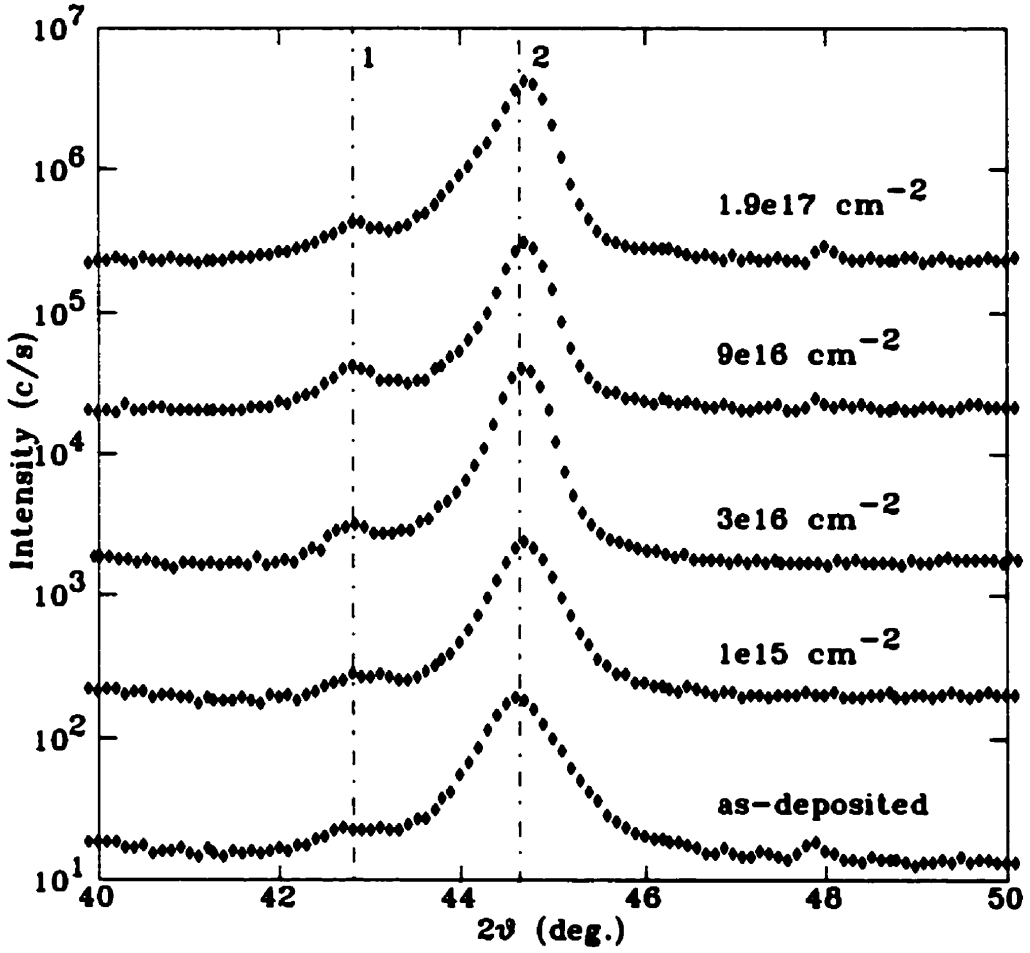

Figure 5.18: The change in the Fe_3O_4(004) Bragg peak (1) and the Ni(111)/Fe(101) Bragg peak (2) for the Si/SiO_2/Ni(500Å)/Fe(500Å) bilayer with irradiation dose. The experimental data is displaced vertically for clarity without altering the scale.

calculated using the Scherrer formula [112, 132] given by:

$$B(2\theta) = \frac{0.94\lambda}{Lcos\theta}, \tag{5.1}$$

where $B(2\theta)$ is the full width in radians subtended by the half maximum intensity of the peak (FWHM) and λ is the x-ray wavelength. It was found that L increases from $\sim$ 140 Å for the as-deposited sample to $\sim$ 305 Å after irradiation with 9×10^{16} ions/cm^2. This result agrees with the results of the TEM analyses presented in section 5.5.

5.5 *TEM and XTEM plots*

Four identical Si/SiO_2/Ni(500Å)/Fe(500Å) bilayers were also deposited in order to probe the effect of ion beam irradiation on their structural properties using plane-view and cross-sectional transmission electron microscopy (TEM and XTEM) techniques.

These bilayers were irradiated to different irradiation doses, namely ϕ = 0, 1 × 10^{15}, 2 × 10^{16} and 1 × 10^{17} ions/cm^2. They were characterized before and after irradiation using low-angle x-ray reflectivity and high-angle x-ray diffraction measurements [128]. The x-ray scans were found to be almost identical to the Si/SiO_2/Ni/Fe bilayer data investigated in the previous sections. TEM and XTEM analyses were carried out on these samples by P. Desjardins[1].

Figure 5.19 shows plane-view TEM images for the as-deposited and the irradiated samples, together with selected-area electron diffraction patterns (SAED). The layers are fully dense with no evidence of inter-grain porosity. The average in-plane grain size increases from about 125 Å for the as-deposited sample to ~350 Å after irradiation at 1 × 10^{17} cm^{-2}.

The most intense diffraction ring in the SAED pattern corresponds to the Ni(111)/ Fe(101) peak in agreement with the XRD results of sec. 5.4. No change in the relative intensities of the various rings was detected following irradiation. The diffraction rings gradually become composed of discrete spots as ϕ increases due to the significant grain growth.

[1]Materials Science and Engineering Department, the Coordinated Science Laboratory, and the Materials Research Laboratory, University of Illinois at Urbana-Champaign.

In part (d) of the figure, at $\phi = 1 \times 10^{17}$ cm^{-2}, two additional rings appear near the center of the diffraction pattern. They correspond to the (222) and the (113) peaks of Fe_3O_4. The Fe_3O_4(004) peak was also observed in the XRD curves.

Figure 5.20 shows XTEM images for the samples at different doses ϕ. The layers are fully dense with no evidence of either inter- or intra-grain porosity in agreement with the plane-view images. Ni and Fe layer thicknesses determined from the micrographs are 485 and 515 Å, respectively, in agreement with the values obtained from XRR measurements. The grain size increases gradually after irradiation in both the in-plane and the out-of-plane directions from $\sim$ 120 and $\sim$ 160 Å, respectively, in the as-deposited sample to $\sim$ 470 and $\sim$ 450 Å for Ni and $\sim$ 440 and $\sim$ 405 Å for Fe after irradiation to 1×10^{17} cm^{-2}. The in-plane grain size values agree with those obtained from the plane-view TEM images and the out-of-plane values agree reasonably well with those obtained from the XRD curves.

We also observe that the interface between the Fe and the Ni layers remains sharp after irradiation and the surface iron oxide layer thickness increases with ϕ, from $\sim$ 30 Å in the as-deposited sample to $\sim$ 100 Å after 1×10^{17} cm^{-2} irradiation, in good agreement with the values obtained from XRR measurements which are given in table 5.2.

It should be noted that the values given in the previously-mentioned table correspond to another sample which was irradiated successively and measured at relatively longer intervals of time than the four identical samples which were irradiated to different doses and measured almost simultaneously. Since the iron oxide thickness values agree remarkably well in both cases, this increase in oxide thickness is mainly attributed to the irradiation process itself, and not caused by longer exposures to ambient air.

5.6 Discussion

In this chapter we have presented an intensive study of the effect of ion beam irradiation on the structure of Ni/Fe bilayers. The samples were deposited by sputtering

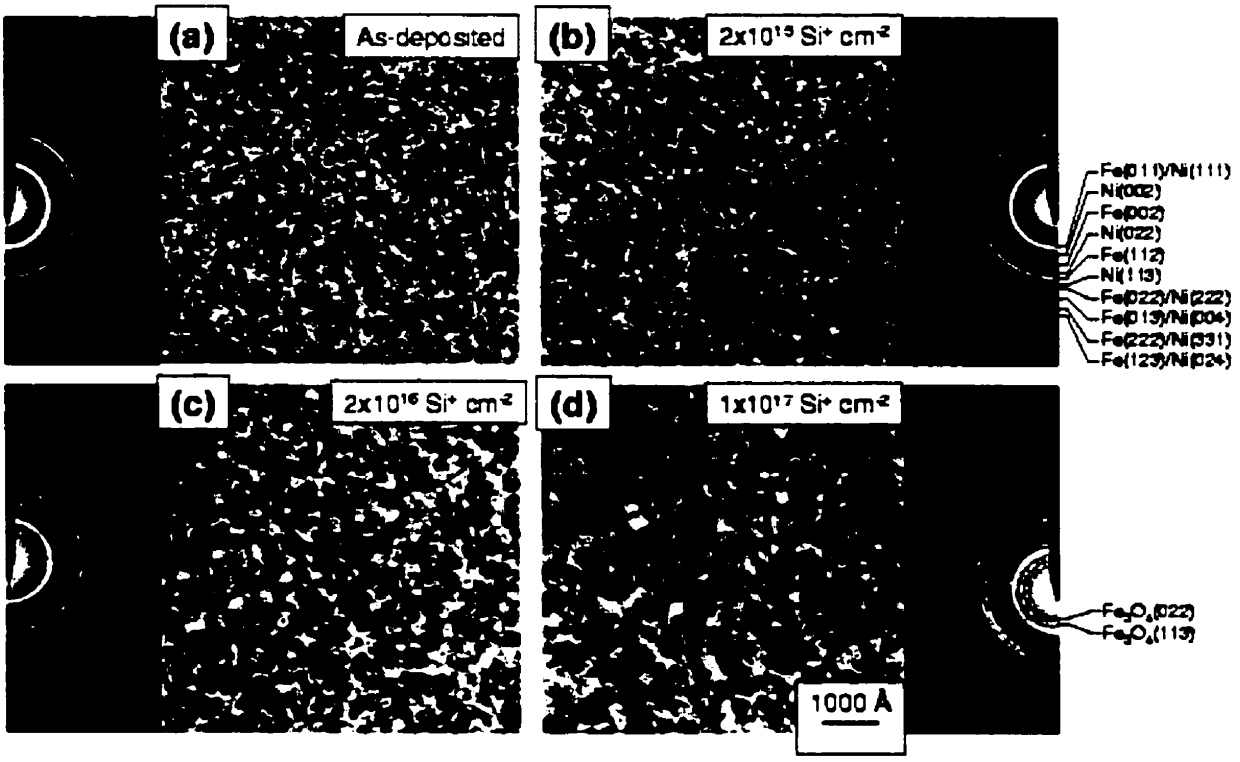

Figure 5.19: Plane-view transmission electron microscopy images for the as-deposited and the irradiated bilayers together with the selected-area electron diffraction patterns.

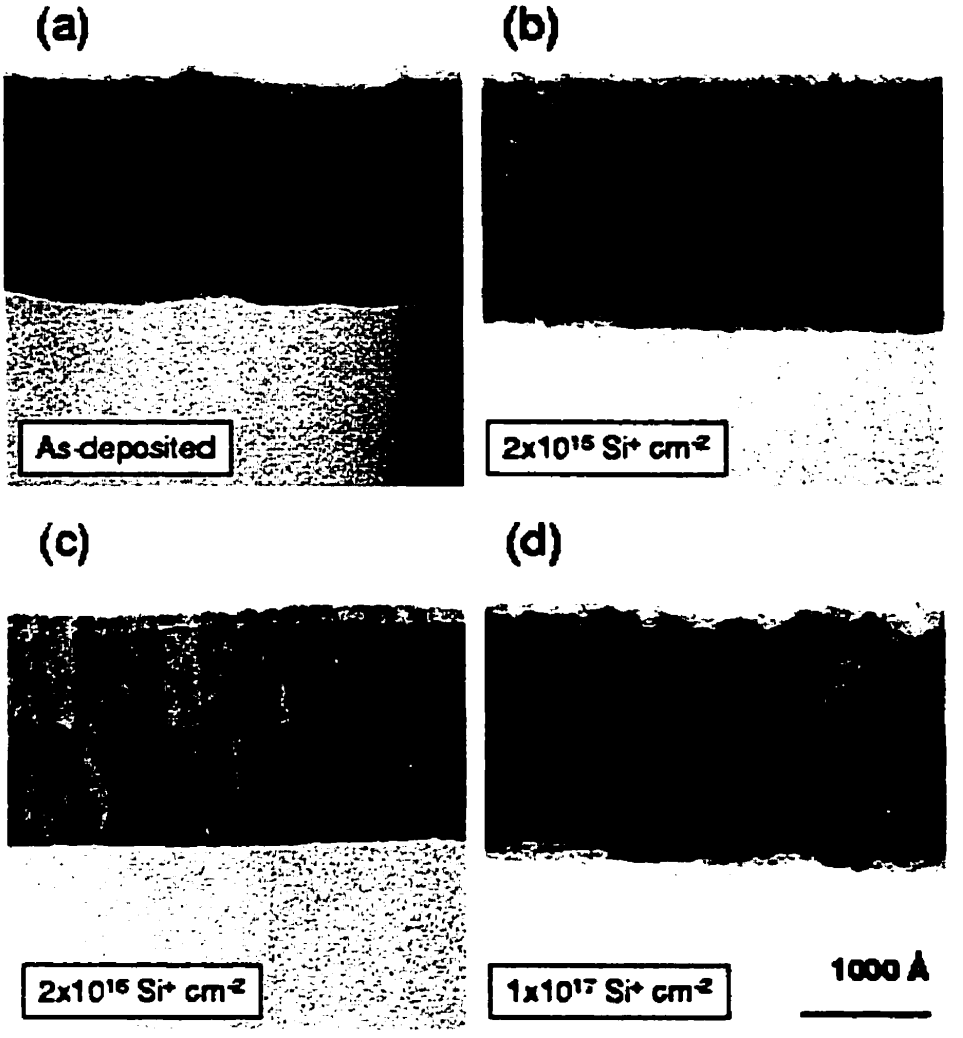

Figure 5.20: Cross-sectional TEM images for the bilayers irradiated at different doses.

techniques and irradiated by 1 MeV Si^+ ions to doses, ϕ, up to 1.9×10^{17} ions/cm^2. The structure was probed using x-ray reflectivity (XRR), x-ray diffuse scattering (XDS), high-angle x-ray diffraction (XRD) and plane-view and cross-sectional transmission electron microscopy (TEM, XTEM) techniques.

It was found in sec. 5.1 that separating the diffuse scattering component from the specular reflectivity component is crucial to the XRR analysis at high doses ϕ, because the diffuse component becomes very large as ϕ increases, sometimes even larger than the specular component.

Information about the structure normal to the interfaces was obtained using XRR techniques and the electron density profile was plotted for the sample at different doses. It was found that the rms roughness of the different interfaces increases with ϕ. The oxide layer thickness also increased from ~ 35 Å in the as-deposited sample to ~ 100 Å at $\phi = 9 \times 10^{16}$ cm^{-2}.

In order to obtain information about the in-plane roughness structure of the sample and the height-height correlation length, ζ, parallel to the interfaces, x-ray diffuse-scattering scans were performed. From the fits we obtain the values of ζ and the exponent h at each irradiation stage. It was found that at low irradiation doses the interfaces are smooth as shown by a value of $h = 1$ and a large value of ~ 220 Å for ζ. The value of h decreases to 0.5 at $\phi = 3 \times 10^{16}$ cm^{-2} and decreases even further to ~ 0.2 at higher doses, while ζ decreases to ~ 16 Å at $\phi = 1.9 \times 10^{17}$ cm^{-2}. This shows that as ϕ increases, the interfaces become more jagged and the hills in the roughness become closer to each other in the plane of the interfaces.

By plotting the roughness of the Fe layer as a function of the square root of irradiation dose we see that $\sigma \propto \phi^{1/2}$ as predicted by the cascade mixing width relation, eq. 2.64. Thus, the ion beam mixing at this interface can be approximated using the ballistic model of ion mixing.

A study of the high-angle XRD pattern is essential in order to probe the crystallographic structure of the bulk material. We found that our sample is polycrystalline with a strong texture of fcc Ni(111) and bcc Fe(101) planes parallel to the substrate

surface. We also found an $Fe_3O_4(004)$ Bragg peak whose intensity increases with ϕ. From the FWHM of our Ni(111)/Fe(101) main Bragg peak and using the Scherrer formula we were able to calculate the grain size to be $\sim$ 140 Å for the as-deposited sample and $\sim$ 305 Å at $o = 9 \times 10^{16}$ cm^{-2}.

This latter result agrees reasonably well with the out-of-plane grain sizes obtained from the XTEM images. Also from these images we found that the Ni/Fe interface remains sharp upon irradiation and the iron oxide thickness values agree remarkably well with the values obtained from XRR analysis.

Finally the plane-view TEM images allowed us to measure the in-plane grain size which also increases upon irradiation. The obtained values agree with the values obtained from the XTEM images. On the other hand, the decrease in the height-height correlation length, ζ, as o increases shows that ζ is not a measure of the grain size but of in-plane correlations on grain surfaces. The SAED rings agree with the Bragg peaks measured using XRD, and show the increase in Fe_3O_4 peak intensity as o increases.

This shows that x-ray diffraction techniques represent a versatile, powerful and non-destructive way to investigate the structure of bilayers, and subsequently, of multilayers, both in the bulk layers as well as at interfaces. By using different measurement techniques, XRR, XDS and XRD, we are able to probe the structure both perpendicular to and parallel to the interfaces, as well as the bulk crystallographic structure of the different layers. Finally, TEM and XTEM results agree well with our x-ray analysis.

6

CONCLUSION

Metallic multilayers consisting of alternating layers of magnetic and non-magnetic materials exhibit interesting giant magnetoresistance (GMR) effects which are useful for a wide range of applications. These magnetic properties depend sensitively on the structural properties, especially at interfaces. Interdiffusion and roughness affect the details of the interlayer magnetic coupling across the interfaces.

In order to study the effect of structure on magnetic properties of thin films and multilayers, experimental techniques must be used to modify the structural properties and various methods are needed in order to probe and analyze the structure.

From our previous studies of Ni/Fe [28] and Co/Cu [40, 41] multilayers, very interesting GMR and magnetotransport properties were found. Ion beam irradiation (IBI) was used in order to induce mixing at the interfaces and proved to be a suitable ex situ technique for systematically modifying the structure of the samples. Furthermore, x-ray scattering techniques are very well established and constitute a very powerful tool for structural characterization.

Therefore, in the present thesis, we chose to study the change in interface structure produced by IBI in Ni/Fe and Co/Cu samples using various x-ray scattering techniques. Since we are mainly interested in interfacial changes, we chose to limit ourselves to the study of bilayer samples in order to reduce the number of interfaces, hence, the number of fit parameters will be reduced leading to a more detailed analysis of interface structure.

First, we reviewed various theoretical derivations of x-ray reflectivity (XRR) and x-ray diffuse scattering (XDS) cross section. We discussed the properties of self-affine

surfaces and introduced the height-height correlation function used in our model. Ballistic and thermodynamic models of ion mixing were also introduced.

We used several x-ray scattering techniques for structural characterization. X-ray reflectivity data were taken in order to obtain information about the structure of the samples in a direction normal to the interfaces, namely, the thickness and root-mean-square (rms) roughness of the different layers and the electron density profile. In order to probe the in-plane lateral structure at interfaces, x-ray diffuse scattering measurements were performed. By analyzing the diffuse-scan data we can distinguish between rough and graded interfaces and obtain information about the in-plane roughness structure, such as the height-height correlation function parameters.

We started by establishing and testing a good setup for our diffractometer, by optimizing the slits settings, the pulse height analyzer settings, by filtering out the K_{α_2} line and by including a new sample holder and new stepping motor controllers.

A normal $\theta - 2\theta$ scan will include both the specular and diffuse components of x-ray scattering intensity. The diffusely-scattered intensity has to be subtracted first from the total intensity before we try to fit the reflectivity. This separation is very important at high irradiation doses because the diffuse scattering component becomes very large relative to the specular component. If we try to fit the total scattered intensity without separating the diffuse part we cannot obtain meaningful fits. We have developed a method of data acquisition and processing which enabled us to separate the two scattering components and to obtain the normalized reflectivity data over several orders of magnitude in reflectivity as well as the diffusely-scattered intensity.

We proved the validity of an N-step model whereby the reflectivity from any given electron density profile can be approximated by dividing the profile into N linear steps and calculating the reflectivity from this structure using a constant value for the electron density at each step. We discussed the various types of interfaces, namely rough and graded interfaces and their representation using different interface profiles. The N-step method was used to simulate four different interface profile functions and

to test their effect on the calculated reflectivity. We concluded that the error-function profile produced the best agreement between the calculations and the experimental data.

A program has been written in C in order to calculate the x-ray specular reflectivity and diffuse scattering intensity following theoretical derivations obtained from literature. A least-squares fitting program was used in order to fit the calculated reflectivity and diffuse scattering intensity to the experimental data and to extract the different structural parameters.

Experimentally, we started by performing a survey of the effect of ion beam irradiation on four bilayers of Ni/Fe and Cu/Co and four single layers of these materials. For fitting purposes, the samples were modeled as a stack of individual layers each represented by a (2×2) matrix. By fitting the XRR data of these samples at different irradiation doses, we obtained the thickness and rms roughness of the different layers as well as their electron density values. We observed that the rms roughness of the different layers increases with increasing dose, ϕ, indicating an increased intermixing at the interfaces. The electron density profiles for these samples were constructed from the fit parameters. No change in the bulk materials electron density was observed. We discussed the limits of reliability of our fits and obtained a good picture for the extent of our model.

However, several disadvantages occurred during this survey, namely the small size of the samples, the inconsistence in the parameters of the as-deposited samples of each configuration, the large thickness of the 2000Å layers which could not be resolved by our setup and the low irradiation doses used. In a more detailed study, we overcame these difficulties by depositing Ni(500Å)/Fe(500Å) bilayers with larger dimensions and irradiating them successively to higher irradiation doses, ϕ, characterizing them at each irradiation stage by XRR, XDS and high-angle x-ray diffraction measurements.

By measuring and fitting the XRR data we obtained the structural parameters normal to the interfaces. We constructed the electron density profiles and found that the main effect of irradiation was to increase the rms roughness of the different

layers which represent more intermixing at the interfaces as ϕ increases. The iron oxide layer thickness in the $Si/SiO_2/Ni/Fe$ bilayer increased from $\sim$ 35 Å in the as-deposited sample to $\sim$ 100 Å at $\phi = 9 \times 10^{16}$ cm^{-2}.

In order to fit the ω-scans, however, the program uses numerical integration which takes a long time to calculate. Therefore, the ω-scan fits were done only for the $Si/SiO_2/Ni(500Å)/Fe(500Å)$ bilayer in order to obtain the parameters of the in-plane height-height correlation function. It was found that at low irradiation doses the interfaces are smooth as shown by a value of $h = 1$, the height-height correlation length is large $\sim$ 220 Å and the rms roughness values are small. As ϕ increases, the interfaces become more jagged as the value of h decreases to 0.5 at intermediate doses and to 0.2 at higher doses. The correlation length decreases to $\sim$ 16 Å at the highest irradiation dose and the rms roughness of the different layers increases systematically with ϕ. The obtained roughness values for the different layers agree very well with the values obtained from the reflectivity fits. Since both graded and rough interfaces reduce the specular reflectivity but only rough interfaces contribute to diffuse scattering, the agreement between roughness values obtained from XRR and XDS fits show that our interfaces are mostly of the rough type.

From XDS fits, we were able to obtain the various parameters for the sample at the highest irradiation dose for which no specular reflectivity was measured. Hence, we were able to fit both the specular and diffuse scans with the same set of parameters and, in addition, the diffuse scattering fits enabled us to analyze the sample structure in the region where the specular reflectivity component was very weak. We found that the intermixing at the interfaces can be approximated by the ballistic model of ion mixing, since $\sigma \propto \phi^{1/2}$ as predicted by the cascade mixing width relation given by equation 2.64.

High-angle x-ray diffraction measurements of the $Si/SiO_2/Ni/Fe$ bilayer were performed in order to study the crystallographic structure of the bulk material. It was found that the sample is polycrystalline with a strong texture of fcc Ni(111) and bcc Fe(101) planes parallel to the substrate surface. An Fe_3O_4(004) Bragg peak was also

observed whose intensity increased with ϕ. The grain size calculated using Scherrer formula increased with irradiation dose. The calculated grain size values agree well with the out-of-plane grain sizes obtained from cross-sectional transmission electron microscopy (XTEM) images. The in-plane grain size also increased upon irradiation as seen from both the plane-view and cross-sectional TEM images. On the other hand, the decrease in the height-height correlation length, ζ, as ϕ increases shows that ζ is not a measure of grain size but of in-plane correlations on grain surfaces.

The positions of the selected-area electron diffraction (SAED) rings agree with the Bragg peaks measured using high-angle XRD, and show the increase in Fe_3O_4 peak intensity as ϕ increases. From the XTEM images it was found that the surface iron oxide layer thickness increases with increasing ϕ from $\sim$ 30 Å in the as-deposited sample to $\sim$ 100 Å at $\phi = 1 \times 10^{17}$ ions/cm^2, in very good agreement with the values obtained from XRR fits. By noting that the XRR fits correspond to another sample which was irradiated successively and measured at relatively longer intervals of time than the four identical samples which were irradiated and measured almost simultaneously, we conclude that the increase in iron oxide thickness is mainly attributed to the irradiation process itself rather than to longer exposures to ambient air.

Hence, by using ion beam irradiation to induce intermixing at the interfaces followed by different x-ray diffraction measurement techniques in order to probe the structure, we were able to analyze the evolution in the structure of our samples both perpendicular to and parallel to the interfaces as a function of total ion dose. The bulk crystallographic structure was also obtained and TEM and XTEM results agreed well with our x-ray analysis.

Future investigations in this field include the study of other combinations of materials since the oscillatory indirect magnetic exchange coupling between magnetic layers separated by non-magnetic spacer layers is a general phenomenon and there is an unlimited number of possibilities for choosing various materials combinations. In the present thesis we were mainly concerned with structural characterization but an interesting study would be to investigate the GMR and magnetotransport properties

of the samples and to relate any change occurring in these magnetic properties upon irradiation to observed structure modifications. This study was performed for the $Si/SiO_2/Ni/Fe$ bilayers by the Thin Films Group of University of Montreal[1] [128].

Another interesting possibility is to study in more detail the roughness structure at interfaces by testing the validity of assuming a self-affine structure. The bilayers study could also be extended to the case of multilayers. Neighbouring interfaces in a multilayer can exhibit totally uncorrelated, partially correlated or perfectly conformal roughness structures. It is possible to investigate cross-correlations between neighbouring interfaces by using different forms for the height-height correlation function.

A growth mode study can be performed on the structure of the samples as a function of time during deposition using different in situ measurement techniques such as in situ helium atom scattering to measure the interlayer spacing during growth [103] and in situ scanning tunneling microscopy [107]. In addition, a more detailed investigation of IBI effects could be performed to test different theories of ion beam mixing, including the ballistic model and the effect of thermodynamic properties on the mixing rate. For example, by changing the masses or the energy of the incident ions or the mass of the target ions, we can investigate the validity of the ballistic model of ion mixing and by trying to mix combinations of materials with different heats of mixing and different cohesive energies, the thermodynamic aspects of ion mixing can be investigated.

[1]Groupe de recherche en physique et technologie des couches minces, Université de Montréal.

BIBLIOGRAPHY

[1] See for example. *Physics, Fabrication and Applications of Multilayered Structures*. edited by P. Dhez and C. Weisbuch. Plenum. New York. 1988; *Metallic Superlattices. Artificially Structured Materials*. edited by T. Shinjo and T. Takada. Elsevier. Amsterdam. 1987; *Synthetically Modulated Structures*. edited by L.L. Chang and B.C. Giessen. Academic. New York. 1985.

[2] Eric E. Fullerton. Ivan K. Schuller. H. Vanderstraeten and Y. Bruynseraede. *Phys. Rev. B* **45**(16). 9292 (1992).

[3] E. Spiller. *Physics. Fabrication and Applications of Multilayered Structures*. edited by P. Dhez and C. Weisbuch. Plenum. New York. 1988. p. 271.

[4] F. Mezei. *Physics. Fabrication and Applications of Multilayered Structures*. edited by P. Dhez and C. Weisbuch. Plenum. New York. 1988. p. 310.

[5] J. Murduck. D.W. Capone II. I.K. Schuller. S. Foner and J.B. Ketterson. *Appl. Phys. Lett.* **52**. 504 (1988).

[6] M.N. Baibich. J.M. Broto. A. Fert. F. Nguyen Van Dau. F. Petroff. P. Etienne. G. Creuzet. A. Friederich and J. Chazelas. *Phys. Rev. Lett.* **61**. 2472 (1988).

[7] S. Hashimoto and Y. Ochiai. *J. Magn. Magn. Mater.* **88**. 211 (1990).

[8] S.S.P. Parkin. R. Bhadra and K.P. Roche. *Phys. Rev. Lett.* **66**. 2152 (1991).

[9] F.J.A. den Broeder. W. Hoving and P.J.H. Bloemen. *J. Magn. Magn. Mater.* **93**. 562 (1991).

[10] Y. Huai. R.W. Cochrane and M. Sutton. *Phys. Rev. B* **48**(4). 2568 (1993).

[11] L.M. Falicov. Daniel T. Pierce. S.D. Bader. R. Gronsky. Kristl B. Hathaway. Herbert J. Hopster. David N. Lambeth. S.S.P. Parkin. Gary Prinz. Myron Salamon. Ivan K. Schuller and R.H. Victora. *J. Mater. Res.* **5**(6). 1299 (1990).

[12] G.R. Taylor. A. Isin and R.V. Coleman. *Phys. Rev.* **165**. 621 (1968); R.V. Coleman. R.C. Morris and D.J. Sellmyer. *Phys. Rev. B* **8**. 317 (1973); R.W. Klaffky and R.V. Coleman. *Phys. Rev. B* **10**. 4803 (1974).

[13] G.G. Cabrera and L.M. Falicov. *Phys. Status Solidi B* **61**. 539 (1974); *ibid.*, **62**. 217 (1974); *Phys. Rev. B* **11**. 2651 (1975).

[14] C. Carbone and S.F. Alvarado. *Phys. Rev. B* **36**. 2433 (1987).

[15] P. Grünberg, R. Schreiber, Y. Pang, M.B. Brodsky and H. Sowers, *Phys. Rev. Lett.* **57**, 2442 (1986); F. Saurenbach, U. Walz, L. Hinchey, P. Grünberg and W. Zinn, *J. Appl. Phys.* **63**, 3473 (1988).

[16] R.E. Camley and J. Barnaś, *Phys. Rev. Lett.* **63**(6), 664 (1989).

[17] D.M. Edwards, J. Mathon, R.B. Muniz and M.S. Phan, *Phys. Rev. Lett.* **67**(4), 493 (1991).

[18] S.S.P. Parkin, N. More and K.P. Roche, *Phys. Rev. Lett.* **64**(19), 2304 (1990).

[19] J.E. Mattson, C.H. Sowers, A. Berger and S.D. Bader, *Phys. Rev. Lett.* **68**(21), 3252 (1992).

[20] A. Fert, A. Barthélémy, P. Etienne, S. Lequien, R. Loloee, D.K. Lottis, D.H. Mosca, F. Petroff, W.P. Pratt and P.A. Schroeder, *J. Magn. Magn. Mater.* **104-107**, 1712 (1992).

[21] S.S.P. Parkin, R.F.C. Farrow, R.F. Marks, A. Cebollada, G.R. Harp and R.J. Savoy, *Phys. Rev. Lett.* **72**(23), 3718 (1994).

[22] S.S.P. Parkin, *Phys. Rev. Lett.* **67**(25), 3598 (1991).

[23] E.E. Fullerton, D.M. Kelly, J. Guimpel and I.K. Schuller, *Phys. Rev. Lett.* **68**, 859 (1992).

[24] X. Bian, J.O. Ström-Olsen, Z. Altounian, Y. Huai and R.W. Cochrane, *Appl. Phys. Lett.* **62**(26), 3525 (1993).

[25] X. Meng, X. Bian, R. Abdouche, W.B. Muir, J.O. Ström-Olsen, Z. Altounian and M. Sutton, *J. Appl. Phys.* **76**(10), 7084 (1994).

[26] M. Suzuki and Y. Taga, *Phys. Rev. B* **52**, 361 (1995).

[27] P. Beliën, R. Schad, C.D. Potter, G. Verbanck, V.V. Moshchalkov and Y. Bruynseraede, *Phys. Rev. B* **50**(14), 9957 (1994).

[28] T. Veres, M. Cai, R. Morel, R.W. Cochrane, R. Abdouche and M. Sutton, *J. Appl. Phys.* **81**(8), 4758 (1997).

[29] X. Bian, X. Meng, J.O. Ström-Olsen, Z. Altounian, W.B. Muir, M. Sutton and R.W. Cochrane, *J. Appl. Phys.* **76**(10), 6796 (1994).

[30] M. Piecuch, *Revue Phys. Appl.* **23**, 1727 (1988).

[31] M.A. El Khakani, G. Marest, N. Moncoffre and J. Tousset, *Nucl. Instr. Met. Phys. Res.* **B52**, 182 (1990).

[32] G. Marest and M.A. El Khakani, *Nucl. Instr. Met. Phys. Res.* **B59/60**, 833 (1991).

[33] Grzegorz Gladyszewski and Andrzej Smal, *Nucl. Instr. Met. Phys. Res.* **B62**, 541 (1992).

[34] C. Tosello, F. Ferrari, R. Brand, W. Keune, G. Marest, M.A. El Khakani, J. Parellada, G. Principi, S. Lo Russo, V. Rigato and S. Enzo, *Nucl. Instr. Met. Phys. Res.* **B80/81**, 417 (1993).

[35] L.F. Schelp, M. Carara, A.D.C. Viegas, M.A.Z. Vasconcellos and J.E. Schmidt, *J. Appl. Phys.* **75**(10), 5262 (1994).

[36] David M. Kelly, Ivan K. Schuller, V. Korenivski, K.V. Rao, Kim K. Larsen, J. Bottiger, E.M. Gyorgy and R.B. van Dover, *Phys. Rev. B* **50**(5), 3481 (1994).

[37] G. Gladyszewski, J. Barnaś, K. Temst, G. Verbanck, R. Schad, P. Beliën, E. Kunnen, F. Bodart and Y. Bruynseraede, *J. Magn. Magn. Mat.* **156**, 381 (1996).

[38] F. Tamisier, C. Jaouen, Ph. Guérin and G. Gladyszewski, *Thin Solid Films* **275**, 247 (1996).

[39] L. Amaral, R.B. Scorzelli, M.E. Brückman, A. Paesano, J.E. Schmidt, T. Shinjo and N. Hosoito, *J. Appl. Phys.* **81**(8), 4773 (1997).

[40] M. Cai, T. Veres, S. Roorda, R.W. Cochrane, R. Abdouche and M. Sutton, *J. Appl. Phys.* **81**(8), 5200 (1997).

[41] M. Cai, T. Veres, R.W. Cochrane, S. Roorda, R. Abdouche and M. Sutton, *Mat. Res. Soc. Symp. Proc.* **504**, 197 (1998).

[42] Grzegorz Gladyszewski, *Thin Solid Films* **204**, 473 (1991).

[43] F.E. Christensen, *Revue Phys. Appl.* **23**, 1701 (1988).

[44] J. Bai, M. Tomkiewicz and P.A. Montano, *Zeitschrift Für Physik B* **97**, 465 (1995).

[45] D. Gibbs, B.M. Ocko, D.M. Zehner and S.G.J. Mochrie, *Phys. Rev. B* **38**(11), 7303 (1988).

[46] A. Braslau, P.S. Pershan, G. Swislow, B.M. Ocko and J. Als-Nielsen, *Phys. Rev. A* **38**(5), 2457 (1988).

[47] P.S. Pershan, A. Braslau, A.H. Weiss and J. Als-Nielsen, *Phys. Rev. A* **35**(11), 4800 (1987).

[48] M. Chladek, C. Dorner, A. Buchal, V. Valvoda and H. Hoffmann, *J. Appl. Phys.* **80**(3), 1437 (1996).

[49] J.B. Kortright, D.D. Awschalom, J. Stohr, S.D. Bader, Y.U. Idzerda, S.S.P. Parkin, I.K. Schuller and H.-C. Siegmann, *J. Magn. Magn. Mat.* **207**(1-3), 7 (1999).

[50] L. Névot and P. Croce, *Revue Phys. Appl.* **15**, 761 (1980).

[51] S.K. Sinha, E.B. Sirota, S. Garoff and H.B. Stanley, *Phys. Rev. B* **38**(4), 2297 (1988).

[52] J. Daillant and O. Bélorgey, *J. Chem. Phys.* **97**(8), 5824 (1992).

[53] V. Holý, J. Kuběna, I. Ohlídal, K. Lischka and W. Plotz, *Phys. Rev. B* **47**(23), 15896 (1993).

[54] V. Holý and T. Baumbach, *Phys. Rev. B* **49**(15), 10668 (1994).

[55] C. Schug, P. Lamparter and S. Steeb, *Physica B* **248**, 62 (1998).

[56] U. Klemradt, M. Funke, M. Fromm, B. Lengeler, J. Peisl and A. Förster, *Physica B* **221**, 27 (1996).

[57] J.B. Kortright, *J. Appl. Phys.* **70**(7), 3620 (1991).

[58] R. Paniago, H. Homma, P.C. Chow, S.C. Moss, Z. Barnea, S.S.P. Parkin and D. Cookson, *Phys. Rev. B* **52**(24), R17052 (1995).

[59] R. Paniago, H. Homma, P.C. Chow, H. Reichert, S.C. Moss, Z. Barnea, S.S.P. Parkin and D. Cookson, *Physica B* **221**, 10 (1996).

[60] M. Jergel, V. Holý, E. Majková, Š. Luby and R. Senderák, *J. Magn. Magn. Mat.* **156**, 117 (1996).

[61] T. Salditt, D. Lott, T.H. Metzger, J. Peisl, G. Vignaud, J.F. Legrand, G. Grübel, P. Hoghoi and O. Schärpf, *Physica B* **221**, 13 (1996).

[62] T. Salditt, T.H. Metzger and J. Peisl, *Phys. Rev. Lett.* **73**(16), 2228 (1994).

[63] S.K. Sinha, M.K. Sanyal, S.K. Satija, C.F. Majkrzak, D.A. Neumann, H. Homma, S. Szpala, A. Gibaud and H. Morkoc, *Physica B* **198**, 72 (1994).

[64] V. Holý, C. Giannini, L. Tapfer, T. Marschner and W. Stolz, *Phys. Rev. B* **55**(15), 9960 (1997).

[65] A.V. Andreev, Yu. V. Ponomarev, I.R. Prudnikov and N.N. Salashchenko, *Phys. Rev. B* **57**(20), 13113 (1998).

[66] Qun Shen, C.C. Umbach, B. Weselak and J.M. Blakely, *Phys. Rev. B* **53**(8), R4237 (1996).

[67] R. Stömmer and U. Pietsch, *J. Phys. D: Appl. Phys.* **29**, 3161 (1996).

[68] V. Nitz, M. Tolan, J.-P. Schlomka, O.H. Seeck, J. Stettner, W. Press, M. Stelzle and E. Sackmann, *Phys. Rev. B* **54**(7), 5038 (1996).

[69] R. Paniago, R. Forrest, P.C. Chow, S.C. Moss, S.S.P. Parkin and D. Cookson, *Phys. Rev. B* **56**(20), 13442 (1997).

[70] B.M. Clemens and J.G. Gay, *Phys. Rev. B* **35**(17), 9337 (1987).

[71] J.-P. Locquet, D. Neerinck, L. Stockman, Y. Bruynseraede and Ivan K. Schuller, *Phys. Rev. B* **39**(18), 13338 (1989).

[72] F.J. Lamelas, H. David He and Roy Clarke, *Phys. Rev. B* **43**, 12296 (1991).

[73] Li Yi, C. Polaczyk and D. Riegel, *J. Magn. Magn. Mat.* **165**(1-3), 227 (1997).

[74] W. Kuch and S.S.P. Parkin, *J. Magn. Magn. Mat.* **184**(2), 127 (1998).

[75] K. Heinz, S. Müller and L. Hammer, *J. Phys.: Condens. Matter* **11**, 9437 (1999).

[76] R.G. Abal and A.M. Llois, *Revista Mexicana de Fisica* **44**(3), 208 (1998).

[77] M. Cai, T. Veres, R. Morel and R.W. Cochrane, *J. Appl. Phys.* **79**(8), pt.2B, 6289 (1996).

[78] O. Donzelli, G. Fratucello, F. Nizzoli, D. Palmeri, F. Lucari and F. D'Orazio, *Magnetic Ultrathin Films, Multilayers and Surfaces, Materials Research Society Symposium Proceedings* **475**, 513 (1997).

[79] Y. Huai, M. Tan and R. Rottmayer, *IEEE Transactions on Magnetics* **34**(4), pt.1, 918 (1998).

[80] W. Tang, C. Gerhards, J. Heise and H. Zabel, *J. Magn. Magn. Mat.* **191**(1-2), 45 (1999).

[81] D.K. Inia, F.W.J. Feiner, W.M. Arnoldbik, A.M. Vredenberg and D.O. Boerma, *Surface & Coatings Technology* **83**(1-3), 65 (1996).

[82] D.K. Inia, F.D. Tichelaar, W.M. Arnoldbik, A.M. Vredenberg and D.O. Boerma, *J. Mat. Res.* **13**(2), 440 (1998).

[83] L. Thome and J. Jagielski, *Nucl. Instr. Met. Phys. Res.: Section B-Beam Interactions with Materials & Atoms* **B106**(1-4), 65 (1995).

[84] A. Perin, R. Gupta, G. Principi, C. Tosello, L.M. Gratton, E. Kuzmann and Z. Klencsar, *Surface & Coatings Technology* **103-104**(1), 93 (1998).

[85] R. Gupta, A. Gupta, D.K. Avasthi, G. Principi and C. Tosello, *Nucl. Instr. Met. Phys. Res.: Section B-Beam Interactions with Materials & Atoms* **156**(1), 153 (1999).

[86] M.J. Hall, E.D. Whitton, D.B. Jardine, R.E. Somekh, J.E. Evetts and J.A. Leake, *Thin Solid Films* **275**(1-2), 195 (1996).

[87] M.J. Hall, D.B. Jardine, J.E. Evetts, J.A. Leake and R.E. Somekh, *J. Magn. Magn. Mat.* **173**(3), 253 (1997).

[88] R. Gao, Y. Liu, S. Yan, D. Zhang and L. Zhang, *Journal of Materials Science & Technology* **14**(2), 139 (1998).

[89] X.S. Wu, Q.S. Bie, Z.S. Lin, A. Hu, H.R. Zhai and S.S. Jiang, *Modern Physics Letters B* **13**(9-10), 325 (1999).

[90] N.D. Telling, M.D. Crapper, D.R. Lovett, S.J. Guilfoyle, C.C. Tang and M. Petty, *Thin Solid Films* **317**(1-2), 278 (1998).

[91] M. Schlesinger, K.D. Bird and D.D. Snyder, *Proceedings of the Second Symposium on Electrochemically Deposited Thin Films*. Electrochem. Soc. p. 97 (1995).

[92] D.S. Lashmore and S.Z. Hua, *Polycrystalline Thin Films: Structure, Texture, Properties, and Applications II*. Symposium. Mater. Res. Soc. p. 161 (1996).

[93] N. Lebbad, J. Voiron, B. Nguyen and E. Chainet, *Thin Solid Films* **275**(1-2), 216 (1996).

[94] M. Shima, L. Salamanca-Riba, T.P. Moffat, R.D. McMichael, *High-Density Magnetic Recording and Integrated Magneto-Optics: Materials and Devices, Materials Research Society Symposium Proceedings* **517**, p.61 (1998).

[95] E. Chassaing, A. Morrone and J.E. Schmidt, *Journal of the Electrochemical Society* **146**(5), 1794 (1999).

[96] J. Thomas, K. Brand, A.A. Gorbunov and K. Wetzig, *Fresenius Journal of Analytical Chemistry* **365**(1-3), 263 (1999).

[97] I. Pape, T.P.A. Hase, B.K. Tanner, H. Laidler, C. Emmerson, T. Shen and B.J. Hickey, *J. Magn. Magn. Mat.* **156**, 373 (1996).

[98] T.P.A. Hase, I. Pape, B.K. Tanner, H. Laidler, P. Ryan and B.J. Hickey, *J. Magn. Magn. Mat.* **177-181**, 1164 (1998).

[99] D.B. Jardine, M.J. Hall, R.E. Somekh and J.E. Evetts, *Thin Solid Films* **275**(1-2), 111 (1996).

[100] K. Kandasamy, M. Masuda and Y. Hayashi, *Journal of Alloys & Compounds* **282**(1-2), 23 (1999).

[101] D.J. Kubinski and H. Holloway, *J. Magn. Magn. Mat.* **165**(1-3), 104 (1997).

[102] W.H. Butler, X-G. Zhang, D.M.C. Nicholson, T.C. Schulthess and J.M. MacLaren, *J. Appl. Phys.* **79**(8), pt.2A, 5282 (1996); *Phys. Rev. Lett.* **76**(17), 3216 (1996).

[103] P.C. Dastoor and W. Allison, *Surface & Interface Analysis* **28**(1), 65 (1999).

[104] D.J. Larson, A.K. Petford-Long and A. Cerezo, *Materials Science & Engineering A - Structural Materials Properties, Microstructure & Processing* **270**(1), 69 (1999); D.J. Larson, A.K. Petford-Long, A. Cerezo and G.D.W. Smith, *Acta Materialia* **47**(15-16), 4019 (1999).

[105] C. Prieto, R. Castaner, J.L. Martinez, A. De Andres, J. Trigo and J.M. Sanz, *J. Magn. Magn. Mat.* **161**, 31 (1996); R. Castaner, C. Prieto, A. De Andres, J.L. Martinez, J. Trigo and J.M. Sanz, *Solid State Communications* **98**(2), 179 (1996).

[106] P. Le Fevre, H. Magnan and D. Chandesris, *Surface Science* **352-354**, 923 (1996).

[107] T.J. Minvielle, R.L. White and R.J. Wilson, *J. Appl. Phys.* **79**(8), pt.2A, 5116 (1996).

[108] K.Y. Kok, M.J. Hall and J.A. Leake, *J. Magn. Magn. Mat.* **156**, 51 (1996).

[109] A. de Bernabé, M.J. Capitán, H.E. Fischer and C. Prieto, *J. Appl. Phys.* **84**(4), 1881 (1998).

[110] E. Chason and T.M. Mayer, *Critical Reviews in Solid State and Materials Sciences* **22**(1), 1 (1997).

[111] M. Born and E. Wolf. *Principles of Optics.* Pergamon, Oxford, 1975.

[112] B.E. Warren. *X-Ray Diffraction.* Dover Publications, Inc., New York, 1990.

[113] B. Pardo, T. Megademini and J.M. André, *Revue Phys. Appl.* **23**, 1579 (1988).

[114] B. Vidal and P. Vincent, *Applied Optics* **23**(11), 1794 (1984).

[115] L.D. Landau and E.M. Lifshitz, *Electrodynamics of Continuous Media.* Pergamon Press, London, 1960.

[116] See references in [115].

[117] P. Croce, *J. Optics (Paris)* **8**(2), 127 (1977); *J. Optics (Paris)* **14**(4), 213 (1983).

[118] A.N. Bloch and S.A. Rice, *Phys. Rev.* **185**, 933 (1969).

[119] M. Kardar, G. Parisi and Y.C. Zhang, *Phys. Rev. Lett.* **56**, 889 (1986).

[120] T. Salditt, T.H. Metzger, Ch. Brandt, U. Klemradt and J. Peisl, *Phys. Rev. B* **51**(9), 5617 (1995).

[121] B.B. Mandelbrodt, *The Fractal Geometry of Nature.* Freeman, New York, 1982.

[122] G. Palasantzas and J. Krim, *Phys. Rev. B* **48**, 2873 (1993); G. Palasantzas, *Phys. Rev. B* **48**, 14472 (1993).

[123] Nastasi and Michael Anthony, *Ion-Solid Interactions*, Cambridge, New York, Cambridge University Press, 1996.

[124] P. Sigmund and A. Gras-Marti, *Nucl. Instr. & Methods* **182/183**, 25 (1981).

[125] Y.-T. Cheng, Thermodynamic and fractal geometric aspects of ion-solid interactions, *Materials Science Reports* **5**(2), 45 (1990).

[126] A.R. Miedema, The heat of formation of alloys, *Philips Technical Review* **36**(8), 217 (1976).

[127] W.L. Johnson, Y.-T. Cheng, M. Van Rossum and M.-A. Nicolet, *Nucl. Instr. & Methods* **B7/8**, 657 (1985).

[128] T. Veres, P. Desjardins, R.W. Cochrane, M. Cai, M. Rouabhi, L. Cheng, R. Abdouche and M. Sutton, *submitted to Thin Solid Films.*

[129] Tianqu Gu. *The Resolution Function of Triple-Crystal X-ray Diffractometer and Its Applications.* Ph.D. thesis, McGill University, 1994.

[130] Yushan Shi. *A High Resolution X-ray Diffractometer for Studying Crystal Epitaxy.* M.Sc. thesis, McGill University, 1987.

[131] A.H. Compton and S.K. Allison. *X-Ray in Theory and Experiment.* D.Van Nostrand Company, Inc., New York, 1946.

[132] B.D. Cullity, *Elements of x-ray diffraction*, Addison-Wesley Publishing Company, Inc., 1978.

[133] *International Tables for X-ray Crystallography.* Vol.III, the Kynoch Press, Birminghan, 1974.

[134] G.K. Wertheim, M.A. Butler, K.W. West and D.N.E. Buchanan, *Rev. Sci. Instrum.* **45**, 1369 (1974).

[135] Yushan Shi. *X-ray Structural Studies of Heteroepitaxy of Gallium-Indium Arsenide on Gallium Arsenide.* Ph.D. thesis, McGill University, 1992.

[136] D.G. Stearns, *J. Appl. Phys.* **65**, 491 (1989).

[137] Yiming Huai. *Structural and Transport Properties of Co/Re and Co/Ti Multilayer Films.* Ph.D. thesis, Université de Montréal, 1992.

[138] V.A. Yakovlev, Q. Liu and E.A. Irene, *J. Vac. Sci. Technol.* **A10**, 427 (1992).

[139] Q. Liu, J.F. Wall and E.A. Irene, *J. Vac. Sci. Technol.* **A12**, 2625 (1994).

[140] T.A. Rabedeau, I.M. Tidswell, P.S. Pershan, J. Bevk and B.S. Freer, *Appl. Phys. Lett.* **59**, 706 (1991); *Appl. Phys. Lett.* **59**, 3422 (1991).

[141] M.T. Tang, K.W. Evans-Lutterodt, G.S. Higahsi and T. Boone, *Appl. Phys. Lett.* **62**, 3144 (1993).

[142] S.C. Woronick, W. Ng, A. Krol, Y.H. Kao and E. Arnold, *J. Appl. Phys.* **69**, 1631 (1991).

[143] S.M. Herald, J.K.D. Jayanetti, A.A. Bright and G.W. Rubloff, *J. Vac. Sci. Technol.* **A8**, 2046 (1990).

[144] E. Chason, T.M. Mayer, A. Payne and D. Wu, *Appl. Phys. Lett.* **60**, 2353 (1992).

[145] *Binary Alloy Phase Diagrams.* Vol.1, p.758-760, Thaddeus B. Massalski. American Society for Metals, Metals Park, Ohio 44073, 1986.

[146] T. Nishizawa and K. Ishida. *Bull. Alloy Phase Diagrams.* 5(2), Apr. 1984.

[147] J.F. Ziegler and J.P. Biersack, *The Stopping and Range of Ions in Solids*, Pergamon Press, New York, 1985.